

# CONTRACTOR REPORT

8024

SAND86-7167  
Unlimited Release  
UC-70

RS-8232-2/65513

C.1

## Modeling of Ground-Water Flow in the Culebra Dolomite at the Waste Isolation Pilot Plant (WIPP) Site: Interim Report



8232-2/065513



00000001 -

A. Haug, V. A. Kelley, A. M. LaVenue, J. F. Pickens  
INTERA Technologies, Inc.  
6850 Austin Center Blvd., Suite 300  
Austin, TX 78731

Printed March 1987

1061483

Issued by Sandia National Laboratories, operated for the United States Department of Energy by Sandia Corporation.

**NOTICE:** This report was prepared as an account of work sponsored by an agency of the United States Government. Neither the United States Government nor any agency thereof, nor any of their employees, nor any of their contractors, subcontractors, or their employees, makes any warranty, express or implied, or assumes any legal liability or responsibility for the accuracy, completeness, or usefulness of any information, apparatus, product, or process disclosed, or represents that its use would not infringe privately owned rights. Reference herein to any specific commercial product, process, or service by trade name, trademark, manufacturer, or otherwise, does not necessarily constitute or imply its endorsement, recommendation, or favoring by the United States Government, any agency thereof or any of their contractors or subcontractors. The views and opinions expressed herein do not necessarily state or reflect those of the United States Government, any agency thereof or any of their contractors or subcontractors.

Printed in the United States of America  
Available from  
National Technical Information Service  
U.S. Department of Commerce  
5285 Port Royal Road  
Springfield, VA 22161

NTIS price codes  
Printed copy: A15  
Microfiche copy: A01

SAND86-7167

**MODELING OF GROUND-WATER FLOW IN THE CULEBRA DOLOMITE  
AT THE WASTE ISOLATION PILOT PLANT (WIPP) SITE:**

**INTERIM REPORT**

Prepared For

SANDIA NATIONAL LABORATORIES  
ALBUQUERQUE, NEW MEXICO

By

A. Haug  
V. A. Kelley  
A. M. LaVenue  
J. F. Pickens

INTERA Technologies, Inc.  
6850 Austin Center Blvd., Suite 300  
Austin, Texas 78731  
(512) 346-2000

Printed March 1987

## EXECUTIVE SUMMARY

This hydrogeologic modeling study has been performed as part of the regional hydrologic characterization of the Waste Isolation Pilot Plant (WIPP) in southeastern New Mexico. The study resulted in an estimation of the transmissivity distribution, hydraulic potentials, flow field, and fluid densities in the Culebra Dolomite Member of the Permian Rustler Formation at the WIPP site.

The three-dimensional finite-difference code SWIFT II was employed for the numerical modeling, using variable-fluid-density and both single- and double-porosity formulations. The variable-fluid-density approach does not, at this stage, include changes in brine density within the model due to local reaction, such as halite dissolution. The spatial scale of the model, 12.24 km by 11.70 km, was chosen to allow simulation of a 62-day pumping test, conducted in fall 1985 at the H-3 hydropad south of the center of the WIPP site. The modeled area includes and extends beyond the WIPP controlled zone (Zone 3).

The work performed consisted of modeling the hydrogeology of the Culebra using two different approaches: (1) steady-state modeling to develop the best estimate of the undisturbed head and fluid-density distribution, i.e., of the situation prior to sinking of the WIPP shafts, which began in 1981; and (2) superimposed transient modeling of local hydrologic responses to excavation of the three WIPP shafts at the center of the WIPP site, as well as to various well tests. Boundary conditions (prescribed constant fluid pressures and densities) were estimated using hydraulic-head and fluid-density data obtained from 40 wells at and near the WIPP site. The transient modeling response in the interior of the model was superimposed on the steady-state baseline utilizing the same boundary conditions.

The initial spatial transmissivity distribution in the Culebra dolomite was obtained using kriging techniques. The resulting initial steady-state model was calibrated against the observed formation pressures and observed fluid densities. Calibration parameters were the prescribed boundary conditions and transmissivities.

The resulting spatial transmissivity distribution is characterized by a high-transmissivity zone extending between the H-11 hydropad (within the WIPP control zone) and the southern model boundary, which is outside the control zone. Modeled transmissivities within this zone are as great as  $2 \times 10^{-4} \text{ m}^2/\text{s}$ . Inclusion of this high-transmissivity zone is necessary in the model to obtain the relatively low freshwater heads observed at both H-11 and DOE-1. The location of the zone is constrained to be east of hole P-17, because placing it further west, between holes H-4 and P-17, does not result in satisfactory agreement between observed and calculated freshwater heads. The final transmissivity distribution is also characterized by a relatively large area of low transmissivities (less than approximately  $10^{-6} \text{ m}^2/\text{s}$ ). This area is mainly near the center of the site, and includes holes H-1, H-2, WIPP holes 12, 18, 19, 21, and 22, P-18, and H-5, in addition to the WIPP shafts.

After calibration of the steady-state model against the best estimate of the undisturbed freshwater heads, the remaining difference between observed and calculated heads is less than 1.1 m for all well locations. Given the uncertainty associated with observed heads, the calibration is considered satisfactory.

Formation-fluid densities within the modeled area range from 1.00 to greater than  $1.10 \text{ g/cm}^3$ . Assuming no internal reaction and complete confinement of the Culebra, it was not possible to calibrate the steady-state model completely against the observed densities. Although the final differences between observed and calculated densities are generally less than  $0.01 \text{ g/cm}^3$ , a difference of about  $0.04 \text{ g/cm}^3$  remains at and near well

P-17, with the measured fluid density exceeding the modeled value. In addition, it was impossible to reproduce fully the north-to-south decrease in formation-water density observed in the western part of the model area. In this area, modeled fluid densities exceed those measured. One reason for these inconsistencies may be that the hydrogeology of the Culebra is influenced by vertical fluxes into or out of the unit, from the overlying Magenta Member (by way of the intervening Tamarisk Member) and/or from the underlying unnamed member of the Rustler or Rustler/Salado contact zone. Another possibility is that boundary conditions for the modeled area are transient on the time scale required for fluid flow.

In order to investigate the possibility of vertical ground-water flow into the Culebra dolomite, scoping calculations were conducted for two areas: (1) the vicinity of P-17; and (2) the western portion of the model area (south of H-6 and west of H-1). Based on these calculations, a high-density (highly-saline) flux from the Rustler-Salado residuum, through the unnamed lower member of the Rustler, into the Culebra appears possible at and near P-17. The order of magnitude of the volumetric flux is estimated to be about  $1.8 \times 10^{-12}$  m/s, or 0.1 l/min, distributed over an area of 1 km<sup>2</sup>. The simulations at P-17 indicate that an even smaller flux of high-density brine can significantly influence the calculated density distribution. In fact, given the estimated vertical head distribution at P-17, a low hydraulic conductivity of less than  $10^{-12}$  m/s had to be assigned to the unnamed member of the Rustler to avoid affecting fluid density within the overlying Culebra. Alternatively, there may be an unresolved problem with the well completion at P-17. In the western model area, a low-density (slightly-saline) flux downward from the Magenta dolomite (via the intervening Tamarisk Member) into the Culebra is possible, consistent with sparse head-potential and brine-density data from the Magenta. Depending on the transmissivities assumed for the Magenta and Tamarisk, a vertical flux of  $5 \times 10^{-12}$  m/s, or 0.3 l/min per km<sup>2</sup>, seems to be possible.

After final calibration of the steady-state model, the following drilling and testing activities at the WIPP shafts and well locations were incorporated into the model and superimposed onto the steady-state head distribution: (1) a simplified but complete shaft history since 1981; (2) three pumping tests and a series of slug tests conducted at the H-2 hydropad in 1982 and 1984; (3) the H-3 convergent-flow tracer test conducted in 1984; (4) the H-3 step-drawdown test conducted in 1985; (5) the H-3 multipad pumping test in 1985 and 1986; and (6) the convergent-flow tracer test at the H-4 pad conducted between 1982 and 1984. The hydraulic situation in the Culebra dolomite was simulated for the period from January 1, 1981 to December 31, 1986.

The transient simulation generally resulted in good agreement between model-calculated and observed long-term freshwater-head histories at the shaft and well locations (e.g., H-1, H-2, H-3, DOE-1, and H-11). This indicates that the transmissivity distribution in this region is realistic. It was not possible, however, to reproduce the short-term observed transient head responses at the shaft location and nearby wells (WIPP-21, WIPP-22, and WIPP-19) to the H-3 multipad test without assuming additional leakage from the Culebra dolomite into the waste-handling shaft. This assumed increase in leakage results in much better agreement between calculated and observed pressures. Thus, it seems likely that the observed freshwater heads near the WIPP shafts in fall 1985 and the first half of 1986 were influenced by two partially concurrent events: (1) the H-3 multipad pumping test; and (2) additional leakage in the waste-handling shaft.

A sensitivity analysis using the double-porosity flow conceptualization of SWIFT II was conducted to assess the possible impact of dual-porosity behavior on model results. For the purpose of regional estimation of the ground-water flow field and head distribution, the double-porosity conceptualization does not provide significantly different results from those obtained using the single-porosity approach.

The modeling study discussed in this interim report is based on the transmissivity data available as of April 1986 as well as on the hydraulic-head data available as of August 1986. The next step of the modeling study will incorporate more recent transmissivity and hydraulic-head data. In addition, the model area will be enlarged and the model will be calibrated to the results of a second (northern) multipad pumping test to be conducted early in 1987. The final results of the latter modeling study will be available early in 1988.



## TABLE OF CONTENTS

	PAGE
EXECUTIVE SUMMARY .....	1
TABLE OF CONTENTS .....	vii
LIST OF FIGURES .....	xi
LIST OF TABLES .....	xxi
LIST OF PLATES .....	xxv
1.0 INTRODUCTION .....	1-1
1.1 Objectives and Scope .....	1-1
1.2 Previous Modeling Studies of Ground-Water Flow in the Culebra Dolomite .....	1-2
1.3 Approach to Modeling of Ground-Water Flow in the Culebra Dolomite .....	1-5
2.0 SITE DESCRIPTION .....	2-1
2.1 General .....	2-1
2.2 Stratigraphy .....	2-1
2.3 Regional Hydrogeology .....	2-3
2.4 Regional Dissolution and the Effects Upon Flow in the Rustler Formation .....	2-5
3.0 MODEL CONCEPTUALIZATION FOR THE CULEBRA DOLOMITE .....	3-1
3.1 SWIFT II Code Description .....	3-1
3.1.1 General Approach .....	3-2
3.1.2 The Global Transient-State Equations for Flow, Heat, Brine, and Radionuclide Transport .....	3-4
3.1.3 The Global Steady-State Equations for Flow and Brine Transport .....	3-7
3.1.4 The Local Transient-State Equations for Flow, Heat, Brine, and Trace Species (Radionuclide) Transport Within the Rock Matrix .....	3-9

## TABLE OF CONTENTS

(continued)

3.2	Geometric Model Description .....	3-12
3.2.1	Horizontal Dimensions (Model Area) .....	3-13
3.2.2	Vertical Dimension .....	3-14
3.2.3	Model Grid .....	3-14
3.2.4	Elevation of the Grid Blocks .....	3-16
3.3	Physical Model Constants .....	3-17
3.3.1	Fluid Properties .....	3-17
3.3.2	Rock Properties .....	3-20
3.3.3	Transport Parameters .....	3-21
3.4	Hydrologic Model Parameters .....	3-22
3.4.1	Initial Transmissivities .....	3-22
3.4.1.1	Theoretical Aspects of Kriging .....	3-23
3.4.1.2	The Universal Kriging Program K603 .....	3-28
3.4.1.3	Analysis of the Observed Transmissivities .....	3-30
3.4.1.4	The Kriged Initial Transmissivities .....	3-33
3.4.2	Storativities .....	3-34
3.5	Initial Boundary Conditions .....	3-35
3.5.1	The Undisturbed Hydrogeologic Situation .....	3-35
3.5.2	Initial Lateral Boundary Conditions .....	3-37
3.5.3	Upper and Lower Boundary Conditions .....	3-38
3.6	Sinks and Sources .....	3-38
3.6.1	The Undisturbed Hydrogeologic Situation .....	3-38
3.6.2	The Hydrologic Situation Since 1981 .....	3-39
3.7	Initial Conditions .....	3-40
4.0	SIMULATION OF FLOW UNDER UNDISTURBED HYDRAULIC CONDITIONS (PRE-SHAFT CONDITIONS) .....	4-1
4.1	Simulation Using the Initial Transmissivities .....	4-1
4.2	Calibration of the Model Using the Observed Freshwater Heads .....	4-2

## TABLE OF CONTENTS

(continued)

4.3	Pressure-Calibrated Model for Undisturbed Hydraulic Conditions .....	4-8
4.4	Sensitivity of the Model to Dispersivity .....	4-12
4.5	Calibration of the Model Using the Observed Formation-Water Densities .....	4-13
4.6	Density-Calibrated Model for Undisturbed Hydraulic Conditions .....	4-17
4.7	Summary of the Steady-State Modeling .....	4-22
5.0	SIMULATION OF TRANSIENT FLOW RESULTING FROM SHAFT ACTIVITIES AND WELL TESTS .....	5-1
5.1	Implementation of Shaft Activities .....	5-1
5.1.1	The Early Shaft History .....	5-2
5.1.2	The Open-Shaft Period .....	5-5
5.1.3	The Shaft Leakage After Shaft Sealing .....	5-7
5.1.4	Implementation of the Shaft History .....	5-8
5.2	Implementation of Well Tests .....	5-8
5.2.1	Well Tests at the H-2 Hydropad .....	5-9
5.2.2	Convergent-Flow Tracer Test at the H-3 Hydropad .....	5-10
5.2.3	Step-Drawdown Test at the H-3 Hydropad .....	5-11
5.2.4	H-3 Multipad Pumping Test .....	5-11
5.2.5	Convergent-Flow Tracer Test at the H-4 Hydropad .....	5-12
5.3	Time-Step Considerations .....	5-12
5.4	Transient Simulation Using the Density-Calibrated Steady-State Model .....	5-13
5.4.1	Simulation of the Early Shaft History .....	5-14
5.4.2	Simulation of the Open-Shaft Period .....	5-15
5.4.3	Simulation of the Shaft Leakage After Shaft Sealing .....	5-15
5.4.4	Simulation of the H-2 Well Tests .....	5-16
5.4.5	Simulation of the H-3 Convergent-Flow Tracer Test .....	5-16

## TABLE OF CONTENTS

(continued)

5.4.6	Simulation of the H-3 Step-Drawdown Test .....	5-17
5.4.7	Simulation of the H-3 Multipad Pumping Test .....	5-17
5.4.8	Simulation of the H-4 Convergent-Flow Tracer Test .....	5-20
5.5	Implementation and Simulation of Additional Leakage at the Shaft Location .....	5-20
5.6	Summary of the Transient Simulation .....	5-25
6.0	SENSITIVITY OF THE MODEL CONCEPTUALIZATION TO VERTICAL FLUXES TO AND FROM THE CULEBRA .....	6-1
6.1	Estimation of Possible Vertical Fluxes .....	6-1
6.1.1	Estimation of Vertical Flux through the Unnamed Lower Member at P-17 .....	6-2
6.1.2	Estimation of Vertical Flux Through the Tamarisk Member in the Western Model Area .....	6-3
6.2	Implementation of a High-Salinity Vertical Flux at P-17 and Simulation of the Undisturbed Hydraulic Conditions .....	6-6
6.3	Implementation of a Low-Salinity Vertical Flux in the Western Model Area and Simulation of the Undisturbed Hydraulic Conditions .....	6-7
6.4	Summary of the Sensitivity Analysis Using Vertical Fluxes .....	6-12
7.0	APPLICATION OF A DOUBLE-POROSITY FLOW CONCEPTUALIZATION .....	7-1
7.1	Introduction .....	7-1
7.2	Estimation of Double-Porosity Parameters .....	7-4
7.3	Preliminary Scoping Calculations .....	7-9
7.4	Discussion of the Double-Porosity Simulation Results .....	7-13
7.5	Conclusions from Double-Porosity Simulations .....	7-14
8.0	CONCLUSIONS .....	8-1

TABLE OF CONTENTS

(continued)

9.0 BIBLIOGRAPHY ..... 9-1

FIGURES

TABLES

APPENDIX A NOTATION FOR SECTION 3.1

APPENDIX B CONVERSION FACTORS

APPENDIX C TRANSMISSIVITIES OF THE CULEBRA DOLOMITE  
(by G.J. Saulnier and A. Haug)

APPENDIX D EQUIVALENT FRESHWATER ELEVATIONS  
(by G.A. Freeze)

APPENDIX E CONSISTENCY OF DENSITIES AND CHEMICAL COMPOSITION OF  
WATER SAMPLES FROM THE CULEBRA DOLOMITE  
(by A.J. Meijer, J.L. Lolcama, and F.J. Pearson)

APPENDIX F REVIEW AND CHRONOLOGY OF KNOWN INFORMATION ON GROUND-WATER  
LEAKAGE INTO THE SHAFTS AT THE WIPP SITE  
(by G.J. Saulnier)

PLATES

## LIST OF FIGURES

- Figure 1.1 Site Location for the Waste Isolation Pilot Plant Showing the Observation-Well Network for Regional Hydrogeologic Characterization Studies
- Figure 1.2 Comparison of Regional Model Areas for Simulating Ground-Water Flow in the Rustler Formation and/or the Culebra Dolomite Member at the WIPP Site
- Figure 2.1 Geologic Column Representative of WIPP Area
- Figure 2.2 The Occurrence of Halite Beds Within the Rustler Formation
- Figure 2.3 Stratigraphic Cross-Section of the Rustler Formation West to East Across the WIPP Site
- Figure 3.1 Idealization of Fracture Sets
- Figure 3.2 Borehole Locations and Model Area
- Figure 3.3 Thickness Distribution of the Culebra Dolomite
- Figure 3.4 Model Grid and Borehole Locations
- Figure 3.5 Grid-Block Center Elevations
- Figure 3.6 Raw and Theoretical Semi-Variograms of the Culebra Transmissivities

## LIST OF FIGURES

(continued)

- Figure 3.7      Kriged Initial Transmissivities of the Culebra Dolomite
- Figure 3.8      Estimation Error of the Initial Transmissivities
- Figure 3.9      Best Estimate of the Undisturbed Freshwater Heads in the  
Culebra Dolomite
- Figure 3.10     Observed Formation-Water Densities in the Culebra Dolomite
- Figure 3.11     Freshwater Heads in the Culebra Dolomite in October 1985
- Figure 3.12     Effect of Shaft Leakage and Other Well Test Activities on the  
Freshwater Heads in the Culebra Dolomite in October 1985
- Figure 4.1      The Calculated Freshwater Heads Using the Initial  
Transmissivities
- Figure 4.2      The Difference Between the Calculated and the Measured  
Freshwater Heads Using the Initial Transmissivities
- Figure 4.3      The Calculated Formation-Water Densities Using the Initial  
Transmissivities
- Figure 4.4      The Pressure-Calibrated Steady-State Transmissivities
- Figure 4.5      The Calculated Freshwater Heads of the Pressure-Calibrated  
Steady-State Model

## LIST OF FIGURES

(continued)

- Figure 4.6 Pressure-Calibrated Steady-State Model: Difference Between the Calculated and the Measured Freshwater Heads
- Figure 4.7 The Calculated Formation-Water Densities of the Pressure-Calibrated Steady-State Model
- Figure 4.8 Pressure-Calibrated Steady-State Model: Difference Between the Calculated and the Measured Formation-Water Densities
- Figure 4.9 Sensitivity Analysis for Dispersivity: Variation of the Calculated Freshwater Heads
- Figure 4.10 Sensitivity Analysis for Dispersivity: Variation of the Calculated Fluid Densities
- Figure 4.11 The Density-Calibrated Steady-State Transmissivities
- Figure 4.12 The Calculated Freshwater Heads of the Density-Calibrated Steady-State Model
- Figure 4.13 Density-Calibrated Steady-State Model: Difference Between the Calculated and the Measured Freshwater Heads
- Figure 4.14 The Calculated Formation-Water Densities of the Density-Calibrated Steady-State Model
- Figure 4.15 Density-Calibrated Steady-State Model: Difference Between the Calculated and the Measured Formation-Water Densities



## LIST OF FIGURES

(continued)

- Figure 4.16 The Transmissivities of the Model with a High Transmissivity Zone Between H-4 and P-17
- Figure 4.17 The Calculated Freshwater Heads of the Steady-State Model with a High-Transmissivity Zone Between H-4 and P-17
- Figure 4.18 Steady-State Model with a High-Transmissivity Zone Between H-4 and P-17: Difference Between the Calculated and the Measured Freshwater Heads
- Figure 4.19 The Calculated Formation-Water Densities of the Steady-State Model with a High-Transmissivity Zone Between H-4 and P-17
- Figure 4.20 Steady-State Model with a High-Transmissivity Zone Between H-4 and P-17: Difference Between the Calculated and the Measured Formation-Water Densities
- Figure 5.1 The Exploratory Shaft Simulated Stresses in the Magenta and Culebra Dolomite Members
- Figure 5.2 H-3b2 Anisotropy and Convergent-Flow Tracer Test: Recorded Pump Rates
- Figure 5.3 H-3b2 Step-Drawdown Test: Recorded Pump Rates
- Figure 5.4 H-3b2 Multipad Pumping Test: Recorded Pump Rates
- Figure 5.5 H-4c Convergent-Flow Tracer Test: Recorded Pump Rates

## LIST OF FIGURES

(continued)

- Figure 6.1 The Calculated Freshwater Heads of the Density-Calibrated Steady-State Model with a Vertical Flux at P-17
- Figure 6.2 Density-Calibrated Steady-State Model with a Vertical Flux at P-17: Difference Between the Calculated and the Measured Freshwater Heads
- Figure 6.3 The Calculated Formation-Water Densities of the Density-Calibrated Steady-State Model with a Vertical Flux at P-17
- Figure 6.4 Density-Calibrated Steady-State Model with a Vertical Flux at P-17: Difference Between the Calculated and the Measured Formation-Water Densities
- Figure 6.5 The Calculated Freshwater Heads of the Steady-State Model with No Vertical Flux
- Figure 6.6 Steady-State Model with No Vertical Flux: Difference Between the Calculated and the Observed Freshwater Heads
- Figure 6.7 The Calculated Formation-Water Densities of the Steady-State Model with No Vertical Flux
- Figure 6.8 Steady-State Model with No Vertical Flux: Difference Between the Calculated and the Observed Formation-Water Densities
- Figure 6.9 The Calculated Freshwater Heads of the Steady-State Model with a Vertical Flux of  $5 \times 10^{-12}$  m/s

## LIST OF FIGURES

(continued)

- Figure 6.10 Steady-State Model with a Vertical Flux of  $5 \times 10^{-12}$  m/s:  
Difference Between the Calculated and the Observed Freshwater  
Heads
- Figure 6.11 The Calculated Formation-Water Densities of the Steady-State  
Model with a Vertical Flux of  $5 \times 10^{-12}$  m/s
- Figure 6.12 Steady-State Model with a Vertical Flux of  $5 \times 10^{-12}$  m/s:  
Difference Between the Calculated and the Observed Formation-  
Water Densities
- Figure 6.13 The Freshwater-Head Differences Caused by a Vertical Flux of  
 $5 \times 10^{-12}$  m/s
- Figure 6.14 The Formation-Water Density Differences Caused by a Vertical  
Flux of  $5 \times 10^{-12}$  m/s
- Figure 7.1 Pressure Response in a Double-Porosity Medium
- Figure 7.2 Comparison Between Single- and Double-Porosity Simulation  
Results at Selected Hydropads
- Figure D.1 Equivalent Freshwater Elevations for the Culebra Dolomite at  
Well H-1
- Figure D.2 Equivalent Freshwater Elevations for the Culebra Dolomite at the  
H-2 Hydropad

## LIST OF FIGURES

(continued)

- Figure D.3      Equivalent Freshwater Elevations for the Culebra Dolomite at the H-3 Hydropad
- Figure D.4      Equivalent Freshwater Elevations for the Culebra Dolomite at the H-4 Hydropad
- Figure D.5      Equivalent Freshwater Elevations for the Culebra Dolomite at the H-5 Hydropad
- Figure D.6      Equivalent Freshwater Elevations for the Culebra Dolomite at the H-6 Hydropad
- Figure D.7      Equivalent Freshwater Elevations for the Culebra Dolomite at the H-7 Hydropad
- Figure D.8      Equivalent Freshwater Elevations for the Culebra Dolomite at the H-8 Hydropad
- Figure D.9      Equivalent Freshwater Elevations for the Culebra Dolomite at the H-9 Hydropad
- Figure D.10     Equivalent Freshwater Elevations for the Culebra Dolomite at the H-10 Hydropad
- Figure D.11     Equivalent Freshwater Elevations for the Culebra Dolomite at the H-11 Hydropad
- Figure D.12     Equivalent Freshwater Elevations for the Culebra Dolomite at Well H-12

## LIST OF FIGURES

(continued)

- Figure D.13 Equivalent Freshwater Elevations for the Culebra Dolomite at Well DOE-1
- Figure D.14 Equivalent Freshwater Elevations for the Culebra Dolomite at Well DOE-2
- Figure D.15 Equivalent Freshwater Elevations for the Culebra Dolomite at Well P-14
- Figure D.16 Equivalent Freshwater Elevations for the Culebra Dolomite at Well P-15
- Figure D.17 Equivalent Freshwater Elevations for the Culebra Dolomite at Well P-17
- Figure D.18 Equivalent Freshwater Elevations for the Culebra Dolomite at Well P-18
- Figure D.19 Equivalent Freshwater Elevations for the Culebra Dolomite at Well WIPP-12
- Figure D.20 Equivalent Freshwater Elevations for the Culebra Dolomite at Well WIPP-13
- Figure D.21 Equivalent Freshwater Elevations for the Culebra Dolomite at Well WIPP-18
- Figure D.22 Equivalent Freshwater Elevations for the Culebra Dolomite at Well WIPP-19

## LIST OF FIGURES

(continued)

- Figure D.23 Equivalent Freshwater Elevations for the Culebra Dolomite at Well WIPP-21
- Figure D.24 Equivalent Freshwater Elevations for the Culebra Dolomite at Well WIPP-22
- Figure D.25 Equivalent Freshwater Elevations for the Culebra Dolomite at Well WIPP-25
- Figure D.26 Equivalent Freshwater Elevations for the Culebra Dolomite at Well WIPP-26
- Figure D.27 Equivalent Freshwater Elevations for the Culebra Dolomite at Well WIPP-27
- Figure D.28 Equivalent Freshwater Elevations for the Culebra Dolomite at Well WIPP-28
- Figure D.29 Equivalent Freshwater Elevations for the Culebra Dolomite at Well WIPP-29
- Figure D.30 Equivalent Freshwater Elevations for the Culebra Dolomite at Well WIPP-30
- Figure D.31 Equivalent Freshwater Elevations for the Culebra Dolomite in the Construction and Salt-Handling Shaft, Waste-Handling Shaft, and Exhaust Shaft
- Figure E.1 Calculated Densities Versus Total Dissolved Solids for Culebra Waters

## LIST OF FIGURES

(continued)

- Figure E.2 Measured Densities Versus Calculated Densities
- Figure E.3 Histogram of Saturation Indices of Celestite, Calcite, and Gypsum
- Figure F.1 Location of the Shafts at the WIPP Site
- Figure F.2 Construction and Sealing Chronology for the Three Shafts at the WIPP Site, with Schematic Representations of Pressure Responses in the Magenta and Culebra Dolomites
- Figure F.3 Piezometer Placement in the Waste-Handling Shaft and the Construction and Salt-Handling Shaft
- Figure F.4 Piezometer Measurements for the Culebra in the Waste-Handling Shaft
- Figure F.5 Piezometer Measurements for the Culebra in the Construction and Salt-Handling Shaft
- Figure F.6 Fluid Pressure Measured by Culebra Piezometers in the Construction and Salt-Handling Shaft, the Waste-Handling Shaft, and the Exhaust Shaft
- Figure F.7 Details of Piezometer Installation
- Figure F.8 Fluid Pressure in the Waste-Handling Shaft and Water Level in WIPP-21 as Measured in the Culebra Dolomite

## LIST OF TABLES

- Table 3.1 Borehole Coordinates
- Table 3.2 Coordinates and Dimensions of the Model Area and the Grid Blocks
- Table 3.3 Elevation and Thickness of the Culebra Dolomite
- Table 3.4 Physical Model Constants
- Table 3.5 Transmissivity of the Culebra Dolomite
- Table 3.6 Results of the Semi-Variogram Analysis
- Table 3.7 Best Estimate of the Undisturbed Freshwater Heads in the Culebra Dolomite
- Table 3.8 Best Estimate of the Undisturbed Formation-Water Densities in the Culebra Dolomite
- Table 3.9 Initial Boundary Conditions
- Table 3.10 Freshwater Heads in the Culebra Dolomite in October 1985
- Table 4.1 The Difference Between the Calculated and the Measured Freshwater Heads for the Initial Steady-State Model Under Undisturbed Conditions
- Table 4.2 The Difference Between the Calculated and the Measured Freshwater Heads for the Pressure-Calibrated Steady-State Model Under Undisturbed Conditions



## LIST OF TABLES

(continued)

- Table 4.3 Density-Calibrated Boundary Conditions
- Table 4.4 The Difference Between the Calculated and the Measured Freshwater Heads for the Density-Calibrated Steady-State Model Under Undisturbed Conditions
- Table 6.1 The Hydraulic Gradient in the Tamarisk Member in the Western Model Area
- Table 7.1 Summary Table of Porosity and Permeability as Determined by Core Laboratories for Selected Samples From the WIPP Site
- Table 7.2 Summary of Best-Fit Input Parameters for m-TFMB and PFB Breakthrough Curves at the H-3 Hydrodpad
- Table 7.3 Summary of Double-Porosity Hydraulic Parameters for the Culebra Dolomite at the WIPP Site
- Table 7.4 Base Case SWIFT II Double-Porosity Model Input Parameters
- Table 7.5 Calculation of Matrix Time Constants for a Range of Matrix Porosities and Block Half Lengths
- Table 7.6 Calculation of Matrix Time Constants for a Range of Matrix Hydraulic Conductivities and Block Half Lengths
- Table 7.7 Calculation of Matrix Time Constants for a Range of Primary-Medium Compressibilities and Matrix Block Half Lengths

**LIST OF TABLES**

(continued)

- Table E.1      Chemical and Physical Data on Culebra Formation-Water Samples
- Table E.2      Summary of Samples with Suspect Density and/or Chemical Data
- Table E.3      Summary of Wells For Which No Reliable Data Are Available on the  
Properties of Culebra Formation Water
- Table F.1      Water-Inflow Measurements for the Waste-Handling Shaft

## LIST OF PLATES

- Plate 1 The Production/Injection Rates and the Transient Freshwater Heads at the Shaft Location Using the Density-Calibrated Model
- Plate 2 The Transient Freshwater Heads at the Well Locations Using the Density-Calibrated Model
- Plate 3 The Production/Injection Rates and the Transient Heads at the Shaft Location Using an Additional Shaft Leakage
- Plate 4 The Transient Freshwater Heads at the Well Locations Using an Additional Shaft Leakage



## 1.0 INTRODUCTION

The modeling studies of ground-water flow in the Culebra Dolomite Member of the Rustler Formation reported here have been performed as part of the regional hydrologic characterization studies for the Waste Isolation Pilot Plant (WIPP) site in southeastern New Mexico (Figure 1.1). The site characterization studies are being conducted in accordance with the Consultation and Cooperation Agreement between the U.S. Department of Energy and the State of New Mexico as part of the evaluation of the suitability of bedded salt of the Salado Formation for isolation of defense transuranic waste. The regional hydrologic characterization studies are being coordinated by Sandia National Laboratories on behalf of the Department of Energy.

### 1.1 Objectives

The objectives of this report are to:

- (1) document the hydrogeologic data base for the Culebra dolomite at the WIPP site (including Culebra elevations, transmissivities, fluid densities, freshwater heads, and hydrologic stresses during the period 1981-1986);
- (2) develop a conceptualization and modeling strategy for describing ground-water flow in the Culebra;
- (3) present the calibration approach and results for simulating ground-water flow in the Culebra under undisturbed hydraulic conditions and during the transient period (1981 to 1986) resulting from shaft activities and well tests (in particular, the H-3 multipad pumping test);

- (4) present the results of sensitivity analyses to assess the impact of vertical fluxes to the Culebra on the freshwater head and fluid-density distributions;
- (5) present the results of calculations and analyses to assess the impact of double-porosity flow on the transient behavior of the simulated hydrogeology in the Culebra dolomite.

The spatial scale for the numerical model utilized in this study was chosen to allow a quantitative evaluation of the H-3 multipad pumping test and to allow a preliminary assessment of ground-water flow in the Culebra at the WIPP site. As such, it encompasses the WIPP site and its immediate surroundings. The model is relatively detailed since it includes the area containing the majority of the available monitoring and test wells in this region.

## 1.2 Previous Modeling Studies of Ground-Water Flow in the Culebra Dolomite

Various modeling studies of ground-water flow at the WIPP site have been conducted since 1978, with particular emphasis on the Permian Rustler Formation. These studies are presented in:

- Final Environmental Impact Statement (FEIS), U.S. DOE (1980) and WIPP Safety Analysis Report, U.S. DOE (1981);
- Cole and Bond (1980);
- D'Appolonia (1980);
- Barr et al. (1983).

The approximate areal extent encompassed by these models is illustrated in Figure 1.2.

The modeling studies presented in the Final Environmental Impact Statement and the WIPP Safety Analysis Report (SAR) were conducted by INTERA during the period 1977-1980. The objectives of these studies were to:

- (1) check consistency or lack of it between various sets of hydrogeologic data;
- (2) calculate the extent of communication (vertical permeabilities) between various hydrologic units;
- (3) delineate heterogeneities (i.e., spatial variation of permeability) existing within each geologic formation;
- (4) determine potentials and/or hydraulic conductivities in areas where data are lacking;
- (5) determine boundary conditions for local scenario and nuclide-transport modeling.

The hydrologic data base of the above-mentioned study was obtained principally from Mercer and Orr (1977) which summarized data existing through February 1977 and from a draft USGS report to Sandia National Laboratories containing the results of well tests and permeability estimates at the WIPP site. The hydrogeologic units included in the modeling studies were the Rustler Formation (conceptualized as a single hydrologic unit), the shallow-dissolution zone along the Rustler-Salado interface in Nash Draw, the Delaware Mountain Group, the Capitan Reef, the Salado Formation, and the Castile Formation.

Cole and Bond (1980) conducted a benchmark check of the modeling studies conducted by INTERA for the FEIS. Their work was performed on behalf of the Office of Nuclear Waste Isolation (ONWI). They utilized the same data and conceptual model, but a different numerical model, for their assessments. Their model, denoted VTT, is a two-dimensional multilayer

model which solves the Boussinesque equations for ground-water flow and allows hydraulic communication between layers with an interaquifer transfer coefficient. The results of their modeling studies showed a very close correspondence to results obtained using the INTERA model.

D'Appolonia (1980) conducted modeling studies of the WIPP site with the objectives of:

- (1) verifying the basic calculational procedures implemented by INTERA in the SAR report for the analyses of breach and transport events;
- (2) evaluating the sensitivity of the results to basic hydrogeologic and geochemical parameters and source-term inputs; and
- (3) reviewing the data base used to define the input parameters.

In these studies, the Rustler Formation and the Bell Canyon aquifer were modeled individually with separate model grids and simulations. Overall, their results and conclusions pertaining to these studies were consistent with the previously conducted studies.

The model developed by Barr et al. (1983) had the principal objectives of:

- (1) simulating the freshwater potential surfaces for the Magenta and Culebra dolomites;
- (2) estimating rates and extents of migration of ideally nonsorbing contaminants injected continuously into the Culebra and Magenta dolomites without disturbing the calculated head distribution.



The model area was selected to include the region containing most of the hydrologic study wells and most of Nash Draw. The Culebra and Magenta dolomites were modeled separately using an anisotropic two-dimensional model, ISOQUAD. The hydrogeologic data base consisted primarily of Mercer (1983) and Gonzalez (1983 a,b). Results of this study indicated slower ground-water movement than calculated in previous studies.

### 1.3 Present Approach to Modeling of Ground-Water Flow in the Culebra Dolomite

The modeling studies of the Culebra presented in this report deal specifically with a spatial scale suitable for interpreting the H-3 multipad pumping test and a transient period encompassing the period from the excavation of the first shaft at the WIPP site in mid-1981 until late 1986. The model-grid area is illustrated in Figure 1.2. The model boundaries were chosen at distances sufficiently far from the H-3 hydropad so as not to be within the region affected by the pumping at the H-3 hydropad.

The modeling methodology consisted of the following steps:

- (1) developing and documenting the hydrogeologic data base (i.e., Culebra thicknesses and elevations, transmissivities, equivalent freshwater heads, fluid densities, and hydrologic impacts of the shafts and well-testing activities);
- (2) employing kriging techniques to analyze the transmissivity data base and to estimate the initial transmissivity distribution of the model. Kriging techniques were further used during the calibration process in order to maintain statistical consistency between the measured transmissivity data of the Culebra and the transmissivities implemented in the model;

- (3) simulating steady-state flow under undisturbed hydrologic conditions (i.e., prior to installation of the first shaft). This simulation was conducted in two stages: (a) calibration of the model for the estimated freshwater-head distribution only, and (b) calibration of the model for both the freshwater-head distribution and the fluid-density distribution;
- (4) simulating the transient response in the Culebra, during the period 1981 to 1986, resulting from the excavation and sealing activities of the WIPP shafts and the major hydraulic- and tracer-testing activities of the regional hydrologic characterization program. The transient model utilizes the pressures and brine concentrations of the density-calibrated steady-state model as initial conditions. The transient events are implemented and the calculated and observed freshwater heads are compared for selected wells;
- (5) conducting a limited sensitivity analysis of the effects of vertical fluxes to the Culebra and the impact of double-porosity flow on the transient model simulations.

This study is an interim step toward a more comprehensive modeling study characterizing the regional hydrogeology of the Rustler Formation at the WIPP site. The next step in the modeling study, which will incorporate results of both testing of individual holes through 1987 and of a second (northern) multipad pumping test to be fielded early in 1987, will be completed in early 1988.

## 2.0 SITE CHARACTERIZATION

### 2.1 General

The WIPP site lies within the geologic region known as the Delaware Basin and more specifically within the geographic region known as Los Medaños. Both the Delaware Basin and Los Medaños region occur within the southern section of the Pecos River portion of the Great Plains Physiographic Province. Los Medaños is a region of gently sloping terrain which rises eastward from the Pecos River to the western caprock of the Llano Estacado, located approximately 40 km to the northeast of the WIPP site (Mercer, 1983).

### 2.2 Stratigraphy

The following stratigraphic summary is limited to a discussion of those sedimentary units which crop out in and around the WIPP site. These formations range in age from Permian to Quaternary as shown in the geologic column illustrated in Figure 2.1. The Delaware Mountain Group represents the Permian Guadalupian Series and is composed of a series of fine-grained clastic rocks. In the WIPP area, the Delaware Mountain Group consists of the Brushy Canyon, the Cherry Canyon, and the Bell Canyon Formations. The Bell Canyon consists of interbedded sandstone and shale which represents the fore-reef facies of a massive Permian reef known as the Capitan Limestone. The Ochoan Series rocks overlie the Guadalupian Series and contain a thick evaporitic sequence which accumulated in the Delaware Basin during Permian time. The Castile Formation is the basal formation of the Ochoan Series and is composed principally of anhydrite and halite with some carbonates and sandstones. Overlying the Castile is the Salado Formation, which is composed of thick beds of halite interbedded with anhydrite, polyhalite, dolomite, and clay. More complete descriptions of the Salado Formation are found in Jones (1973, 1975). Overlying the Salado Formation is the Rustler Formation, which is the most water-transmissive formation in the area (Mercer, 1983).

The Rustler Formation has been divided into five separate members based upon lithology (Vine, 1963). They are in ascending order: (1) the unnamed lower member composed of massive siltstone overlain by alternating beds of halite, siltstone, and anhydrite; (2) the Culebra Dolomite Member; (3) the Tamarisk Member composed of two zones of massive to bedded anhydrite separated by a thick sequence of halite and siltstones; (4) the Magenta Dolomite Member; and (5) the Forty-niner Member composed of two thick anhydrite zones separated by a silty-halite unit, as in the Tamarisk. The Rustler Formation lithology presented above represents the lithological succession encountered in borehole P-18 which Snyder (1985) believes to be a complete unaltered section. The Rustler lithology varies across the model area. Further discussion of this variability is contained in Section 2.4. The Rustler Formation is conformably overlain by the Upper Permian Dewey Lake Red Beds, a series of interbedded siltstones and sandstones. These beds have prevalent vertical fractures which are generally gypsum filled.

In the eastern portion of the WIPP site, the Dewey Lake Red Beds are unconformably overlain by a Triassic clastic sequence deposited in a transitional depositional complex of fluvial, deltaic, and lacustrine environments. These units are collectively referred to as the Dockum Group.

Overlying the Dockum Group, where present, and the Dewey Lake Red Beds in the WIPP site area, is a sequence of poorly sorted continental deposits of Quarternary Age. These are, in ascending order, the Gatuña Formation, the Mescalero Caliche, and Recent Alluvium and other surficial deposits. The Gatuña Formation consists of a sequence of pale reddish-brown terrestrial sandstones and conglomerates which were laid down after a maximum cycle of erosion within the Pecos River Valley during a much more humid pluvial time (Bachman, 1980). Izette and Wilcox (1982) dated an ash bed in the upper portion of the Gatuña as middle Pleistocene (600,000 yrs. B.P.) by mineralogy and fission-track dating.

Overlying the Gatuña Formation is the Mescalero caliche which is a pedogenic caliche formed in the C horizon of a paleosol during a tectonically and climatically stable period following the deposition of the Gatuña Formation (Bachman, 1980). The Mescalero caliche has been dated as being Pleistocene (510,000-410,000 yrs. B.P.) through uranium-series disequilibrium techniques (Bachman, 1980). Overlying the caliche are a series of Holocene surficial deposits which consist of sheetlike deposits of surface sand, sand soil, and sand dunes.

### 2.3 Regional Hydrogeology

In this report, the discussion of the regional hydrogeology will be limited to the Rustler Formation and the uppermost Salado Formation. There are three significant water-transmissive horizons above the waste-emplacment horizon located in the Salado Formation. These are, in ascending order, (1) the Rustler-Salado "contact" residuum, which varies in position between the Rustler-Salado contact itself and a position within the uppermost Salado Formation (in Nash Draw); (2) the Culebra Dolomite Member; and (3) the Magenta Dolomite Member (Mercer, 1983).

The Rustler-Salado contact residuum is transmissive in some areas around the WIPP site (Mercer, 1983). In Nash Draw and areas immediately west of the WIPP site, the contact exists as a dissolution residue capable of transmitting water. Robinson and Lang (1938) referred to this residuum making up the contact as the "brine aquifer". As one moves eastward from Nash Draw toward the Livingston Ridge surface, dissolution in the uppermost Salado, at the Rustler-Salado contact, and within the unnamed lower member of the Rustler Formation decreases and the transmissivity of this interval decreases. Transmissivities for the Rustler-Salado residuum range from  $2.2 \times 10^{-10}$  to  $8.6 \times 10^{-6}$  m<sup>2</sup>/s in Nash Draw and from  $3.2 \times 10^{-11}$  to  $5.4 \times 10^{-8}$  m<sup>2</sup>/s eastward from Livingston Ridge (Mercer, 1983). In the waste-handling shaft, no water inflows from this interval were observed during excavation and shaft mapping (Holt and Powers, 1984).

The Culebra dolomite is considered to be the most transmissive hydrogeologic unit in the WIPP-site area. Mercer (1983) describes ground-water flow within the Culebra as being southerly in Nash Draw and south to southwesterly beneath the Livingston Ridge surface. Reported values for transmissivity in the Culebra in the Nash Draw area range from  $1.9 \times 10^{-5}$  to  $1.3 \times 10^{-3}$  m<sup>2</sup>/s (Mercer, 1983). Within the model area, the transmissivity ranges from  $2.1 \times 10^{-9}$  to  $1.2 \times 10^{-3}$  m<sup>2</sup>/s (Table 5.5). Hydraulic gradients in the Culebra at the WIPP site range from  $1.3 \times 10^{-3}$  to  $3.8 \times 10^{-3}$  (Mercer, 1983). As a general trend, total dissolved solids increase from west to east across the WIPP site and the model area. For a more detailed discussion of the geochemistry of the Culebra at the WIPP site, see Appendix E.

Ground water in the Magenta dolomite generally flows from the north toward the westsouthwest (Mercer, 1983). In most areas east of Nash Draw, and east and south of the H-6 hydropad, the Magenta exists as a confined system with very low transmissivity (less than or equal to  $4.3 \times 10^{-7}$  m<sup>2</sup>/s). The difference between Magenta and Culebra hydraulic potentials generally increases eastward, with the Magenta having higher potentials. In areas of Nash Draw, the Magenta is generally at water-table conditions and may have a stronger hydraulic connection to other units in the Rustler Formation. In other parts of Nash Draw, the Magenta is unsaturated. Magenta transmissivities range as high as  $3.8 \times 10^{-4}$  to  $5.7 \times 10^{-4}$  m<sup>2</sup>/s immediately east of Nash Draw.

Although the Rustler-Salado residuum, the Culebra Dolomite Member, and the Magenta Dolomite Member are generally found to be the primary transmissive units within the Rustler, zones of relatively high transmissivity have been tested locally in the Rustler Formation outside of these horizons (Chaturvedi and Channell, 1985). In a few cases, discrete argillaceous zones within the Forty-niner Member and the Tamarisk Member have produced water at equivalent rates to the Culebra or the Magenta upon testing (Mercer and Orr, 1979; Beauheim, 1986).

#### 2.4 Regional Dissolution and the Effects Upon Flow in the Rustler Formation

Based upon observations of outcrops, core, and detailed shaft mapping, the Culebra can be characterized as a fractured medium, at least locally, at the WIPP site (Chaturvedi and Rehfeldt, 1984; Holt and Powers, 1984). As the magnitude of fracturing and development of secondary porosity increases, the Culebra transmissivity generally increases (Chaturvedi and Channell, 1985). The presence and degree of fracturing in the Culebra dolomite is thought to be directly related to the amount of dissolution of halite occurring below the Culebra (Snyder, 1985).

Dissolution within the Rustler Formation is observed both at the surface within Nash Draw, and in the subsurface at the WIPP site. Nash Draw, located immediately west of the WIPP site, is a depression resulting from both dissolution and erosion (Bachman, 1981). In Nash Draw, members of the Rustler are actively undergoing dissolution and locally contain caves, sinks, and tunnels typical of karst morphology in evaporitic terrain.

Bachman (1980) identified three types of dissolution occurring in the Delaware Basin: local dissolution, regional dissolution, and deep-seated dissolution. Local dissolution is near-surface dissolution where surface or ground waters penetrate soluble strata through joints or fractures, causing local dissolution and possible collapse and fill, as well as dissolution features such as shallow caves above the regional water table. Regional dissolution occurs when chemically unsaturated water penetrates to permeable beds, where it migrates laterally, dissolving soluble units which it contacts. On a regional scale, the consequence of such dissolution appears to be removal of highly soluble rock types, such as halite, combined with displacement and fracturing of adjacent rocks. Deep-seated dissolution occurs well below the water table, forming caverns within the rock.

At the WIPP site, regional dissolution is thought to have occurred within the Rustler Formation in the past (Snyder, 1985). However, there is some controversy as to whether this dissolution front is still active. Bachman (1985) feels that most of the dissolution in the Rustler predates or occurred during a much more humid time (Gatunian Time) in southeastern New Mexico over 500,000 years before present. Bachman (1985) does suggest, however, that dissolution is still active in Nash Draw and in areas very close to Livingston Ridge.

In the Rustler Formation at the WIPP site, most investigators feel that a westward increase in regional dissolution is reflected by a decrease in the number and thickness of halite beds and subsequent thinning of the Rustler Formation (Figure 2.2). The stratigraphic level of the first occurrence of salt is in the upper Rustler along the eastern margin of the WIPP site, and progressively moves down-section through the Rustler as one moves west. As the bedded halites are dissolved, insoluble residues remain, forming beds of mudstones, siltstones, and chaotic breccia with a clay matrix. Figure 2.3 shows a west to east cross-section taken between wells P-6, H-3, DOE-1, and P-18. Halite beds in the non-dolomitic members tend to be thin and grade westward into the residuum. Although most investigators concur with the premise that a dissolution front exists in the Rustler Formation at the WIPP site (Cooper and Glanzman, 1971; Powers et al., 1978; Mercer, 1983; Chaturvedi and Rehfeldt, 1984; and Snyder, 1985), there are investigators who oppose this concept and believe that the westward decrease in halite within the Rustler represents depositional limits (Lambert, 1983; Holt and Powers, 1984). Holt and Powers (1984) reported that in their detailed mapping of the Rustler in the waste-handling shaft, no post-depositional dissolution features were identified.

Whether or not the dissolution front hypothesis is correct, there are general trends associated with the presence or lack of bedded halite within the Rustler Formation. As shown in Figure 2.2, as the presence



of bedded halite within the Rustler increases, so does the thickness of the formation. Generally, as the amount of halite in the Rustler decreases, the transmissivity of the dolomitic members increases, presumably as a result of increased fracturing of the units as a result of halite removal and subsequent foundering and collapse of the more competent dolomite beds. In parts of Nash Draw, hydraulic potentials in the Magenta and Culebra are essentially the same. As one moves eastward onto the Livingston Ridge surface, the difference in hydraulic potentials between these two units increases. This could represent the increase in the effectiveness of the Tamarisk Member as a confining unit (or aquitard) with decreased halite removal.



### 3.0 MODEL CONCEPTUALIZATION FOR THE CULEBRA DOLOMITE

This chapter describes the conceptualization of the model in general. It comprises a description of the computer code, a discussion of the assimilation and evaluation of the hydrogeologic data base, as well as a description of the basic model properties (e.g., extents, grid, physical parameters, boundary conditions, etc.).

#### 3.1 Swift II Code Description

Having evolved from the U.S. Geological Survey Waste Injection Program SWIP (Intercomp, 1976), the Sandia Waste-Isolation Flow and Transport Model, SWIFT, has been continuously developed and maintained since 1975. It is a fully transient, three-dimensional finite-difference code which solves the coupled equations for flow and transport in geologic media. The processes considered are:

- fluid flow
- heat transport
- dominant-species miscible displacement (brine migration)
- trace-species miscible displacement

Dominant-species miscible displacement refers to brine migration, whereas trace-species miscible displacement applies to the transport of solutes at concentrations not significantly affecting the fluid-flow parameters and may include radionuclide-chain transport. The model was developed for applications related to radionuclide transport and, hence, the following discussions refer specifically to radionuclides. However, the model is general and can handle the transport of any trace species undergoing sorption or first-order losses.

The first three processes are coupled via fluid density and viscosity. Together they provide the velocity field on which the fourth process depends (Dillon et al., 1978; Reeves and Cranwell, 1981; Finley and Reeves, 1981).

In 1984, the capability of SWIFT was enhanced to include fractured media, a free-water surface, and extended boundary conditions. The new code was designated SWIFT II.

The SWIFT II model has been selected for interpreting the H-3 multipad pumping test because it has a variable-density formulation and is designed to simulate flow and transport processes in both porous and fractured media.

A comprehensive description of the theory and implementation of the SWIFT II model was presented in Reeves et al. (1986a). Two other documents related to the SWIFT II code have been published, namely a data input guide for SWIFT II (Reeves et al., 1986b), and verification-validation tests for both SWIFT codes (Ward et al., 1984).

Because of the comprehensive documentation already available, the following sections are restricted to a brief discussion of the basic equations used by SWIFT II (Reeves et al., 1986a).

### 3.1.1 General Approach

The SWIFT II model is designed to simulate flow and transport processes in both single and double-porosity media. The analyst designates the fractured regions of the system to which dual porosity is to be applied. In those particular regions, two sets of equations are solved, one for the fracture processes and the other for the matrix processes. The fracture-porosity equations describing flow and transport for the fractured regions are identical to the single-

porosity equations for the nonfractured zone, except for sink terms giving the losses to the matrix. Consequently, one general set of equations which applies to both zones is presented, which will be called the global set of equations. The matrix-porosity equations for the fractured zone differ somewhat from their global counterparts. Therefore, a separate set of equations is presented which will be called the local set of equations. As was mentioned before, a variable-density formulation is used throughout. Density, viscosity, porosity, and enthalpy may be strongly dependent on one or more of pressure, temperature, and brine concentration, but not on trace-species or radionuclide concentrations. For this reason, the flow, heat, and brine equations are termed the primary equations.

A steady-state solution option is provided for the global primary equations with two qualifications. First, it is assumed that heat transport is basically a transient process. Certainly, this is true for high-level nuclear waste repositories, a dominant application for the code. Thus, heat transport, like radionuclide transport, is not included in the steady-state option. Secondly, it is assumed that matrix processes are negligible at steady state. Consequently, the state equations for the matrix porosity are not solved for the steady-state option. Of course, the code will permit transient solution of radionuclide transport (with or without dual porosity) in conjunction with steady-state solution of the primary equations since this is perceived as a desirable simulation procedure.

In the following sections, the order of presentation is that of global transient equations followed by global steady-state equations followed by local transient equations.

### 3.1.2 The Global Transient-State Equations for Flow, Heat, Brine, and Radionuclide Transport

The transport equations are obtained by combining the appropriate continuity and constitutive relations and have been presented by several authors, including Cooper (1966), Reddell and Sunada (1970), Bear (1979), and Aziz and Settari (1979). Sink terms  $\Gamma$  are included for fractured zones in which losses to the rock matrix are significant. The resulting relations may be stated as follows<sup>1</sup>:

Fluid:

$$\begin{array}{rcccl}
 - \nabla \cdot (\rho \underline{u}) & - & q & - & q_W \\
 \text{convection} & & \text{production}^2 & & \text{sink/source}^3 \\
 & + & R'_C & - & \Gamma_W \\
 & & \text{salt} & & \text{loss to} \\
 & & \text{dissolution} & & \text{matrix} \\
 & & & = & \frac{\partial}{\partial t} (\phi \rho)
 \end{array} \quad (3-1)$$

Heat:

$$\begin{array}{rcccl}
 - \nabla \cdot (\rho H \underline{u}) & + & \nabla \cdot (\underline{E}_H \cdot \nabla T) & - & H_I q & - & H q & - & q_H \\
 \text{convection} & & \text{conduction/} & & \text{injected}^4 & & \text{produced} & & \text{sink/} \\
 & & \text{dispersion} & & \text{enthalpy} & & \text{enthalpy} & & \text{source} \\
 & - & (H \Gamma_W + \Gamma_H) & = & \frac{\partial}{\partial t} [\phi \rho U + (1-\phi) \rho_R U_R] & & & & \\
 & & \text{loss to matrix} & & \text{accumulation in fluid and rock} & & & & 
 \end{array} \quad (3-2)$$

<sup>1</sup> All terms are defined in Appendix A.

<sup>2</sup> This term refers to fluid loss (production) or fluid gain (injection) through wells.

<sup>3</sup> This term refers to a sink/source other than a well. A positive sign denotes a sink, and a negative sign denotes a source.

<sup>4</sup> This is a source term since, by the adopted sign convention, the rate of fluid injection is inherently negative.

Brine:

$$\begin{aligned}
 & - \nabla \cdot (\rho \hat{C} \underline{u}) & + \nabla \cdot (\rho \underline{E}_C \cdot \nabla \hat{C}) & - \hat{C}_I q & - \hat{C} q \\
 & \text{convection} & \text{dispersion/} & \text{injected} & \text{produced} \\
 & & \text{diffusion} & \text{brine} & \text{brine} \\
 & + R_C & - (\hat{C} \Gamma_W + \Gamma_C) & = \frac{\partial}{\partial t} (\phi \rho \hat{C}) & (3-3) \\
 & \text{salt} & \text{loss to matrix} & \text{accumulation} & \\
 & \text{dissolution} & & & 
 \end{aligned}$$

Radionuclide r:

$$\begin{aligned}
 & - \nabla \cdot (\rho C_r \underline{u}) & + \nabla \cdot (\rho \underline{E}_C \cdot \nabla C_r) & - C_r q & - q_r & + q_{wr} \\
 & \text{convection} & \text{dispersion/} & \text{produced} & \text{sink/} & \text{waste} \\
 & & \text{diffusion} & \text{component} & \text{source} & \text{leach} \\
 & - (C_r \Gamma_W + \Gamma_r) & + \sum_{s=1}^N k_{rs} \lambda_s [\phi \rho C_s + (1-\phi) \rho_R W_s] & & & (3-4) \\
 & \text{loss to} & \text{generation of component} & & & \\
 & \text{matrix} & \text{r by decay of s} & & & \\
 & - \lambda_r [\phi \rho C_r + (1-\phi) \rho_R W_r] & = \frac{\partial}{\partial t} [\phi \rho C_r + (1-\phi) \rho_R W_r] & & & \\
 & \text{decay of component r} & \text{accumulation} & & & 
 \end{aligned}$$

Several quantities in Equations (3-1) - (3-4) require further definition in terms of the basic parameters. The tensors in Equations (3-2), (3-3), and (3-4) are defined as sums of dispersion and molecular terms:

$$\underline{E}_C = \underline{D} + D_m \underline{I} \quad (3-5)$$

and

$$\underline{E}_H = D_p \underline{C} + K_m \underline{I} \quad (3-6)$$

where

$$D_{ij} = \alpha_T u \delta_{ij} + (\alpha_L - \alpha_T) u_i u_j / u \quad (3-7)$$

in a Cartesian system. Also, sorption of radionuclides is included via an assumption of a nonlinear Freundlich equilibrium isotherm:

$$W_r = \kappa_r (\rho C_r)^{\eta_r} \quad (3-8)$$

Equations (3-1) - (3-4) are coupled by auxiliary relations for:

Darcy velocity:

$$\underline{u} = - (k/\mu) \cdot (\nabla p - \frac{\rho g}{g_c} \nabla z) \quad (3-9)$$

porosity:

$$\phi = \phi_0 [1 + c_R (p - p_0)] \quad (3-10)$$

fluid density:

$$\rho = \rho_0 [1 + c_W (p - p_0) - c_T (T - T_0) + c_C \hat{C}] \quad (3-11)$$

fluid viscosity:

$$\mu = \mu_R(\hat{C}) \exp [B(\hat{C})(T^{-1} - T_R^{-1})] \quad (3-12)$$

fluid enthalpy:

$$H = U_0 + U + p/\rho \quad (3-13)$$



fluid internal energy:

$$U = c_p(T - T_0) \quad (3-14)$$

rock internal energy:

$$U_R = c_{pR}(T - T_0) \quad (3-15)$$

where parameter  $c_C$  in Equation (3-11) is defined in terms of an input density range  $(\rho_I - \rho_N)$  and the reference density  $\rho_0$ :

$$c_C = (\rho_I - \rho_N)/\rho_0 \quad (3-16)$$

Furthermore, an internal energy  $U_0$  is included in Equation (3-13) to account for the difference in reference conditions as specified by the analyst and the reference conditions specified internally for the enthalpy.

### 3.1.3 The Global Steady-State Equations for Flow and Brine Transport

In safety evaluations for nuclear-waste repositories, quite often the time frame of interest may extend over many thousands of years. Typically, the assumption of time-invariant flow and brine conditions is justified in such cases due to the lack of specific data for such a long period of time. For the fluid flow, the overall effect of transient rainfall boundary conditions may have a minor effect on radionuclide transport. Duguid and Reeves (1976) have shown this for a combined saturated-unsaturated simulation of tritium transport averaged over a period of only one month. For the brine transport, transient effects at depth likely will be negligible also. For the heat transport, however, the radionuclides stored within a repository will provide a transient source of heat for thousands of years. Thus, heat transport is considered here to be a transient process and is not included as a steady-state option.

Two steady-state options have been included. The first option permits solution of the time-independent flow equation:

Fluid (steady-state):

$$\begin{array}{ccccccc}
 -\nabla \cdot (\rho \underline{u}) & - & q & - & q_W & + & R'_C & = & 0 & (3-17) \\
 \text{conduction} & & \text{production} & & \text{sink/} & & \text{salt} & & & \\
 & & & & \text{source} & & \text{dissolution} & & & 
 \end{array}$$

In both options the accumulation and the matrix-loss term are set to zero, as shown explicitly in Equation (3-17). For the steady-state fluid-flow option, however, the salt dissolution term is also set to zero, and the presence of brine and heat are included by way of the mechanisms of a variable density and a variable viscosity.

The second option permits a coupled time-independent solution for both fluid flow, Equation (3-17), and brine transport:

Brine (steady-state):

$$\begin{array}{ccccccc}
 -\nabla \cdot (\rho \hat{C} \underline{u}) & + & \nabla \cdot (\rho \underline{E}_C \cdot \nabla \hat{C}) & - & \hat{C}_I q & - & \hat{C} q & & & \\
 \text{convection} & & \text{dispersion/} & & \text{injected} & & \text{produced} & & & \\
 & & \text{diffusion} & & \text{brine} & & \text{brine} & & & \\
 & & & & & & & & & \\
 & & & & + & R_C & = & 0 & & (3-18) \\
 & & & & & \text{salt} & & & & \\
 & & & & & \text{dissolution} & & & & 
 \end{array}$$

In this case, in addition to a variable density and a variable viscosity, the salt-dissolution term is non-zero, in general. However, for the purposes of this report, the salt-dissolution term was assumed to be zero.

### 3.1.4 The Local Transient-State Equations for Flow, Heat, Brine, and Trace Species (Radionuclide) Transport Within the Rock Matrix

The flow and transport processes occurring within the rock matrix are conceptualized as being orthogonal to the fractures. Thus, it is assumed that the fractures provide the only means for large-scale movements through the entire system while the matrix provides most of the storage of the system. The approach used here to treat the fracture-matrix system is similar to that used by Bear and Braester (1972), Huyakorn et al. (1983), Pruess and Narasimhan (1982), Tang et al. (1981), Grisak and Pickens (1980), Streltsova-Adams (1978), and Rasmuson et al. (1982).

The equations used here for the matrix are very similar to those presented in Section 3.1.2. They are as follows:

Fluid (matrix):

$$\begin{aligned}
 -\nabla \cdot (\rho' \underline{u}') &+ \Gamma'_W &= \frac{\partial}{\partial t} (\phi' \rho') & \quad (3-19) \\
 \text{conduction} & \text{gain from} & \text{accumulation} & \\
 & \text{fracture} & &
 \end{aligned}$$

Heat (matrix):

$$\begin{aligned}
 -\nabla \cdot (\rho' H' \underline{u}') &+ \nabla \cdot (E'_H \nabla T') + (H' \Gamma'_W + \Gamma'_H) \\
 \text{convection} & \text{conduction/} & \text{gain from} & \\
 & \text{dispersion} & \text{fracture} & \\
 & & & \\
 & = \frac{\partial}{\partial t} [\phi' \rho' U' + (1-\phi) \rho_R U'_R] & \quad (3-20) \\
 & \text{accumulation in fluid} & \\
 & \text{and rock} &
 \end{aligned}$$

Brine (matrix):

$$\begin{aligned}
 -\nabla \cdot (\rho' \hat{C}' \underline{u}') &+ \nabla \cdot (\rho' E'_C \hat{C}') + (\hat{C}' \Gamma'_W + \Gamma'_C) \\
 \text{convection} & \text{dispersion/} & \text{gain from} & \\
 & \text{diffusion} & \text{fracture} & \\
 & & & \\
 & = \frac{\partial}{\partial t} (\phi' \rho' \hat{C}') & \quad (3-21) \\
 & \text{accumulation} &
 \end{aligned}$$

Radionuclide r (matrix):

$$\begin{array}{rcl}
 -\nabla \cdot (\rho' C'_r u') & + & \nabla \cdot (\rho' E'_C \nabla C'_r) + \sum_s k_{rs} \lambda'_s K'_s \phi' \rho' C'_s \\
 \text{convection} & & \text{dispersion/} \\
 & & \text{diffusion} \\
 & & \text{generation of component} \\
 & & \text{r by decay of s}
 \end{array}$$

$$\begin{array}{rcl}
 -\lambda'_r K'_r \phi' \rho' C'_r & + & (C'_r \Gamma'_W + \Gamma'_r) = \frac{\partial}{\partial t} (K'_r \phi' \rho' C'_r) \\
 \text{decay of} & & \text{gain from} \\
 \text{component r} & & \text{fracture} \\
 & & \text{accumulation}
 \end{array} \quad (3-22)$$

Both convection and dispersion terms are retained in Equations (3-19) through (3-22). These terms arise only through fluid-density changes and likely will be negligible except for highly pressurized and/or highly heated regions. It is anticipated that either parallel fractures or intersecting sets of parallel fractures will be treated (Figure 3.1). For the former, a prismatic block is invoked in the numerical solution, and for the latter, either prismatic or spherical blocks may be used to approximate the actual matrix geometry. Thus, either one-dimensional Cartesian or spherical geometry may be used for the local matrix equations. In either case, the interior boundary is assumed to be a reflective no-flow boundary. The fracture/matrix interface provides a source ( $\Gamma'$ ) which is identical to the fracture loss ( $\Gamma$ ) within a geometrical scaling factor.

Many of the coefficients of Equations (3-19) through (3-22) require further specification. The coefficients of the second-order transport terms are defined as follows:

$$E'_C = D' + D'_m \quad (3-23)$$

$$E'_H = D' \rho' c_p + K'_m \quad (3-24)$$

$$D' = \alpha'_L u' \quad (3-25)$$

For the rock matrix, diffusion is expected to dominate the dispersion  $E'_C$ , in contrast to the dispersion ( $\underline{E}_C$ ) for the global simulation. Consequently, the dependence of diffusion upon temperature is expected to be much more significant than in the global system and is included through the linear relation:

$$D'_m = D'_{m0} [1 + \delta'(T' - T_0)] \quad (3-26)$$

Sorption of radionuclides within the matrix is included via the assumption of a linear equilibrium isotherm:

$$K'_r = 1 + \rho_R k'_{dr} (1 - \phi') / \phi' \quad (3-27)$$

Equations (3-19) through (3-22) are coupled by four auxiliary relations for

Darcy velocity (matrix):

$$\underline{u}' = - (k' / \mu') \nabla p' \quad (3-28)$$

Porosity (matrix):

$$\phi' = \phi'_0 [1 + c'_R (p' - p_0)] \quad (3-29)$$

Fluid density (matrix):

$$\rho' = \rho_0 [1 + c'_W (p' - p_0) - c'_T (T' - T_0) + c'_C \hat{C}'] \quad (3-30)$$

Fluid viscosity (matrix):

$$\mu = \mu_R(\hat{C}') \exp [B(\hat{C}')((T')^{-1} - T_R^{-1})] \quad (3-31)$$

Three auxiliary equations are required by Equation (3-20):

Fluid enthalpy (matrix):

$$H' = U_o + U' + p'/\rho' \quad (3-32)$$

Fluid internal energy (matrix):

$$U' = c_p(T' - T_o) \quad (3-33)$$

Rock internal energy (matrix):

$$U_R' = c_{pR}'(T' - T_o) \quad (3-34)$$

Parameter  $c_c$  is defined by Equation (3-16), and it is assumed in Equation (3-28) that gradients of the elevation head are of negligible importance in determining Darcy velocities within the matrix (i.e., medium is nondeforming).

### 3.2 Geometric Model Description

With SWIFT II chosen as the computer code, the next step of the regional model conceptualization was the selection of the geometric model properties. They consist of the horizontal and vertical model dimensions in general and the grid block sizes and grid block elevations in particular. The criteria for the selection of the geometric model properties, as well as the selected properties themselves, are summarized in the following sections.

### 3.2.1 Horizontal Dimensions (Model Area)

The approximate locations of the boreholes in the WIPP area are shown in Figure 3.2. Different symbols are used for wells which (possibly) reacted to the 62 days of pumping at H-3b2 and for those which are judged not to have responded measurably to the pumping.

The Universal Transverse Mercator (UTM) coordinates of the wells which are open to the Culebra dolomite are given in Table 3.1. Most of the data were obtained from a satellite positioning survey performed in 1984 (Hydro Geo Chem, 1985). For those wells where no satellite positioning survey coordinates were available the UTM coordinates were calculated using the Township Range coordinates as reported in the Basic Data Reports issued by Sandia National Laboratories for each borehole. For several of the H-series hydropads, the Township Range coordinates were obtained from land surveys conducted by D. Reddy, New Mexico Land Surveyor.

The horizontal model dimensions (model area) shown in Figure 3.2 were chosen based on the areal distribution of the wells which showed responses to the H-3 multipad pumping test. The UTM coordinates of the model-area corners, as well as the dimensions of the model area are given in Table 3.2. As illustrated in Figure 3.2, all wells that responded to the H-3 multipad pumping test lie within the model area. One principle of the modeling investigations was to reproduce the observed transient pressures at these wells. All reacting wells are at least 1 km away from the model boundaries. Thus, the effect of the model boundaries on the results of the modeling at the well locations can be expected to be negligible. Additionally, several of the wells which did not respond to the H-3 multipad pumping test are situated within the model area. They are important for the modeling study because they indicate which parts of the model area should not be significantly influenced by the pumping at H-3b2.

### 3.2.2 Vertical Dimension

The actual modeling study was restricted to simulate the hydrogeology of the Culebra dolomite only. Therefore, the vertical model dimension is identical to the thickness of the Culebra dolomite.

The thickness of the Culebra dolomite in the WIPP area is only known at the borehole locations (Sandia National Laboratories, 1981a,b, 1982a,b,c,d, 1983a,b,c, Sandia National Laboratories and U.S. Geological Survey, 1979a,b,c,d,e,f, 1980a,b,c,d,e,f,g, 1982, 1983; Jones, 1978). It varies between 5.6 and 11.3 m (Table 3.3).

The distribution of the thickness data shows a clear maximum between 7 and 8 m (Figure 3.3). Therefore, 8 m was considered to be representative and used throughout the modeling study for both the thickness of the Culebra and the vertical dimension of the model.

### 3.2.3 Model Grid

After the definition of the horizontal and vertical model dimensions, the dimensions of the individual grid blocks were assigned, i.e., the model grid was established. One criterion of the gridding was that the grid-block centers should coincide, wherever possible, with the locations of boreholes which are used as observation wells in the Culebra. Thus, it is possible to compare directly the calculated formation pressures and formation-water densities with the observed values. A second (code specific) rule for the gridding was that the ratio of the dimensions of two adjacent grid blocks should not exceed a factor of two because of the possible introduction of truncation errors.

With these constraints in mind, the model area was discretized using an irregular grid of 29 x 32 grid blocks (Figure 3.4). As listed in



Table 3.2, the length or width of the grid blocks vary between 120 m at the center of the model area and 1180 m in the outer regions of the model area. On the vertical scale, the model grid comprises only one layer of grid blocks with a height of 8 m. Thus, the model grid consists of a total of 928 grid blocks. Naturally, the resolution of any model is restricted by the number and size of the grid blocks. Increasing the number of grid blocks increases the resolution, but also the computation time and the storage requirements, i.e., the overall costs of the study. It is not recommended to increase the resolution of the model beyond the resolution provided by the observed data. For the actual study, the resolution provided by the observed data is given by the spatial distribution of the wells from which the data were obtained. Consequently, the grid of the model should reflect the spatial distribution of the wells. Since one of the modeling objectives was to simulate the H-3 multipad pumping test, the resolution was increased in the region at and adjacent to the H-3 hydropad.

As described above and illustrated in Figure 3.4, the model grid was designed such that every well or hydropad corresponds to a separate grid block in the model. Thus, the resolution of the model can be expected to be adequate for the existing data base.

In the vertical direction, the existing hydrogeologic data of the Culebra dolomite provide no resolution. There are no separate transmissivity data corresponding to various levels within the Culebra dolomite. Therefore, a single layered grid was considered to be sufficient with respect to the existing data base.

It is obvious that there are many different but similar grids which could be used for modeling the hydrogeologic situation in the Culebra dolomite. Thus, the grid shown in Figure 3.4 is not unique in terms of suitability for the given problem. However, any grid suited for a

model of the Culebra dolomite that is based on the existing data base should have the following characteristics:

1. grid-block centers which coincide with or are near to existing observation wells;
2. the ratio of the dimensions of two adjacent grid blocks should not exceed a factor of two (code-specific rule), and
3. about 1,000 grid blocks (minimum, resulting from the above two criteria).

Experience has shown that the code equations for flow and transport are relatively insensitive to the exact grid block dimensions as long as the second of the three above-mentioned conditions is followed. Thus, modeling results can be expected to be very similar no matter what discretization is chosen as long as it shows the above-listed three characteristics. With respect to interpreting pumping tests, Tomasko (personal communication) has conducted a sensitivity analysis using a two-dimensional finite-difference model to illustrate that the numerical solution is accurate at the first node outside the block containing the pumping well.

#### 3.2.4 Elevation of the Grid Blocks

Like the thickness, the elevation of the Culebra dolomite in the WIPP area is known only at the borehole locations (Sandia National Laboratories, 1981a,b, 1982a,b,c,d, 1983a,b,c, Sandia National Laboratories and U.S. Geological Survey, 1979a,b,c,d,e,f, 1980a,b,c,d,e,f,g, 1982, 1983; Jones, 1978). As listed in Table 3.3, the known values for the middle of the Culebra range from 777.9 m above sea level (a.s.l.) at P-18 to 886.1 m a.s.l. at H-7 in the model area. This variation was considered to be too large to be neglected in a ground-water flow

system with variable fluid density. Consequently, the elevation of each model grid block was estimated using the values in Table 3.3. The resulting elevations of the grid blocks, as used for the model, are shown contoured in Figure 3.5. There are relatively high elevations in the western part of the model area with an absolute high (894.6 m a.s.l.) in the southwest corner, while lower elevations prevail in the eastern part. However, there is no general slope but a rather irregular "topography" in the model area, which shows features like a valley (along the axis P-18 to DOE-2) or local highs (between P-15 and H-7b1). This irregular "topography" may result from two processes: dissolution of halite and gypsum in the underlying portion of the Rustler Formation and upper Salado Formation, with consequent collapse of the residual rock; and hydration of anhydrite to gypsum in the underlying zones, which increases the thickness of the hydrated layer (Snyder, 1985).

### 3.3 Physical Model Constants

#### 3.3.1 Fluid Properties

The compressibility of water is a temperature-dependent parameter (Langguth and Voigt, 1980) which varies between  $5.10 \times 10^{-10} \text{ m}^2/\text{N}$  at  $0^\circ\text{C}$  and  $4.41 \times 10^{-10} \text{ m}^2/\text{N}$  at  $45^\circ\text{C}$ . The temperature of the formation water in the Culebra dolomite generally lies between  $20$  and  $25^\circ\text{C}$ , (INTERA, 1986). A value of  $4.53 \times 10^{-10} \text{ m}^2/\text{N}$  ( $25^\circ\text{C}$ ) was chosen for the modeling study.

Although not directly used for this modeling study which assumed isothermal conditions, the SWIFT II computer code requires the thermal expansion factor as data input. A value of  $2.07 \times 10^{-4} \text{ }^\circ\text{C}^{-1}$  was chosen from the literature (Kuchling, 1982).

Similarly, the heat capacity of water must be defined for SWIFT II. A value of  $4.18 \times 10^3$  J/kg°C was obtained from the literature (Kuchling, 1982).

Because the formation fluid in the model is handled by SWIFT II as a mixture of two miscible fluids, the densities of the two fluids have to be entered with the model parameters. The first fluid, which is denoted "water" by SWIFT II, was given a density of  $1000 \text{ kg/m}^3$ . The second fluid, internally designated as "brine", was assigned a density of  $2000 \text{ kg/m}^3$ . With this assignment the following equation for calculating the formation-water density is valid:

$$\rho \text{ [g/cm}^3\text{]} = \hat{C} + 1.0 \quad (3-35)$$

Thus, a direct comparison is possible between field-density data, which are usually given in  $\text{g/cm}^3$ , and the model output, where the calculated density  $\rho$  is not printed out but rather the fractional brine concentration ( $\hat{C}$ ).

It is necessary to emphasize that these two fluids (water and brine) are virtual fluids only for data input and output purposes. Thus, the values of the virtual fluid densities for water and brine do not have to correspond to values found in nature. The model simulations resulting in calculated formation pressures and Darcy velocities utilize a single fluid with a formation-water density that varies spatially.

The last fluid property to be defined for SWIFT II is the fluid viscosity. In general, the fluid viscosity is temperature- and solute-concentration dependent (Equation (3-12)). Although SWIFT II contains a very flexible temperature and density-dependent formulation of the viscosity, the modeling study was performed using a constant fluid viscosity. This is acceptable because the modeled region is

considered to be isothermal and the density variations within the model area are only moderate. The viscosity of pure water varies between  $1.79 \times 10^{-3}$  Pa s at 0°C and  $0.60 \times 10^{-3}$  Pa s at 45° (Langguth and Voigt, 1980). As mentioned before, the temperature of the formation water in the Culebra dolomite generally lies between 20 and 25°C (INTERA 1986). Therefore, a pure-water viscosity of  $0.92 \times 10^{-3}$  Pa s (25°C) was selected (Langguth and Voigt, 1980).

Muller et al. (1981) showed the viscosity dependence on solute concentrations (with less than 10 to 15 moles per liter (mol/l) of dissolved solids to be:

$$\mu(T, \hat{C}) = \mu(T, \hat{C} = 0) (1 + \sum A_i(T) C_i) \quad (3-36)$$

where: T = temperature of the fluid

$\mu(T, \hat{C} = 0)$  = viscosity of pure water at temperature T

$A_i(T)$  = temperature dependent coefficients for each ion i

$C_i$  = concentration of dissolved ion i (mol/L)

$\hat{C}$  =  $\sum C_i$

For the calculation of the fluid viscosity used during the modeling study, a mean fluid density of  $1.05 \text{ g/cm}^3$  was considered to be representative of the formation fluid within the model area (see also Section 3.5.1). Furthermore it was assumed that the main constituents of the dissolved solids are sodium and chlorine. Thus, a density of  $1.05 \text{ g/cm}^3$  corresponds to a NaCl concentration of about 0.86 mol/l (1 mol = 58.44 g). While the  $A_i$  of  $\text{Cl}^-$  at 25°C is about 0.0, the  $A_i$  of  $\text{Na}^+$  is about 0.03 at 25°C (Muller et al., 1981). Using Equation (3-36),

$$\begin{aligned}
\mu (25^\circ\text{C}, 0.86 \text{ mol/l}) &= 0.92 \times 10^{-3} \text{ Pa s } (1 + 0.09 * 0.86) \\
&= 0.99 \times 10^{-3} \text{ Pa s} \\
&\approx 1.0 \times 10^{-3} \text{ Pa s.}
\end{aligned}$$

Thus, a constant fluid viscosity of  $1 \times 10^{-3}$  Pa s was considered to be representative for the formation fluid in the Culebra dolomite and used throughout the modeling study.

### 3.3.2 Rock Properties

The porosity data of the Culebra dolomite available during the conceptualization of the model were obtained from laboratory analyses on cores. These analyses were performed using permeability to air and helium porosity techniques on eighteen one-inch diameter core plugs (Boyle's Law technique, Core Laboratories, 1986). The resulting porosities range from 0.07 to 0.30. A representative value of 0.20 was chosen as the global porosity (single-porosity conceptualization) and as the matrix porosity (double-porosity conceptualization) for the model.

As for the formation fluid, a compressibility has to be assigned to the pore structure of the formation. This compressibility used by SWIFT II is not identical to the rock compressibility normally used in hydrogeological studies, because it does not include the rock porosity. However, this "rock compressibility" ( $C_R$ ), together with the compressibility of the formation fluid ( $C_W$ ), the porosity ( $\phi$ ), the fluid density ( $\rho$ ), and the thickness ( $\Delta x_3$ ) of the aquifer, defines the storativity of the aquifer:

$$S = \phi \rho g \Delta x_3 (C_R + C_W) \quad (3-37)$$

Since the storativity of the Culebra dolomite has been documented from several pumping tests ( $2 \times 10^{-5}$ , see Section 3.4.2), a rock

compressibility of  $7.57 \times 10^{-10} \text{ m}^2/\text{N}$  was calculated using the fluid compressibility as defined in Section 3.3.1, a porosity of 0.2, an average fluid density of  $1.05 \text{ g/cm}^3$ , and an aquifer thickness of 8 m. Such a calculated rock compressibility lies well within the range of compressibility values ( $10^{-10} - 10^{-8} \text{ m}^2/\text{N}$ ) given by Freeze (1975) for jointed rocks.

Although not directly used for the modeling study, SWIFT II requires the density and the heat capacity of the rock as data input. Values of  $2500 \text{ kg/m}^3$  and  $800 \text{ J/kg}^\circ\text{C}$  were obtained from the literature for the rock density and the rock heat capacity, respectively (Kuchling, 1982).

### 3.3.3 Transport Parameters

Using the variable-density formulation of SWIFT II, the transport equation for brine (Equation 3-3 in Section 3.1) is solved. Therefore, three transport parameters must be assigned: the longitudinal dispersivity, the transverse dispersivity, and the molecular diffusivity in the porous medium.

Based on the observed heterogeneities (Section 3.4) in the Culebra dolomite, the thickness of the Culebra dolomite, and on the arguments concerning scale-dependent dispersion presented in Pickens and Grisak (1981 a,b) a longitudinal dispersivity of 50 m was assigned. The transverse dispersivity was assigned a value of 2.5 m using a ratio of transverse to longitudinal dispersivity of 0.05 (Bear, 1972; Pickens and Grisak, 1981 a,b). These values were generally used during the modeling study but were modified for a sensitivity analysis concerning the impact of different dispersivity values on the calculated fluid-density distribution (Section 4.4).

The molecular diffusivity in the geologic medium, which is required by SWIFT II, is defined as:

$$D'_{mo} = D^{\circ} \phi T^* \quad (3-38)$$

Using a free-water diffusion coefficient  $D^{\circ} = 2 \times 10^{-9} \text{ m}^2/\text{s}$  (value for  $\text{Cl}^-$  at  $25^{\circ}\text{C}$ ; Lerman, 1979), a porosity  $\phi = 0.2$  (Section 3.3.2), and a tortuosity factor  $T^* = 0.5$  (Bear, 1972), a molecular diffusivity  $D'_{mo} = 2 \times 10^{-10} \text{ m}^2/\text{s}$  was calculated. This value was considered to be representative of the Culebra dolomite and its formation water.

### 3.4 Hydrologic Model Parameters

#### 3.4.1 Initial Transmissivities

The transmissivities were treated as isotropic in the model. The final transmissivities used by the model were obtained from model calibration. The calibration process matches the model-calculated formation pressures and densities to the observed pressures and densities by varying the transmissivities of the individual grid blocks. In order to start the calibration process, initial transmissivities are required. These initial values normally are estimated based on existing data.

In this modeling study, the transmissivity data derived from boreholes in the WIPP area were analyzed by means of kriging techniques. Then the existing transmissivity data from field studies and the statistical properties of this data set were used to estimate (i.e., to "krige") the initial transmissivities for each grid block. Additionally, the spatial distribution of the estimation error, which reflects the uncertainty in the estimation, was obtained.



In the following sections, some theoretical aspects of kriging are briefly discussed, then a short summary of the practical use of the employed kriging program is presented, and finally, the analysis of the observed transmissivities is summarized.

#### 3.4.1.1 Theoretical Aspects of Kriging

Kriging is a useful method for evaluating the spatial structure of a regionalized variable (e.g., the transmissivity) of a formation and in generating estimates of the variable once its spatial structure is known (de Marsily, 1982). Kriging is a best linear unbiased estimator (BLUE) that uses a linear combination of all available data to estimate a variable's value and the error of estimation which reflects the uncertainty in the estimation.

There are a number of assumptions which are made in order to apply kriging to any regionalized data of a formation. First, the data field is assumed to be a random function constructed of random variables (Journel and Huijbregts, 1978). The second hypothesis usually used in random-function theory is that of stationarity. Stationarity assumes that the mean, variance, and higher-order moments of the transmissivity field's probability density function (PDF) are stationary in space, i.e., the same at any point in the formation (de Marsily, 1982). The third hypothesis used is that of ergodicity. Ergodicity implies that the unique realization available (i.e., the observed data) behaves in space with the same PDF as the random function describing the transmissivity field (de Marsily, 1982).

Weak stationarity refers to a condition in which only the first two moments (mean and variance) are stationary in space. Often though, the variance of a regionalized variable increases as the size of the studied area increases (de Marsily, 1982). Therefore, a hypothesis

is needed that is less restrictive than weak stationarity. The intrinsic hypothesis, proposed by Matheron (1971), requires that only the variance of the first increment of  $Z(x)$  is finite where  $Z$  is the random function, i.e., transmissivity. This requires the mean of the first increment to be a function of the distance of the increment only, not of the location  $x$ . The mean is usually assumed to be constant and is often set to equal zero. When this is true, the variance of the first increment defines a function called the variogram.

The variogram is a curve generated by the observed data that reflects the spatial correlation length of the regionalized variable being studied. It is constructed by plotting the average  $\gamma(h)$  versus the average  $h$ , where  $\gamma(h)$  is one half the mean square difference between all possible pairs of points a "lag" distance ( $h$ ) apart. Usually a range of distances are specified in order to group all possible distances between pairs of points into distance intervals. The mean square difference for each distance interval is then calculated as is the average distance between pairs. The average  $\gamma(h)$  and the average  $h$  are then plotted to generate the raw semi-variogram curve. One limitation with this method is that between 30 to 50 pairs need to be within each distance interval in order for the  $\gamma(h)$  to be representative of the property, i.e., transmissivity (Journel & Huijbregts, 1978).

Sometimes a drift or trend is present in the raw semi-variogram. The drift describes the gradual and regular manner in which the mean values of the phenomena behave over the region (Skrivan and Karlinger, 1980). If a drift exists, it must be removed from the raw semi-variogram and the residuals used to generate another semi-variogram which is utilized through the rest of the analysis (Neuman, 1984). A generalized kriging approach deals with the drift in a different manner than the universal kriging method described

above. Generalized kriging does not require a semi-variogram, which is meaningless if a drift is present. Instead, generalized covariance functions that are composed of polynomials are used. The objective is to use higher-order differences to filter out low-order polynomials associated with the drift.

In ordinary kriging, once the raw semi-variogram has been calculated and adjusted for a drift, a theoretical model is used in the kriging system of equations to estimate punctual or block values of the regionalized variable (e.g., transmissivity). Most kriging codes provide a number of theoretical models to choose from including linear, spherical, exponential, and Gaussian. The reader is referred to Delhomme (1978) for a description of these models.

The three parameters that are used to fit a theoretical model to a raw semi-variogram are the sill, the range, and the nugget. These parameters are estimated from the raw semi-variogram and are then checked with the theoretical model for consistency with the data. This procedure is explained later in the text (Section 3.4.1.2). The sill is the value a semi-variogram curve asymptotically approaches with increasing spaces between data points. Often the sill is clear from the raw semi-variogram and should be equal to the variance of the observed data. The range is the distance between data points at which the sill is reached beyond which there is no correlation. The nugget is the value of the theoretical semi-variogram at infinitesimal distances.

In kriging, a system of equations is solved in order to determine the values of linear interpolators assigned to each observed point. These interpolators change with each new estimation location. For instance, the linear interpolator is greater for an observed point closer to the estimation location and lower for an observed point further away. The semi-variogram is used in solving for these interpolators and in the calculation of the estimation error.

For a more detailed explanation of the kriging equations and or random variable theory, the reader is referred to Journel and Huijbregts (1978).

The general equation used for estimating a value at a given location is:

$$Z_o^* = \sum_{i=1}^n \lambda_o^i Z(x_i, y_i) \quad (3-39)$$

where  $Z_o^*$  = the estimated value at  $(x_o, y_o)$

$\lambda_o^i$  = the linear interpolator relating point  $(x_i, y_i)$  to  $(x_o, y_o)$ .

Note: the superscript  $i$  is only a location parameter, not an exponential.

$n$  = the number of observed points

$Z(x_i, y_i)$  = the observed points

These linear interpolators must be chosen such that the estimate is unbiased (giving no systematic over- or under-estimation), and optimal (with minimum mean square error) (Delhomme, 1978). These requirements are used to check the consistency of the theoretical semi-variogram mentioned earlier. Kriging is an exact interpolator, meaning the exact measured value is preserved. For example, if an estimate was performed at the location of a measured point, the kriged estimate would simply be the measured value.

The uncertainty of the estimate (estimation error) is usually represented by the square root of the variance of the estimation error, i.e., the standard deviation error. The formula used to calculate the estimation error is:

$$\sigma_o = \left[ \sum_{i=1}^n \lambda_o^i \gamma(x_i - x_o) + \sum_{i=1}^M \mu_i f_o^i \right]^{\frac{1}{2}} \quad (3-40)$$

where  $\sigma_o$  = the standard deviation of the estimate at  $(x_o, y_o)$

$\gamma(x_i - x_o)$  = value of  $\gamma(h)$  from the semi-variogram where  $h$  is the distance between the observed points  $(x_i, y_i)$  and  $(x_o, y_o)$

$M$  = number of terms in drift ( $M=1$  for no drift)

$n$  = number of observed points

$f_o^i$  = drift terms. Note: if a drift is not present then

$$\sum_{i=1}^m f_o^i \text{ is equal to } 1. \quad (3-41)$$

$\mu$  = Lagrange multiplier

The estimation error at a point beyond the range distance from any of the observed data points is equal to the square root of the sill. This can be seen from the above equation. The unbiased condition of the linear interpolators requires  $\sum \lambda_o^i$  to equal one. Beyond the range, every  $\gamma(h)$  value will equal the sill by definition. Thus, in the absence of a drift, the estimation error of a point beyond the range is always equal to the square root of the sill.

Knowing the estimation error is, in principle, not enough to determine the confidence interval of the estimates. However, one can very often assume that the error is Gaussian (de Marsily, 1982).

In this case, for instance, the 95% confidence interval is  $\pm 2\sigma_0$ ,  $\sigma_0$  being the standard deviation or estimation error (Equation 3-40). Then the estimate of a value at a given location, with 95% confidence, is:

$$Z_0^{*95} = Z_0^* \pm 2\sigma_0 \quad (3-42)$$

where  $Z_0^{*95}$  = the estimated confidence interval at  $(x_0, y_0)$  at 95% confidence level

$Z_0^*$  = the estimated value at  $(x_0, y_0)$   
(Equation 3-39)

$\sigma_0$  = estimation error (Equation 3-40)

Many other distribution functions also are valid for a  $\pm 2\sigma_0$  confidence interval at 95%. Consequently this expression is very often used even if the error distribution (e.g., Gaussian) is not exactly known (de Marsily, 1982).

It is also possible to use other confidence intervals which represent different confidence levels. For instance, the interval  $\pm\sigma_0$  (i.e., the estimation error) represents a 68% confidence level, and the interval  $\pm 3\sigma_0$  a 99.7% confidence level (Marsal, 1967). However, the  $\pm 2\sigma_0$  interval is most commonly used.

#### 3.4.1.2 The Universal Kriging Program K603

The observed transmissivity data of the Culebra dolomite at the WIPP site were analyzed using the United States Geological Survey (USGS) Universal Kriging Program K603 (Skriwan and Karlinger, 1980).

The K603 code requires the locations of the observed data (i.e., borehole coordinates), the observed values (i.e., measured transmissivities), and the lag intervals used for separating the distances between observed data points into groups. Once the raw semi-variogram is calculated, one must determine a mathematical model that reflects the major features observed in the raw semi-variogram. K603 supplies five types of theoretical models to match the raw variogram. This fitting procedure is performed by removing a drift or trend if present, and then adjusting the sill and the range of the theoretical expression until the desired match is achieved. A drift may indicate that the assumption of weak stationarity does not hold because the mean value of the average square differences is no longer constant. If the drift varies slowly (i.e., less than quadratic) relative to the working scale then one may still assume that weak stationarity applies to the first increment (Delhomme, 1978). However, if a predominant drift or trend is observed in the raw variogram, a general procedure to remove the drift, such as least squares, is usually performed before fitting the theoretical semi-variogram to the raw data. The removal of this drift is required to preserve the weak stationarity of the first increment.

Once the theoretical semi-variogram has been fitted to the raw semi-variogram, the K603 code has an option (denoted option 2) that checks the validity of the semi-variogram. Option 2 is a modified split-sample technique in which all of the data points are individually suppressed and estimated by kriging the remaining points (Skrivan and Karlinger, 1980). Taking the average difference between the estimated values and the observed values allows calculation of an average estimate variance. The objective is to adjust the parameters in the theoretical semi-variogram until the model is theoretically consistent (Gambolati and Volpi, 1979). This means that there is no systematic bias (i.e., the kriged average error is approximately equal to zero) which requires:

$$\frac{1}{n} \sum_{i=1}^n (Z_i - Z_i^*) = 0 \quad (3-43)$$

where  $Z_i$  = observed value at  $i$

$Z_i^*$  = kriged estimated value at  $i$

$n$  = number of observed data points

and also that the kriging errors are consistent with the predicted variance (i.e., the average ratio of theoretical to calculated variance is approximately equal to one) which requires that the mean square error is equal to one:

$$\frac{1}{n} \sum_{i=1}^n \left( \frac{Z_i - Z_i^*}{\sigma_z} \right)^2 = 1 \quad (3-44)$$

Once the consistency of the theoretical semi-variogram is reached, option 3 of K603 may be used to interpolate values at desired locations within the study area. This option requires the theoretical variogram type, its sill and range, the observed data, and the points where the estimation is desired to be input to the code. The code then prints out the estimated values at designated points and the error or standard deviation associated with the estimations.

#### 3.4.1.3 Analysis of the Observed Transmissivities

All transmissivities of the Culebra dolomite which were available during the conceptualization of the model and their corresponding references are listed in Appendix C. Table 3.5 shows the transmissivity values which were selected as the data set for the semi-variogram analysis.



Because transmissivity is generally assumed to be log-normally distributed (Freeze, 1975; de Marsily, 1982), the logarithms of the transmissivity values were used (Table 3.5) to determine the log spatial structure present in the model area.

A number of directional semi-variograms were constructed to determine if a drift or trend was present, but the required number of pairs (30-50) could not be obtained within each specified distance interval (class). The problem could be reduced by increasing the distance intervals in the semi-variogram, but this decreases the resolution and, therefore, was not done. Subsequently, a non-directional semi-variogram was calculated (Table 3.6, Figure 3.6). The raw semi-variogram approaches an asymptotic value of 2.4 as the lag distance increases to 5 km. The fluctuations in the curve past this point do not reveal any pertinent information about the spatial structure of the transmissivity field and should not be misconstrued as evidence for a drift. The raw semi-variogram has been extended to zero as there is no basis for estimating a nugget with these data. This is not to say that there is no uncertainty associated with these data. The uncertainty in the measurements could have been assigned to each observed data point, but was not because the values of the uncertainty have not been quantified. Therefore, the uncertainty of the measurements was assumed to be zero in this analysis.

The exponential theoretical semi-variogram described by the equation in Table 3.6 was fitted to the raw semi-variogram (Figure 3.6). The consistency of this choice was verified using option 2 of K603 where a kriged average error of 0.066 and a reduced mean square error of 1.007 were calculated. Other theoretical models were used to fit the raw semi-variogram, but the exponential type used gave the best consistency-check values.

The range of spatial correlation determined in this analysis (3.9 km) lies on the lower end of a distribution of ranges for aquifers in consolidated materials presented by Hoeksema and Kitanidis (1985). They determined a probability distribution of ranges having a minimum of 1.4 km, a median value of 14.72 km, and maximum of 44.5 km. The Culebra spatial correlation range also compares favorably to the results presented in the study by Delhomme (1979). Therefore, the 3.9-km range determined in this study appears reasonable in comparison with published results and may be a good representation of the spatial correlation length. However, the data base for the semi-variogram analysis was rather small. As Table 3.6 shows, most distance intervals (classes) contain only the minimum number of pairs (30-50). Therefore, only a non-directional variogram was calculated, from which rather general conclusions (e.g., sill, range, nugget) can be drawn. More advanced analytical techniques (e.g., directional semi-variogram and drift analysis) require a larger data base and can be performed as soon as additional data (e.g., from ERDA-9, WIPP-12, WIPP-13, WIPP-18, WIPP-19, WIPP-21, and WIPP-22) are available.

The statistical treatment of the Culebra transmissivity data base available as of April 1986 indicates that the transmissivities are correlated over a distance of approximately 3.9 km. For separation distances greater than this value, the estimated transmissivity will be equal to the mean value of the sample and will have an estimation error equal to the square root of the sill. Due to the sparsity of the sample, it was not possible to determine if the transmissivity data had a significant drift. Even though the kriged transmissivity data are based on a small sample, they provide a useful and unbiased set of hydraulic parameters for numerical calibration of the regional ground-water flow system. As more data become available, the initial transmissivity field can be modified and compared with the calibrated values to locate any apparent discrepancies. If any

major differences are found, the calibration process can then be repeated using the updated set of transmissivities.

#### 3.4.1.4 The Kriged Initial Transmissivities

The exponential semi-variogram (Table 3.6, Figure 3.6) was used (option 3 of the code K603) to estimate the transmissivities at the 928 locations within the model area, which correspond to the grid-block centers of the model. Figure 3.7 shows the contour map generated using the logarithms of these transmissivities, which were used for the first simulations with SWIFT II. In the following, they are referred to as initial transmissivities. Because the uncertainties of the observed transmissivities were not known, a zero uncertainty was assumed (see also previous section). This simplification results in estimation errors (see below) which are too low. Therefore, the estimation errors should be used as a qualitative indicator of the uncertainty of the kriged transmissivities rather than quantitatively correct values.

The estimation errors associated with the kriged initial transmissivities are shown contoured in Figure 3.8. On that map, a series of contours surround each well reflecting the rapid increase in the estimation error (i.e., the uncertainty) as the distance from each well increases. This is related to the range of the semi-variogram used for the estimation of the initial transmissivities.

Because the input data for the kriging are logarithms of the transmissivities, the estimation errors are also logarithmic values. Therefore the contour line with a value of 1 in Figure 3.8 represents (with the restriction outlined above) an uncertainty of  $\pm 1$  order of magnitude at 68% confidence level or  $\pm 2$  orders of magnitude at 95% confidence level. As the contour map shows, the logarithms of the estimation errors are less than one only in the

immediate neighborhood of the boreholes, i.e., an area generally less than 1.6 km in diameter.

The maximum possible estimation error (1.43) is equal to the square root of the sill (2.05). This is because of the intrinsic hypothesis used in this analytical method which states that the first two moments of the first increment are stationary. This means that beyond the range, the estimated value will always be the mean of the sample (i.e., the observed values) and have an estimation error equal to the square root of the sill of the semi-variogram (e.g., between the wells H-12, P-18 and H-5; see Figures 3.7 and 3.8). Due to the large uncertainty associated with those estimated values, it is possible to modify the initial transmissivities in those areas during later model calibration without giving up consistency with the observed data.

### 3.4.2 Storativities

The storativity of the Culebra dolomite is fairly well documented from several pumping tests (Seward, 1982; Mercer 1983; Gonzalez, 1983a). The reported values range from  $1 \times 10^{-9}$  to  $8 \times 10^{-4}$ . Because values near  $2 \times 10^{-5}$  are common, this value was considered to be representative for the Culebra dolomite in general and, consequently, used throughout the modeling study. This value is consistent with Lohman's (1972) rule of thumb for confined homogeneous aquifers:

$$S = (3.3 \times 10^{-6}) \Delta x_3 \quad (3-45)$$

which provides a storativity of  $S = 2.6 \times 10^{-5}$  for an aquifer with a thickness  $\Delta x_3 = 8$  m. .

Theoretically, it is also possible to use statistical methods (e.g., kriging) in order to analyse the spatial distribution of the

storativity. However, because the existing data base was rather small (only 11 values), the storativities were not kriged.

### 3.5 Initial Boundary Conditions

The Culebra dolomite at the boundaries of the model area is not impermeable, and the boundaries are not necessarily parallel to the potential ground-water flow lines. Therefore, no-flow boundaries are not representative of the real situation. Prescribed pressure boundaries with prescribed formation-water densities are more appropriate.

Thus, for the modeling study, the lateral boundary conditions were obtained from the best estimate of the undisturbed regional hydrogeologic situation (Figures 3.9 and 3.10). This approach is briefly discussed in the following sections. As with the transmissivities, the initial lateral boundary conditions were modified during the later model calibration.

#### 3.5.1 The Undisturbed Hydrogeologic Situation

The undisturbed hydrogeologic situation can be characterized ideally by the long-term mean formation pressures and the long-term formation-water densities.

The long-term mean formation pressures, which will be referred to herein as undisturbed pressures, can be expressed as equivalent freshwater heads\*. Because of the varying elevation of the Culebra

---

\* The term "freshwater head" as used in the main body of this report is equivalent to the term "freshwater elevation above mean sea level", because the values are always related to mean sea level. It refers to the elevation of a column of freshwater that would exert a pressure at the elevation of the Culebra equal to the measured formation pressure.

dolomite (Section 3.2.4), freshwater heads are easier to interpret than pressures. Therefore, in this report, all pressure data are presented as equivalent freshwater heads although the model calculations were made using the formation pressures. However, because of the spatially non-constant density of the formation water, the freshwater heads can be misleading; they should be used for qualitative interpretation only. For correct calculations (e.g., calculating the ground-water flux or the direction of the ground-water flow at a given point), the formation pressure together with the elevation of the Culebra dolomite and the density of the formation fluid should be used. For the undisturbed hydrogeologic situation, the heads will be referred to as the undisturbed freshwater heads.

The undisturbed pressures in the Culebra dolomite can be derived from or estimated using long-term water-level data measured in observation wells. During the conceptualization of the model the published water-level data were reviewed (Gonzalez, 1983b; INTERA Technologies and Hydro Geo Chem, 1985; INTERA Technologies, 1986) and best estimates of the undisturbed formation pressure were derived (Appendix D). In addition, unpublished water-level data (U.S.G.S. water-level data from the WIPP site, 1976-1983; P. Davies, personal communication) were reviewed and used to refine the estimates based on the above listed publications. The resulting data set, which subsequently was used throughout the modeling study, is shown in Table 3.7. The contour map (Figure 3.9) of the freshwater heads provides a qualitative impression of the undisturbed hydrologic situation. The general pattern (north-south gradients in general with low heads at DOE-1, H-11, and P-17) is consistent with previously published maps (e.g., Mercer, 1983).

The undisturbed formation-water densities can be derived from the densities measured during long-term pumping or production tests in the Culebra dolomite. All formation-water density data from the Culebra dolomite that were available during the conceptualization of the model

were reviewed and checked for consistency with the results of hydrochemical analyses (Appendix E). Table 3.8 shows the density values selected as the data set for the modeling study. Like the freshwater heads, the densities are also shown as a contour map (Figure 3.10). Thus, the spatial density distribution is characterized by high densities ( $1.09 \text{ g/cm}^3$  and more) in the eastern part of the model area, a north-south stretching transition zone ( $1.02\text{-}1.08 \text{ g/cm}^3$ ) in the middle, and low densities ( $1.00\text{-}1.01 \text{ g/cm}^3$ ) in the western part. This simplified description is complicated by intermediate densities along the western part of the northern model boundary. Thus, the low-density zone is surrounded in the east, the north, and most likely in the west by higher densities. The simulation of this spatial density distribution with the estimated hydraulic potential distribution (Figure 3.9) is one of the major problems of the modeling study.

### 3.5.2 Initial Lateral Boundary Conditions

Using the spatial distribution of the best estimate of both the undisturbed freshwater heads and the formation-water densities, the freshwater heads and the formation-water densities were estimated at the outer edges of all grid blocks along the model boundaries (Table 3.9). These values were then used to calculate the formation pressures and the fractional brine concentrations (Section 3.3.1) along the model boundaries. The implemented boundary conditions can be characterized as prescribed pressures and prescribed brine concentrations. Thus, during the simulation, the prescribed pressures are maintained along the outer edges of the model area, and the inflow from outside the model area is assigned the prescribed fractional brine concentration, while the brine concentration of the outflow is defined by the model-calculated value at the center of the concerned grid block.

### 3.5.3 Upper and Lower Boundary Conditions

During the conceptualization of the model, it was initially assumed that the geologic formations above and below the Culebra dolomite are of very low permeability and any flux into or from the Culebra dolomite through these confining beds can be neglected. Consequently, no-flow boundaries were assumed and implemented at the top and the bottom of the Culebra dolomite. However, at a later stage of the modeling study it became apparent that the assumption of an absolutely impermeable layer above and below the Culebra dolomite (i.e., the Tamarisk Member and the unnamed lower member, respectively) is probably an oversimplification of the real situation. A sensitivity analysis was conducted by incorporating a local vertical flux through the Tamarisk Member and the unnamed lower member into the Culebra dolomite. The conceptualization and implementation of the vertical flux are discussed in Chapter 6.

## 3.6 Sinks and Sources

### 3.6.1 The Undisturbed Hydrogeologic Situation

Under undisturbed (i.e., natural) hydrogeologic conditions it is assumed that no sinks or sources exist in the Culebra dolomite. Any fluxes in or out of the upper and lower boundary of the Culebra are not considered to be sinks or sources, but rather boundary conditions (Section 3.5.3). With this first conceptualization, only the undisturbed (steady-state) hydrology of the Culebra dolomite was modeled (Chapter 4). It has been assumed that steady-state formation pressures and fluid densities can be defined for the modeled region. Testing the validity of this assumption is beyond the scope of this modeling study.



### 3.6.2 The Hydrologic Situation Since 1981

Since the summer of 1981, the hydrogeology of the Culebra dolomite has been influenced by drilling and excavating three shafts (waste-handling shaft, construction and salt-handling shaft, and exhaust shaft) at the center of the WIPP site (see chronology and discussion of shaft-construction activities in Appendix F). In addition, several wells have been drilled or recompleted in the model area and numerous well-testing activities, some of very long durations (i.e., H-4 tracer test), have been conducted since 1981 (Appendix D). Consequently, the hydraulic situation at the beginning of or during the H-3 multipad pumping test can not be considered to be undisturbed. For illustration purposes, the hydraulic heads in October 1985 (i.e., at the beginning of the H-3 multipad pumping test) are listed in Table 3.10 and shown as a contour map in Figure 3.11. A comparison of Figure 3.11 with Figure 3.9 (undisturbed situation) or Figure 3.12 (showing the difference between Figures 3.9 and 3.11 as a contour map) reveals a large drawdown cone caused by the different activities at the WIPP site since 1981.

The center of the drawdown cone coincides with the location of the shafts. The diameter of the drawdown cone was about 7 km, the depth was about 33 m at the shaft location, assuming 926 m a.s.l. for the undisturbed freshwater head (Figure 3.9) and 893 m a.s.l. for the freshwater head in October 1985. The latter freshwater head was derived from pressure measurements in the waste-handling shaft (WHS) (using 710 kPa as an average gage pressure measured by the transducers PE 207 and PE 208, which are located at elevation 820.5 m a.s.l. in the waste-handling shaft; see additional details in Appendix F). The drawdown at the wells H-1 and H-2 were 12.2 m and 7.1 m, respectively. These numbers illustrate the order of magnitude of the disturbance of the hydraulic system in the Culebra dolomite.

The implementation of these disturbances at the WIPP site, which are transient by their nature, was achieved using the wellbore submodel of SWIFT II (Reeves et al., 1986a). This submodel allows injection or withdrawal of water from the model at specified locations (i.e., at the well locations). Details of the implementation are discussed in Chapter 5. Similarly, the H-3 multipad pumping test was implemented using the above mentioned wellbore submodel. This implementation is discussed in detail in Chapter 5.

### 3.7 Initial Conditions

The first stage of the model study attempted to simulate the undisturbed hydrogeologic situation at the WIPP site (Chapter 4) using steady-state solutions for pressure and brine (see Section 3.1.3). Because the initial pressures and brine concentrations do not affect the results of steady-state modeling, they were initialized as 101.3 kPa and 0.0, respectively.

During the subsequent phases of the modeling study, when the effect of shaft leakage, well-test activities, and the H-3 multipad pumping test (Chapter 5) were simulated, the steady-state solutions for pressure and brine of the undisturbed hydrogeologic situation were used as the initial conditions for the transient simulations.

#### 4.0 SIMULATION OF FLOW UNDER UNDISTURBED HYDRAULIC CONDITIONS (PRE-SHAFT CONDITIONS)

The first stage of the modeling study comprised the simulation of flow under undisturbed conditions. For this purpose, the model was implemented using the conceptualization as described in the previous chapter, and calibrated (1) against the best estimates of the undisturbed formation pressures or freshwater heads, and (2) against the best estimate of the formation fluid densities. This approach and the results are discussed in the following sections.

##### 4.1 Simulation Using the Initial Transmissivities

For the first modeling step, the kriged initial transmissivities (Section 3.4.1.4), the initial boundary conditions (Section 3.5.2), no-flow boundaries above and below the Culebra dolomite (Section 3.5.3), and no sinks or sources were used. The steady-state equations were solved for formation pressures and brine concentrations at the grid-block centers.

The results of this initial run are summarized in Figures 4.1, 4.2 and 4.3. Figure 4.1 shows the calculated freshwater heads, which are derived from the calculated formation pressures, as a contour map. A comparison with the contour map for the observed values (Figure 3.9) shows that there is a fair agreement between both maps. However, there are major head differences at H-11b3, DOE-1, and H-3b2. These differences are displayed more clearly in Figure 4.2, where the differences between the calculated and the observed freshwater heads are presented as a contour map.

The numeric values on which Figure 4.2 is based are listed in Table 4.1. Accordingly, the sum of the squared differences (between the calculated and the observed freshwater heads) at the 14 observation wells is

349.36 m<sup>2</sup>, which corresponds to a mean squared difference of 24.95 m<sup>2</sup>. As Table 4.1 shows, the calculated freshwater heads are generally too high; consequently, the kriged initial transmissivities in the southern part of the model are, in general, too low.

The calculated formation-water densities, which are derived from the calculated fractional brine concentrations, are presented in Figure 4.3. A comparison with the contour map for the observed values (Figure 3.10) shows that both maps are in fair agreement in the eastern part of the model area. In the western part, the agreement is good only along the northern model boundary. The modeled density distribution does not show the relatively low densities observed at H-1, H-2b, H-4b, P-14, and P-15. This inconsistency is caused by the model-calculated flow field (graphically shown in Figures 4.1 and 4.3 as Darcy-velocity vectors) which results in water (with densities of 1.04 g/cm<sup>3</sup>) flowing from the northern boundary to the south and southwest. Thus, the calculated formation-water densities are consistent with the calculated flow field but not with the observed density data.

#### 4.2 Calibration of the Model Using the Observed Freshwater Heads

The next step of the modeling study was to improve the agreement between the calculated and the observed formation pressures (or freshwater heads), i.e., to calibrate the model against the observed undisturbed freshwater heads. The fitting parameters of this calibration process were the transmissivities of the individual grid blocks.

In order to maintain consistency with the measured transmissivities in the model area, the initial transmissivities were modified during the calibration using the following approach. Additional data points with transmissivities (specified on the basis of judgement) were added to the data base used for the estimation ("kriging") of the grid-block transmissivities by the kriging program K603 (Section 3.4.1). Subsequently,

the modified transmissivity distribution was calculated by K603 using the enlarged (artificial) data base. Using this approach, it was possible to modify the grid-block transmissivities between the observation wells and still be consistent with the measured data. In addition, the spatial distribution of the modified kriged transmissivities has at least similar gradients and statistical properties as the original data set. Therefore, the kriged modified transmissivities are considered to be more representative for the real situation at the WIPP site than initially kriged transmissivities that are subsequently modified without consideration of the statistical properties.

This approach is thought to be new (i.e., not found in our review of the literature) and was introduced mainly because it eases the calibration process considerably. However, it is similar to de Marsily's (1982) idea of using "pilot points" during the calibration of a hydrologic model. These pilot points are determined in de Marsily's approach from an inverse simulation given the measured transmissivities and the measured hydraulic heads. Thus, the measured heads drive the changes in the transmissivity field through the inverse code. In the approach used in this modeling study, the transmissivities at the additional data points are simply deterministic estimates.

De Marsily recommends in his work the computation of a raw semi-variogram of the transmissivities at the "pilot points" after completion of the calibration process. A comparison of this "pilot point" semi-variogram with the theoretical semi-variogram, which was selected using the measured transmissivities, will show whether the "pilot point" transmissivities are consistent with the statistical properties of the observed data base. This consistency check was not performed in the present study. However, it is considered to be a useful step that should be included in future work. While conducting this consistency check is recommended, it is not an absolutely necessary step during the model calibration. It is presently planned to conduct this check during

the next step of the modeling study, which will incorporate results of both testing of individual wells during 1986 and 1987 and of a second (northern) multipad pumping test to be fielded early in 1987.

It should be emphasized that the calibration method described in this report has to be further tested and developed as a practical tool. Its rigorous stochastic credentials are as yet unproven, although we feel that it is as equally well-founded as de Marsily's technique (R. A. Freeze, personal communication).

As described above, the additional data points were added to or modified in the kriging data base in order to improve the consistency with the observed pressures (or freshwater heads). The aim of that calibration process was to reduce the differences between the observed and model-calculated heads to less than one meter at each observation well. This one meter criterion was selected based on the uncertainty of the observed (field-measured) values, which is believed to be of similar magnitude. These uncertainties in the observed values are the result of such factors as the use of various measurement systems to determine the downhole water levels or pressures, the uncertainties in the ground surface elevations, and the uncertainty in the estimate of the average density of the fluid in the wells.

The resulting transmissivities, which are referred to in this report as "pressure-calibrated steady-state transmissivities", are shown as the contour map in Figure 4.4. The (+) symbols which coincide with the locations of the observation wells indicate where transmissivities have been derived from field tests. The other (+) symbols represent the locations of prescribed transmissivities chosen for modifying the initial transmissivity distribution. A comparison with the initial transmissivities (Figure 3.7) essentially shows that the following modifications were made during the calibration process:

1. The grid blocks along the eastern model boundary and between H-12, P-18, and H-5 were assigned generally low transmissivities ( $T = 10^{-8}$  to  $10^{-7}$  m<sup>2</sup>/s). This is consistent with the hypotheses that the high transmissivities in the Culebra dolomite are caused mostly by dissolution effects and that the extent of dissolution decreases toward the east (Snyder, 1985). Accordingly, low transmissivities would be expected east of the dissolution front, i.e., along the eastern model boundary (Figure 2.2). Lowest transmissivities ( $10^{-8}$  m<sup>2</sup>/s or less) occur where no halite is apparently missing from the Rustler Formation.
2. A high-transmissivity zone ( $T = 1 \times 10^{-5}$  to  $2 \times 10^{-4}$  m<sup>2</sup>/s) was introduced between H-11b3 and the southern boundary in order to reduce the formation pressures at DOE-1 and H-11. In order to protect P-17 from too much drainage by this high transmissivity zone and maintain consistency with the pressures measured at P-17, the area around P-17 had to remain at its initial transmissivity ( $T = 1.8 \times 10^{-6}$  m<sup>2</sup>/s).
3. A low-transmissivity zone ( $T = 10^{-7}$  m<sup>2</sup>/s and less) was placed between WIPP-12 and H-5 in order to reduce the ground-water flow from the northern boundary towards DOE-1 and H-11. This measure reduced further the pressure at those two wells. The same pressure reduction could have been achieved by assigning even higher transmissivities (more than  $2 \times 10^{-4}$  m<sup>2</sup>/s) to the drainage zone south of H-11. However, the combination of low transmissivities north of DOE-1 and high transmissivities south of H-11 is considered to be more reasonable for representing the real situation at the WIPP site rather than just very high transmissivities south of H-11 only, because there is no other evidence (e.g., from well tests) of the occurrence of a zone with very high transmissivities (more than  $2 \times 10^{-4}$  m<sup>2</sup>/s) in the area south of H-11.

4. In order to obtain the observed pressure gradient between H-3 and H-2/H-1, the transmissivities in that area had to be increased relative to the kriged initial transmissivities. The resulting transmissivities ( $T = 4 \times 10^{-7}$  to  $1 \times 10^{-5} \text{ m}^2/\text{s}$ ) are consistent with the analytical interpretation of the H-3 multipad pumping test by Beauheim (in preparation) to obtain average transmissivities between H-3 and wells H-2 and H-1.

The correlation length of the transmissivities derived from the semi-variogram analysis (Section 3.4.1.3) is much larger than the average grid-block size in the central part of the model area. Therefore, the transmissivities of the grid block with a grid block center that does not exactly coincide with an observed data point (i.e., a well location) is influenced by the modifications described above, even if there is a well located within the grid block. The reason for this is one of the characteristics of kriging, which always uses all data points within the correlation length for the estimation of the value at a given point unless this point coincides with a data point.

As shown in Figure 3.4, the grid block centers generally do not exactly coincide with the well locations, although having coincident positions was attempted when the model grid was established (Section 3.2.3). Thus, after the calibration of the model, the transmissivities of the grid blocks which correspond to the locations of H-1 and H-2 are higher than measured in H-1 or H-2. This discrepancy is considered acceptable because the results of the single-well hydraulic tests at these wells are not necessarily representative for  $50,000 \text{ m}^2$ , i.e., the grid block size at H-1 or H-2.

5. After implementing all the transmissivity modifications described above, it was found that the pressures at H-1, H-2 and H-3b2 were



too low, although the gradients between them were correct. The transmissivities between H-3 and DOE-1/H-11 were consistent with the analytical interpretation by Beauheim (in preparation) and, therefore, they were not changed in order to increase the pressures of H-1, H-2, and H-3. Thus, to increase the pressures in the H-1, H-2, and H-3 region, the transmissivities between WIPP-13 and H-1 were increased to  $1 \times 10^{-5} \text{ m}^2/\text{s}$ . These transmissivities are consistent with the preliminary results of hydraulic testing performed in WIPP-13, which indicate a transmissivity between  $1 \times 10^{-6}$  and  $1 \times 10^{-5} \text{ m}^2/\text{s}$  (INTERA, unpublished estimate).

This intermediate transmissivity zone between WIPP-13 and H-1 caused a pressure increase at P-14, which had to be compensated by also increasing the transmissivities east of P-15 by half an order of magnitude.

The above-described transmissivity modifications were implemented step by step, gradually improving the agreement between the calculated and the observed pressures (or freshwater heads). However, there is no unique spatial transmissivity distribution that best fits the observed data. The reason for this lies simply in the large number of individual transmissivities (one for each of the 928 grid blocks), which in theory could be modified independently and in very small steps resulting in an almost infinite number of spatial transmissivity distributions.

Thus, the transmissivity distribution shown in Figure 4.4 represents only one possibility to calibrate the steady-state model to the undisturbed formation pressures or freshwater heads. However, in order to maintain consistency with the observed transmissivity data, the transmissivity distribution of any calibrated model will most likely show the following characteristics (as compared to the kriged initial transmissivities).

1. Either a very high-transmissivity zone between H-11 and the southern boundary, or a combination of a high-transmissivity zone there and a low-permeability barrier between WIPP-12 and H-5.
2. Slightly increased transmissivities in the area of H-1, H-2, and H-3.
3. A zone of increased transmissivity either between WIPP-13 and H-1 or between H-6 and H-1/H-2, or generally higher transmissivities between DOE-2 and H-1.

The hydrologic properties of the model using the transmissivities shown in Figure 4.4 are discussed in the following section.

#### 4.3 Pressure-Calibrated Model for Undisturbed Hydraulic Conditions

The results of the simulation using the same model parameters as the initial run (Section 4.1) but the pressure-calibrated steady-state transmissivities (Section 4.2) are summarized in Figures 4.5, 4.6, 4.7, and 4.8.

Figure 4.5 shows a contour map of the calculated freshwater heads which were derived from the calculated formation pressures. Additionally, the flow field is presented with Darcy-velocity vectors. A comparison with the contour map of the observed values (Figure 3.9) shows that there is a very good agreement between the maps. The remaining discrepancies are displayed in Figure 4.6, where the differences between the calculated and the observed freshwater heads are contoured.

The numeric values on which Figure 4.6 is based are listed in Table 4.2. The sum of the squared head differences for the observation wells is  $3.42 \text{ m}^2$ , which corresponds to a mean squared difference of  $0.24 \text{ m}^2$ . The largest head differences occur at P-17 ( $-0.94 \text{ m}$ ) and H-11 ( $+0.88 \text{ m}$ ).

Thus, the calibration criterion to reduce the difference to less than 1 m (Section 4.2) was achieved. Therefore, the model was considered to be calibrated against the undisturbed, long-term freshwater heads. In the following chapters this model is referred to as the "pressure-calibrated steady-state model".

The flow field of the pressure-calibrated steady-state model (Figure 4.5) can be characterized with respect to Darcy velocities as follows.

1. In the eastern model area (H-12, P-18, H-5), very low Darcy velocities (less than  $10^{-9}$  m/s or less than 0.03 m/y) occur because of the low transmissivities. Similarly, low Darcy velocities prevail in the area between WIPP-12, WIPP-21, P-18, and H-5, because low transmissivities have been implemented in this region during the calibration process.
2. Very low Darcy velocities (less than  $10^{-9}$  m/s or less than 0.03 m/y) can also be seen in the area of P-15, H-4, and P-17, and to the south of that area, where low transmissivities impede ground-water flow.
3. Darcy velocities between  $10^{-9}$  m/s (0.03 m/y) and  $5 \times 10^{-9}$  m/s (0.15 /y) occur in the area from H-6 and DOE-2 in the north to P-15 and H-4 in the south.
4. Relatively high Darcy velocities ( $10^{-8}$  m/s or 0.03 m/y and more) were calculated for the western part of the model area and the high-transmissivity zone between H-11 and the southern boundary. These areas correspond to relatively high transmissivities (Figure 4.4).

Thus, in general, the Darcy velocities are closely correlated to the transmissivities assumed for the Culebra dolomite. Similarly, the flow paths depend strongly on the transmissivity distribution. As Figure 4.5 shows, there are two main ground-water flow paths associated with the high transmissivities in the model area: the first one flowing from north to south along the western model boundary, and the second one starting between H-6 and DOE-2 in the north, flowing to the south to H-2, turning south-eastward, passing H-3 and DOE-1 and flowing again to the south from H-11 to the southern model boundary.

The calculated formation-water densities, which are derived from the calculated fractional brine concentrations, are presented in Figure 4.7. A comparison with the calculated densities of the initial run (Figure 4.3) shows that there are only minor differences. The general pattern, i.e., high densities ( $1.08 - 1.10 \text{ g/cm}^3$ ) in the eastern part and intermediate densities ( $1.03 - 1.05 \text{ g/cm}^3$ ) almost everywhere else, remained the same. The differences between the observed densities and the model-calculated values are displayed as a contour map in Figure 4.8. Accordingly, the model calculated values are too low at DOE-1, H-11, and P-17. This is caused by the rather low-density water that flows from the central part of the model (region of H-1, H-2, and H-3) to DOE-1 and H-11 and then through the high-transmissivity zone to the southern model boundary (Figure 4.7). Because the transmissivities north and east of H-11 and DOE-1 are relatively low, only a small amount of high-density water reaches the location of DOE-1 and H-11. Consequently, the calculated fluid density there is almost the same as in the central region (H-1, H-2, H-3). Additional calibration work to decrease the differences between the observed and the calculated density values at DOE-1 and H-11 is described in Section 4.5.

As Figure 4.8 further demonstrates, the calculated densities at H-1, H-2, H-4, P-14, and P-15 are too high. With the flow field of the pressure-calibrated steady-state model, the calculated densities at

these locations are governed by the densities assigned to the northern boundary conditions of the western half of the model. It is obvious that with the boundary conditions implemented (lateral prescribed pressure and prescribed density boundary conditions, but no vertical flux into or out of the Culebra dolomite) and a general hydraulic gradient from south to north, it is almost impossible to obtain a north-south density gradient as apparently observed between H-6 and H-2 or between DOE-2 and H-1 (Figure 3.10).

Assuming that the measured densities are representative for the formation water in the area of the boreholes from which the samples were taken, there are several alternative approaches to address the problem.

1. The boundary conditions assigned to the northern model boundary may not represent the real situation. As Figure 3.10 reveals, the densities assigned to the western part of the model boundary are governed by the values observed at WIPP-25, H-6, DOE-2, and WIPP-30. During the definition of the boundary conditions it was assumed that interpolation (as conducted by the contouring program) between the boreholes would provide a spatial density distribution representative of the real situation. This assumption is probably valid if the connecting line between the boreholes (between which the interpolation is done) is more or less parallel to the ground-water flow, but not necessarily valid if the connection line is perpendicular to the ground-water flow (as it is in the present case). In the latter case, the density distribution between two wells can be rather heterogeneous. Thus, the densities for the boundary conditions were modified in the subsequent calibration described in Section 4.5 in order to improve the consistency between the calculated and observed formation-fluid densities.
2. There may be water with low mineralization leaking through the Tamarisk Member into the Culebra dolomite, or highly mineralized

water rising through the unnamed lower member of the Rustler Formation. Such a vertical flux could cause the irregular spatial density distribution observed. The testing of this possibility was attempted by locally implementing a vertical, low-density or high-density flux into the modeled Culebra dolomite. The conceptualization and implementation of this vertical flux and the effects on the spatial density distribution are discussed in Chapter 6.

3. The observed density distribution may not represent a steady state. This would mean that the higher densities in the northwestern part of the model represent the front of more saline water coming from the north and replacing older, less saline water. This theory is difficult to verify and also difficult to implement as a conceptualization of the model. Modeling this process would require a transient simulation covering several thousand years. Therefore, it was not further pursued within the scope of this modeling study.

#### 4.4 Sensitivity of the Model to Dispersivity

Before further model calibration (i.e., against the observed densities) was conducted, the pressure-calibrated steady-state model was used to investigate the sensitivity of the model to changes in the longitudinal and transverse dispersivity.

As discussed in Section 3.3.3, longitudinal and transverse dispersivities of 50 m and 2.5 m, respectively, were selected and used throughout the modeling. However, because of the uncertainties associated with the estimation of these transport parameters, a systematic parameter variation was performed.

During this parameter-sensitivity study, the longitudinal dispersivity was varied using 10 m, 20 m, 50 m, 100 m, and 200 m. This range in longitudinal dispersivity is considered adequate for the regional scale

of the ground-water flow system that is being modeled. The transverse dispersivity was changed accordingly so that the ratio of transverse to longitudinal dispersivity stayed constant at 0.05.

The results of simulations using this parameter variation are shown in Figures 4.9 and 4.10, where the calculated freshwater heads and the density distributions are shown for a longitudinal dispersivity of 50 m (chosen as the standard case) and for dispersivity values of 10 m and 200 m. As seen, the effect of varying the dispersivities is very small in the range from 10 m to 200 m. Thus, the model can be considered to be insensitive to changes in dispersivity. The reason for this is the fact that there are no really strong density contrasts (over small to intermediate distances) in the calculated spatial density distribution of the calibrated steady-state model.

#### 4.5 Calibration of the Model Using the Observed Formation-Water Densities

The next step of the modeling study was to improve the agreement between the calculated and the observed formation-water densities. As discussed in Appendix E, the observed density data can be associated with an error of 0.5 - 0.6 percent inherent to the hydrogeochemical analyses and the evaluation methods. This error does not include any possible error caused by contamination of the water samples by non-formation waters (e.g., drilling fluid). Although methods exist to check the hydrogeochemical consistency of water samples with the formation from which they were taken (Appendix E), it is difficult to quantify the error caused by contamination unless the chemistry of the contaminant fluid and its percentage in the sample is known (e.g., as a result of drilling fluid tracer application). However, these hydrogeochemical consistency checks have demonstrated that in general the water samples appear to be representative for the Culebra dolomite (Appendix E.). Therefore, the possible error due to contamination is not likely to exceed the

analytical error, resulting in an estimated overall error of about 1% of the observed density values. Thus, the accuracy of the observed formation-water densities is assumed to be  $\pm 0.01 \text{ g/cm}^3$ , unless the hydrogeochemical consistency checks indicate a higher possible error (Appendix E, Table E.3).

Accordingly, the aim of the calibration process was defined to reduce the difference between the observed and the model calculated densities to less than or equal to  $0.01 \text{ g/cm}^3$  at those borehole locations where reliable water samples have been taken. Of course, calibration against the undisturbed formation pressures (or freshwater heads) had to be maintained during calibration to the observed formation-water densities.

The starting point of this calibration stage was the transmissivities and the boundary conditions of the pressure-calibrated steady-state model. The model transmissivities were step-wise modified using the approach described in Section 4.2.

The resulting transmissivities, which are referred to in this report as 'density-calibrated steady-state transmissivities', are shown as a contour map in Figure 4.11. A comparison with the pressure-calibrated steady-state transmissivities (Figure 4.4) shows that the following modifications were made during the calibration process:

1. The high-transmissivity zone ( $T = 2 \times 10^{-4} \text{ m}^2/\text{s}$ ) between H-11 and the southern model boundary was shifted three grid blocks to the west in order to direct the low-density ground water coming from the model center (H-1, H-2, H-3) more to the west. In addition, the low transmissivities between H-5 and P-18 introduced during the calibration against the undisturbed heads (Section 4.2) were removed, allowing more high-density ground water flowing from the northeastern corner to the area of DOE-1 and H-11. This additional flow from the northeast did not significantly increase the heads at



DOE-1 and H-11 because the high transmissivity in the south was placed in a wider grid block allowing more water to be drained without increasing the transmissivity of the zone itself. As a result of these changes, the calculated formation-water density at DOE-1 and H-11 was increased by about  $0.04 \text{ g/cm}^3$ .

2. In order to maintain the head at P-17, it was necessary to increase the number of "artificial" points with low transmissivities around P-17. Nonetheless, it proved to be difficult to avoid too much drainage at P-17 as a result of the high-transmissivity zone, while maintaining sufficient drainage from the area at DOE-1 and H-11. Therefore, the question arises whether the best estimate of the undisturbed head for P-17 (911.2 m, Table 3.7) is accurate. As Figure 3.9 shows, the contour lines in general are smooth. One exception is the 912 m elevation line near P-17 which indicates a freshwater elevation somewhat too high for the general pattern. Taking into account the local hydraulic gradient in the neighborhood of P-17 (about  $2\text{m/km}$ ), a hydraulic head of 910 m a.s.l. seems to be more representative than the previously estimated 912.2 m a.s.l.

One possible reason for an overestimated head value at P-17 might be that the estimate of the density of the borehole fluid used for the calculation of the freshwater head is wrong. Assuming for instance an effective borehole fluid density of  $1.04 \text{ g/cm}^3$ , a freshwater head of 909.6 m (using 842.4 m a.s.l. for the center of the Culebra dolomite and 907.0 m a.s.l. for the water level in the well) would result and fit much better to the regional pattern. This explanation is supported by the difficulties in calibrating the model such that the calculated formation-fluid density at P-17 is  $1.060 \text{ g/cm}^3$  (see Section 4.6).

With the above-mentioned changes in the transmissivities, it was possible to improve the consistency between the calculated and the observed formation-water densities at DOE-1 and H-11. As discussed in Section 4.3, the calculated densities at the well locations depend strongly on the prescribed densities of the boundary conditions along the northern model boundary. Therefore, the prescribed densities for the boundary conditions were step-wise modified during the calibration against the observed formation-water densities. The resulting boundary conditions are listed in Table 4.3. A comparison with the initial boundary conditions (Table 3.9) shows that essentially the following modifications were made:

1. The prescribed formation-water densities along the western model boundary and along the western part of the northern model boundary were lowered except directly north of H-6. Consequently, the calculated densities at H-1, H-2, H-4, P-14, P-15, and H-7 were lowered, while the value at H-6 remained more or less the same. Thus, the agreement between the calculated and the observed formation-water densities is satisfactory (i.e., the difference is less than  $0.01 \text{ g/cm}^3$  for most wells). However, the assignment of a rather high density ( $1.039 \text{ g/cm}^3$ ) north of H-6 does not really solve the problem of understanding the reason for the relatively high density at H-6 from a scientific point of view, but rather transfers it to the outside of the model area. Therefore, the question of why relatively different formation-water densities occur in the western part of the model area was not answered by the present modeling study (see also Section 6.1.2).
2. The prescribed formation-water densities along the northern model boundary between DOE-2 and H-5 were adjusted in order to calibrate the calculated formation-fluid densities in the eastern part of the model area.

The above-described modifications of the transmissivities and the changes in the densities of the boundary conditions were implemented step by step, gradually improving the agreement between the calculated and the observed formation-fluid densities while trying to maintain the achieved calibration against the observed freshwater heads. The results of this calibration are discussed in the following section.

#### 4.6 Density-Calibrated Model for Undisturbed Hydraulic Conditions

The results of the simulation using the modified transmissivities and boundary conditions described in the previous section are shown in Figures 4.12 through 4.15.

Figure 4.12 shows the calculated freshwater heads as a contour map. The differences between the calculated and the observed freshwater heads are listed in Table 4.4 and presented as a contour map in Figure 4.13.

A comparison with the corresponding Figures 4.5 and 4.6 and Table 4.2 of the pressure-calibrated model shows that the calculated heads were only slightly changed by the calibration against the observed formation-water densities. The sum of the squared head differences for the observation wells increased from  $3.43 \text{ m}^2$  (Table 4.2) to  $4.57 \text{ m}^2$  (Table 4.4). This increase results mainly from a higher freshwater head at H-11 and from lower values at H-4 and P-17, which are caused by shifting the high-transmissivity zone (south of H-11) to the west (see previous section). It would have been possible to reduce the difference between the calculated and the observed freshwater heads at either H-11 or at P-17 and H-4, but causing an increased difference at the other location. Thus, the calculated heads and head differences of the density-calibrated model as shown in Figures 4.12 and 4.13 are a balanced compromise with an error of  $+1.08 \text{ m}$  and  $-1.07 \text{ m}$  at H-11 and P-17, respectively (Table 4.4). As already discussed in the previous section, the measured freshwater head at P-17 may not be representative for that location.

Therefore, it was felt that the achieved pressure calibration at P-17 and H-11 was sufficient, and no further attempts to improve the calibration were made.

A second area where the calibration against the observed freshwater heads deteriorated during the density calibration was in the central region (H-1, H-2, H-3). For instance, the error at H-3 increased from -0.16 m to -0.97 m (Tables 4.2 and 4.4). However, the increased errors are still within the 1-m calibration limit, defined in Section 4.2. Therefore, the calibration of the central region was still considered to be sufficient.

The calculated formation-water densities and the differences between the calculated and the observed densities are shown in Figure 4.14 and 4.15, respectively. A comparison with the corresponding figures (Figures 4.5 and 4.6) of the pressure-calibrated model shows that the agreement between the calculated and the observed densities was improved significantly. As discussed in Section 4.5, the aim of the calibration process was to reduce the absolute differences between the observed and the calculated densities to less than or equal to  $0.01 \text{ g/cm}^3$ . As Figure 4.15 demonstrates, this aim was reached at all borehole locations except at P-17, H-3, and DOE-1.

The difference at P-17 ( $-0.04 \text{ g/cm}^3$ ) is by far the largest in the model area. It is a direct result of the simulated flow field (Figure 4.14) which carries low-density water from the central region to the high-transmissivity zone between H-11 and P-17, causing relatively low densities at P-17 ( $1.020 \text{ g/cm}^3$  instead of  $1.060 \text{ g/cm}^3$ ). There is no possibility of obtaining significantly higher densities at P-17 with this flow field. Significant changes of this flow field are restricted by the following facts:

1. The relatively low freshwater heads at DOE-1 and H-11 require a high-transmissivity zone between these two boreholes and the southern boundary.
2. The transmissivity between DOE-1/H-11 and the central region (H-1, H-2, H-3) cannot be changed significantly and still be consistent with the interpretation of the H-3 multipad pumping test by Beauheim (in preparation). Thus, there will always be a rather strong flow of low-density ground water from the central region to the area of DOE-1 and H-11.
3. The transmissivities north and east of DOE-1 must be two to three orders of magnitude lower than the transmissivities of the high-transmissivity zone south of H-11 in order to obtain the observed head distribution (DOE-2, H-5, DOE-1, H-11, H-12). Therefore, it is not possible to increase the transmissivities north of DOE-1 significantly (e.g., in order to bring more high-density water into the area of DOE-1 and H-11) without increasing the transmissivities of the high-transmissivity zone. However, the possible range of the permeability of the high-transmissivity zone is given by the results of the kriging analysis, which shows for the region south of H-11 a transmissivity of about  $4 \times 10^{-6} \text{ m}^2/\text{s}$  (Figure 3.7) and estimation errors of about 1.3 on the log scale. Using  $\pm 2\sigma_0$  as the confidence interval (95% confidence level), the possible transmissivities range from  $1 \times 10^{-8}$  to  $1.5 \times 10^{-3} \text{ m}^2/\text{s}$ . Thus, the implemented transmissivities of the high-transmissivity zone ( $2 \times 10^{-4} \text{ m}^2/\text{s}$ ) are already significantly higher than would be estimated by the kriging analysis, although they are still well within the 95% confidence interval. However, it was felt that the transmissivities should not be increased much more without having additional evidence for the existence of such a very high transmissivity zone in the southern part of the model area. Consequently, the transmissivity in the area between WIPP-12, H-3, P-18, and DOE-1 cannot be changed significantly.

4. The exact position of the high-transmissivity zone in the southern model area can be varied. However, moving it to the east directs the low-density ground-water flow coming from the central area (H-1, H-2, and H-3) more to the east causing the densities to be too low at DOE-1 and H-11. Moving it more to the west improves the density fit for DOE-1 and H-11, but lowers the calculated heads at H-4 and P-17 too much. Thus, the position shown in Figure 4.11 is a compromise between having low densities at DOE-1 and H-11 and low heads at P-17 and H-4.

During the calibration process, the high-transmissivity zone was placed between H-4 and P-17 in order to increase the calculated formation-fluid density at P-17 (Figure 4.16). The best fit to the observed values that could be obtained with this variation is shown in Figures 4.17 through 4.20. As these figures show, it was possible to direct the low-density ground water more to the west, but not enough to reach an acceptable agreement between the calculated and the observed densities at P-17. The calculated heads at H-11 and DOE-1 are too high, because the high-transmissivity zone is too far away. In addition, the calculated heads at H-4 and P-17 are too low, because the high-transmissivity zone drains too much water from that area. Even the general head distribution (Figure 4.17) is less consistent with the observed pattern (Figure 4.9) than the head distribution (Figure 4.12) resulting from positioning the high-transmissivity zone east of P-17. Because there is apparently no way to obtain a good overall agreement between calculated and observed freshwater heads with the high-transmissivity zone placed between H-4 and P-17, this conceptualization was not pursued further during the calibration process.

As a consequence, there does not appear to be any possibility of changing significantly the general flow field shown in Figure 4.12 without sacrificing the consistency between calculated and observed

heads and densities. Therefore, it is not possible to obtain a good agreement between the calculated and the observed formation fluid densities at P-17 with the given model conceptualization. There are two possible explanations for this density inconsistency.

1. The observed density at P-17 may not be representative for the borehole location (see also previous section). This question can be only answered by additional, carefully monitored, long-term production tests at P-17.
2. The observed high densities at P-17 may be a local phenomenon caused by vertical ground-water flow (e.g., from the Rustler-Salado contact residuum through the unnamed lower member of the Rustler Formation) into the Culebra dolomite. This possibility was further investigated by conducting a sensitivity analysis concerning vertical flux (see Chapter 6).

Because there is apparently no immediate way to solve the problem with the density at P-17, the inconsistency was left during the remainder of the modeling study, except for the sensitivity analysis mentioned above.

A similar problem exists with the formation-water density at H-6. The observed value is about  $1.04 \text{ g/cm}^3$ . As already discussed, the boreholes south of H-6 show lower formation-water densities. With the simulated flow field it is difficult to obtain this kind of spatial density distribution. As described in the previous section, an acceptable agreement between calculated and observed density values was obtained by assigning generally low densities to the northern model boundary, except directly north of H-6. It was already mentioned that this heterogeneous boundary condition only transfers the problem to the outside of the model area but does not explain the apparent hydrogeologic phenomenon. Again, one possible explanation might be the occurrence of vertical flux into the Culebra dolomite, either from above or below, causing a spatial density distribution that cannot be explained by horizontal flux only.

Hydropad H-3 is the second location within the density-calibrated steady-state model where the difference between the calculated and the observed formation-water densities exceeds  $0.01 \text{ g/cm}^3$  (Figure 4.15). The observed density is  $1.04 \text{ g/cm}^3$  while the calculated one is about  $1.02 \text{ g/cm}^3$ . The low calculated densities are mainly a result of the southeast-directed ground-water flow in the central region (H-1, H-2, and H-3). This flow direction depends on the local spatial transmissivity distribution. Locally changing the transmissivities results in different calculated densities at H-3. Because the transmissivities in the central region are the fitting parameters for the future calibration during the transient modeling, and therefore subject to changes, it was not attempted to improve the density fit at H-3 during the calibration against the observed formation-water densities.

The third borehole where the difference between the observed and the calculated formation-water densities exceeds  $0.01 \text{ g/cm}^3$  is DOE-1 (Figure 4.15). There the observed value is  $1.090 \text{ g/cm}^3$  while the density-calibrated model calculated density is  $1.074 \text{ g/cm}^3$ . Similar to H-3, the density at DOE-1 depends strongly on the local transmissivity distribution in the central model area (shaft location, H-1, H-2, and H-3). Because this area will be subject to changes during the calibration against the transient data and, more important, because the observed density value of DOE-1 may not be representative of the formation-water at that location (Appendix E), improving the fit at DOE-1 was not attempted.

#### 4.7 Summary of the Steady-State Modeling

Starting with the initial kriged transmissivities and the initial boundary conditions, the steady-state model was step-wise calibrated against the best estimate of the undisturbed freshwater heads and the observed long-term formation-water densities.



Compared with the kriged initial transmissivity distribution, the resulting transmissivity distribution (Figure 4.11) of the density-calibrated steady-state model is characterized by a high-transmissivity zone ( $T = 2 \times 10^{-4} \text{ m}^2/\text{s}$ ) between H-11 and the southern model boundary. This high-transmissivity zone is necessary in order to obtain the observed relatively low freshwater heads at H-11 and DOE-1. Placing it between H-4 and P-17 does not result in a satisfactory agreement between the calculated and the observed freshwater heads.

The difference between the calculated and observed freshwater heads (Figure 4.13) is less than 1.1 m for all well locations and less than 1 m in general. Taking into account the uncertainty associated with the observed freshwater heads, the calibration of the steady-state model can be considered satisfactory.

The pressure-calibrated steady-state model was used to investigate the sensitivity of the model to changes in dispersivity. A systematic parameter variation with the longitudinal and transverse dispersivities demonstrated that the steady-state model is insensitive to changes in dispersivity.

The difference between the observed and calculated formation-fluid densities (Figure 4.13) is generally less than  $0.01 \text{ g/cm}^3$ , i.e., sufficient. A large inconsistency ( $-0.040 \text{ g/cm}^2$ ) exists between the observed and the calculated densities at P-17. It was not possible to reconcile the model at P-17 with the existing data. Possible reasons are (1) the measured density value of P-17 is not representative for the formation fluid in the Culebra dolomite at that location or (2) the measured density value represents a rather local phenomenon possibly caused by vertical flux from either above or below the Culebra dolomite.

A second inconsistency between calculated and observed densities ( $-0.021 \text{ g/cm}^3$ ) remains at H-3. Because the calculated density at H-3 depends strongly on the local transmissivity distribution which will be changed during future calibration against the transient data, it was not attempted to improve the steady-state density calibration at H-3. At DOE-1, a difference between calculated and observed densities of  $-0.016 \text{ g/cm}^3$  was not eliminated, mainly because the observed value may not be representative for the formation water at that location. However, given the constraints of the model conceptualization and the accuracy of the field data, the steady-state model can be considered to be calibrated against the observed formation-water densities.

## 5.0 SIMULATION OF TRANSIENT FLOW RESULTING FROM SHAFT ACTIVITIES AND WELL TESTS

The original scope of the modeling study was to evaluate only the H-3 multipad pumping test, i.e., to simulate the transient behavior of the Culebra dolomite in response to this test. However, during the preparation of the data base and the development of the modeling approach, it became obvious that the hydraulic conditions in the Culebra dolomite have been influenced by drilling and testing activities at the shafts and the well locations since 1981 (Section 3.6.2). Consequently, it was not possible to simulate realistically the H-3 multipad pumping test by simply assuming undisturbed hydraulic conditions at the beginning of the test. It was necessary to implement the major disturbing events (i.e., shaft activities and well tests) in order to obtain initial hydraulic conditions that are representative of the hydraulic situation in the Culebra dolomite at the beginning of the H-3 multipad pumping test.

The implementation and simulation of the shaft activities and the well tests that are considered to be important, as well as the simulation of the H-3 multipad pumping test, are discussed in the following sections.

### 5.1 Implementation of Shaft Activities

As already discussed in Section 3.6.2, the hydrogeology of the Culebra dolomite has been influenced by drilling and excavating three shafts (waste-handling shaft, construction and salt-handling shaft, and exhaust shaft) at the center of the WIPP site. These shaft activities have been by far the most important hydrologic disturbance at the WIPP site since 1981, resulting in changes of more than 10 m in the piezometric surface at the central part of the WIPP site (Section 3.6.2).

### 5.1.1 The Early Shaft History

The first shaft excavated was the construction and salt-handling shaft, formerly called the exploratory shaft (Appendix F). A detailed history of the shaft construction was reported by Fenix and Scisson (1982). This history was used by Stevens and Beyeler (1985) to model the effect of the shaft drilling and shaft completion on the hydrologic response at the H-1, H-2, and H-3 wells in both the Magenta and the Culebra Dolomite Members of the Rustler Formation. As demonstrated by Stevens and Beyeler (1985), the effect of the exploratory-shaft construction on the pressures in the Culebra dolomite was significant at the well locations H-1, H-2, and H-3.

A synopsis of drilling and construction events relevant to this study is summarized below (modified after Stevens and Beyeler, 1985):

- 04 July 81 : Start of reverse-rotary drilling with 3.68-m diameter. Land-surface elevation is about 1039.4 m a.s.l.
  
- 04 August 81 : Drilled into the top of the Culebra dolomite (Figure 5.1).
  
- 09 August 81 : Drilled through the bottom of the Culebra dolomite. The drilling-fluid level in the shaft fell below the bottom of the Magenta dolomite (about 847.4 m a.s.l.). Consequently, the fluid pressure in the Culebra dolomite (center at 822 m a.s.l.) fell below 350 kPa.
  
- 15 August 81 : Drilling-fluid level in the shaft fell below the bottom of the Culebra dolomite; subsequently, ground-water flow from the Culebra dolomite into the

shaft was unrestricted and the Culebra dolomite was exposed to atmospheric pressure (about 101 kPa).

24 October 81 : Drilling stopped 701 m below land surface; the borehole was filled with brine to about 77 m below land surface (962 m a.s.l.). The brine density was not reported. Stevens and Beyeler (1985) estimated the ratio of the density of the brine to the density of the formation fluid to be about 1.3. The formation-fluid density at the shaft location is not exactly known, but likely to be between 1.02 g/cm<sup>2</sup> (e.g., at the well H-1) and 1.04 g/cm (e.g., at H-3 or DOE-2). Consequently, it can be assumed that the density of the brine was about 1.3 g/cm<sup>3</sup>, which is rather high. Using this density, the pressure at the center of the Culebra dolomite can be calculated to be 1886 kPa. The corresponding equivalent freshwater head equals 1004.0 m a.s.l.

25 October 81 : Brine was continually added to the shaft. The  
to drilling fluid level, which was occasionally  
15 November 81 reported, rose about 35 m over the time period.  
It is likely that a considerable amount of brine invaded the Culebra dolomite during that time period.

16 November 81: The drilling fluid level in the shaft was at about 997.2 m a.s.l., resulting in a pressure of about 2334 kPa at the center of the Culebra dolomite (assuming 1.30 g/cm<sup>3</sup> as brine density). This corresponds to an equivalent freshwater head of 1049.7 m a.s.l.

- 16 November 81 : The casing was lowered into the shaft. Stevens and  
to  
03 December 81 : Beyeler (1985) assumed that the brine either over-  
flowed the borehole while the casing was being  
lowered or the brine level was at ground level.  
This assumption results in a calculated formation  
pressure in the Culebra dolomite of 2873 kPa or an  
equivalent freshwater head of 1104.6 m a.s.l.
- 04 December 81 : Beginning December 4, the annular space between the  
to  
06 December 81 : Beyeler (1985) again made the assumption that the  
brine in the shaft was either overflowing onto the  
land surface or was at land surface. Thus it can be  
assumed that the formation pressure in the Culebra  
dolomite was about the same as during the casing  
installation. On December 6, the cement-sealing  
operation ended.

Thus, the early shaft history comprises the time period from July 1981 through December 1981. The effects of the activities at the exploratory shaft during that time period on the hydrologic situation at the locations of H-1, H-2, and H-3 can be seen in the corresponding diagrams in Appendix D (Figures D.1, D.2, and D.3). All three figures show a sudden decrease of the freshwater elevation in the third quarter of 1981, which was caused by the first exposure of the Culebra dolomite to atmospheric pressure. The peak elevation, caused by filling the exploratory shaft with brine in December 1981, is also clearly shown on all three diagrams. The subsequent decrease of the freshwater elevations in 1982 reflects the end of the influence by the exploratory shaft and the exposure of the Culebra dolomite to atmospheric pressure at the ventilation shaft (Section 5.1.2). Although the above-discussed early shaft activities did not significantly influence the hydrologic situation

in the Culebra dolomite in 1985, they were incorporated into the simulations because their effects represent an excellent test of the behavior of the transient model. The effect of the shafts over the total period of 1981 to 1985, however, did have a pronounced influence on the pressure distribution in the Culebra at the start of the H-3 multipad test in 1985.

#### 5.1.2 The Open-Shaft Period

The drilling of the ventilation shaft (1.83-m diameter), which was widened two years later and renamed the waste-handling shaft (5.8-m diameter), was started in December 1981 and completed in February 1982. Drilling-fluid-level data from this time period were not available. Therefore, it was assumed that, similar to the drilling of the exploratory shaft (Section 5.1.1), the drilling-fluid level fell below the Culebra dolomite on January 15, 1982. Subsequently, the ground-water flow from the Culebra dolomite into the shaft was unrestricted, i.e., the Culebra dolomite was again exposed to atmospheric pressure. The ventilation shaft remained open and draining prior to excavation as the waste-handling shaft between November 1983 and August 1984.

The third of the three shafts, the exhaust shaft, was started as a 7-7/8-inch pilot hole in October 1983. It was drilled out to an 11-inch diameter in December 1983. The shaft was then raise-bored to 1.83-m diameter from December 1983 to February 1984. Although the liner plate at the elevation of the Culebra dolomite was grouted during shaft construction in December 1984, considerable seepage through the lining was observed (more than 1 liter/min; details see Appendix F). An additional grouting and sealing of the Culebra dolomite was conducted in June and July 1985. The exact date for which the sealing of the Culebra dolomite was effective is not known. Based on the recorded pressures at the waste-handling shaft

(Appendix F, Figure F.2), it was assumed for modeling purposes that the Culebra dolomite at the exhaust shaft was sealed on July 15, 1985. At the scale of the model, the three shafts can be considered to be a single hydrologic factor in the model. Consequently, it was assumed for the modeling study that the Culebra dolomite was exposed to atmospheric pressure from January 15, 1982 through July 15, 1985. During this time period, the ground-water flow from the Culebra dolomite into at least one of the shafts was assumed to be unrestricted.

The drawdown at the well locations H-1, H-2, and H-3 caused by the open shafts can be seen in the corresponding diagrams in Appendix D (Figures D.1, D.2, and D.3). Subsequent to spring 1983, the drawdown at these wells was disturbed by other activities (e.g., pumping tests). Therefore, the long-term drawdown caused by the open shaft can only be estimated. The drawdown can be estimated to be about 14 m at H-1, about 4 m at H-2, and about 2.8 m at H-3.

The recorded data of H-4, H-5, H-6, P-15, and P-17 (Appendix D, Figures D.4, D.5, D.6, D.16, D.17) do not show a clear response to the construction work at the shafts, partly because their water levels were disturbed by other factors. It was assumed that the effect of the open shafts at these well locations was less than 1 m.

No water-level data for the time period before 1984 were available for the locations of DOE-1, H-11, WIPP-18, WIPP-19, WIPP-21, and WIPP-22. Therefore, it is not possible to estimate the effect of the shaft construction on the formation pressures at these locations.



### 5.1.3 The Shaft Leakage After Shaft Sealing

As mentioned before, the last of the three shafts (i.e., the exhaust shaft) was lined and sealed in July 1985. However, the sealing in all three shafts is not fully effective, allowing formation water from the Culebra to leak through the shaft seals (Appendix D and F). Pressure transducers monitor the formation pressure behind the shaft sealing. Both the observed leakage and the measured formation pressures indicate that the Culebra dolomite did not return to its undisturbed hydrologic situation but is developing a new hydrologic equilibrium, with a formation-pressure drawdown cone around the shaft location. The depth and the size of the new drawdown cone will be governed by the long-term pressure at the shaft location and the remaining leakage rates.

Thus, at the beginning of the H-3 multipad pumping test in October 1985, the hydrologic situation of the Culebra aquifer was somewhere between the situation in the first half of 1985, which is characterized by a Culebra dolomite which has been exposed to atmospheric pressure for 4 years, and a new hydrologic equilibrium defined by the remaining shaft leakage (Section 3.6.2).

The existing data (Appendix D) indicate that the Culebra freshwater elevation at the shaft location between July 1985 and October 1985 was somewhere between 885 and 900 m a.s.l. There are no documented measurements of the total shaft leakage for that time period. Leak-rate measurements taken in the waste-handling shaft in 1986 range between 0.5 and 2 l/min. For the first transient simulations, a total leak rate (for all three shafts) of 2 l/min was assumed for the sealed but leaking shafts.

#### 5.1.4 Implementation of the Shaft History

In order to simulate the shaft history outlined in the previous sections, a sink/source at the shaft location was included in the model. Technically this was done by placing a pumping/injection well in the grid block that corresponds to the location of the three shafts. The early shaft history (Section 5.1.1) and the open-shaft period (Section 5.1.2) were simulated using the pressure-controlled mode of the wellbore submodel (Reeves et al., 1986a). Using this model option, the transient pressures at the shaft location during that time period were prescribed. The corresponding leak or injection rate was automatically adjusted by SWIFT II during the simulation so that the prescribed pressures were maintained at the grid-block center.

For the simulation of the sealed but leaking shafts (Section 5.1.3), the rate-controlled mode of the wellbore submodel (Reeves et al., 1986a) was used. As discussed in Section 5.1.3, an estimated leak rate of 2 l/min was used. This leak rate was modified later in the modeling study in order to fit the calculated pressures to the observed data (Section 5.5).

#### 5.2 Implementation of Well Tests

Since 1981, the hydrogeology of the Culebra dolomite has not only been disturbed by the shaft activities discussed in the previous section but also by numerous well tests. Important for the hydraulic situation in the central part of the model area were the tests performed at H-2, H-3, and H-4. Consequently, the tests on these wells or hydropads that were considered to be relevant and for which sufficient data were available were implemented in the model.

In the following sections, the tests which meet the above-mentioned criteria are briefly described and their implementation discussed.

#### 5.2.1 Well Tests at the H-2 Hydropad

The test history of the H-2 hydropad is rather complicated (Appendix D, Figure D.2), consisting of a number of slug, pumping, and tracer tests. However, for this modeling study, only tests conducted since 1981 were considered, mainly because earlier tests are not likely to have an influence on the hydrologic situation in the Culebra dolomite in 1985 or 1986.

Based on unpublished information (test field notebooks by Hydro Geo Chem and INTERA Technologies, Inc.), the following major tests have been conducted at the H-2 hydropad since 1981:

- a pumping test at H-2b2 (October 13-16, 1983) with an average pumping rate of 1.47 l/min (calculated for a 36-hour pumping period);
- a second pumping test at H-2b2 (November 8-17, 1983) with an average pumping rate of 1.07 l/min;
- bailing at H-2b1, H-2b2, and H-2c between June 7, 1984 and July 2, 1984. The volumes of ground water removed from the different boreholes during the different tests totaled about 8100 l. This corresponds to an average production rate of 0.23 l/min during that time period;
- a third pumping test at H-2b2 (July 17 - August 2, 1984). During eight pumping periods, about 2600 l were removed from that borehole. This corresponds to an average pumping rate of 0.11 l/min during the time period.

Numerous additional tests or similar activities were performed since 1981, but because they did not last more than 3 or 4 days, they were not considered to be important enough to be implemented into the model. Also, recirculation tracer tests performed at the WIPP site were not considered, because these tests do not represent a net removal of ground water from the Culebra.

The well history at the H-2 hydropad was complicated by drilling activities (e.g., H-2b2 in summer 1983), well reconditioning (e.g., all wells at the H-2 hydropad in winter 1983/1984), packer movements and transducer installations (e.g., H-2b1 in July 1984). Sufficient data on these activities were not available to allow incorporation of them into the model. Thus, only the four tests outlined above were implemented into the model using the SWIFT II wellbore submodel (rate-controlled mode).

#### 5.2.2 Convergent-Flow Tracer Tests at the H-3 Hydropad

After completion of the H-3 hydropad early in 1984, the first major test conducted at that hydropad was the convergent-flow tracer test (Hydro Geo Chem, 1985; Kelley & Pickens, 1986). The activities associated with this test included well development, a pumping test designed to evaluate the transmissivity of the Culebra dolomite at the H-3 hydropad, and the pumping period corresponding to the convergent-flow tracer test. The pump rates associated with these activities are plotted in Figure 5.2. The first two pumping periods (well development) were very short and, therefore, they were not incorporated into the model. The first pump period lasted from April 23 through May 7, 1984. An average production rate of 15 l/min was used. On May 7, the pumping rate was lowered in order to prepare for the convergent-flow tracer test which had to be performed under regulated-flow conditions. As Figure 5.2 shows, a pumping rate of about 11.4 l/min was maintained between May 7 and June 3, 1984. During the following days, until the

end of the test on June 12, 1984, somewhat higher pumping rates were recorded. An average pumping rate of 13.2 l/min was selected for modeling purposes for this latter period.

In summary, the convergent-flow tracer test was implemented as a pumping test using 15 l/min for the time period from April 23 to May 7; 11.4 l/min from May 7 to June 3; and 13.2 l/min from June 3 to June 12, 1984.

### 5.2.3 Step-Drawdown Test at the H-3 Hydropad

A step-drawdown test was performed at the H-3 hydropad between June 20 and July 10, 1985 (INTERA, 1986). Using the well H-3b2 as a pumping well, the pumping rate was step-wise increased (Figure 5.3) and the response in the surrounding wells recorded (Appendix D).

As illustrated in Figure 5.3, the following average pumping periods and rates were implemented:

June 20 - June 24, 1985	:	7.75 l/min
June 24 - June 28, 1985	:	15.0 l/min
June 28 - July 5, 1985	:	18.0 l/min
July 5 - July 10, 1985	:	19.25 l/min

These four pumping periods with the corresponding pumping rates were implemented using the rate-controlled mode of the SWIFT II wellbore submodel.

### 5.2.4 H-3 Multipad Pumping Test

The pumping period of the H-3 multipad pumping test was from October 15, 1985 through December 16, 1985 (INTERA, 1986). Using the H-3b2 well as the pumping well, an average of about 18.5 l/min (Figure 5.4) was removed over a time period of 62 days.

The H-3 multipad pumping test was incorporated into the model using the rate-controlled mode of the SWIFT II wellbore submodel.

#### 5.2.5 Convergent-Flow Tracer Test at the H-4 Hydropad

A long-term tracer test was conducted at the H-4 hydropad from October 24, 1982 to October 15, 1984 (Hydro Geo Chem, 1985; Kelley and Pickens, 1986). The withdrawal well was H-4c. The pumping rate during the tracer test (Figure 5.5) can be generally divided into two separate flow periods. The first flow rate started October 24, 1982 with a pumping rate of about 1 l/min and was held until June 10, 1983. At that time, the pumping rate was doubled to 2 l/min and maintained until August 9, 1983. As Figure 5.5 shows, the pumping rate fluctuated around 1.86 l/min during the following months until June 20, 1984. Slightly higher pumping rates, with an estimated average of 2 l/min, were recorded from June 20, 1984 until the end of the tracer test on October 15, 1984.

Similar to the other well tests, the H-4 convergent-flow tracer test was implemented into the model using the rate-controlled mode of the SWIFT II wellbore submodel.

### 5.3 Time-Step Considerations

During the assimilation and evaluation of the transient data available on the Culebra heads at the WIPP site, it became obvious that drilling and excavating the shafts had been by far the most important disturbance on the hydrologic system during recent years (Section 5.1). Therefore, it was decided that the transient simulation in this modeling study should cover the whole shaft history from its beginning in July 1981 to the present (fall 1986). For convenience, January 1, 1981 was selected as the beginning of the simulation time scale.

A sensitivity analysis indicated that the transient behavior simulated by the model is insensitive to the length of the time steps. However, the transient resolution of the simulation of each of the hydrologic disturbances is a direct function of the number and the length of the time steps. Taking into account the length of time to be simulated (more than 5 years) and the transient resolution of the observed head data (e.g., Appendix D), it was felt that a resolution of one day was appropriate. Consequently, the smallest time step used in this modeling study had a length of one day. In order to optimize the efficiency of the simulation, the minimum time step was only used at the beginning of a new activity, e.g., at the start of a test or after drilling a shaft. Similar to the common practice of reducing monitoring frequency during a hydraulic test, the length of subsequent time steps was increased (e.g., 2, 4, 8, 16 days). An arbitrary maximum of 32 days was chosen for the time steps. For illustration purposes, the time steps employed are graphically shown together with other transient-simulation information in Plates 1 and 3.

#### 5.4 Transient Simulation Using the Density-Calibrated Steady-State Model

The transient simulation of the shaft activities (Section 5.1) and the well tests (Section 5.2) was conducted using the steady-state solution for pressure and brine concentration of the density-calibrated steady-state model (Section 4.6) as initial conditions. The time steps were implemented as discussed in Section 5.3. The transient results of the simulation are displayed in Plates 1 and 2.

As discussed in Section 5.1, the shaft activities were modeled employing prescribed pressures at the shaft location (Plate 1) for most of the simulation period. During the simulation, SWIFT II calculated the corresponding production or injection rates which are also plotted in Plate 1. Especially for the early shaft history (1981-1982), the

different production or injection rates caused either by exposing the Culebra dolomite to atmospheric pressure or by filling the shaft with brine can be easily recognized. After summer 1985, the shaft leakage was simulated by prescribing the production rate. The corresponding response is shown in the graph displaying the freshwater heads at the shaft location.

All the well tests were simulated using prescribed pumping rates (Section 5.2), as displayed in the other graphs in Plate 1.

The calculated transient freshwater heads of some of the well locations are plotted in Plate 2. For comparison, the observed data are also shown in Plate 2. In many cases there is a very good agreement between the calculated and the observed data. In the following subsections, the transient response from the shaft activities and the well tests are briefly discussed.

#### 5.4.1 Simulation of Early Shaft History

The effects of the early shaft history in 1981 and 1982 (Section 5.1.1) were observed at H-1, H-2, and to a lesser extent at H-3. In all three wells, the calculated freshwater heads follow closely the observed values. This indicates that the transmissivities used between the shaft and H-1, H-2, and H-3 are approximately correct. Because the observed pressure response resulting from filling the shaft with brine ( $1.30 \text{ g/cm}^3$ ) is very well matched by the calculated value, the transmissivities used can be changed only if the density of the brine is also changed (see Section 5.1.1). The fact that the calculated drawdown at H-1 resulting from the first exposure of the shaft to atmospheric pressure is somewhat smaller than was observed may indicate that the transmissivity between H-1 and the shaft location could be somewhat higher. In this case, a lower density would have to be used for the injected brine.



The early shaft history likely caused very strong head changes at the locations of WIPP-22 and WIPP-21 and to a lesser extent at WIPP-19 and WIPP-18. However, no observed data exist from these wells for the years 1981 and 1982, because the wells were not completed so as to obtain Culebra heads prior to summer 1985.

#### 5.4.2 Simulation of the Open-Shaft Period

The drawdown cone caused by the open shafts from 1982 through 1985 (Section 5.1.2) has been observed at H-1, H-2, and to a lesser extent at H-3. In general, the agreement between the observed and the calculated transient data is acceptable (Plate 2). At H-1, the observed long-term drawdown is larger than the calculated one, indicating that a slightly modified transmissivity distribution (e.g., generally lower transmissivities north of H-1 and the shafts or higher transmissivities between H-1 and the shaft) might result in a better agreement between the observed and the measured transmissivities. But it must be emphasized that because of the good agreement between the calculated and the observed drawdown at H-3, the model transmissivities used between the shaft and H-3 must be approximately representative of the real situation. The drawdown caused by the open shafts would also have been observed at the wells WIPP-21, WIPP-22, WIPP-19, and WIPP-18 if they had been recompleted in the Culebra before 1985.

#### 5.4.3 Simulation of the Shaft Leakage After Shaft Sealing

The sealing of the last shaft (exhaust shaft) in summer 1985 (Section 5.1.3) reduced considerably the ground-water flow from the Culebra dolomite into the shafts (Plate 1). The freshwater-head increase can be seen in the corresponding graph for the shaft location (Plate 1) and in the graph of H-1 (Plate 2). The sealing can also be recognized at H-2 and H-3 (Plate 2), but the pressure recovery is complicated by the recovery from the H-3 step-drawdown test. It is likely that the

recovery could have been observed at the WIPP wells north of the shaft locations if these wells had not been undergoing recompletion and recovery from the recompletion activities. In general, the calculated pressure recovery seems to be consistent with the observed values.

#### 5.4.4 Simulation of the H-2 Well Tests

The well tests at H-2 were implemented as described in Section 5.2.1. The corresponding production rates are shown in the corresponding graph of Plate 1. Compared to the other well tests, these tests were only minor hydrologic stresses on the Culebra dolomite. Thus, the effects of the H-2 well tests are barely visible at other well locations (Plate 2). The head data for H-2 exhibit considerable scatter, apparently as a result of both testing at H-2 and activities at the shafts and other hydropads. Therefore, it is difficult to assess whether the calculated response to the implemented H-2 well tests is representative of the real situation or not.

#### 5.4.5 Simulation of the H-3 Convergent-Flow Tracer Test

The implementation of the H-3 convergent-flow tracer test is discussed in Section 5.2.2. The corresponding production rates are shown in the H-3 graph of Plate 1. As Plate 2 shows, the calculated and the observed drawdown at the H-3 hydropad are in good agreement. The convergent-flow tracer test probably caused a drawdown at H-1 and H-2, but the response is disturbed by other factors, i.e., it cannot be identified in the observed data. A small drawdown is observable at H-11 and DOE-1. At DOE-1, the calculated freshwater heads agree well with the observed data. At H-11 the heads are influenced by a test conducted at the H-11 hydropad (which was not simulated).

#### 5.4.6 Simulation of the H-3 Step-Drawdown Test

The H-3 step-drawdown test was implemented as described in Section 5.2.3. The corresponding production rates are shown in Plate 1. As Plate 2 shows, the calculated and the observed drawdown at the H-3 hydropad are in good agreement, although the calculated recovery is faster than the observed one. Due to lack of data, the response from the step-drawdown test is not visible at H-1 and H-2. As with the convergent-flow tracer test, the step-drawdown test caused small responses at DOE-1 and H-11. In both wells, the calculated and observed responses are in very good agreement. This indicates that the transmissivity field of the model between H-3 and DOE-1 and H-11 is reasonably representative of the real situation.

#### 5.4.7 Simulation of the H-3 Multipad Pumping Test

The implementation of the H-3 multipad pumping test is discussed in Section 5.2.4. The pumping rate is shown in Plate 1 and the corresponding transient responses are shown in Plate 2.

At the H-3 hydropad pad, the calculated drawdown is somewhat smaller than the one observed in the pumping well H-3b2 (lowermost values of the H-3 hydrograph in Plate 2). For the simulation, a large well index of  $1 \text{ m}^2/\text{s}$  was used. Additional details on the use of the well index are presented in Reeves et al. (1986a). Due to this high well index, the model does not simulate any skin effects in the production well. From a technical point of view, it would have been possible to calibrate the well index at H-3 such that the calculated drawdown matches the observed drawdown of the pumping well. However, because the pumping rate at H-3 is known and fixed, the well index becomes a pure fitting parameter and would not provide additional information about the hydrologic system in the Culebra dolomite. As with the two previous tests at the H-3 hydropad, the calculated recovery after the

H-3 multipad pumping test is faster than observed. This may indicate that the storativity in the H-3 area is somewhat higher than the value of  $2 \times 10^{-5}$  used in the model.

The observed data at H-1 and H-2 exhibit a drawdown and recovery in response to the H-3 multipad test. At H-2 the observed and calculated drawdowns have about the same magnitude, while at H-1 the observed drawdown is considerably larger than the calculated drawdown. In both wells, the observed recovery is much slower than the calculated recovery. Unfortunately, good observed data for these wells are not available for the periods during the H-3 convergent-flow tracer test and the H-3 step-drawdown test. Therefore, it is not possible to identify whether the disagreement between H-1 and H-2 calculated and observed data from the H-3 multipad pumping test is caused by using non-representative model parameters (e.g., transmissivities) or by other disturbances.

At H-11 and DOE-1, a response to the H-3 multipad pumping test was observed. The calculated responses matched the observed ones very well. This confirms the indication from previous tests conducted at H-3 that the model transmissivities between H-3 and H-11 and DOE-1 are probably representative of the real situation.

At WIPP-21, and to a lesser degree at WIPP-22 and WIPP-19, strong drawdowns during the H-3 multipad pumping test and subsequent slow recoveries were observed. The densities of the borehole fluids in these boreholes during the test are not well known. Therefore, in the following discussion only the changes in freshwater heads are considered, rather than the absolute freshwater heads. A comparison of the calculated data and the recorded changes in heads shows that much smaller responses were calculated by the model. This is somewhat surprising because, for the model in general, the agreement between the calculated and the observed transient freshwater heads is good.

However, the disagreement between the calculated and the observed data implies that either the model transmissivities used are not at all representative of the real situation or that some other event caused the drawdown of WIPP-21 and the other WIPP wells to the north. Considering that the observed drawdown at WIPP-21 is larger than that observed at H-1, rather large transmissivities would be required between H-3 and WIPP-21 in order to allow such a response. At present, no data exist to support such a high-transmissivity feature between WIPP-21 and H-3.

Similar to the water-level response at WIPP-21, transducer measurements in the Culebra in the waste-handling shaft showed a sudden pressure drop during the H-3 multipad pumping test (Plate 1). The equivalent freshwater-head drawdown is more than twice as large as the observed drawdown at H-1. However, the model-calculated drawdown at the waste-handling shaft is negligible. The observed recovery at the shaft location is slow and linear, as opposed to the rather steep recovery at H-3. All this leads to the conclusion that a very unusual transmissivity distribution would be required to allow the shafts to respond as observed to the H-3 multipad pumping test. On the other hand, the transmissivities between the shaft location and H-3 as used in the model must be at least approximately representative of the real situation, because the response at H-3 from the early shaft history and the open-shaft period is correctly simulated (Sections 5.4.1 and 5.4.2). Therefore, it was concluded that the large drawdowns at the shaft location and at WIPP-21 must be caused by something other than the H-3 multipad pumping test.

One possibility is that during the H-3 multipad pumping test an additional leakage of ground water from the Culebra occurred in one of the shafts, causing the sudden pressure drop. This would explain why the drawdown at the shaft is greater than at H-1. It could further explain why the measurements in the different shafts differ so much

(Appendix D, Figure D.31), because, assuming the transducers in all of the shafts have good hydraulic connection to the Culebra, one would have expected similar pressure responses in all shafts if they were responding only to the pumping at the H-3 hydropad. Furthermore, additional leakage occurring at one of the shafts would explain the observed but not calculated response in WIPP-19, WIPP-21, and WIPP-22. Finally, it could account for the smaller calculated-than-observed drawdowns and slower observed recoveries of H-1 and H-2. Therefore, this possibility was further investigated at a later stage of the modeling study (Section 5.5).

#### 5.4.8 Simulation of the H-4 Convergent-Flow Tracer Test

The implementation of the convergent-flow tracer test at the H-4 hydropad is discussed in Section 5.2.5. The implemented pumping rates are graphically shown in Plate 1. The calculated and the observed responses at H-4 are plotted in Plate 2.

As Plate 2 shows, the effect of the H-4 convergent-flow tracer test is restricted to the H-4 hydropad because of the low transmissivities in the region of H-4. As the H-4 hydrograph in Plate 2 shows, the agreement between the calculated and the observed freshwater heads is very good. This indicates that the employed model transmissivities in the area of the H-4 hydropad are generally representative of the real situation.

#### 5.5. Implementation and Simulation of Additional Leakage at the Shaft Location

The transient simulation of the shaft activities and well tests as described in Sections 5.1 and 5.2 resulted generally in a good agreement between calculated and observed freshwater heads at the well locations. The largest discrepancy was the fact that a large drawdown observed at

the shaft location and the WIPP wells north of the shafts during the H-3 multipad pumping test was not reproduced by the model. It was concluded that this drawdown was not caused by the H-3 multipad pumping test but by an additional removal of ground water from the Culebra dolomite somewhere else, likely in one of the shafts.

The recorded freshwater heads at the shaft locations (Appendix D, Figure D.31) show a much larger pressure drop in the waste-handling shaft than in the construction and salt-handling or the exhaust shafts. Therefore, it is likely that the principal cause of the drawdown in the region of the shafts was located in the waste-handling shaft.

The existing records of the waste-handling shaft show no special activity or any unusual phenomena for the time period when the measured pressure drop occurred. However, the shafts are known to be leaking (Appendix F) and an additional leak could have developed in the waste-handling shaft around December 1, 1985. For instance, the opening of an additional crack in the concrete liner of the shaft could have caused the observed sudden and sharp pressure drop. As the recorded data show, the freshwater head at the waste-handling shaft remained low for about one month and then rose at an almost constant rate during the subsequent month. This linear recovery is very atypical for a well when the withdrawal of ground water is suddenly stopped. Therefore, it cannot be assumed that the new leak was closed or repaired in January 1986. Rather, the observed recovery data indicate a slow and constant reduction of the leak rate over a period of several months. The reduction could be caused by a gradual plugging of the leakage path with, for example, calcium carbonate or gypsum. As the hydrochemical analyses have shown (Appendix E), the Culebra ground water appears to be saturated with respect to carbonate and gypsum under in-situ conditions. Ground water leaking through a fissure in the shaft liner is exposed to a different temperature and pressure which changes the hydrochemical equilibrium. Hence, ground water saturated under formation conditions

can become oversaturated while seeping through a fissure in the shaft wall and result in a precipitation of the corresponding minerals. Observations in the shafts support the theory that minerals precipitate from ground water leaking through fissures in the shaft wall. For instance, Mr. Gallerani (personal communication) has reported the occurrence of a white, hard precipitate associated with fractures in the shaft walls. This precipitate is presumably calcium carbonate, since Mr. Gallerani reported a reaction with HCl (personal communication).

Based on the discussion above, the following working hypothesis was developed. Around December 1, 1985, a new crack in the grouted wall of the waste-handling shaft was opened, thus allowing a direct pressure decline in the Culebra. The cause of the event is unknown, but the walls of tunnels or shafts always undergo minute movements which can cause separations in the liner or in the grouting. During the following 30 days, the new leak remained open causing the observed pressure depression at the waste-handling shaft. A smaller response can be seen in the records of the other two shafts and the WIPP wells to the north of the shafts (Plate 2). During and subsequent to January 1986, the crack was gradually closed by precipitating minerals resulting in a linear pressure increase at the shaft location. Thus, the observed freshwater heads at the WIPP site during and after the H-3 multipad pumping test are likely to be the result of superimposed responses to two different processes, i.e., the pumping at H-3b2 and the leakage in the waste-handling shaft.

Unfortunately, no quantitative leak-rate measurements in the shafts were made before January 24, 1986. However, the observed data gained during the subsequent months (Appendix D, Table D.1) show a steady decline of the leak rates from about 1.8 l/min in January to about 0.5 l/min in June 1986. Thus, the existing data are at least consistent with the hypothesis outlined above.



To evaluate this working hypothesis further, an additional leakage was incorporated into the transient model. In order to simulate the sudden pressure drop in December 1985, a prescribed pressure of about 435 kPa was employed at the shaft location, starting December 1, 1985. This prescribed pressure corresponds to a freshwater head of about 856 m, which is consistent with the observed data (Appendix D, Figure D.31). Using the pressure controlled mode of the SWIFT II wellbore submodel, the necessary leak rates were calculated during the simulation.

To simulate the gradually declining leak rate, the rate-controlled mode of the wellbore submodel was used from January 1, 1986 through August 15, 1986. Starting with a prescribed leakage of about 2.95 l/min, the rate was linearly reduced to 2 l/min in August 1986. The starting leak rate was found using the last model-calculated leak rate during the pressure-controlled simulation in December 1985. The latter number is the same as used for the simulation of the remaining shaft leakage in the first transient model (Section 5.4). After August 15, 1986, a constant leak rate of 2 l/min was utilized.

The prescribed and calculated leak rates and freshwater heads at the shaft location are plotted in Plate 3. A comparison with the observed data show that the calculated heads at the shaft location follow closely the waste-handling shaft data. It seems to be very difficult to obtain such a good agreement between the observed and the calculated data for the waste-handling shaft by means other than those described above. The graph displaying the corresponding leak rates shows the steady decline during 1986 after the initial peak in December 1985. As already mentioned, no leakage measurements were made in December 1985. Also, the measurements made in 1986 have to be associated with large possible errors, e.g., caused by the unknown percentage of evaporation (for details see Appendix F). With these uncertainties in mind, the employed or calculated leak rates can be considered to be consistent with the existing observed data.

The calculated freshwater heads at the well locations surrounding the shaft are plotted in Plate 4. A comparison with Plate 2 shows that at H-1 and H-2 the agreement between the calculated and the observed freshwater heads could be improved. For this comparison, it has to be taken into account that there was already a difference between the calculated and the observed data at the beginning of the H-3 multipad pumping test. Therefore, the head changes rather than the absolute head values should be considered. Although the agreement at H-1 and H-2 is not yet perfect, it indicates that implementation of an additional shaft leakage was a step in the right direction, leaving room for further improvements by modifying slightly the transmissivities or the storativities.

At the WIPP wells north of the shaft location, the implementation of additional shaft leakage resulted in a response which has the same order of magnitude as the observed one. As discussed in Section 5.4, the densities of the borehole fluids in the WIPP wells were not well known. Therefore, the head changes rather than the absolute head values should be used for comparing the observed and the calculated data. Although the calculated responses at the WIPP wells are still smaller than those observed, the model results support the hypothesis of the additional leakage. The remaining discrepancies could probably be reduced by increasing the transmissivities north of the shaft location.

It can be concluded that the implementation of an additional shaft leakage can explain the observed drawdown at the WIPP wells north of the shaft location during the H-3 multipad pumping test. Furthermore, the assumption of such an additional leak presently seems to be the most likely possibility to explain the observed transient freshwater heads. From a modeling point of view, the occurrence of an additional and poorly documented leak in the waste-handling shaft during the H-3 multipad pumping test is unfortunate because it complicates further the already very complicated hydraulic situation in the Culebra dolomite at the WIPP site.

## 5.6 Summary of the Transient Simulation

Between 1981 and 1986, the hydraulic conditions in the Culebra dolomite have been influenced by drilling and testing activities at the shafts and the well locations. The following activities and tests were incorporated into the model: a simplified but complete shaft history since 1981, three pumping tests and a series of slug tests at the H-2 hydropad in 1983 and 1984, the H-3 convergent-flow tracer test in 1984, the H-3 step-drawdown test in 1985, the H-3 multipad pumping test in 1985, and the H-4 convergent-flow tracer test between 1982 and 1984. Using the steady-state solutions for pressure and brine concentration of the density-calibrated steady-state model as initial conditions, the hydraulic situation in the Culebra dolomite was simulated for the time period from January 1, 1981 to December 31, 1986. Variable timesteps between 1 and 32 days in length were used.

In general, the model-calculated freshwater heads at the shaft and at the well locations are in good agreement with the observed data, especially at H-1, H-2, H-3, DOE-1, and H-11. This leads to the conclusion that the model transmissivities used between H-3 and H-1, H-2, DOE-1, and H-11 are reasonably representative of the real transmissivity distribution. However, it was not possible to reproduce the sudden pressure drop and the subsequent slow linear recovery that was observed at the shaft location and at WIPP-19, WIPP-21, and WIPP-22 during and after the H-3 multipad pumping test. This leads to the hypothesis that in early December 1985 an additional fissure in the liner of the waste-handling shaft opened causing the sudden pressure drop. This fissure remained open and was gradually plugged during the subsequent months by precipitating minerals (e.g., carbonate) which restricted more and more of the flow of ground water into the shaft. As a consequence, the hydraulic system in the Culebra dolomite at the shaft location reacted with a slow and almost linear pressure recovery.

In summary, the existence of additional leakage rather than a discrete high-permeability feature between H-3 and the shafts appears to be the most plausible because the effect of the early-shaft history could be simulated accurately at the H-3 hydropad, whereas the shaft response could not be reproduced with pumping at the H-3 hydropad utilizing the same transmissivity distribution.

In order to test this hypothesis, an additional leakage was implemented at the shaft location and the simulation was carried out over the period from 1981 through 1986. The calculated freshwater heads at the shaft location followed closely the observed data in the waste-handling shaft. The calculated freshwater heads of the WIPP wells to the north of the shaft location show a response of about half the size of the observed one. The agreement between the observed and calculated freshwater heads at H-1 and H-2 was also improved by the additional shaft leakage. Although further calibration work will be necessary in order to reproduce exactly the observed data at, for instance, WIPP-21, the model results indicate that such additional shaft leakage can explain the observed drawdown at the shaft location itself and the WIPP wells north of it. Furthermore, the assumption of additional leakage with the transient characteristics as described above seems to be the most likely possibility of explaining the observed transient freshwater heads. However, additional model calibration is required in order to improve the agreement between the model-calculated and the observed data.

## 6.0 SENSITIVITY OF THE MODEL CONCEPTUALIZATION TO VERTICAL FLUXES TO AND FROM THE CULEBRA DOLOMITE

During the modeling study, it was generally assumed that the geologic units above and below the Culebra dolomite are of very low permeability and any flux into or from the Culebra dolomite through these confining beds could be neglected (Section 3.5.3.). During the calibration of the steady-state model against the observed formation-water densities (Sections 4.5 and 4.6), it became obvious that it is very difficult, if not impossible, to obtain the observed spatial density distribution (Figure 3.10) by employing horizontal flux in the Culebra only. The assumption of absolutely impermeable layers above and below the Culebra dolomite may be an oversimplification of the real situation (Section 2.4). Consequently, a local vertical flux (through the Tamarisk Member and the unnamed lower member) into the Culebra dolomite was implemented in an attempt to improve the agreement between the calculated and the observed formation-water densities. However, an improved agreement between the model and the real hydrogeologic situation does not prove the existence of any assumed vertical flux in reality, although it does represent a strong argument for the existence of such a vertical flux. The main purpose of the model calculations using vertical fluxes was to provide an approximate quantification of the fluxes required to improve the model fit and to indicate the areas where such fluxes might occur.

### 6.1 Estimation of Possible Vertical Fluxes

Prior to implementation of a vertical flux into the model, some scoping calculations were conducted in order to determine the possible order of magnitude of a vertical flux in the different model areas. In the following, some of these calculations or estimations are briefly discussed.

### 6.1.1 Estimation of Vertical Flux through the Unnamed Lower Member at P-17

As discussed in Sections 4.5 and 4.6, it was not possible to calibrate the steady-state model such that there was an acceptable agreement between the calculated and the observed formation-water density data at well P-17. Therefore, the location of P-17 was selected for the estimation of a possible vertical flux. Because there were no difficulties in calibrating the model at the surrounding borehole locations (e.g., H-4, H-11, and H-12), it was assumed that the vertical flux at P-17 is a local phenomenon.

The model-calculated formation-water densities were considerably lower than the observed values (Section 4.5 and 4.6). Therefore, a vertical flux of high-salinity ground water was assumed. At the P-17 location, no occurrence of halite in the layers above the Culebra dolomite (i.e., the Tamarisk Member and the Forty-Niner Member) is reported in the literature (Mercer, 1983). Halite is known to be present in the unnamed lower member. Furthermore, a formation-water density of  $1.19 \text{ g/cm}^3$  is reported for the Rustler-Salado contact residuum at P-17 (Mercer, 1983). Therefore, a vertical flux of high-salinity ground water from below into the Culebra dolomite was assumed.

The following geological and hydrogeological data of the P-17 area are available (Mercer, 1983):

- Thickness of the unnamed lower member: about 40 m;
- Freshwater elevation in the Rustler-Salado contact residuum: about 920.5 m a.s.l.;
- Freshwater elevation in the Culebra dolomite: about 908 m a.s.l.

Thus, an upward-directed hydraulic gradient of 0.3 m/m can be calculated for the unnamed lower member at P-17. This hydraulic gradient does not reflect any variation of the ground-water densities in the different geologic layers at P-17, because it was calculated using the equivalent freshwater heads. Taking into account the density variation at P-17 ( $1.06 \text{ g/cm}^3$  in the Culebra,  $1.19 \text{ g/cm}^3$  in the Rustler-Salado contact residuum), a "density-corrected hydraulic gradient" of 0.18 m/m can be calculated.

No permeability data were available for the unnamed lower member which consists of breccia, claystone, siltstone, silty sandstone, gypsum, anhydrite, and halite. Therefore, a very low matrix permeability in general and somewhat higher permeabilities along fractures and faults can be assumed. The effective permeability for vertical flux is then defined by the permeabilities along the fractures.

Experience gained in other studies has shown that on a regional scale even confining beds usually have vertical hydraulic conductivities of  $1 \times 10^{-11}$  m/s or more (e.g., Bredehoeft et al., 1982). Using a hydraulic conductivity of  $1 \times 10^{-11}$  m/s and a hydraulic gradient of 0.18 m/m, a flux of  $1.8 \times 10^{-12}$  m/s through the unnamed lower member can be calculated. This is equivalent to a flux of 0.1 l/min through an area of  $1 \text{ km}^2$ . The effect of such a small flux on the model-calculated fluid densities at P-17 is discussed in Section 6.2.

#### 6.1.2 Estimation of Vertical Flux Through the Tamarisk Member in the Western Model Area

As previously discussed (e.g., Section 4.6), it is difficult to obtain the north-south gradient of the formation-water density observed in the Culebra dolomite in the western part of the model area (Figure 3.10) with the current model conceptualization (e.g., modeling the Culebra dolomite as a single, completely confined layer). During the

calibration of the density-calibrated steady-state model, this problem was not solved but circumvented by assigning heterogeneous density boundary conditions along the northern model boundary (Section 4.5) which resulted in a satisfactory agreement between the calculated and observed formation-water densities at the borehole locations. However, the heterogeneous boundary conditions used for the density-calibrated steady-state model may not be representative for the real spatial density distribution in the Culebra dolomite. Therefore, the possibility that the observed north-south density gradient is caused by a vertical flux into the Culebra dolomite was investigated in more detail.

The possibility that the observed formation-water density at H-6 is a rather local phenomenon, caused by a high-salinity vertical flux from below, can be excluded because the hydraulic gradient in the unnamed lower member is directed downward (Mercer, 1983). It is assumed that the observed densities at H-6 are representative for the area along the western part of the northern model boundary (Figure 3.10). Thus, boundary conditions with prescribed densities between 1.03 and 1.04 g/cm<sup>3</sup> were assigned to the northern model boundary west of DOE-2. As demonstrated by the pressure-calibrated steady-state model (Figures 4.7 and 4.8), the resulting calculated densities at the wells H-1, H-2, H-4, H-7, P-14, and P-17 are higher than the observed values. Consequently, a flux of low-salinity water into the Culebra dolomite has to be assumed in order to improve the fit between calculated and observed formation-water densities. Because the fluid densities at several wells in the western part of the model area are concerned, the vertical flux was assumed to be a regional rather than a local phenomenon.

The reported chemistry of ground water from the Rustler-Salado contact residuum indicates a high mineralization in the western model area (e.g., 1.225 g/cm<sup>3</sup> at H-2, 1.126 g/cm<sup>3</sup> at P-14, 1.16 g/cm<sup>3</sup> at P-15; Mercer, 1983). Therefore, a vertical flux of fresh ground water from



the Rustler-Salado contact residuum through the unnamed lower member is not possible.

The observed formation-water densities in the Magenta dolomite in the western part of the model area are known to be low (e.g., 1.012 g/cm<sup>3</sup> at H-2, 1.007 g/cm<sup>3</sup> at H-6, 1.017 g/cm<sup>3</sup> at H-4; Mercer, 1983). In addition, the hydraulic gradient between the Magenta and the Culebra dolomite is directed downward in the western model area (Table 6.1). The gradient is about 1.8 m/m in the central part of the model area (H-3) and seems to decline gradually towards the western model boundary, where only 0.034 m/m are observed (WIPP-25). These gradients are not corrected for variable-density effects because the density differences between the Culebra and the Magenta formation waters are small.

A vertical flux of low-salinity water from the Magenta dolomite through the Tamarisk Member into the Culebra dolomite seems to be possible in the western part of the model area. Because there is a near-neutral hydraulic gradient reported at H-6 (Table 6.1), the area of the flux into the Culebra dolomite has to be restricted to the western model area south of H-6. To the east, the area of possible vertical flux is limited by the occurrence of more highly mineralized formation water in the Culebra dolomite at the WIPP wells north of the shaft location, at H-3, and at P-17 (i.e., there is no evidence of such a low-salinity vertical flux east of the connecting line between WIPP-13 and P-17). Consequently, the area marked in Figure 6.5 (about 58.5 km<sup>2</sup>) was selected for the further calculations as the area of possible downward vertical flux of low-salinity ground water.

No hydraulic conductivity data for the Tamarisk Member in the western model area are reported in the literature. Due to the lack of data, a vertical hydraulic conductivity of  $1 \times 10^{-11}$  m/s was assumed for the Tamarisk Member (the same value was assumed for the unnamed lower

member; Section 6.1.1). As mentioned above, vertical hydraulic gradients between 0.034 m/m and 1.8 m/m can be calculated for the Tamarisk in the western model area. An arbitrary value of 0.5 m/m, constant over the area marked in Figure 6.5 was selected for the further scoping calculations. Using a hydraulic conductivity of  $1 \times 10^{-11}$  m/s and the selected vertical hydraulic gradient of 0.5 m/m, a flux of  $5 \times 10^{-12}$  m/s through the unnamed lower member was calculated. This is equivalent to a flux of 0.3 l/min through an area of  $1 \text{ km}^2$ .

Thus, the occurrence of low-salinity vertical fluxes through the Tamarisk Member into the Culebra dolomite with the above-calculated magnitude (about  $5 \times 10^{-12}$  m/s) may be possible. The sensitivity of the model to such a flux is further discussed in Section 6.3.

## 6.2 Implementation of a High-Salinity Vertical Flux at P-17 and Simulation of the Undisturbed Hydraulic Conditions

Based on the scoping calculations discussed in Section 6.1.1, an area of about  $1 \text{ km}^2$  at P-17 was selected for the sensitivity analysis (Figure 6.1). Using the density-calibrated steady-state model, various fluxes between  $1 \times 10^{-11}$  m/s and  $5 \times 10^{-13}$  m/s of high-salinity water (with a specific density of  $1.19 \text{ g/cm}^3$ ) were implemented and the steady-state solutions for pressure and brine concentration were calculated. Technically, this was achieved by implementing seven rate-controlled injection wells in the P-17 area. For illustrative purposes, the results of the model with an implemented flux of  $1 \times 10^{-12}$  m/s are shown in Figures 6.1 through 6.4. This very small flux is sufficient to cause an increased calculated formation-water density of  $1.060 \text{ g/cm}^3$  at P-17 (Figure 6.3), which is identical to the observed density (Figure 6.4). The freshwater head at P-17 was raised by the vertical flux from 910.1 to 910.3 m a.s.l. (Figure 6.1). Consequently, the difference between the calculated and the observed freshwater heads was reduced from -1.1 m

(density-calibrated steady-state model, Section 4.6) to -0.9 m (Figure 6.2).

The implemented vertical flux of  $1 \times 10^{-12}$  m/s at the P-17 area corresponds to a very low vertical hydraulic conductivity of  $5.7 \times 10^{-12}$  m/s (assuming 0.18 m/m as vertical hydraulic gradient, Section 6.1.1) in the unnamed lower member of the Rustler Formation. This hydraulic conductivity is even lower than the hydraulic conductivity assumed for the unnamed lower member in the scoping calculations (Section 6.1.1). Therefore, the possibility that the relatively high densities observed at P-17 are at least partially caused by an upward flux of high-salinity water cannot be excluded. Moreover, it seems to be difficult to exclude the possibility of any influence on the formation-water density in the Culebra dolomite by vertical ground-water movement through the unnamed lower member of the Rustler Formation wherever upward hydraulic gradients exist.

As far as the model conceptualization is concerned, it can be concluded that the calculated freshwater heads are moderately sensitive to a local vertical flux at the P-17 area, i.e., a vertical flux of about  $1 \times 10^{-12}$  m/s causes an increase in the calculated freshwater heads of 0.2 m. Furthermore, it can be concluded that the calculated formation-water densities are very sensitive to a local vertical flux (with a specific density of  $1.19 \text{ g/cm}^3$ ) at the P-17 area, i.e., a vertical flux of  $1 \times 10^{-12}$  m/s causes an increase of  $0.04 \text{ g/cm}^3$  on the calculated densities.

### 6.3 Implementation of a Low-Salinity Vertical Flux in the Western Model Area and Simulation of the Undisturbed Hydraulic Conditions

Based on the scoping calculations in Section 6.1.2, the sensitivity of the model to a low-salinity vertical flux into the Culebra dolomite (at the area marked in Figure 6.5) was investigated. First, the density-calibrated steady-state model with the initial boundary conditions re-

implemented (Table 3.9) along the western part of the northern model boundary was used to calculate the undisturbed freshwater heads and formation-water densities. Figures 6.5 through 6.8 display the results (freshwater heads, differences between calculated and observed freshwater heads, formation-water densities, differences between calculated and observed formation-water densities) for a zero flux into the Culebra dolomite. A comparison with the results of the density-calibrated steady-state model with the modified density boundary conditions (Figures 4.12 - 4.15) reveals that the results are very similar except for the formation-water densities in the southwestern model area. In this area, the calculated densities (Figures 6.7 and 6.8) are about  $0.02 \text{ g/cm}^3$  higher due to the higher formation-water densities assigned to the northern model boundary west of DOE-2 (see above).

Subsequently, various flux rates into the Culebra, spatially constant over the area marked in Figure 6.5, were implemented and the steady-state solutions for freshwater head and formation-water density were calculated. Technically, this was achieved by assigning a recharge to the specified area (Figure 6.5). The specific density of the recharge was assumed to be  $1.00 \text{ g/cm}^3$  (i.e., the fractional brine concentration was assigned 0.0) because the available data base on the formation-water densities in the Magenta dolomite was not considered to be detailed enough to justify any other specific value or even a spatial variation of the recharge-fluid density.

For illustration purposes, the results of the model with an implemented flux of about  $5 \times 10^{-12} \text{ m/s}$  (equivalent to a recharge rate of 18 l/min over an area of  $58.5 \text{ km}^2$ ) are shown in Figures 6.9 through 6.12. A comparison with the results of the zero-flux model (Figures 6.5 through 6.8) shows that both the calculated freshwater heads and the formation-water densities are influenced by the additional flux into the model. For example, the heads at P-15 have been increased by 7.2 m while the densities have been lowered by  $0.01 \text{ g/cm}^3$ . Thus at P-15, the rather

small vertical flux has a significant effect on the model results, while at other locations, the effect is much smaller. For example, at P-14, the freshwater head and the density have been increased only by 0.7 m and decreased by  $0.006 \text{ g/cm}^3$ , respectively.

In order to demonstrate the spatial distribution of the effect of the implemented recharge or flux, the differences between the model results with flux ( $5 \times 10^{-12} \text{ m/s}$ ) and without flux have been contoured and plotted (Figures 6.13 and 6.14). Figures 6.13 and 6.14 also can be interpreted as the average model sensitivity to a vertical flux of  $5 \times 10^{-12} \text{ m/s}$  over the specified area with vertical flux.

Analogous computer runs have been performed with different flux rates (e.g.,  $1 \times 10^{-12} \text{ m/s}$  and  $1 \times 10^{-11} \text{ m/s}$ ), but, because they show similar results, the corresponding plots have not been included in this report.

The following conclusions can be drawn from the sensitivity analysis employing a spatially constant vertical flux of low-salinity water into the Culebra dolomite at the western model area (Figures 6.5 through 6.14):

- 1) The sensitivity of the model to vertical flux differs from location to location. The spatial sensitivity distributions with respect to the heads and to the densities are not identical (Figures 6.13 and 6.14).
- 2) The model shows an area of high sensitivity with respect to both the freshwater heads and the densities around P-15 and H-4. This sensitivity is directly correlated to the low transmissivity in that area (Figure 4.10). The horizontal flux in the Culebra is small in that area because of the low transmissivity. Even a very small additional flux into the Culebra can cause major changes in the calculated heads and the densities. As Figures 6.10 and 6.12 show,

the effect of the implemented flux is much greater than acceptable with respect to the observed data. Consequently, in reality any vertical flux in the area of P-15 and H-4 is probably very small (e.g.,  $1 \times 10^{-12}$  m/s or less).

- 3) Medium sensitivity to vertical flux exists in areas with intermediate transmissivities (e.g., in the area of H-1, H-2, H-3, and P-17). There, the vertical flux ( $5 \times 10^{-12}$  m/s) has caused increased heads by about 1.5 m and decreased densities between  $0.015 \text{ g/cm}^3$  and  $0.035 \text{ g/cm}^3$ . The increased heads are fully compatible with the observed data because the differences (Figure 6.10) could easily be eliminated by slightly recalibrating the transmissivities. As far as the decreased densities at H-1 and H-2 are concerned, the vertical flux has changed them in the right direction (Figures 6.8 and 6.12). The remaining differences to the observed values can be eliminated by increasing the vertical flux in that area to about  $1 \times 10^{-11}$  m/s. A vertical flux at H-1 and H-2 of  $1 \times 10^{-11}$  m/s is consistent with the existing density data base.

At H-3, the calculated densities were lowered too much (Figures 6.8 and 6.12). However, as discussed in Section 4.5, the local transmissivity field at H-3 is not considered to be fully calibrated. Therefore, it is not yet possible to conclude that in reality there must be a very small vertical flux through the Tamarisk Member at H-3.

At P-17, the calculated formation-water densities are too low with or without the vertical flux. However, as demonstrated in the previous section, at P-17 the formation-water density may be governed by a high-salinity vertical flux from below (Section 6.2).

- 4) Low sensitivity was found in areas with high transmissivities (e.g., at P-14). There, the vertical flux changed the heads and the

densities only slightly (Figures 6.13 and 6.14). Thus, in order to reduce the difference between the calculated and the observed densities at P-14, considerably higher flux rates (about  $2 \times 10^{-11}$  m/s) are required.

- 5) Based on the previous statements, it can be concluded that the employment of a spatially constant vertical flux can reveal the sensitivity of the model to vertical flux but that such a constant flux is not representative for the real situation. For the real situation, a spatial flux distribution has to be assumed which is correlated somewhat to the hydraulic conductivities of the Culebra dolomite. From the hydrogeologic point of view, this can be assumed because the same processes which have caused the variation of the hydraulic conductivity in the Culebra dolomite may also have caused a similar variation in the layers above the Culebra dolomite.
- 6) Although employing a spatially constant vertical flux over a large area may not be adequate (see above), it was nevertheless possible to create a calculated density distribution by implementing a constant flux of  $5 \times 10^{-12}$  m/s which, as a pattern, is similar to the observed density distribution (Figures 6.11 and 3.10). Therefore, by incorporating a spatially variable vertical flux in the western model area, it should be possible to obtain a calculated density distribution which is consistent with the observed data.

Further data assimilation and data evaluation are required in order to provide the data base necessary for more detailed simulations. For example, a consistent data base with regard to the transmissivities, observed freshwater heads, and formation-water densities in the Magenta dolomite has to be prepared. Based on that, a spatially variable flux can be derived and incorporated into the model. Further steps may include the use of a multi-layered model which allows simultaneous simulation of ground-water flow in all members of the Rustler Formation.

#### 6.4 Summary of the Sensitivity Analysis Using Vertical Fluxes

Because of the difficulties in simulating the observed spatial formation-water density distribution by modeling the Culebra dolomite as a completely confined layer with ground-water flow only in the horizontal direction, the possibility of the occurrence of ground-water flow from and to the Culebra through the confining beds was investigated.

First, preliminary scoping calculations were conducted for two areas: 1) the location of P-17, and 2) the western model area (south of H-6 and west of H-1). Based on these calculations, a high-salinity flux from the Rustler-Salado contact residuum through the unnamed lower member of the Rustler Formation into the Culebra dolomite near P-17 is considered to be likely. The order of magnitude of this flux was estimated to be about  $1.8 \times 10^{-12}$  m/s. In addition, a low-salinity vertical flux through the Tamarisk Member into the Culebra dolomite seems to be possible. The magnitude of the low-salinity flux was estimated to be  $5 \times 10^{-12}$  m/s.

Simulations using a high-salinity vertical flux in the P-17 area indicate that even smaller fluxes than estimated can significantly influence the calculated density distribution. Furthermore, it is difficult to exclude the possibility of a vertical flux at that location. Similarly, simulations using a low-salinity vertical flux in the western model area indicate that the observed density distribution can be influenced by vertical ground-water movement downward through the Tamarisk Member.

The sensitivity analysis using vertical flux should be considered to be the starting point of additional investigations which include data collection and evaluation as well as model calculations. The use of a multi-layered model considering the complete Rustler Formation is considered appropriate based on the scoping calculations and model simulations conducted in this chapter.



## 7.0 APPLICATION OF A DOUBLE-POROSITY FLOW CONCEPTUALIZATION

### 7.1 Introduction

The simulations presented in Sections 4, 5, and 6 assume that the Culebra is an equivalent porous media. Several investigators (Rehfeldt, 1984; Chaturvedi and Rehfeldt, 1984; Kelley and Pickens, 1986; and Beauheim, 1986, and in preparation) have discussed the possibility that the Culebra is a fractured rock possessing both primary and secondary porosity. In order to investigate the effects of double porosity on the regional-flow modeling, we have performed additional calculations which are presented in this section. The hydraulic testing methods and interpretation approaches for hydraulic and tracer tests utilized by Sandia National Laboratories and their contractors during 1985 and 1986 have provided quantification of fracture-flow and transport properties where appropriate. To date, both tracer tests (Kelley and Pickens, 1986) and hydraulic tests (Beauheim, 1986, and in preparation) have been analyzed using double-porosity models at the WIPP site. A double-porosity solute-transport analysis of tracer tests was performed on tracer tests performed at the H-3 hydropad, and double-porosity hydraulic test analyses have been performed at the H-3 hydropad and well DOE-2.

The concept of a double-porosity medium was first proposed by Barenblatt et al. (1960) in order to model flow in fractured rock. Streltsova-Adams (1978) presents a four-fold classification of dual-porosity reservoirs. The Culebra is modeled as a class-one dual-porosity reservoir, which is termed a fractured medium whose primary porosity contains the majority of the fluid storage volume while the transmissivity of the combined system is due to the secondary medium. Inherent to our model conceptualization of a double-porosity medium is the concept that the medium consists of two separate, interacting and overlapping continua. It is also assumed that a representative elementary volume of the aquifer exists containing portions of both the primary and secondary media.

There are two basic types of double-porosity hydraulic models in use: (1) the restricted interporosity-flow model, also known as a pseudo-steady-state model (Warren and Root, 1963); and (2) an unrestricted model, also referred to as the transient model (Kazemi et al., 1969). In the restricted interporosity-flow model, the spatial variation of hydraulic-head gradients in the matrix block is ignored and fluid flux from the matrix to the fractures is in response to the difference in the average hydraulic heads in the fractures and matrix. In the second unrestricted interporosity-flow model, the spatial variation of hydraulic-head gradients within the matrix is considered and flow from the matrix to the fractures is governed by a linear-diffusion process.

Ideally, when pressure versus log time is plotted for a double-porosity reservoir, one observes two semi-log straight-line regions connected by a sigmoid curve as shown in Figure 7.1 (Warren and Root, 1963; Streltsova-Adams, 1978). The first semi-log straight line is indicative of the homogeneous pressure response of the secondary medium alone and the second semi-log straight line is indicative of the homogeneous pressure response of the total system (i.e., both primary and secondary media). The curve separating these two straight lines represents the transient pressure response within the primary medium in a local region around the wellbore.

It should be noted that if an unrestricted interporosity-flow model is used, the transition pressure response between the two semi-log straight lines is linear and does not exhibit the inflection point predicted by restricted interporosity-flow models (Kazemi et al., 1969; and Streltsova, 1983).

The point where the transition curve, or straight line, departs from the first semi-log straight line ( $t_1$  of Figure 7.1) represents the beginning of primary-medium pressure response. When the transition curve meets the second semi-log straight line ( $t_2$ ), the primary and secondary media

are fully coupled. Both  $t_1$  and the shape of the transition region will vary, based upon which type of interporosity-flow model one chooses, but in theory  $t_2$  will be predicted to be the same by either model.

The ideal double-porosity pressure response described above and shown in Figure 7.1 is essentially a local phenomenon which will only be observed in the near field (Deruyck et al., 1982). Data from observation wells that are not in the near field can be fit adequately with models that neglect double-porosity transient effects. Through hydraulic interpretation of the H-3 multipad test, Beauheim (in preparation) found that only the wells on the H-3 hydropad could be fit by double-porosity type curves. The remaining observation wells could be fit by conventional single-porosity type curves.

To characterize single-porosity flow to a well requires the hydraulic diffusivity, the wellbore storage coefficient, and the skin properties of the region immediately surrounding the wellbore. The parameters necessary to characterize double-porosity flow to a well are the same as those needed for characterizing homogeneous single-porosity flow with the addition of two more parameters: the dimensionless secondary-system storativity ( $\omega$ ); and the interporosity-flow coefficient ( $\lambda$ ) (Warren and Root, 1963). The dimensionless secondary-system storativity is the ratio of the secondary storativity to the total system storativity and in equation form is defined as:

$$\omega = \frac{\phi_f C_r}{\phi_f C_r + \phi_m C'_r} \quad (7-1)$$

where  $\phi_f$  = secondary-medium porosity (fractures)  
 $C_r$  = secondary-medium compressibility  
 $\phi_m$  = primary-medium porosity (matrix)  
 $C'_r$  = primary-medium compressibility

The interporosity-flow coefficient can be considered a dimensionless primary to secondary permeability ratio and in equation form is defined as:

$$\lambda = \alpha \frac{k_m}{k_f} r_w^2 \quad (7-2)$$

where:  $\alpha$  = geometrical shape factor  
 $k_m$  = permeability of the matrix  
 $k_f$  = permeability of the fracture  
 $r_w$  = radius of the wellbore

In equation form, the geometrical shape factor is equal to:

$$\alpha = \frac{4n(n+2)}{L_m^2} \quad (7-3)$$

where  $n$  = number of normal sets of fractures  
 $L_m$  = characteristic dimension of the matrix block

When cubes are modeled conceptually as spheres, the shape factor is equal to:

$$\alpha = \frac{15}{r_m^2} \quad (7-4)$$

where  $r_m$  = radius of the spherical matrix element or one-half the fracture spacing

## 7.2 Estimation of Double-Porosity Parameters

In order to model a rock as a double-porosity medium, one must establish media properties for both the primary (matrix) and secondary (fracture) systems. The parameters characterizing the Culebra which must be known in order to model flow with a double-porosity model include:

- hydraulic conductivity of the primary medium;
- hydraulic conductivity of the secondary medium;
- porosity of the primary medium;
- porosity of the secondary medium;
- compressibility of the primary medium;
- compressibility of the secondary medium;
- representative matrix-block length.

Other parameters which do not represent direct input into the SWIFT II model, yet are input indirectly, are the dimensionless secondary system storativity ( $\omega$ ) and the dimensionless interporosity-flow coefficient ( $\lambda$ ). These parameters are estimated using equations 7-1 and 7-2.

#### Hydraulic Conductivity of the Primary Medium

Core Laboratories, Inc. (1986) performed permeability and porosity measurements on selected core samples from wells H-2b, H-3b2, H-3b3, H-4b, and H-6b. Table 7.1 summarizes the results from these measurements. These values of intrinsic permeability were converted to hydraulic conductivities assuming a fluid viscosity equal to  $1 \times 10^{-3}$  Pa s and a mean fluid density equal to  $1.05 \text{ g/cm}^3$  (see Section 3.3.1). The mean vertical hydraulic conductivity based upon 14 measurements is  $5.1 \times 10^{-8}$  m/s, whereas the mean horizontal hydraulic conductivity based upon 9 measurements is equal to  $1.4 \times 10^{-8}$  m/s. The primary medium is assumed to be isotropic and homogeneous in this model. Considering the small number of core measurements taken, all values of permeability ( $n=23$ ) were averaged to yield a primary-medium hydraulic conductivity equal to  $3.7 \times 10^{-8}$  m/s.

There are regions within the model area, such as the area surrounding P-18, which have been tested to yield hydraulic conductivities lower in magnitude than  $3.7 \times 10^{-8}$  m/s. To prevent inconsistencies within the model (i.e., primary hydraulic conductivities greater than

secondary hydraulic conductivities), the primary hydraulic conductivity for the entire model region was assigned the lowest field-measured hydraulic conductivity,  $2.63 \times 10^{-10}$  m/s. This hydraulic conductivity is considered to be representative of a lower limit for the primary medium.

#### Hydraulic Conductivity of the Secondary Medium

The hydraulic conductivity distribution of the secondary medium is considered to be isotropic and heterogeneous. The hydraulic conductivity values are derived from the single-porosity steady-state model calibration (see Section 3.4).

#### Porosity of the Primary Medium

As is shown in Table 7.1, porosities derived from core samples range from 0.07 to 0.3. As in the single-porosity conceptualization (see Section 3.3.2), a matrix porosity of 0.2 was chosen as a representative value.

#### Porosity of the Secondary Medium

Porosity values for the secondary medium should be derived from solute-transport calculations performed for the Culebra at the WIPP site. Tracer tests have been performed at hydropads H-2, H-3, H-4, and H-6. Because of the differences between test types, testing procedures, and analysis techniques, transport-parameter comparison between these tests is difficult. In addition, the tracer tests performed at the H-3 hydropad are the only tests which to date have been analyzed with a double-porosity transport model. Results from the H-3 tracer-test analysis appear in Table 7.2. For modeling purposes, the secondary porosity is assumed equal to  $2 \times 10^{-3}$ . It is understood that this number is uncertain with respect to being

representative over the model area, since it was determined at a single hydropad location.

#### Compressibility of the Primary Medium

The compressibility of the primary medium is taken to be equal to the single-porosity rock compressibility as calculated in Section 3.3.2. The primary-system compressibility is equal to  $7.57 \times 10^{-10} \text{ m}^2/\text{N}$  assuming a primary porosity of 0.2, an average fluid density of  $1.05 \text{ gm/cm}^3$ , and an aquifer thickness equal to 8 m.

In order to preserve the single-porosity storativity in the double-porosity model, the primary-medium compressibility was lowered to  $6.81 \times 10^{-10} \text{ m}^2/\text{N}$ .

#### Compressibility of the Secondary Medium

The compressibility of the secondary system was taken to be equal to  $7.57 \times 10^{-9} \text{ m}^2/\text{N}$ , i.e., approximately one order of magnitude greater than the primary compressibility. This decision is based upon two lines of reasoning. Both Domenico (1972) and Freeze and Cherry (1979) suggest that the compressibility of a jointed rock is approximately one order of magnitude greater than the compressibility of a sound rock. Also, with the availability of double-porosity hydraulic parameters for the Culebra (Table 7.3), one can approximate the ratio between the primary and secondary compressibilities. From Equation 7-1, one can see that the dimensionless secondary-system storativity ( $\omega$ ) is composed of both the primary and secondary porosities and compressibilities. By assuming that the primary and secondary porosities are equal to 0.2 and  $2 \times 10^{-3}$ , respectively, and that  $C_r/C'_r$  is equal to 10, Equation 7-1 yields a dimensionless secondary-system storativity equal to 0.09. The average observed  $\omega$  reported in Table 7.1 is 0.13, which compares relatively well with the calculated  $\omega$  of 0.09.

### Matrix-Block Length

As introduced in Section 3.1.4, the matrix may be conceptualized as being intersected by parallel non-intersecting fractures or intersecting sets of fractures (Figure 3.1). From review of both literature and Culebra core from several boreholes at the WIPP site, it was concluded that both horizontal and high-angle fractures are present in the Culebra within the WIPP area (Kelley and Pickens, 1986). Therefore, for this modeling exercise the Culebra matrix is assumed to be bounded by three orthogonal sets of fractures and, numerically, the matrix is approximated by spheres whose diameters are equivalent to the fracture spacing.

Because of the large degree of heterogeneity within the Culebra at the WIPP site, it is probably inaccurate to model the entire model region with one matrix-block size. Since the matrix-block length data base is extremely limited, knowledge of its variability across the WIPP site cannot be estimated. Therefore, as a first approximation the matrix-block size is considered to be a homogeneous property within the modeled region. Based upon double-porosity tracer-test analyses, Kelley and Pickens (1986) report matrix-block sizes ranging from 0.25 to 2.1 m at the H-3 hydropad (Table 7.2). From hydraulic double-porosity test results (Table 7.3), matrix-block lengths can be calculated, but they are not in agreement with double-porosity tracer-test results and are more than an order of magnitude greater than the observed thickness of the Culebra. Due to obvious problems in conceptualizing block sizes larger than the aquifer thickness, the block size is based upon tracer-test analyses and core descriptions. Matrix-block length in the present simulations will vary from 1 to 4 m with 2 m being chosen as the initial input value. Table 7.4 lists the initial input parameters for the SWIFT II double-porosity simulations. All fluid properties and other physical constants not discussed in this section are equal to the values appearing in Table 3.4.



### 7.3 Preliminary Scoping Calculations

As a precursor to the numerical simulations utilizing SWIFT II, simple analytical relationships were used to provide an estimate of the double-porosity flow effects to be expected. In this portion of the report, both theoretical and conceptual models will be introduced to predict both the behavior and necessity of a double-porosity flow model for simulation of transient flow in the Culebra at the scale chosen for this study.

Streltsova (1983) notes that the time required for equilibration between fracture and matrix (up to 99%) is:

$$\tau_e = 2.5 L_m^2 / D_m' \quad (7-5)$$

where  $L_m$  = matrix-block half length;  
 $D_m'$  = matrix hydraulic diffusivity.

This relationship is derived from a solution to the diffusion equation for a fixed, but time-dependent, pressure at the fracture/matrix interface and a no-flow boundary condition at the symmetry boundary in the matrix. The significance of this relationship is that all matrix blocks, regardless of their distance from the hydraulic disturbance, will reach equilibrium with the fracture fluid at the same time, assuming homogeneous matrix properties. For any time greater than the matrix time constant ( $\tau_e$ ), the reservoir hydraulic response is typical of a single-porosity reservoir with composite properties of both media. The pressure behavior after  $t > \tau_e$  corresponds to the second semi-log straight line for the total system ( $t > t_2$  of Figure 7.1).

Equation 7-5 can be used to predict if transient double-porosity pressure responses will be an important factor in the time frame of a modeling effort. For time greater than  $\tau_e$ , the system behaves as a

single-porosity system and it becomes more efficient and as accurate to model the system as such. For times less than  $\tau_e$ , one must model the system as a double-porosity system to simulate the correct pressure response. Double-porosity transient pressure responses can be modeled by a code such as SWIFT II if one uses time steps much smaller than the matrix time constant ( $\tau_e$ ).

In Equation 7-5, the matrix hydraulic diffusivity ( $D_m'$ ) can be expanded to:

$$D_m' = \frac{K_m}{\rho g \phi_m (\alpha + \beta)} \quad (7-6)$$

where  $K_m$  = hydraulic conductivity of the matrix;  
 $\rho$  = density of the reservoir fluid;  
 $\phi_m$  = porosity of the matrix;  
 $\alpha$  = compressibility of the matrix;  
 $\beta$  = compressibility of water.  
 $g$  = gravitational acceleration

By substituting Equation 7-6 into 7-5, one can see that the parameters which introduce the greatest degree of uncertainty in calculating the time constant ( $\tau_e$ ) are matrix-block half length, hydraulic conductivity, porosity, and the compressibility of the matrix. To address the uncertainty, each of these parameters were given ranges and an associated time constant was calculated. The matrix time constant is inversely proportional to hydraulic conductivity of the matrix and proportional to the matrix-block half length squared.

For the first set of time-constant calculations, both matrix porosity and matrix-block half length were allowed to vary (Table 7.5). Porosity was varied from 0.1 to 0.3, which is representative of the observed core analysis range of 0.07 to 0.29 (Table 7.1). Matrix-block half length was varied from 0.5 to 4 m, which corresponds to a fracture-spacing

range of 1 to 8 m. The calculations utilized a primary-medium hydraulic conductivity equal to  $2.63 \times 10^{-10}$  m/s. The minimum time constant calculated is  $8.3 \times 10^2$  s, and the maximum is  $5.3 \times 10^5$  s or approximately 6 days.

For the second set of time-constant calculations, both hydraulic conductivity of the matrix and matrix-block half length were varied (Table 7.6). Hydraulic conductivity was varied from  $2.6 \times 10^{-10}$  to  $2.6 \times 10^{-7}$  m/s, which is comparable to the observed core hydraulic conductivities which were calculated to range from  $8.3 \times 10^{-11}$  to  $5.4 \times 10^{-7}$  m/s. The minimum time constant is 5 s, and the highest is  $3.6 \times 10^5$  s or approximately 4 days.

For the third set of time-constant calculations, both matrix compressibility and matrix-block half length were varied (Table 7.7). As described in Section 7.2, the primary-medium compressibility is equal to  $6.81 \times 10^{-10}$  m<sup>2</sup>/N. Freeze and Cherry (1979) show that the compressibility of a sound rock may vary up to three orders of magnitude. Therefore, for sensitivity purposes, primary-medium compressibility was varied from  $6.81 \times 10^{-11}$  to  $6.81 \times 10^{-9}$  m<sup>2</sup>/N. This range is not meant to represent an observed range of values for the Culebra but is chosen to show the time-constant sensitivity to primary-medium compressibility. The minimum time constant calculated is 2550 s and the largest is  $2.2 \times 10^{-6}$  s or approximately 25 days.

For those matrix parameters thought to be most representative of the Culebra (Table 7.4), the time constant ( $\tau_e$ ) is equal to  $2.2 \times 10^4$  s or approximately six hours. These calculations show that even in the most conservative case the time to reach coupled-pressure response between the primary and secondary media is approximately 25 days. For the time-constant calculations thought to be most representative of the Culebra, coupling of the two media takes place within 6 hours. In areas where the primary medium hydraulic conductivity is greater than

$2.63 \times 10^{-10}$  m/s, for example at the H-3 hydropad, the time constant is substantially less. This conclusion is strengthened by the findings of Beauheim (in preparation) which show that the transient double-porosity pressure response at H-3 is complete within one hour.

Based upon these time-constant calculations, the Culebra dolomite is expected to behave hydraulically as a single-porosity reservoir for all times greater than a day. If one desired to model the local transient double-porosity hydraulic response on a hydropad scale during the H-3 multipad test, one would need to decrease time steps to increments much less than the calculated time constant for the matrix. For purposes of modeling regional flow at the WIPP site, this would be inappropriate for investigating the long-term transient effects of the shaft activities and local pumping during pumping tests.

As previously stated, the assumption that both the single- and double-porosity solutions will be identical after a time equal to the time constant assumes a constant fluid density within the reservoir. Brine transport should remain transient for much larger time periods than the pressure field. This should affect global fractional brine concentrations and ultimately the calculated freshwater elevations. It is not felt that these effects will be significant and the single- and double-porosity simulations should remain very close. Due to the very small time constants in relation to the duration of the hydraulic disturbances being modeled, the reservoir will behave as a single-porosity medium with a composite hydraulic diffusivity representative of both the primary and secondary media combined. This implies that for regional-scale flow studies at the WIPP site, single-porosity models are adequate if the transmissivity is representative of the secondary medium and the storage coefficient is representative of the primary medium. However, due to the much smaller molecular diffusivity of the primary medium, it is felt that a double-porosity model is necessary to model solute transport (i.e., for a breach scenario) in the more permeable regions of the Culebra at the WIPP site.

To verify these conceptual inferences and scoping calculations, a series of double-porosity simulations were conducted using SWIFT II.

#### 7.4 Discussion of the Double-Porosity Simulation Results

A double-porosity simulation was performed with the transient density-calibrated model discussed in Section 5.5. The input parameters, which are different than those used in the single-porosity run, appear in Table 7.4. The matrix is modeled as spheres which conceptually represent vertical and horizontal fractures within the Culebra.

The differences between the single-porosity and double-porosity simulations are minimal. Figure 7.2 shows equivalent freshwater head at the H-1 and H-3 hydropads for both single- and double-porosity simulations. The greatest observed difference between the two simulations is 0.2 m and occurs due to the operations at the construction and salt-handling shaft and waste-handling shaft from October 24, 1981 to February 21, 1982. Within the remainder of the simulation time period, both models predict freshwater elevations identical to within a few centimeters.

Figure 7.2 also shows equivalent freshwater heads versus time at the H-3 hydropad. At H-3, the greatest observed difference is approximately 0.02 m and again occurs during shaft operations from August 7, 1981 to February 21, 1982. During this period the Culebra was drilled in the construction and salt-handling shaft and brine was added to the shaft. After the Culebra was cemented in the construction and salt-handling shaft, the Culebra was drilled in the waste-handling shaft (see Section 5.1).

In Section 7.3 it was predicted that, 24 hours after a given hydraulic disturbance, one could expect the single- and double-porosity simulations to match. This conclusion was based upon the assumption that brine concentration does not vary in space or time. In fact, brine

concentration is variable. Therefore, the single- and double-porosity solutions should not agree until the fracture and matrix equilibrate with respect to brine concentration. By using Equation 7-5 and replacing hydraulic diffusivity with molecular diffusivity, one can calculate the time it would take for this equilibration to take place within 99%. Assuming a tortuosity of 0.5, a free-water diffusion coefficient of  $2 \times 10^{-9} \text{ m}^2/\text{s}$ , and a porosity of 0.2, the molecular time constant equals approximately 400 years. As is reflected in Figure 7.2, the transient brine effect upon the double-porosity solution becomes insignificant at much earlier times.

The reason that the transient brine effect becomes insignificant to the global-pressure solution at such early times is that the gradient between the fracture and the matrix is largest at early times and quickly decreases. Although the fracture and the matrix exchange solutes to some degree throughout the simulation, the late time changes in brine concentration within the global blocks caused by diffusion into the matrix are minimal. Therefore, at late times the brine concentration in the global block (the pressure from which the water level is calculated) essentially remains constant.

#### 7.5 Conclusions from Double-Porosity Simulations

This double-porosity simulation yields two significant findings for future modeling efforts within the Culebra at the WIPP site.

- (1) Double-porosity pressure effects are insignificant in regional-scale hydrologic modeling.
- (2) A transient variable-density single-porosity model appears to be adequate for modeling multipad-scale tests within the Culebra.

## 8.0 CONCLUSIONS

Based on the evaluation of the existing data base (Chapter 3), on the result of the steady-state and transient simulations (Chapter 4 and 5), and on the sensitivity analyses (Chapter 6 and 7), the following main conclusions were developed.

1. The existing field transmissivity data on the Culebra dolomite were analyzed by means of kriging techniques and used to estimate the initial transmissivity distribution of the modeled region under steady-state flow conditions. The initial transmissivity distribution is characterized by intermediate transmissivities ( $T = 10^{-6} - 10^{-5} \text{ m}^2/\text{s}$ ) which prevail in large parts of the model area. Higher transmissivities ( $T = 10^{-5} - 10^{-4} \text{ m}^2/\text{s}$ ) occur in the western part of the model area while lower transmissivities ( $T = 10^{-7} - 10^{-9} \text{ m}^2/\text{s}$ ) were found at H-4 and P-17 as well as in the eastern part of the model area.
2. In order to calibrate the steady-state model, it was necessary to incorporate a high-transmissivity zone ( $T = 10^{-4} \text{ m}^2/\text{s}$  or more) into the model between H-11 and the southern model boundary (with or without a low transmissivity zone ( $T=10^{-7} \text{ m}^2/\text{s}$  and less) between WIPP-12 and H-5). The presence of this high-transmissivity zone is evidenced by the lower hydraulic gradients observed in the southern part of the model. In addition, it is necessary to drain enough water from the area of H-11 and DOE-1 so that the calculated steady-state freshwater heads are consistent with the observed values. The exact location of the high-transmissivity zone is unknown, but best model results were obtained by placing it about 1 km east of P-17. Currently, it is not possible to calibrate the model with the high-transmissivity zone implemented west of P-17.

3. Simulating the Culebra dolomite as a single, completely confined layer is probably an oversimplification of the real situation. It is possible to calibrate the steady-state model against the best estimate of the undisturbed freshwater heads. It is not possible to calibrate the steady-state model such that the observed formation-fluid density distribution is completely reproduced by the model. One of the possible reasons for the remaining discrepancies between the calculated and the observed density distributions is that the hydrogeology of the Culebra dolomite is influenced by vertical fluxes through the confining layers above and below the Culebra dolomite.
  
4. A sensitivity analysis with respect to the possibility of vertical fluxes into the Culebra dolomite was conducted. The results indicate that the steady-state model is moderately sensitive to vertical flux as far as the pressures are concerned. The model is very sensitive to vertical flux with respect to the formation-water densities. In addition, it is possible to remove some of the remaining inconsistencies between the calculated and the observed density distributions by using vertical flux. Furthermore, it is considered to be difficult to exclude the possibility of any vertical flux into or out of the Culebra dolomite. Therefore, future modeling studies should not attempt to simulate the Culebra dolomite as a completely confined hydraulic system but rather as a leaky-confined aquifer. Collection of fluid data on heads and permeabilities of the other Rustler members would aid this modeling considerably.
  
5. It is not possible to simulate realistically the H-3 multipad pumping test without consideration of pretest transient events because the hydraulic situation in the Culebra dolomite has been influenced since 1981 by various drilling and testing activities at the shafts and the borehole locations. An evaluation of the water-level



measurements led to the conclusion that the activities in the three shafts were the dominant hydraulic disturbances during these years. Therefore, a simplified but complete shaft pressure history was implemented into the transient model.

6. The transient modeling, which included the simulation of the shaft history as well as of several well tests, resulted generally in good agreement between the calculated and the observed pressures at the well locations. The agreement is good enough to allow the conclusion that the model transmissivities used between H-3 and H-1, H-2, DOE-1, H-11, and the shafts are reasonably representative of the real transmissivity distribution.
7. It was not possible to simulate the observed transient pressures at the shaft location and at the WIPP wells north of it (WIPP-22, WIPP-21, WIPP-19) during the H-3 multipad pumping test by implementing only the recorded shaft history and well tests. It was hypothesized that an additional leakage in the waste-handling shaft had caused the additional pressure drawdown in the above-mentioned wells. The implementation of such additional leakage during the latter part of the H-3 multipad pumping test and the subsequent recovery period resulted in a much better agreement between the calculated pressures (at WIPP-22, WIPP-21 and WIPP-19) and the observed data. Thus, it seems likely that the observed freshwater heads in the fall of 1985 and the first half of 1986 were influenced by two partially concurrent events: the H-3 multipad pumping test and an additional leakage in the waste-handling shaft.
8. A sensitivity analysis using the double-porosity flow conceptualization of SWIFT II was conducted in order to assess the impact on the model results caused by simplifying the model conceptualization to a single-porosity approach. For the purpose of regional flow-field determination, the double-porosity flow conceptualization

does not provide significantly different results from those obtained using the single-porosity conceptualization. Therefore, the use of a single-porosity, or porous-medium-based, modeling approach is considered valid for the spatial and temporal model scales presented in this report.

## 9.0 BIBLIOGRAPHY

- Aziz, K. and A. Settari, 1979. Petroleum Reservoir Simulation, Applied Science Publishers, Ltd., London, 476 p.
- Bachman, G.O., 1980. Regional Geology and Cenozoic History of Pecos Region, South-eastern, New Mexico. U.S. Dept. of the Interior Geological Survey, Open-File Report 80-1099, 116 p.
- Bachman, G.O., 1981. Geology of Nash Draw, Eddy County, New Mexico. U.S. Geological Survey, Open File Report 81-31, 8 p.
- Bachman, G.O., 1985. Assessment of Near-Surface Dissolution at and Near the Waste Isolation Pilot Plant (WIPP), Southeastern New Mexico, Sandia National Laboratories, Contractor Report SAND84-7178, 33 p.
- Barenblatt, G.I., Y.P. Zheltov, and I.N. Kochina, 1960. Basic concepts in the theory of seepage of homogeneous liquids in fissured rocks (strata), Journal of Applied Mathematics and Mechanics (USSR), Vol. 24 No. 5, p. 1286-1303.
- Barr, G.E., W.B. Miller, D.D. Gonzalez, 1983. Interim Report on the Modeling of the Regional Hydraulics of the Rustler Formation. Sandia National Laboratories, SAND83-0391, 58 p.
- Bear, J., 1972. Dynamics of Fluids in Porous Media. American Elsevier Publishing Company, New York, 764 p.
- Bear, J., 1979. Hydraulics of Groundwater. McGraw-Hill, New York, 567 p.
- Bear, J., and C. Braester, 1972. Simultaneous flow of immiscible liquids in a fractured medium, in Fundamentals of Transport Phenomena in Porous Media, Developments in Soil Sciences, 2, International Association for Hydraulic Research, Elsevier Publishing Company, Amsterdam, p. 177-202.

- Beauheim, R.L., in preparation. Analysis of Pumping Tests of the Culebra Dolomite Conducted at the H-3 Hydropad at the Waste Isolation Pilot Plant (WIPP) Site. Sandia National Laboratories, SAND86-2311.
- Beauheim, R. L., 1986. Hydraulic-Test Interpretations for Well DOE-2 at the Waste Isolation Pilot Plant (WIPP) Site. Sandia National Laboratories, SAND86-1364, 89 p.
- Bredehoeft, J.D., W. Back, and B.B. Hanshaw, 1982. Regional ground-water flow concepts in the United States: Historical perspective in Recent Trends in Hydrogeology, T.N. Narasimhan, ed., Geological Society of America, Special Paper 185, p. 297-316.
- Chaturvedi, L. and K. Rehfeldt, 1984. Groundwater occurrence and the dissolution of salt at the WIPP radioactive waste repository site. American Geophysical Union, EOS, July 3, 1984, p. 457-459.
- Chaturvedi, L., and J.K. Channell, 1985. The Rustler Formation as a Transport Medium for Contaminated Groundwater. New Mexico Environmental Evaluation Group, EEG-32, 85 p.
- Cole, C.R. and F.W. Bond, 1980. Assessment of Effectiveness of Geologic Isolation Systems: Comparison of INTERA and WISAP Consequence Model Application. Report prepared by Pacific Northwest Laboratory for Office of Nuclear Waste Isolation under contract to U.S. Department of Energy, PNL-3070, UC-70, 50 p.
- Cooper, H., 1966. The equation of ground-water flow in fixed and deforming coordinates. Journal of Geophysical Research, V.71, p. 4783-4790.
- Cooper, J.B., and V.M. Glanzman, 1971. Geohydrology of Project Gnome Site, Eddy County, New Mexico. U.S. Geological Survey, Professional Paper 712-A, 24 p.

- Core Laboratories, Inc., 1986. Special Core Analysis Study for INTERA Technologies, WIPP Site, File Number: SCAL 203-850073, Core Laboratories Inc., Aurora, Colorado.
- D'Appolonia Consulting Engineers, Inc., 1980. Modeling Verification Studies: Long-Term Waste Isolation Assessment. Report prepared for Westinghouse Electric Corporation under contract to U.S. Department of Energy.
- Delhomme, J.P., 1978. Kriging in the hydrosiences. Advances in Water Resources, V.1 No. 5, p. 251-266.
- Delhomme, J.P., 1979. Spatial variability and uncertainty in groundwater flow parameters: A geostatistical approach. Water Resources Research V.15, No. 2, p. 269-280.
- de Marsily, G., 1982. Spatial variability of properties in porous media: A stochastic approach. NATO Advanced Study Inst., Mechanics of Fluids in Porous Media Symp., Newark, Delaware.
- Deruyck, B.G., D.P. Bourdet, G. DaPrat, and H.J. Ramey, Jr., 1982. Interpretation of Interference Tests in Reservoirs with Double Porosity Behavior-Theory and Field Examples, SPE paper 11025 presented at the 57th Annual Fall Technical Conference and Exhibition of the Society of Petroleum Engineers, held in New Orleans, Louisiana, September 26-29, 1982, 18 p.
- Dillon, R.T., R.B. Lantz, and S.B. Pahwa, 1978. Risk Methodology for Geologic Disposal of Radioactive Waste: The Sandia Waste-Isolation Flow and Transport (SWIFT) Model. NUREG/CR-0424 and SAND78-1267, Sandia National Laboratories, Albuquerque, New Mexico.

- Domenico, P.A., 1972. Concepts and Models in Groundwater Hydrology. International Series in the Earth and Planetary Sciences, McGraw-Hill Book Co., New York, 406 p.
- Duguid, J.O., and M. Reeves, 1976. A comparison of mass transport using average and transient rainfall boundary conditions. in Finite Elements in Water Resources, W.G. Gray, G.F. Pinder and C.A. Brebbia eds., Proceedings of the First International Conference on Finite Elements in Water Resources, Princeton University, July, 1976, Pentech Press, p. 2.25-2.36.
- Fenix and Scisson, Inc., 1982. SPDV Exploratory Shaft Hole History; Albuquerque, New Mexico. Consultants report prepared for the U.S. Department of Energy, 37 p.
- Finley, N.C., and M. Reeves, 1981. SWIFT Self-Teaching Curriculum: Illustrative Problems to Supplement the User's Manual for the Sandia Waste-Isolation Flow and Transport Model (SWIFT), NUREG/CR-1968 and SAND81-0410, Sandia National Laboratories, Albuquerque, New Mexico.
- Freeze, R.A., 1975. A stochastic-conceptual analysis of one-dimensional groundwater flow in nonuniform homogeneous media. Water Resources Research, V.11, No. 5, p. 725-741.
- Freeze, R.A., and J.A. Cherry, 1979. Groundwater. Prentice-Hall, Inc., Englewood Cliffs, New Jersey, 604 p.
- Gambolati, G., and G. Volpi, 1979. Groundwater contour mapping in Venice by stochastic interpolators, 1, theory. Water Resources Research, V.15, No. 2, p. 281-290.
- Gonzalez, D.D., 1983a. Groundwater Flow in the Rustler Formation, Waste Isolation Pilot Plant (WIPP), Southeast New Mexico (SENM): Interim Report. Sandia National Laboratories, SAND82-1012.

- Gonzalez, D.D., 1983b. Hydrogeochemical Parameters of Fluid-Bearing Zones in the Rustler and Bell Canyon Formations: Waste Isolation Pilot Plant (WIPP) Southeastern New Mexico (SENM). Sandia National Laboratories, SAND83-0210.
- Grisak, G.E., and J.F. Pickens, 1980. Solute transport through fractured media, 1, The effect of matrix diffusion. Water Resources Research, V.16, No. 4, p. 563-572.
- Hoeksema, R.J., and P.K. Kitanidis, 1985. Analysis of the spatial structure of properties of selected aquifers. Water Resources Research, V.21, No. 4, p. 563-572.
- Holt, R.M., and D.W. Powers, 1984. Geotechnical Activities in the Waste Handling Shaft, Waste Isolation Pilot Plant (WIPP) Project Southeastern New Mexico. U.S. Department of Energy, WTSD-TME-038.
- Huyakorn, P.S., B.H. Lester, and J.W. Mercer, 1983. An efficient finite element technique for modeling transport in fractured porous media 1. Single species transport. Water Resources Research, V.19, No. 3, p. 841-854.
- Hydro Geo Chem, Inc., in preparation, a. Aquifer Tests at the H-4 Hydropad, Waste Isolation Pilot Plant (WIPP), Southeastern New Mexico, Basic Data and Interpretations. Unpublished contractor report prepared for Sandia National Laboratories.
- Hydro Geo Chem, Inc., in preparation, b. Aquifer Tests at the H-5 Hydropad, 1981, Waste Isolation Pilot Plant (WIPP), Southeastern New Mexico (SENM): Basic Data and Interpretations. Unpublished contractor report prepared for Sandia National Laboratories.

Hydro Geo Chem, Inc., in preparation, c. Aquifer Tests at the H-6 Hydropad, 1981, Basic Data and Interpretations. Unpublished contractor report prepared for Sandia National Laboratories.

Hydro Geo Chem, Inc., in preparation, d. Convergent Flow Tracer Tests at the H-6 Hydropad, Waste Isolation Pilot Plant (WIPP), Southeastern New Mexico (SENM). Unpublished contractor report prepared for Sandia National Laboratories.

Hydro Geo Chem, Inc., in preparation, e. Horizontal Anisotropy of the Culebra Dolomite at the H-4, H-5, H-6 Hydropads, Waste Isolation Pilot Plant (WIPP), Southeastern New Mexico (SENM). Unpublished contractor report prepared for Sandia National Laboratories.

Hydro Geo Chem, Inc., 1985. WIPP Hydrology Program, Waste Isolation Pilot Plant, SENM, Hydrologic Data Report #1. Sandia National Laboratories, Contractor Report SAND85-7206.

Hydro Geo Chem, Inc., 1986. Two-Well Recirculation Tracer Tests at the H-2 Hydropad, Waste Isolation Pilot Plant (WIPP), Southeastern New Mexico. Sandia National Laboratories, Contractor Report SAND86-7092, 33 p.

Izette, G.A., and R.E. Wilcox, 1982. Map Showing Localities and Inferred Distributions of the Huckleberry Ridge, Mesa Falls and Lava Creek Ash Beds (Pearlette Family Ash Beds) of Pliocene and Pleistocene Age in the Western United States and Southern Canada. U.S. Geological Survey Miscellaneous Investigations Series Map I-1325.

INTERA Technologies, Inc., 1986. WIPP Hydrology Program, Waste Isolation Pilot Plant, SENM, Hydrologic Data Report #3. Sandia National Laboratories, Contractor Report SAND86-7109.



- INTERA Technologies, Inc., and Hydro Geo Chem, Inc., 1985. WIPP Hydrology Program, Waste Isolation Pilot Plant, SENM, Hydrologic Data Report #2. Sandia National Laboratories, Contractor Report SAND85-7263.
- INTERCOMP Resource Development and Engineering, Inc., 1976. Development of Model for Calculating Disposal in Deep Saline Aquifers, Parts I and II, U.S. Geological Survey Water Resources Investigation 76-61, PB-256903, National Technical Information Service, Washington, D.C., 263 p.
- Jarolimek, L., M.J. Timmer, and R.F. McKinney, 1983a. Geotechnical Activities in the Exploratory Shaft - - Selection of the Facility Interval, Waste Isolation Pilot Plant (WIPP) Project Southeastern New Mexico, US DOE, TME 3178.
- Jarolimek, L., M.J. Timmer, and D.W. Powers, 1983b. Correlation of Drillhole and Shaft Logs, Waste Isolation Pilot Plant (WIPP) Project, Southeastern New Mexico. US DOE, TME 3179.
- Jones, C.L., 1973. Salt Deposits of Los Medanos Area, Eddy and Lea Counties, New Mexico. U.S. Geological Survey Open-File Report, 4339-7, p. 67.
- Jones, C.L., 1975. Potash Resources in Part of Los Medanos Area of Eddy and Lea Counties, New Mexico. U.S. Geological Survey, Open File Report 75-407, 37 p.
- Jones, C.L., 1978. Test Drilling for Potash Resources: Waste Isolation Pilot Plant Site, Eddy County, New Mexico. U.S. Geological Survey Open File Report 78-592, Vol. 1 & 2, 431 p.
- Journel, A.G., and C. T. Huijbregts, 1978. Mining Geostatistics, Academic, Press, London, 600 p.

- Kafritsas, J., and R.L. Bras, 1981. The practice of kriging, Technical Report 263, Ralph M. Parsons Lab., Mass, Inst. of Technol., Cambridge, 107 p.
- Kazemi, H., M.S. Seth, and G.W. Thomas, 1969. The interpretation of interference tests in naturally fractured reservoirs with uniform fracture distribution. Transactions of the Society of Petroleum Engineering A.I.M.E., 246, p. 463-472.
- Kelley, V.A., and J.F. Pickens, 1986. Interpretation of the Convergent-Flow Tracer Tests Conducted in the Culebra Dolomite at the H-3 and H-4 Hydropads At The Waste Isolation Pilot Plant (WIPP) Site, Sandia National Laboratories, Contractor Report SAND86-7161.
- Kuchling, H., 1982. Taschenbuch der Physik. Verlag Harri Deutsch, Thun und Frankfurt, 678 p.
- Lambert, S.J., 1983. Dissolution of Evaporites in and Around the Delaware Basin Southeastern New Mexico and West Texas. Sandia National Laboratories, SAND82-0461, 96 p.
- Lang, W.B., 1938. Geology of the Pecos River Between Laguna Grande de la Sal and Pierce Canyon, in Geology and Ground-Water Conditions of the Pecos River Valley. New Mexico State Engineer 12th and 13th Biennial Reports, p. 80-86.
- Langguth, H.-R., and Voigt, R., 1980. Hydrogeologische Methoden, Springer-Verlag, New York, 486 p.
- Lerman, A., 1979. Geochemical Processes. John Wiley and Sons, New York, 481 p.
- Lohman, S.W., 1972. Ground-Water hydraulics. U.S. Geological Survey Professional Paper 708, 70 p.

- Marsal, D., 1967. Statistische Methoden fuer Erdwissenschaftler. E. Schweitzerbart'sche Verlagsbuchhandlung, Stuttgart, FRB, 152 p.
- Matheron, G., 1971. The Theory of Regionalized Variables and its Applications. Cahiers du Centre de Morphologie Mathematiques, 1, Ecole de Mines, Fontainbleau, France, 211 p.
- Mercer, J.W., 1983. Geohydrology of the Proposed Waste Isolation Pilot Plant Site, Los Medanos Area, Southeastern New Mexico. U.S. Geological Survey Water-Resources Investigation Report 83-4016, 113 p.
- Mercer, J.W. and B.R. Orr, 1977. Review and Analysis of Hydrogeologic Conditions Near the Site of a Potential Nuclear-Waste Repository, Eddy and Lea Counties, New Mexico. U.S. Geological Survey Open File Report 77-123, 35 p.
- Mercer, J.W. and B.R. Orr, 1979. Interim Data Report on the Geohydrology of the Proposed Waste Isolation Pilot Plant Site Southeast New Mexico. U.S. Geological Survey, Water-Resources Investigations Report 79-98, 178 p.
- Muller, A.B., N.C. Finley, F.J. Pearson, Jr., 1981. Geochemical Parameters Used in the Bedded Salt Reference Repository Risk Assessment Methodology. NUREG/CR-1996 and SAND81-0557, Sandia National Laboratories, Albuquerque, New Mexico.
- Neuman, S.P., 1984. Role of Geostatistics in Subsurface Hydrology. in G. Verly and others, eds., Geostatistics for Natural Resources Characterization, Part 2, North Atlantic Treaty Organization Advanced Study Institute Series, D. Reidel Publishing Co., Dordrecht, Holland, p. 787-811.

- Pickens, J.F., and G.E. Grisak, 1981a. Scale-dependent dispersion in a stratified granular aquifer. *Water Resources Research*, V.17, No. 4, p. 1191-1211.
- Pickens, J.F., and G.E. Grisak, 1981b. Modeling of scale-dependent dispersion in hydrogeologic systems. *Water Resources Research*, V.17, No. 6, p. 1701-1711.
- Powers, D.W., S.J. Lambert, S.E. Shaffer, L.R. Hill, and W.D. Weart, editors, 1978. *Geologic Characterization Report, Waste Isolation Pilot Plant (WIPP) Site, Southeastern New Mexico. Volumes I and II.* Sandia National Laboratories, SAND78-1596.
- Preuss, K., and T.N. Narasimhan, 1982. A practical method for modeling fluid and heat flow in fractured porous media. *Society of Petroleum Engineers, Paper No. SPE 10509, 6th Symp. Proc.*, p. 254-283.
- Rasmuson, A., T.N. Narasimhan, and I. Neretnieks, 1982. Chemical transport in a fissured rock: Verification of a numerical model. *Water Resources Research* V.18, No. 5, p. 1479-1492.
- Reddell, D.L., and D.K. Sunada, 1970. *Numerical Simulation of Dispersion in Ground-Water Aquifers, Hydrology Papers, Number 41, Colorado State University, 79 p.*
- Reeves, M., and R.M. Cranwell, 1981. *User's Manual for the Sandia Waste-Isolation Flow and Transport Model (SWIFT), Release 4.81, Sandia National Laboratories, NUREG/CR-2324 and SAND81-2516, 145 p.*
- Reeves, M., D.S. Ward, N.D. Johns, and R.M. Cranwell, 1986a. *Theory and Implementation for SWIFT II, the Sandia Waste-Isolation Flow and Transport Model, Release 4.84. Sandia National Laboratories, NUREG/CR-3328 and SAND83-1159, 189 p.*

- Reeves, M., D.S. Ward, N.D. Johns, and R.M. Cranwell, 1986b. Data Input Guide for SWIFT II, The Sandia Waste-Isolation Flow and Transport Model for Fractured Media, Release 4.84. Sandia National Laboratories, NUREG/CR-3162 and SAND83-0242, 144 p.
- Rehfeldt, K., 1984. Sensitivity Analysis of Solute Transport in Fractures and Determination of Anisotropy Within the Culebra Dolomite. New Mexico Environmental Evaluation Group, EEG-27, 46 p.
- Robinson, T.W. and W.B. Lang, 1938. Geology and Ground-water Conditions of the Pecos River Valley in the Vicinity of Laguna Grande de la sal, New Mexico. New Mexico State Engineer, 12th & 13th Biennial Reports, p. 77-100.
- Sandia National Laboratories, 1981a. Basic Data Report for Drill Hole WIPP 15 (Waste Isolation Pilot Plant WIPP). SAND79-0274.
- Sandia National Laboratories, 1981b. Basic Data Report for Drill Hole WIPP 34 (Waste Isolation Pilot Plant-WIPP). SAND81-2643. 52 p.
- Sandia National Laboratories, 1982a. Simulated-Waste Experiments Planned for the Waste Isolation Pilot Plant (WIPP). SAND82-0547.
- Sandia National Laboratories, 1982b. Basic Data Report for Drillhole AEC 7 (Waste Isolation Pilot Plant-WIPP). SAND79-0268. 96 p.
- Sandia National Laboratories, 1982c. Basic Data Report for Drillhole WIPP 14 (Waste Isolation Pilot Plant-WIPP). SAND82-1783. 36 p.
- Sandia National Laboratories, 1982d. Basic Data Report for Deepening of Drillhole WIPP 13 (Waste Isolation Pilot Plant-WIPP). SAND82-1880. 54 p.

Sandia National Laboratories, 1982e. Basic Data Report for Drillhole WIPP 12 (Waste Isolation Pilot Plant-WIPP). SAND82-2336.

Sandia National Laboratories, 1983a. Basic Data Report for Drillhole ERDA 6 (Waste Isolation Pilot Plant-WIPP). SAND79-0267.

Sandia National Laboratories, 1983b. Basic Data Report for Drillhole AEC 8 (Waste Isolation Pilot Plant-WIPP). SAND79-0269.

Sandia National Laboratories, 1983c. Basic Data Report for Drillhole ERDA 9 (Waste Isolation Pilot Plant-WIPP). SAND79-0270.

Sandia National Laboratories and U.S. Geological Survey, 1979a. Basic Data Report for Drillhole WIPP 13 (Waste Isolation Pilot Plant-WIPP). SAND79-0273. 16 p.

Sandia National Laboratories and U.S. Geological Survey, 1979b. Basic Data Report for Drillhole WIPP 25 (Waste Isolation Pilot Plant-WIPP). SAND79-0279. 26 p.

Sandia National Laboratories and U.S. Geological Survey, 1979c. Basic Data Report for Drillhole WIPP 26 (Waste Isolation Pilot Plant-WIPP). SAND79-0280. 31 p.

Sandia National Laboratories and U.S. Geological Survey, 1979d. Basic Data Report for Drillhole WIPP 27 (Waste Isolation Pilot Plant-WIPP). SAND79-0281. 20 p.

Sandia National Laboratories and U.S. Geological Survey, 1979e. Basic Data Report for Drillhole WIPP 28 (Waste Isolation Pilot Plant-WIPP). SAND79-0282. 33 p.

Sandia National Laboratories and U.S. Geological Survey, 1979f. Basic Data Report for Drillhole WIPP 29 (Waste Isolation Pilot Plant - WIPP). SAND79-0283. 19 p.

Sandia National Laboratories and U.S. Geological Survey, 1980a. Basic Data Report for Drillhole WIPP 18 (Waste Isolation Pilot Plant - WIPP). SAND79-0275. 18 p.

Sandia National Laboratories and U.S. Geological Survey, 1980b. Basic Data Report for Drillhole WIPP 19 (Waste Isolation Pilot Plant - WIPP). SAND79-0276.

Sandia National Laboratories and U.S. Geological Survey, 1980c. Basic Data Report for Drillhole WIPP 21 (Waste Isolation Pilot Plant - WIPP). SAND79-0277. 18 p.

Sandia National Laboratories and U.S. Geological Survey, 1980d. Basic Data Report for Drillhole WIPP 22 (Waste Isolation Pilot Plant - WIPP). SAND79-0278. 21 p.

Sandia National Laboratories and U.S. Geological Survey, 1980e. Basic Data Report for Drillhole WIPP 30 (Waste Isolation Pilot Plant - WIPP). SAND79-0284. 19 p.

Sandia National Laboratories and U.S. Geological Survey, 1980f. Basic Data Report for Drillhole WIPP 32 (Waste Isolation Pilot Plant - WIPP). SAND80-1102. 25 p.

Sandia National Laboratories and U.S. Geological Survey, 1980g. Basic Data Report for Drillhole WIPP 33 (Waste Isolation Pilot Plant - WIPP). SAND80-2011. 27 p.

Sandia National Laboratories and U.S. Geological Survey, 1982. Basic Data Report for Drillhole WIPP 11 (Waste Isolation Pilot Plant - WIPP). SAND79-0272.

Sandia National Laboratories and U.S. Geological Survey, 1983. Basic Data Report for Drillhole ERDA 10 (Waste Isolation Pilot Plant - WIPP). SAND79-0271.

Seward, P.D., 1982. Abridged Borehole Histories for the Waste Isolation Pilot Plant, (WIPP) Studies. Sandia National Laboratories, SAND82-0080, 79 p.

Skrivan, J. and M. Karlinger, 1980. Semi-Variogram Estimation and Universal Kriging Program, U.S. Geological Survey Technical Report PB81-120560, 98 p.

Snyder, R.P., 1985. Dissolution of Halite and Gypsum, and Hydration of Anhydrite to Gypsum, Rustler Formation in the Vicinity of the Waste-Isolation Pilot Plant, Southeastern New Mexico. U.S. Geological Survey, Open-File Report 85-229, 11 p.

Stevens, K. and W. Beyeler, 1985. Determination of Diffusivities in the Rustler Formation from Exploratory Shaft Construction at the Waste Isolation Pilot Plant in Southeastern New Mexico. U.S. Geological Survey Water-Resources Investigations Report 85-4020, 32 p.

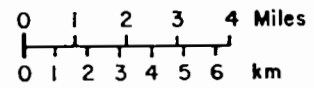
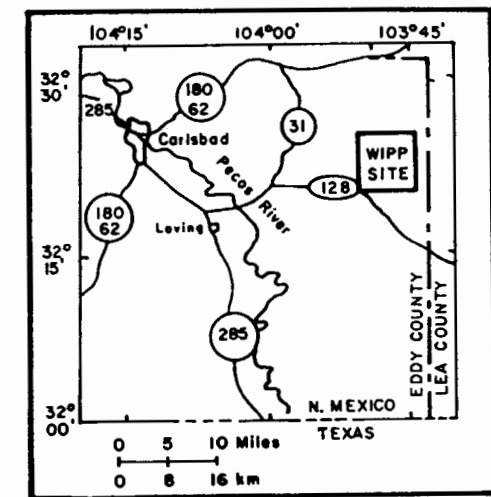
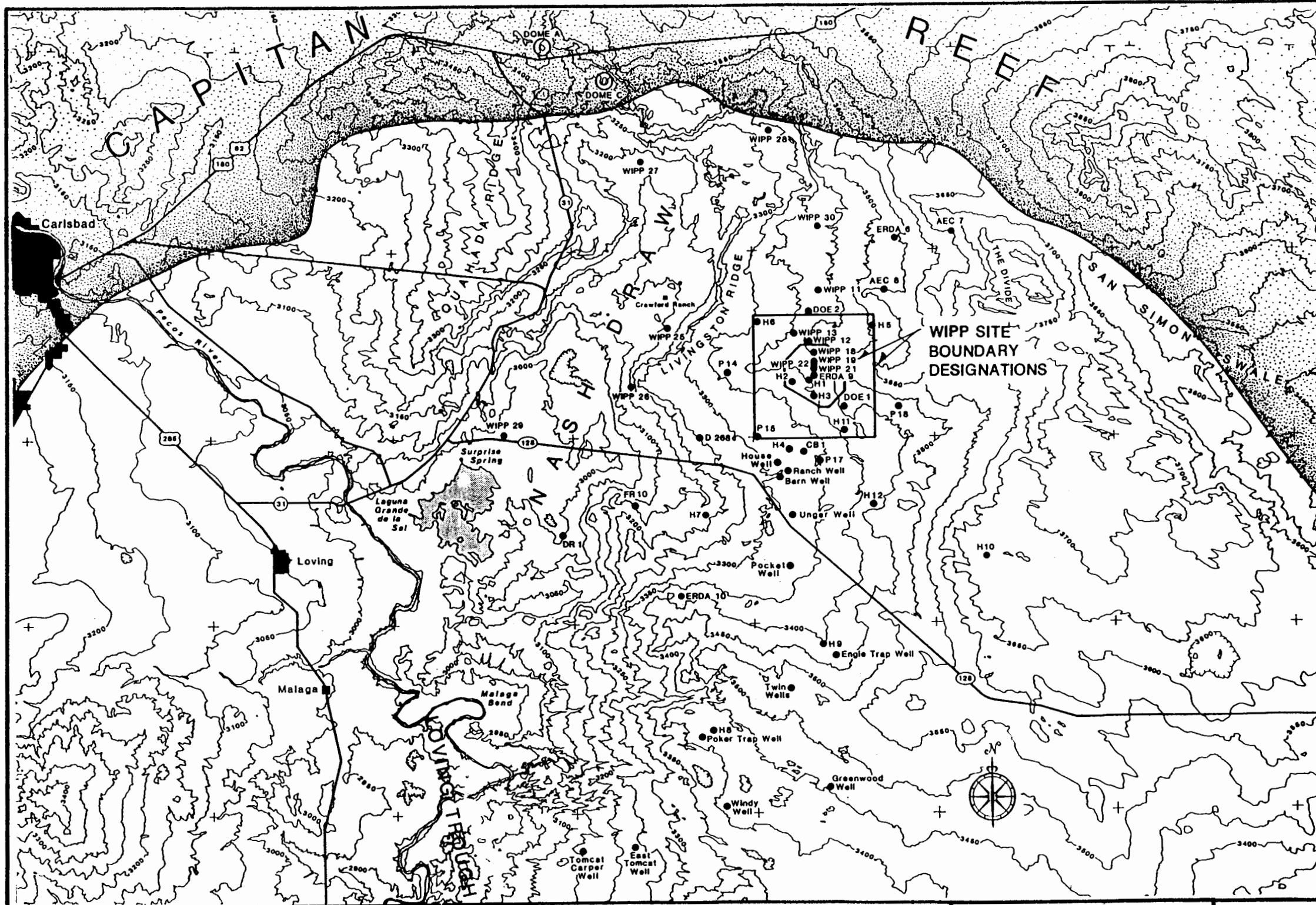
Streltsova-Adams, T.D., 1978. Well hydraulics in heterogeneous aquifer formations. Advances in Hydroscience, V.T. Chow ed., V.11, p. 357-423.

Streltsova, T.D., 1983. Well pressure behavior of a naturally fractured reservoir. Society of Petroleum Engineers Journal, 23(5), p. 769-780.



- Tang, D.H., E.O. Frind, and E.A. Sudicky, 1981. Contaminant transport in fractured porous media, 1, Analytical solution for a single fracture. Water Resources Research, V.17, No. 3, p. 555-564.
- U.S. Department of Energy, 1980. Final Environmental Impact Statement, Waste Isolation Pilot Plant, DOE/EIS-0026, UC-70, Volume 2.
- U.S. Department of Energy, 1981. Waste Isolation Pilot Plant, Safety Analysis Report. Five Volumes.
- Vine, J.D., 1963. Surface Geology of the Nash Draw Quadrangle, Eddy County, New Mexico. U.S. Geological Survey Bulletin 1141-B, 46 p.
- Ward, D.S., M. Reeves, and L.E. Duda, 1984. Verification and Field Comparison of the Sandia Waste-Isolation Flow and Transport Model (SWIFT), Sandia National Laboratories, NUREG/CR-3316 and SAND83-1154, 155 p.
- Warren, J.E., and P.J. Root, 1963. The behavior of naturally fractured reservoirs, Society of Petroleum Engineering Journal, September, p. 245-255.





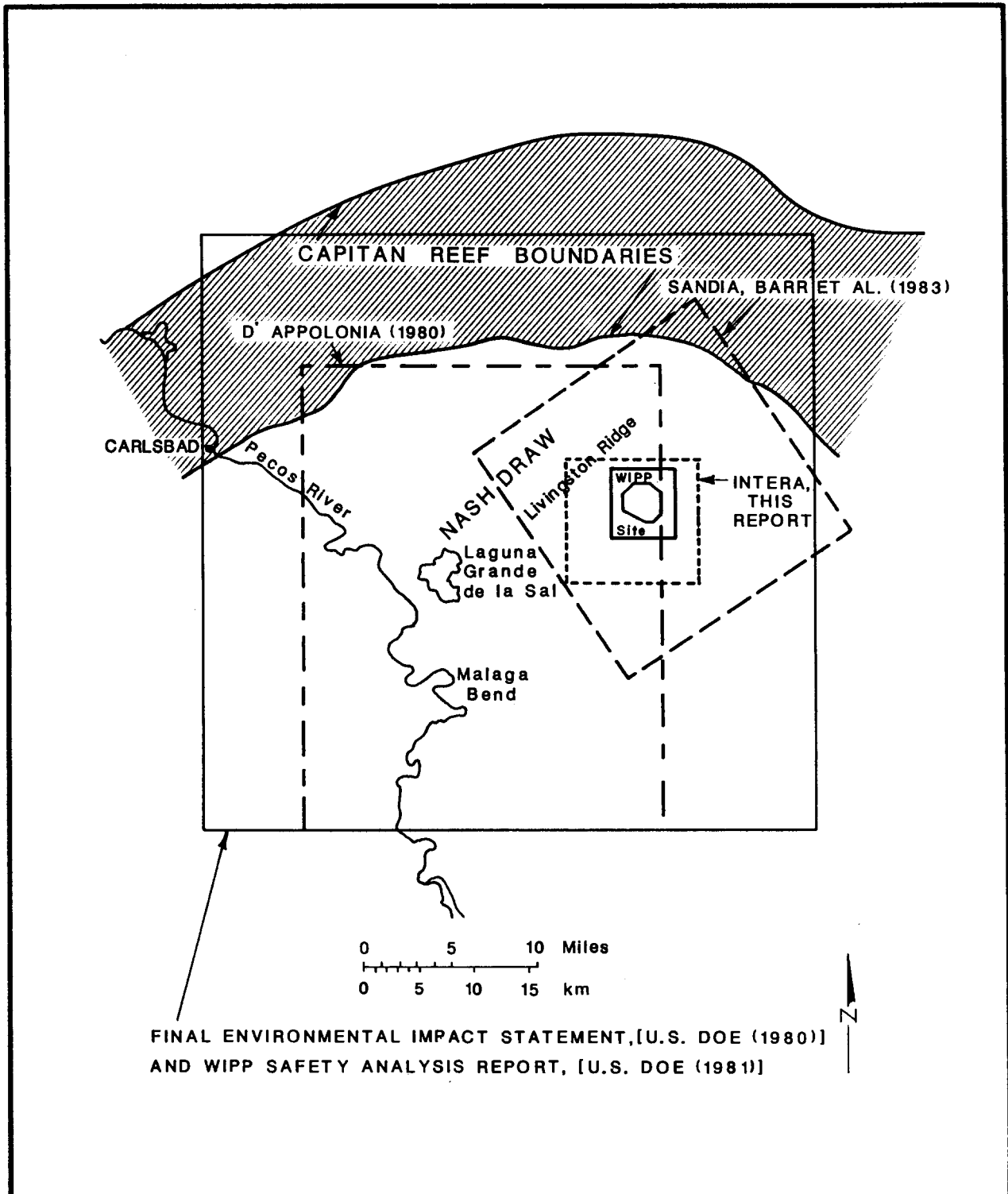
NOTE: THIS MAP ILLUSTRATES THE PRINCIPAL FEATURES OF THE WIPP SITE AND VICINITY. CONTOURS SHOW APPROXIMATE RELIEF. CONTOUR INTERVAL IS 50 FEET

Drawn by	Date
Checked by	Date
Revisions	Date

Site Location for the Waste Isolation Pilot Plant Showing the Observation-Well Network for Regional Hydrogeologic Characterization Studies

**INTERA Technologies**

Figure 1.1



FINAL ENVIRONMENTAL IMPACT STATEMENT, [U.S. DOE (1980)]  
 AND WIPP SAFETY ANALYSIS REPORT, [U.S. DOE (1981)]

Drawn by	Date
Checked by	Date
Revisions	Date

Comparison of Regional Model Areas for  
 Simulating Ground-Water Flow in the Rustler  
 Formation and/or the Culebra Dolomite Member  
 at the WIPP Site

**INTERA** Technologies

Figure 1.2

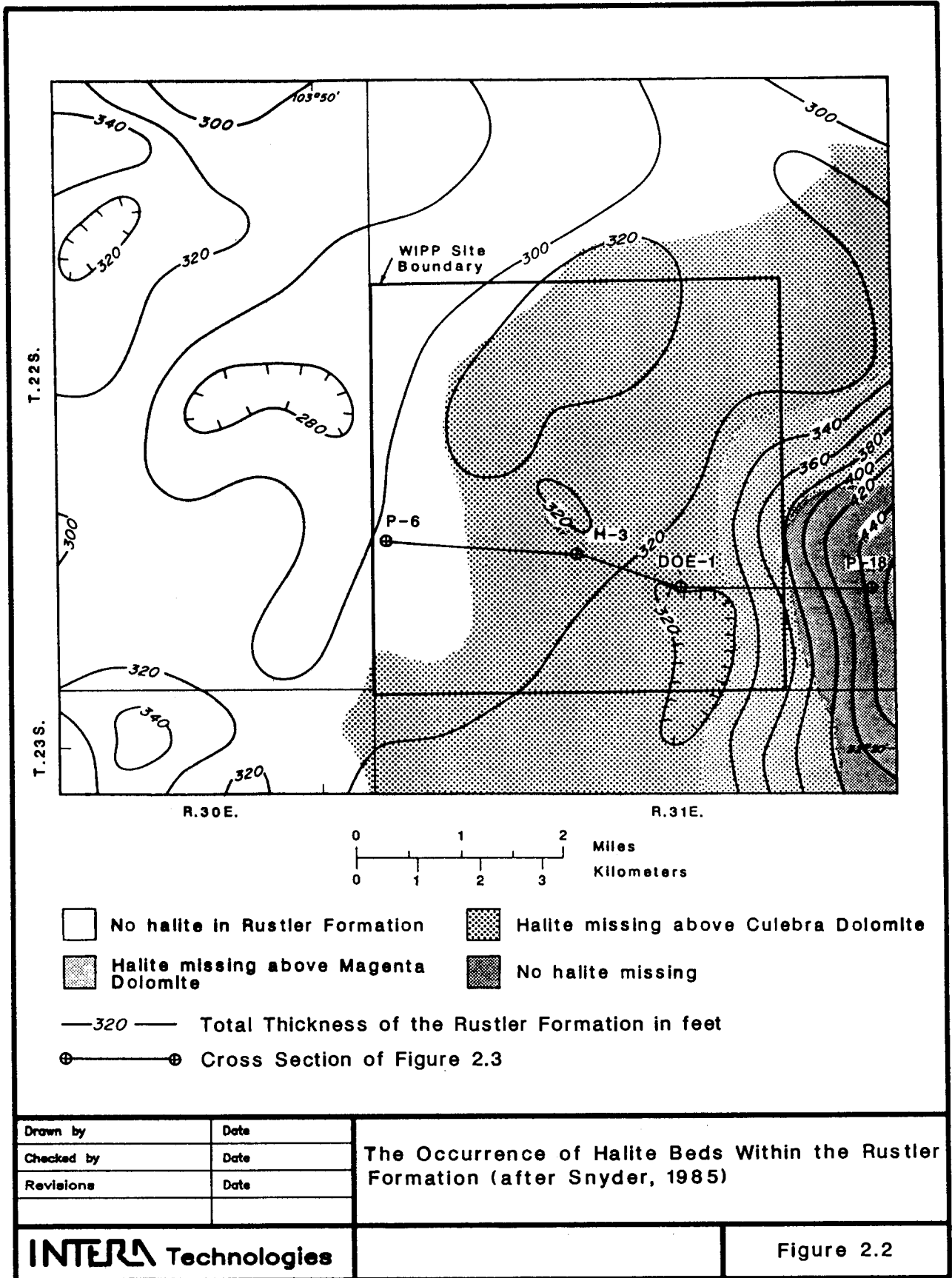
SYSTEM	SERIES	GROUP	FORMATION	MEMBER
RECENT	RECENT		SURFICIAL DEPOSITS	
QUATERNARY	PLEISTOCENE		MESCALERO CALICHE	
			GATUÑA	
TRIASSIC		DOCKUM	UNDIVIDED	
PERMIAN	OCHOAN		DEWEY LAKE RED BEDS	
			RUSTLER	Forty-niner
				Magenta
				Tamarisk
				Culebra
			Unnamed	
	SALADO	Upper		
		McNutt		
		Lower		
	CASTILE			
		GUADALUPIAN	DELAWARE MOUNTAIN	BELL CANYON
CHERRY CANYON				
BRUSHY CANYON				

Drawn by	Date
Checked by	Date
Revisions	Date

Geologic Column Representative of WIPP Area  
(after Powers et al., 1978)

**INTERA** Technologies

Figure 2.1



Drawn by	Date
Checked by	Date
Revisions	Date

The Occurrence of Halite Beds Within the Rustler Formation (after Snyder, 1985)

**INTERA Technologies**

Figure 2.2

WEST

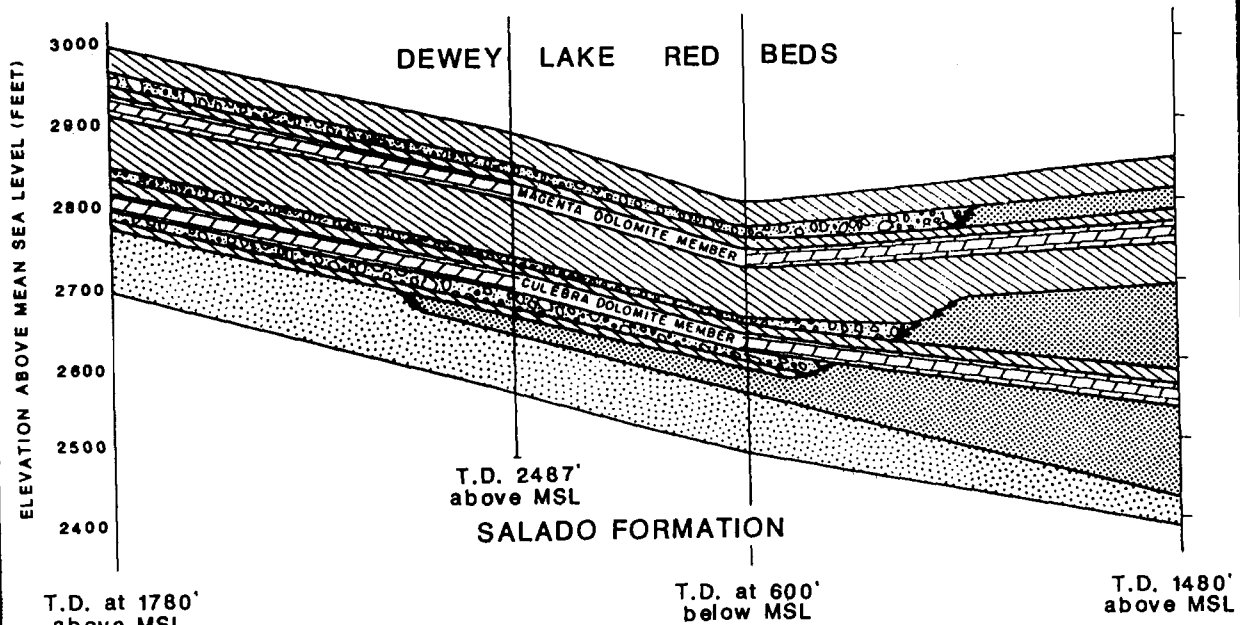
EAST

P-6  
(G.L.-3353.5')

H-3  
(G.L.-3389')

DOE-1  
(G.L.-3465')

P-18  
(G.L.-3479')



0 3000 feet  
 0 900 meters

Vertical exaggaration 20x

- Halite
- Anhydrite with gypsum
- Dolomite
- Siltstone
- Breccia and claystone

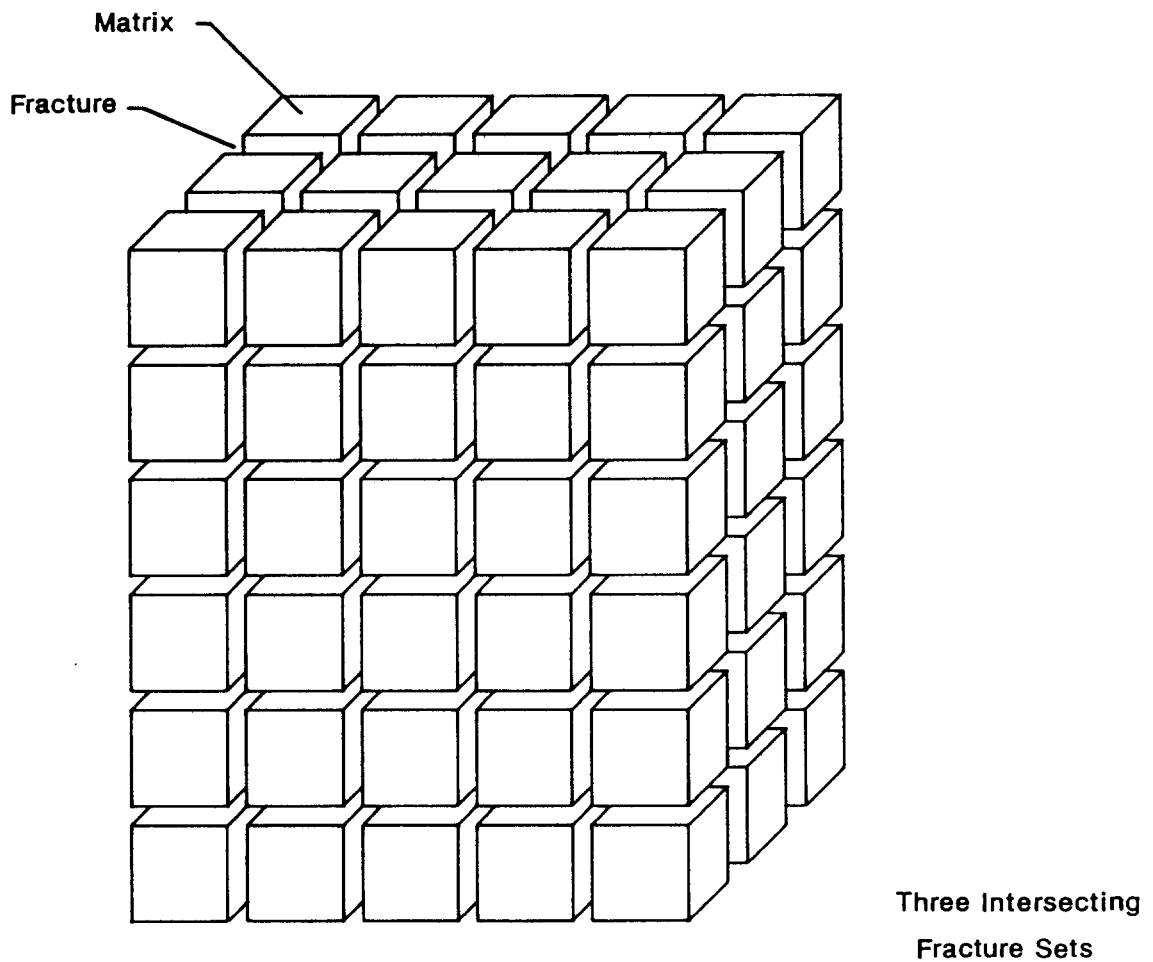
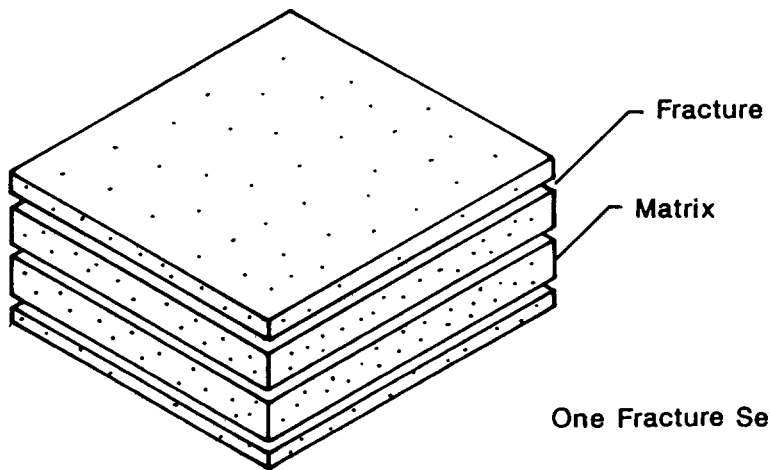
See Figure 2.2 for location of the cross section

Drawn by	Date
Checked by	Date
Revisions	Date

Stratigraphic Cross-Section of the Rustler Formation West to East Across the WIPP Site (after Chaturvedi and Channell, 1985)

**INTERA** Technologies

Figure 2.3



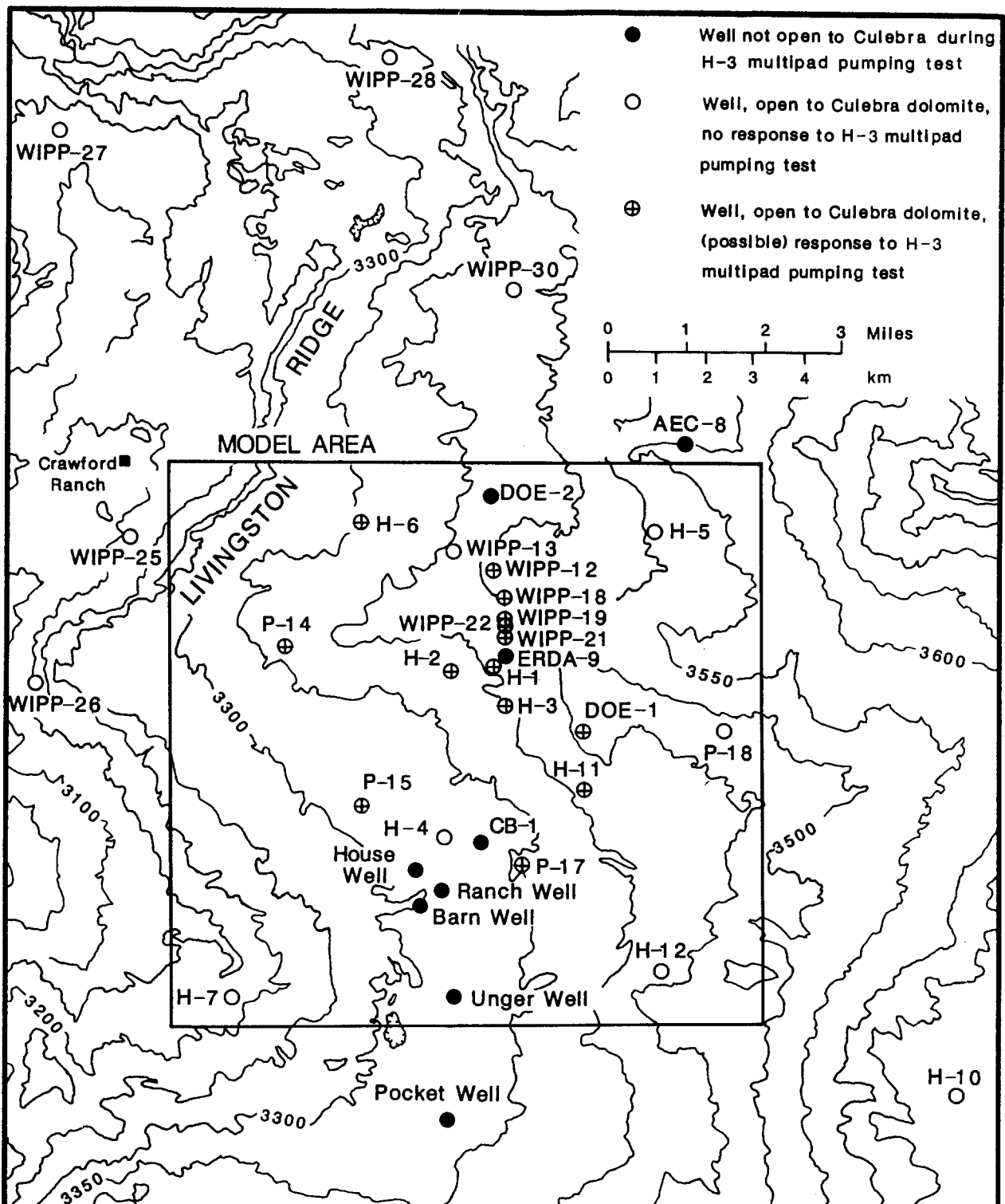
Drawn by	Date
Checked by	Date
Revisions	Date

**Idealization of Fracture Sets  
(after Reeves et al., 1985)**

**INTERA Technologies**

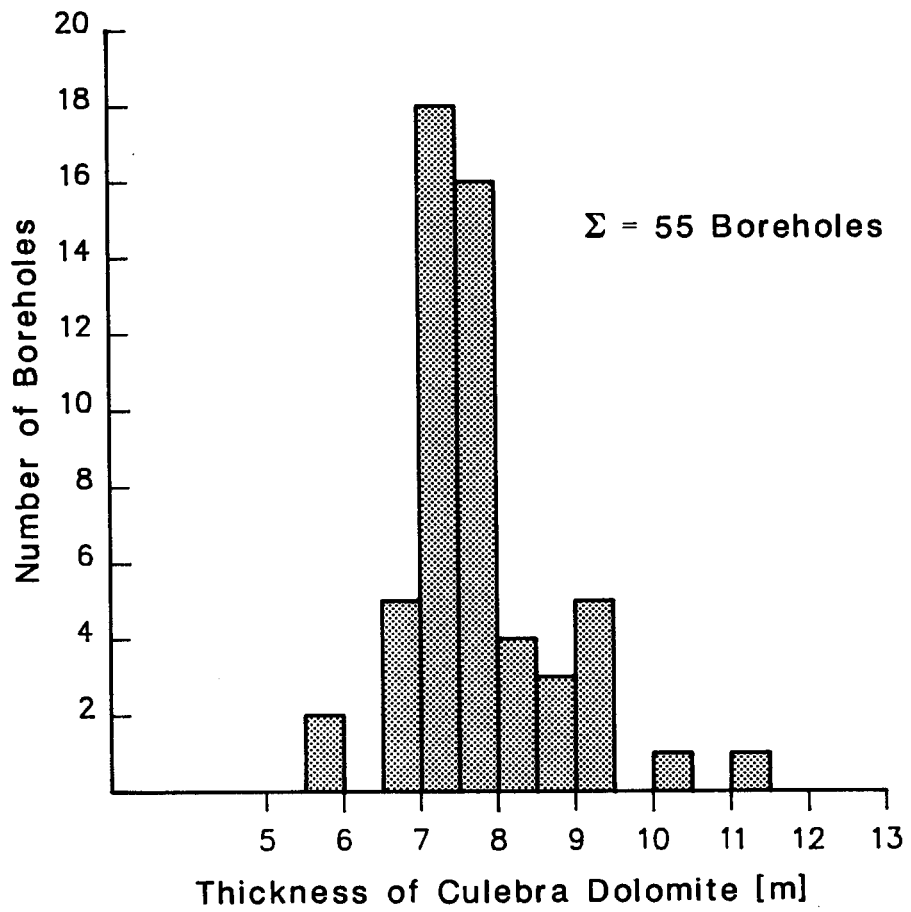
Figure 3.1





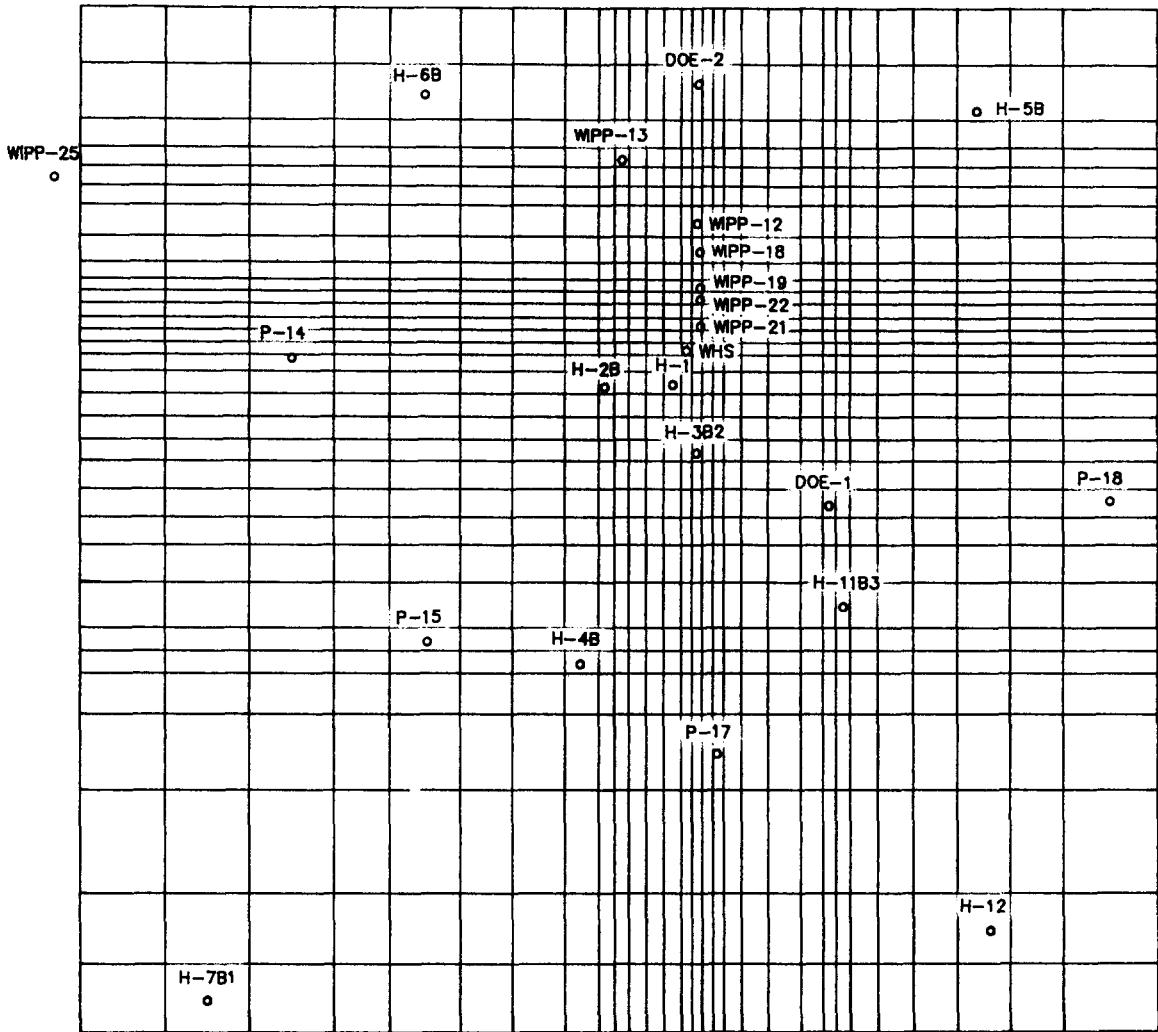
Drawn by	Date
Checked by	Date
Revisions	Date

**Borehole Locations and Model Area**

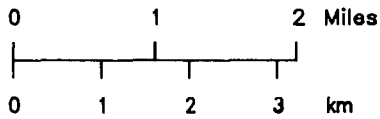


Drawn by	Date	Thickness Distribution of the Culebra Dolomite.
Checked by	Date	
Revisions	Date	
<b>INTERA Technologies</b>		Figure 3.3

MODEL GRID 1.2



○ Observation Well



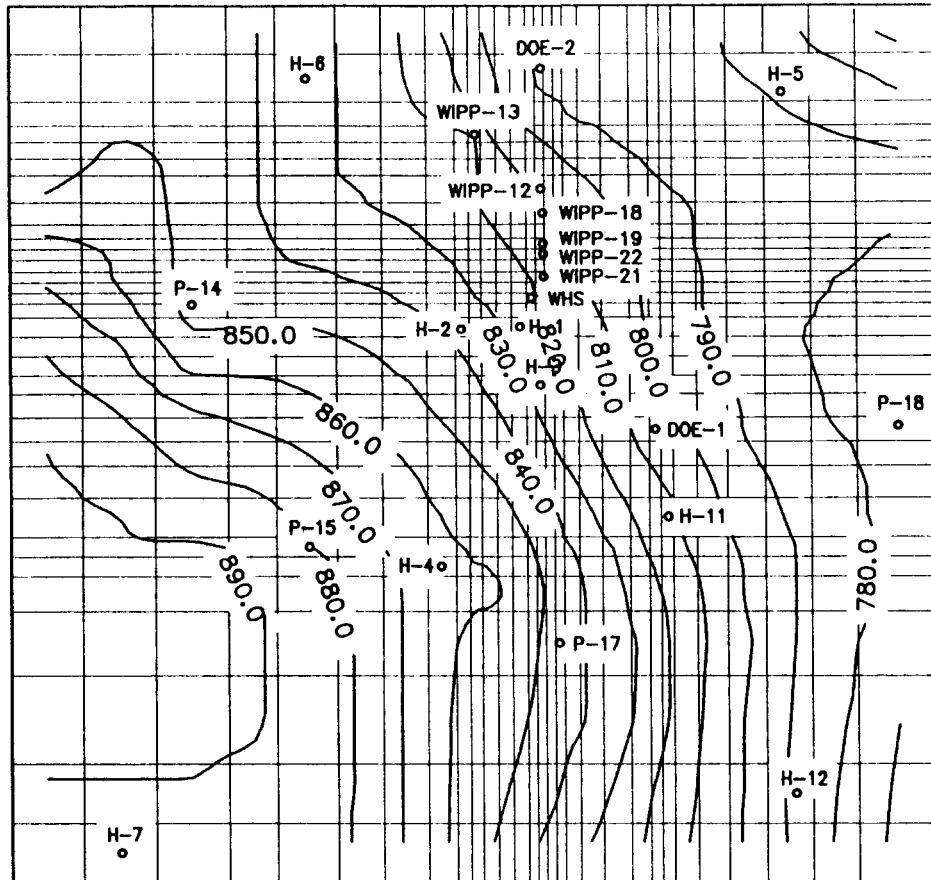
Drawn by	Date
Checked by	Date
Revisions	Date

Model Grid and Borehole Locations

**INTERA** Technologies

Figure 3.4

MODEL AREA



o Observation Well

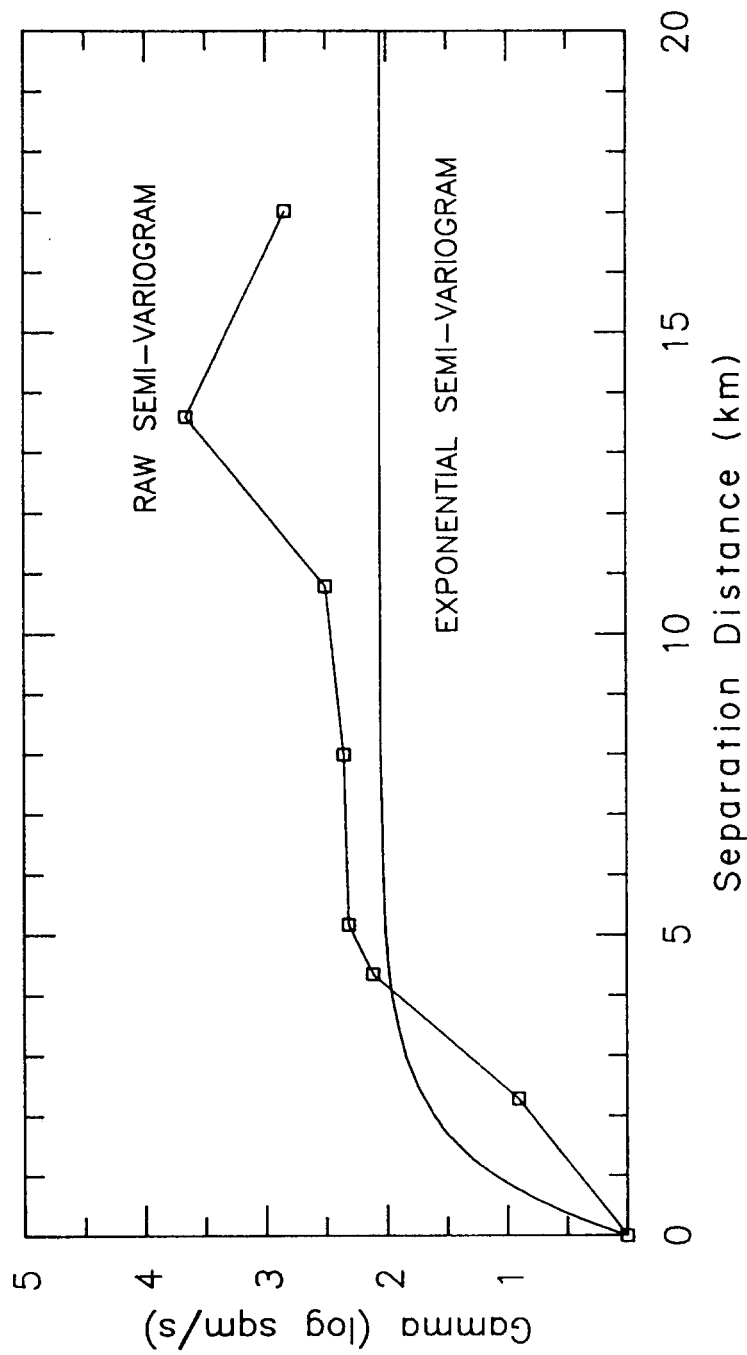
Elevations in m a.s.l.  
 Contour Scale: Linear  
 Contour Interval: 10 m

Drawn by	Date
Checked by	Date
Revisions	Date

Grid-Block Center Elevations  
 (Middle Culebra Dolomite Elevations)

**INTERA** Technologies

Figure 3.5



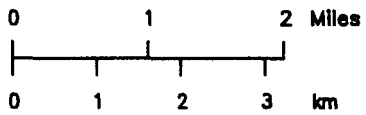
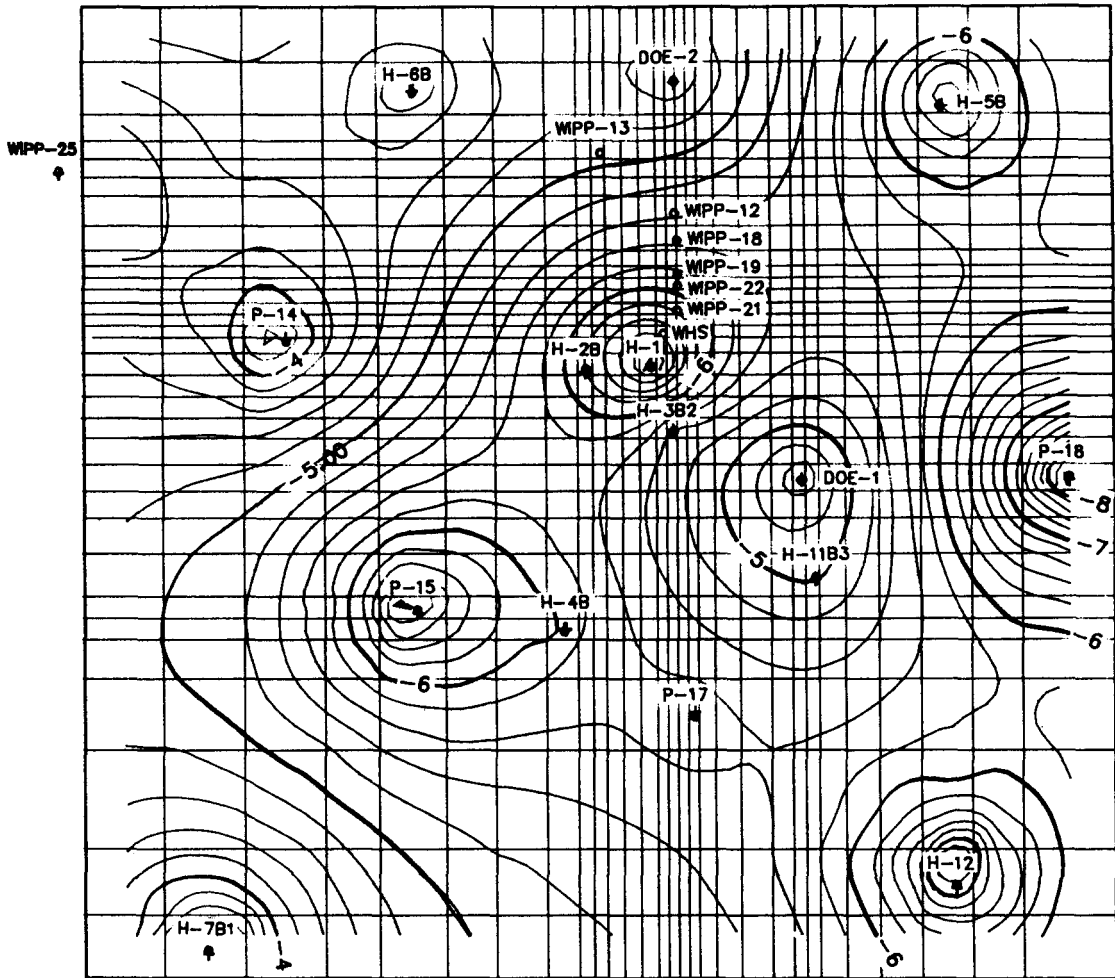
Drawn by	Date
Checked by	Date
Revisions	Date

Raw and Theoretical Semi-Variograms  
of the Culebra Transmissivities

**INTERA** Technologies

Figure 3.6

MODEL GRID 1.2



○ Observation Well  
 + Data Point  
 Transmissivities in  $m^2/s$   
 Contour Scale: Logarithmic  
 Contour Interval:  $0.2 \log m^2/s$

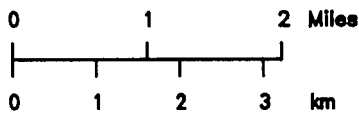
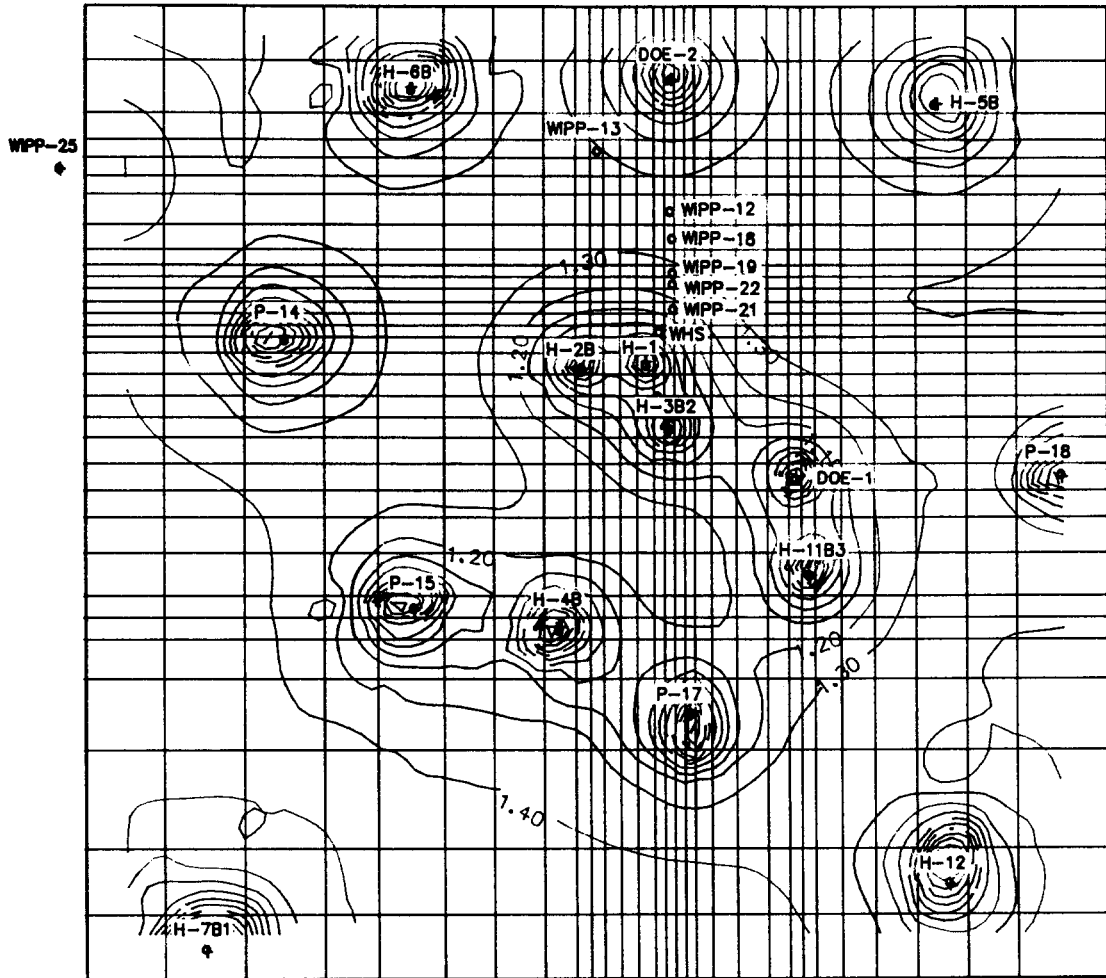
Drawn by	Date
Checked by	Date
Revisions	Date

Kriged Initial Transmissivities of the Culebra Dolomite

**INTERA** Technologies

Figure 3.7

MODEL GRID 1.2



○ Observation Well

+ Data Point

Contour Scale: Logarithmic

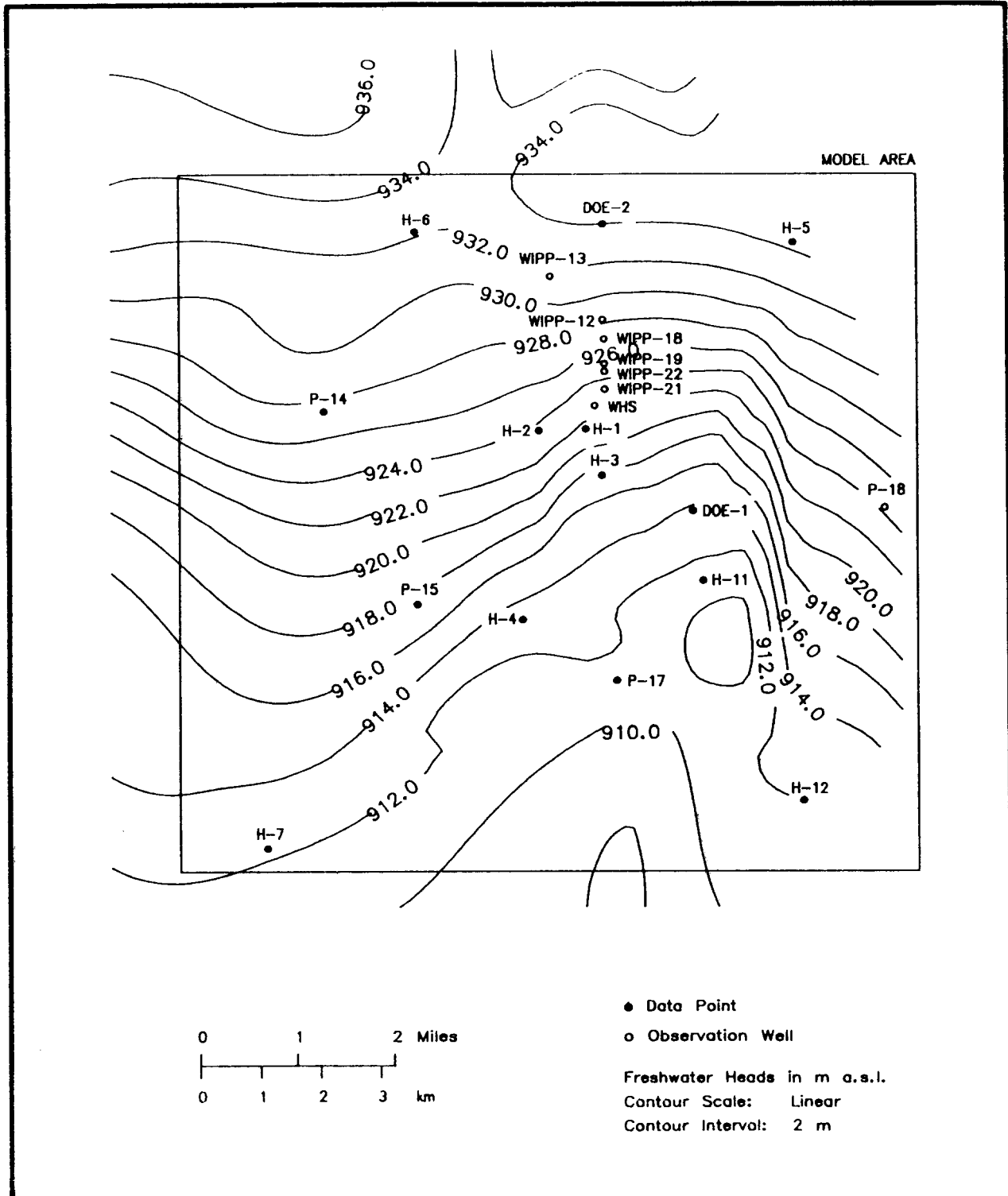
Contour Interval: 0.1 log m<sup>2</sup>/s

Drawn by	Date
Checked by	Date
Revisions	Date

Estimation Error of the Initial Transmissivities

**INTERA** Technologies

Figure 3.8



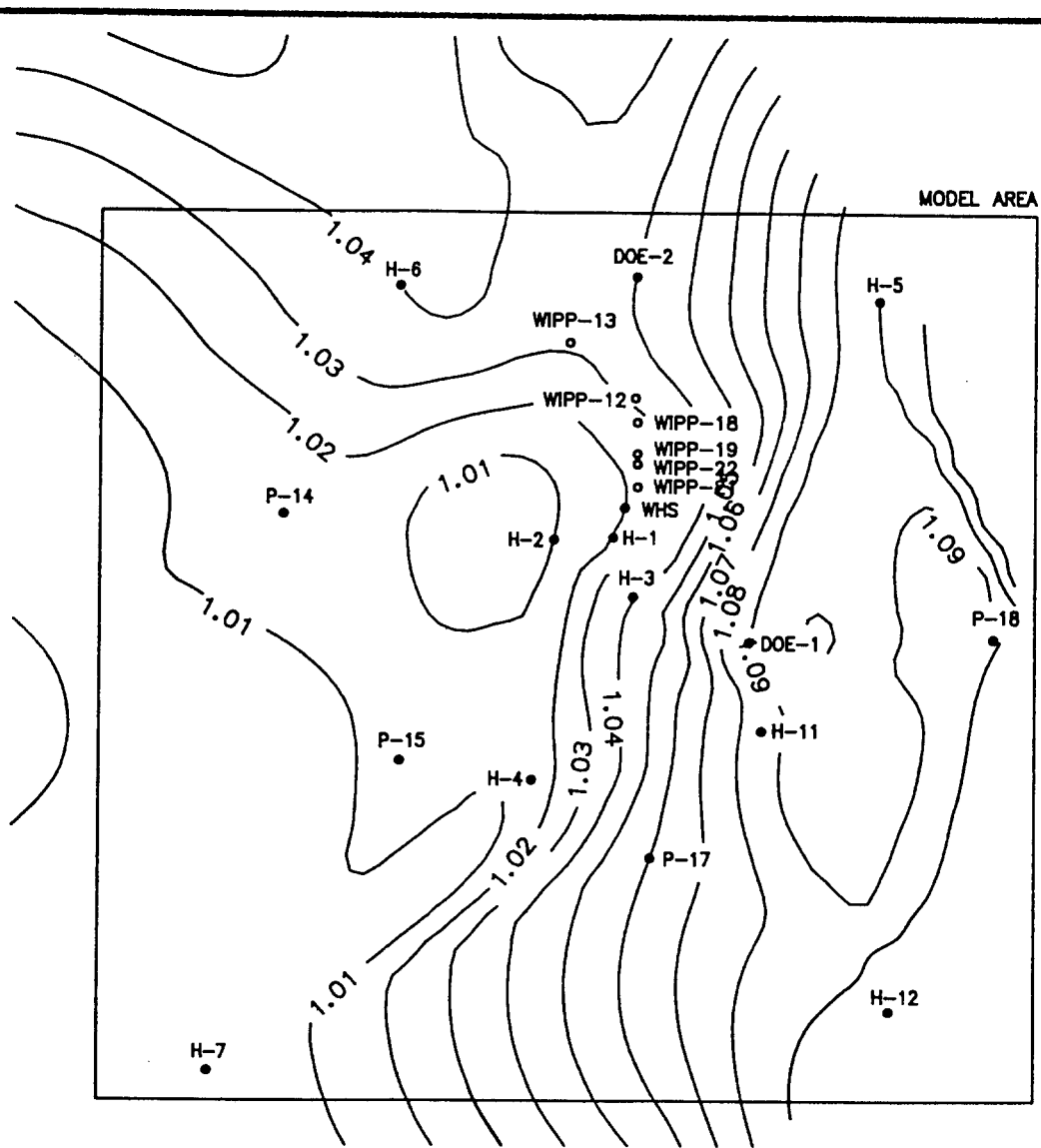
Drawn by	Date
Checked by	Date
Revisions	Date

**Best Estimate of the Undisturbed  
Freshwater Heads in the Culebra Dolomite**

**INTERA Technologies**

Figure 3.9





- Data Point
- Observation Well

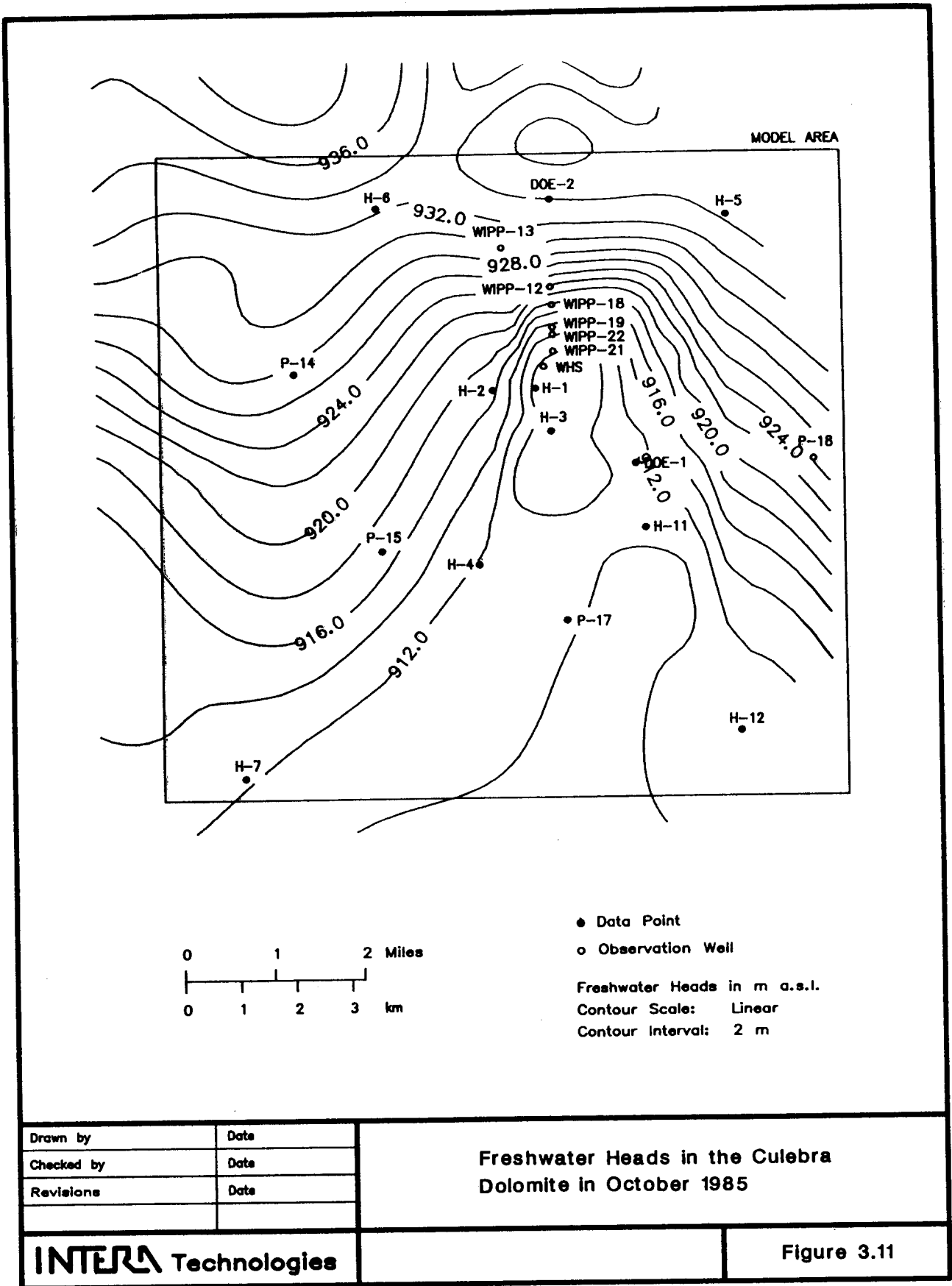
Formation-Water Densities in g/ccm  
 Contour Scale: Linear  
 Contour Interval: 0.01 g/ccm

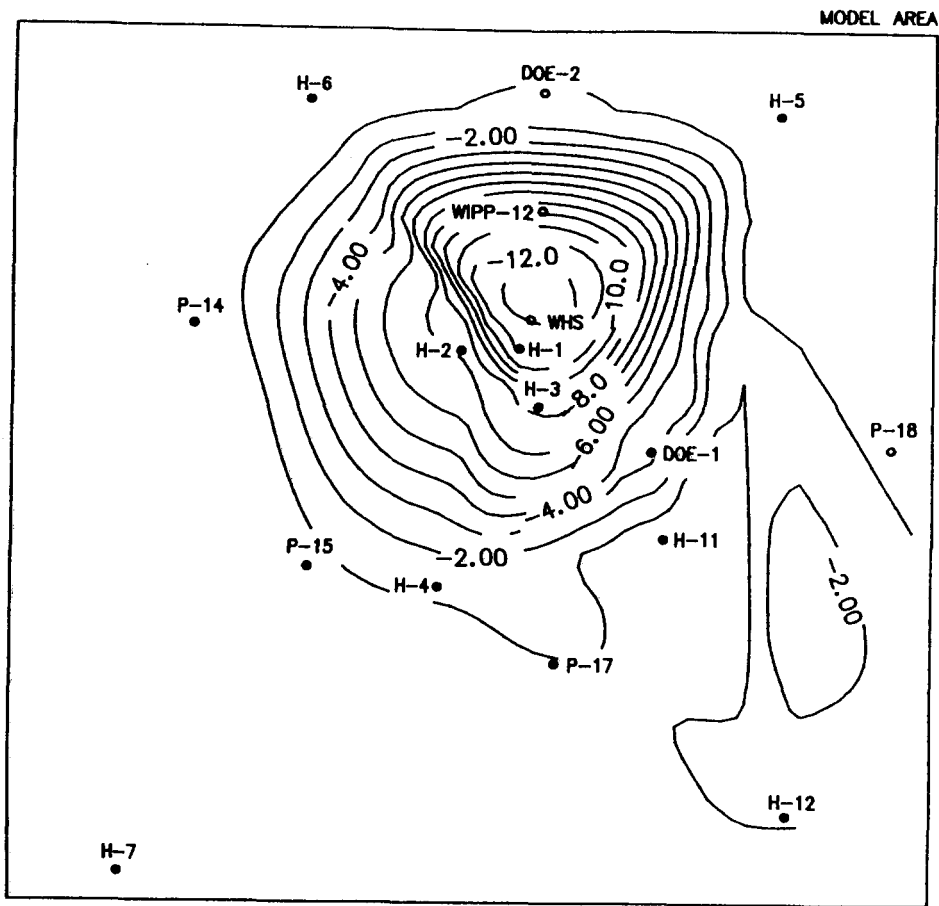
Drawn by	Date
Checked by	Date
Revisions	Date

**Observed Formation-Water Densities  
 in the Culebra Dolomite**

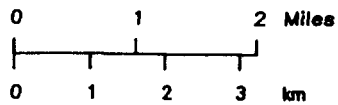
**INTERA Technologies**

**Figure 3.10**





The Contour Lines Indicate the Difference Between the Undisturbed Freshwater Heads (1980) and the Freshwater Heads Observed in October 1985.



- Data Point
- Observation Well

Freshwater-Head Differences in m  
 Contour Scale: Linear  
 Contour Interval: 1 m

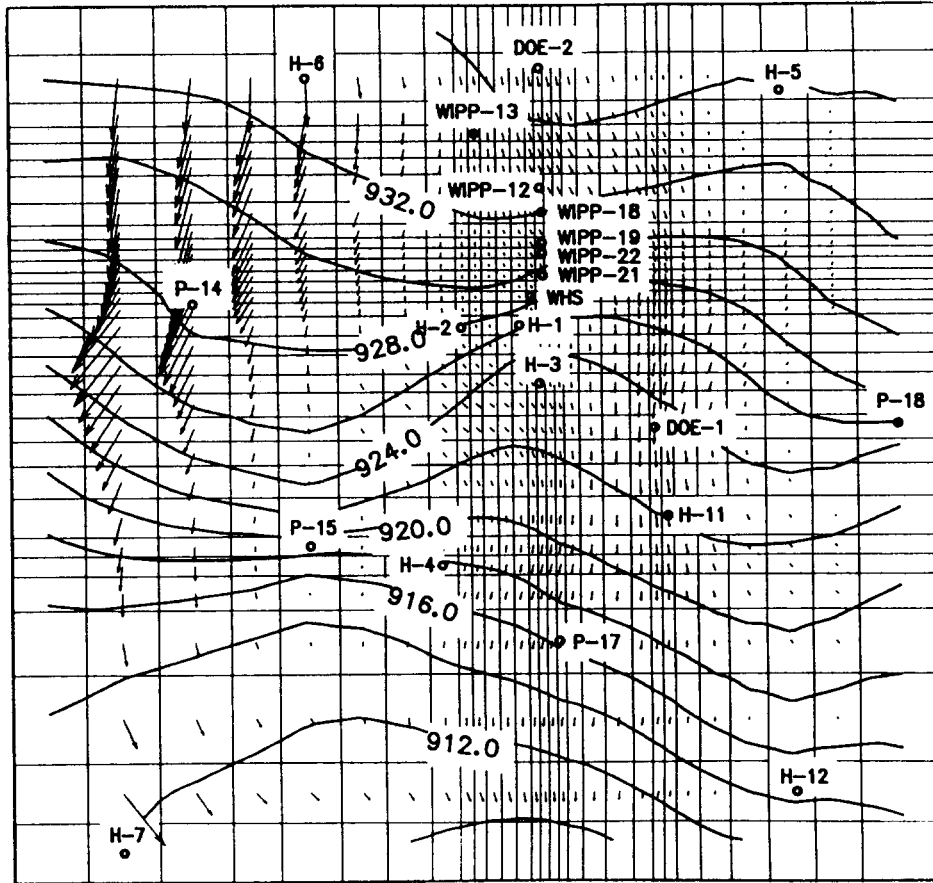
Drawn by	Date
Checked by	Date
Revisions	Date

**Effect of Shaft Leakage and Other Well Test Activities on the Freshwater Heads in the Culebra Dolomite in October 1985**

**INTERA Technologies**

Figure 3.12

MODEL AREA



→ Darcy Velocity Vector:  $1.E-8$  m/s  
(Linear Scale)



o Observation Well

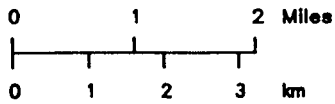
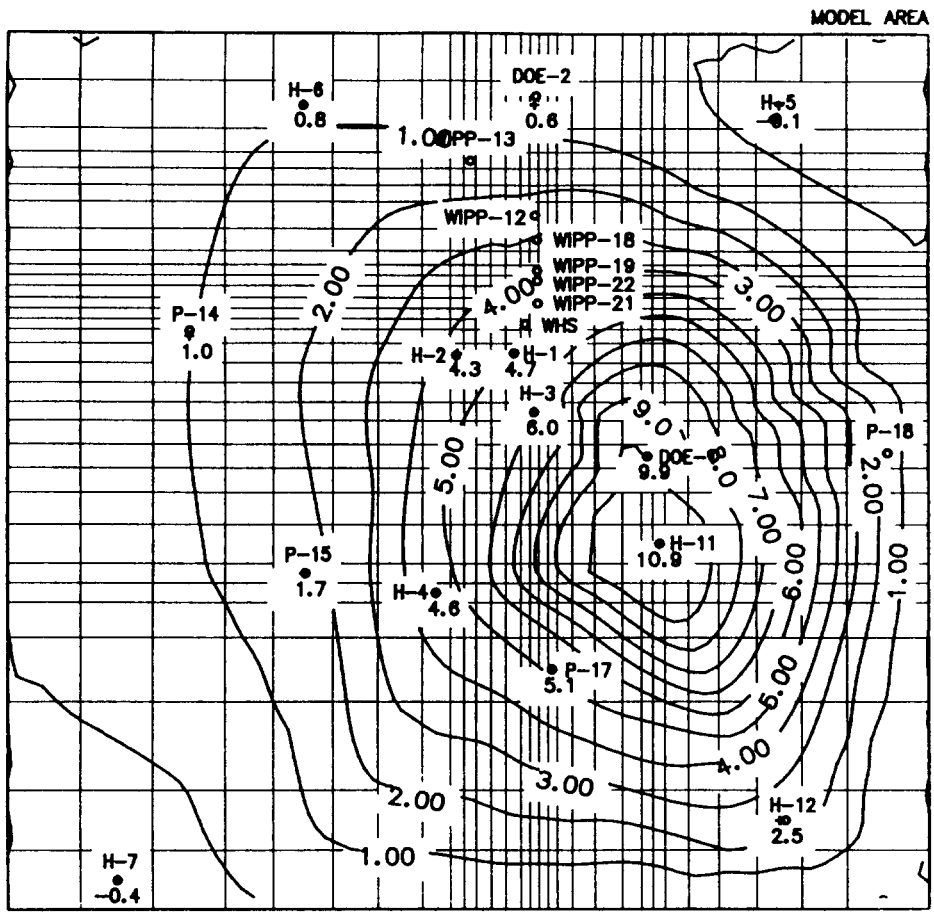
Freshwater Heads in m a.s.l.

Contour Scale: Linear

Contour Interval: 2 m

Drawn by	Date
Checked by	Date
Revisions	Date

The Calculated Freshwater Heads  
Using the Initial Transmissivities



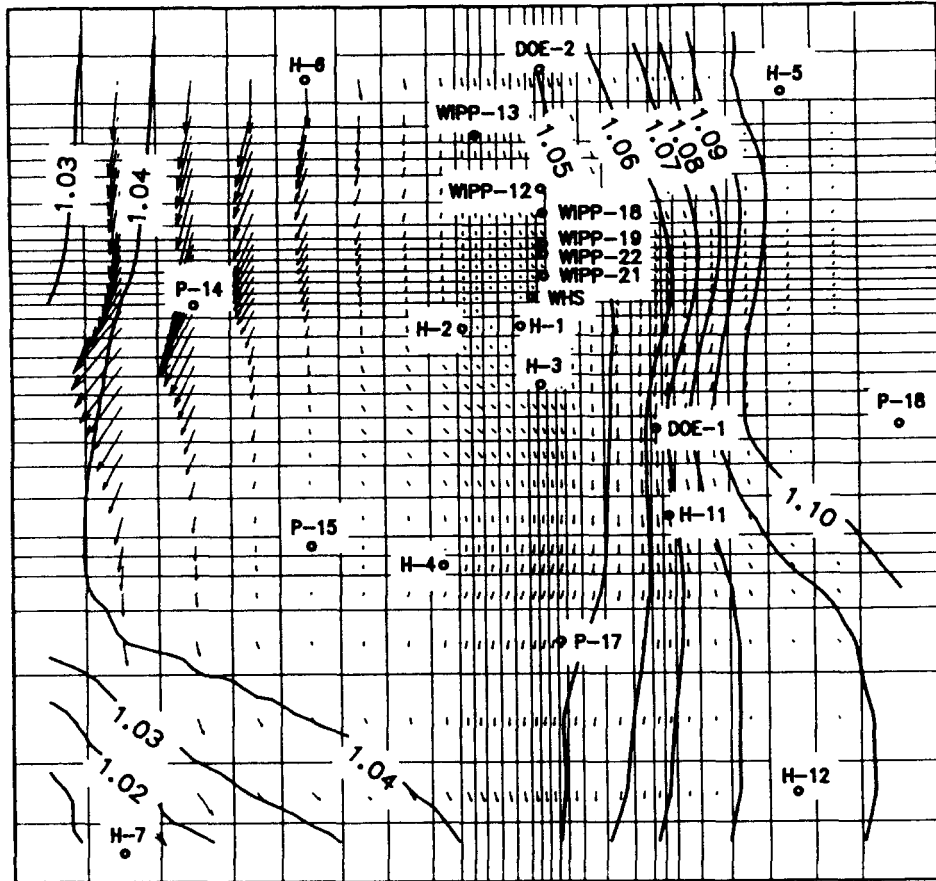
- + Data Point
- o Observation Well

Freshwater—Head Differences in m  
 Contour Scale: Linear  
 Contour Interval: 1.0 m

Drawn by	Date
Checked by	Date
Revisions	Date

The Difference Between the Calculated  
 and the Measured Freshwater Heads  
 Using the Initial Transmissivities

MODEL AREA



→ Darcy Velocity Vector:  $1.E-8$  m/s  
(Linear Scale)



o Observation Well

Formation-Water Densities in g/ccm

Contour Scale: Linear

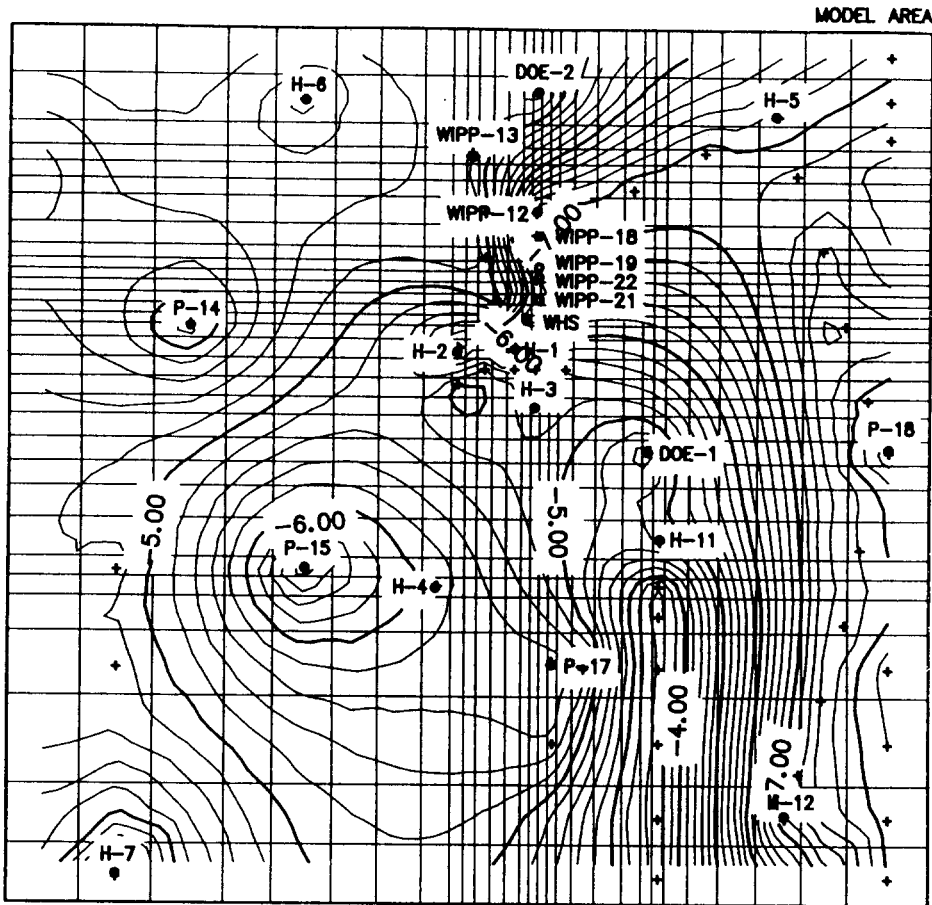
Contour Interval: 0.01 g/ccm

Drawn by	Date
Checked by	Date
Revisions	Date

The Calculated Formation-Water Densities  
Using the Initial Transmissivities

**INTERA** Technologies

Figure 4.3

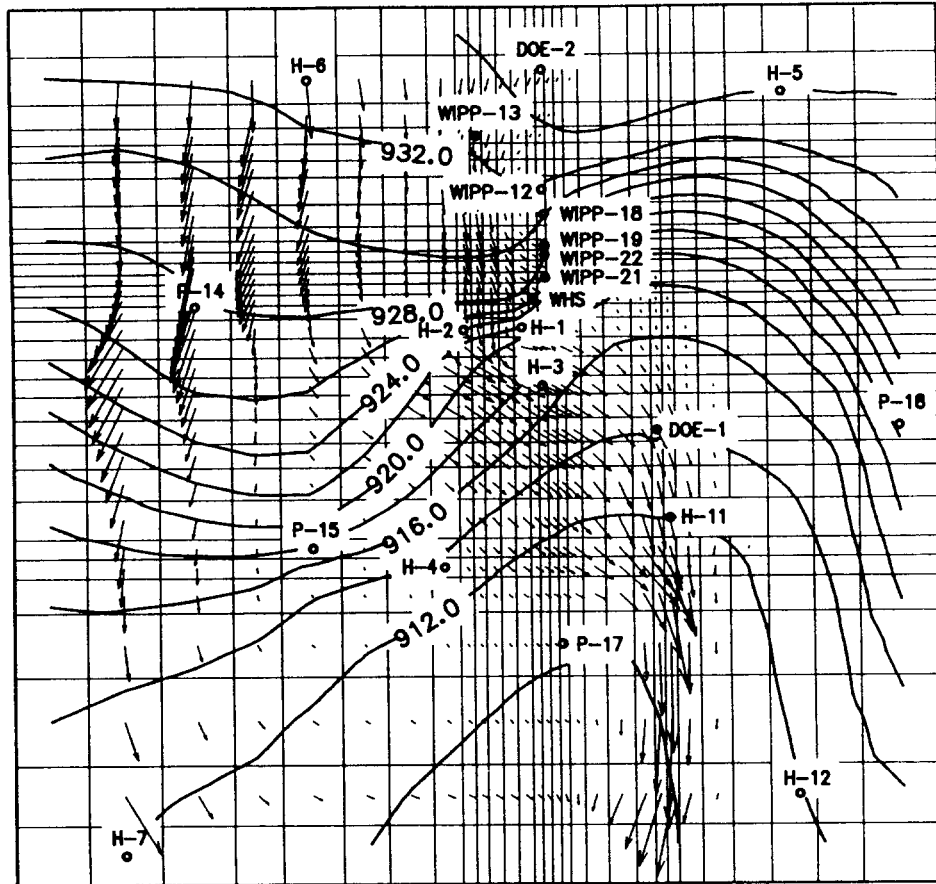


+ Data Point  
 o Observation Well  
 Transmissivities in sqm/s  
 Contour Scale: Logarithmic  
 Contour Interval: 0.2 log sqm/s

Drawn by	Date
Checked by	Date
Revisions	Date

The Pressure-Calibrated Steady-State Transmissivities

MODEL AREA



→ DARCY VELOCITY VECTOR: 1.E-8 m/s  
(Linear Scale)



o Observation Well

Freshwater Heads in m a.s.l.

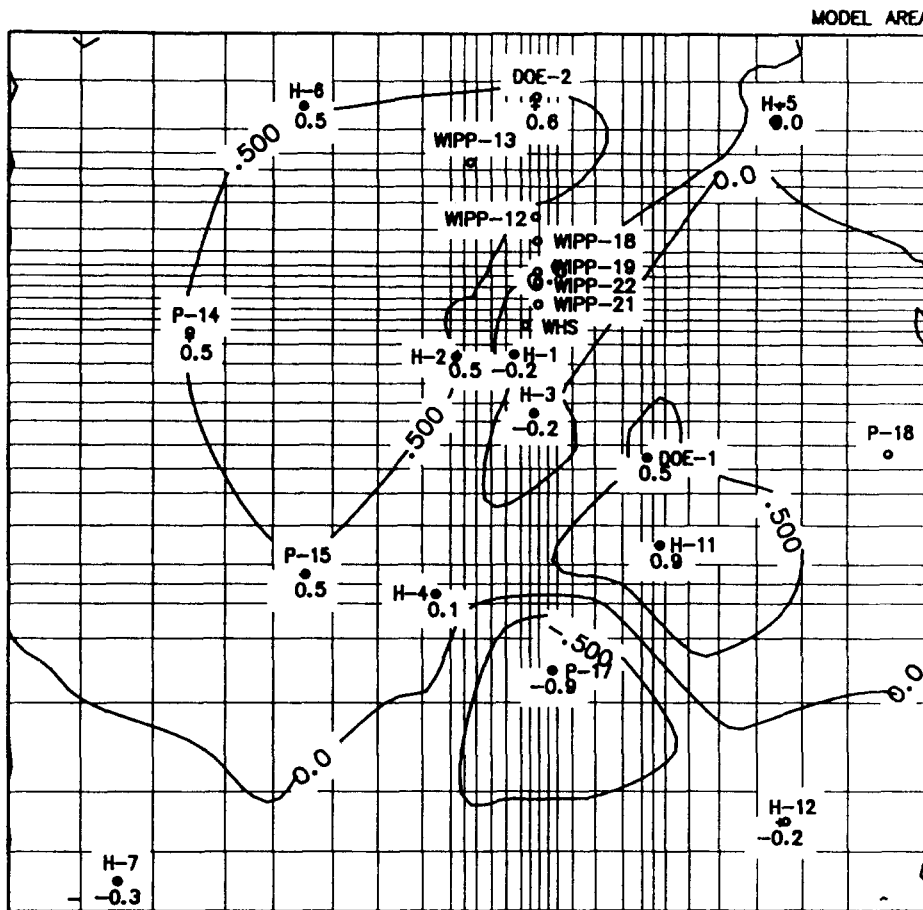
Contour Scale: Linear

Contour Interval: 2 m

Drawn by	Date
Checked by	Date
Revisions	Date

The Calculated Freshwater Heads of the Pressure-Calibrated Steady-State Model





- + Data Point
- o Observation Well

Freshwater—Head Differences in m  
 Contour Scale: Linear  
 Contour Interval: 0.5 m

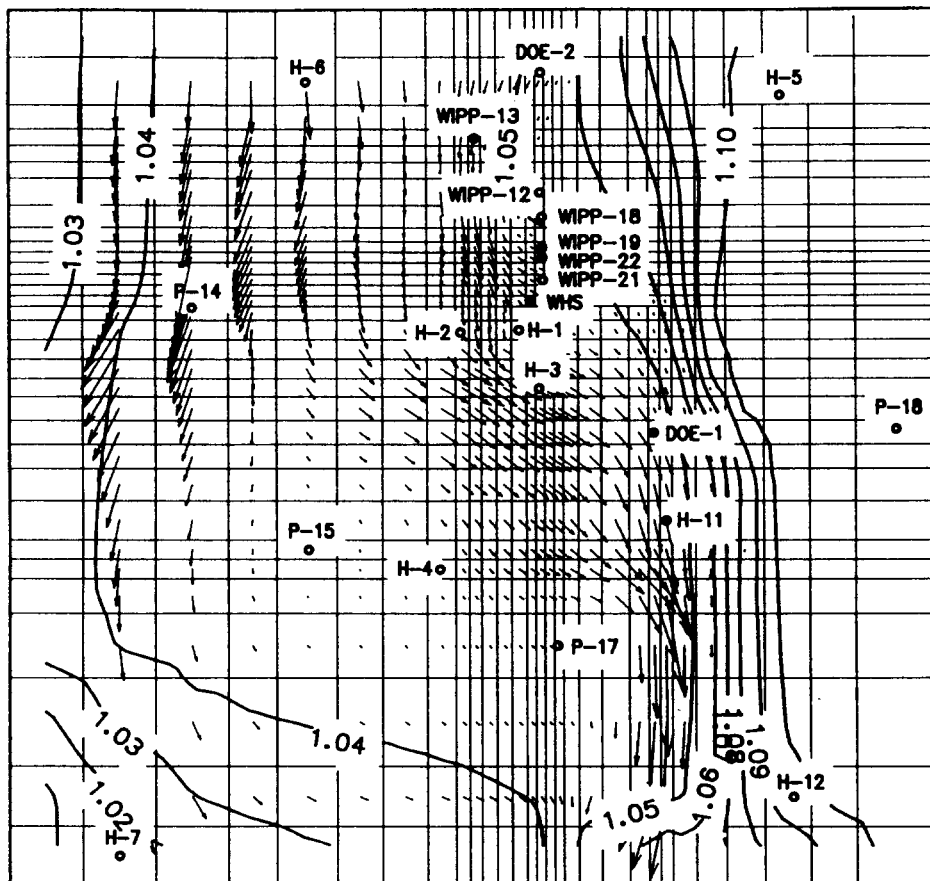
Drawn by	Date
Checked by	Date
Revisions	Date

Pressure-Calibrated Steady-State Model:  
 Difference Between the Calculated and the  
 Measured Freshwater Heads

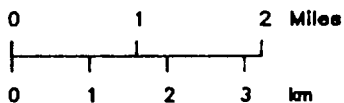
**INTERA** Technologies

Figure 4.6

MODEL AREA



→ Darcy Velocity Vector: 1.E-8 m/s  
(Linear Scale)



o Observation Well

Formation-Water Densities in g/ccm

Contour Scale: Linear

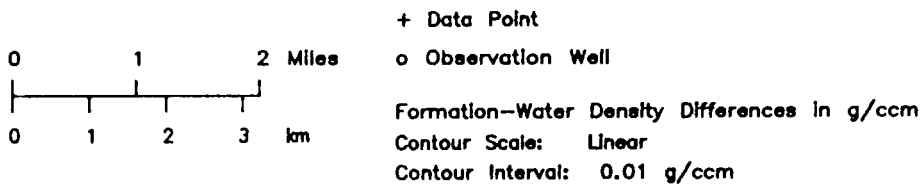
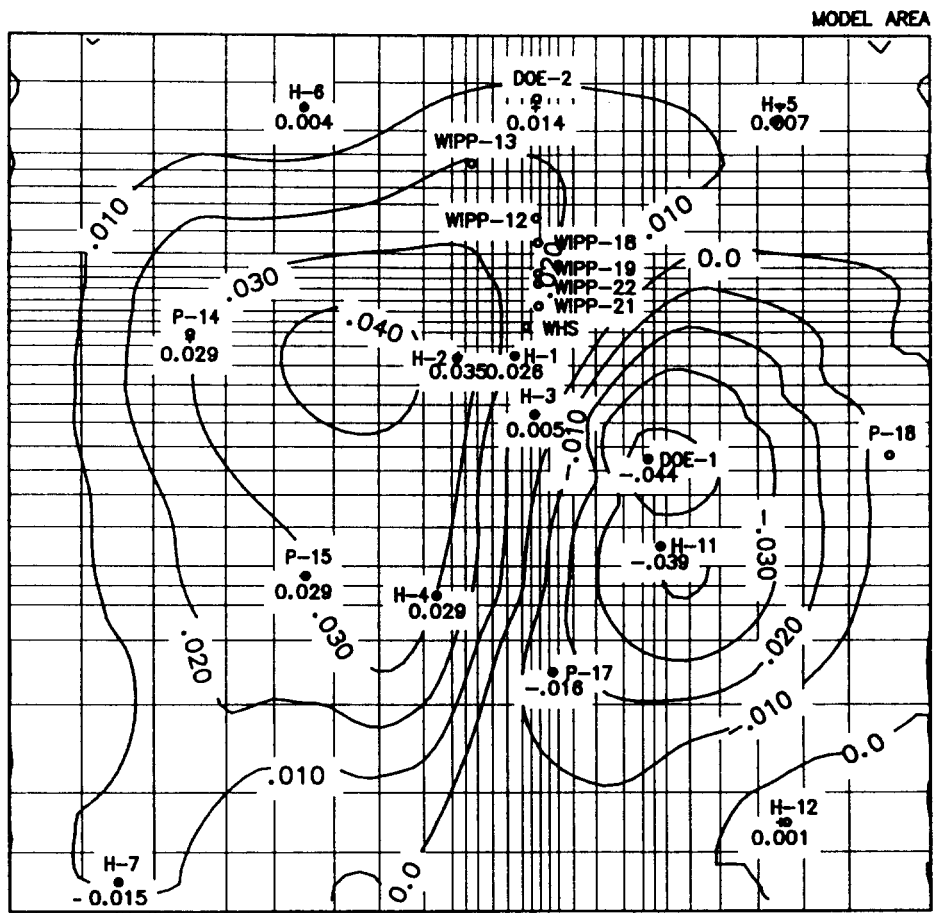
Contour Interval: 0.01 g/ccm

Drawn by	Date
Checked by	Date
Revisions	Date

The Calculated Formation-Water Densities of  
the Pressure-Calibrated Steady-State Model

**INTERA** Technologies

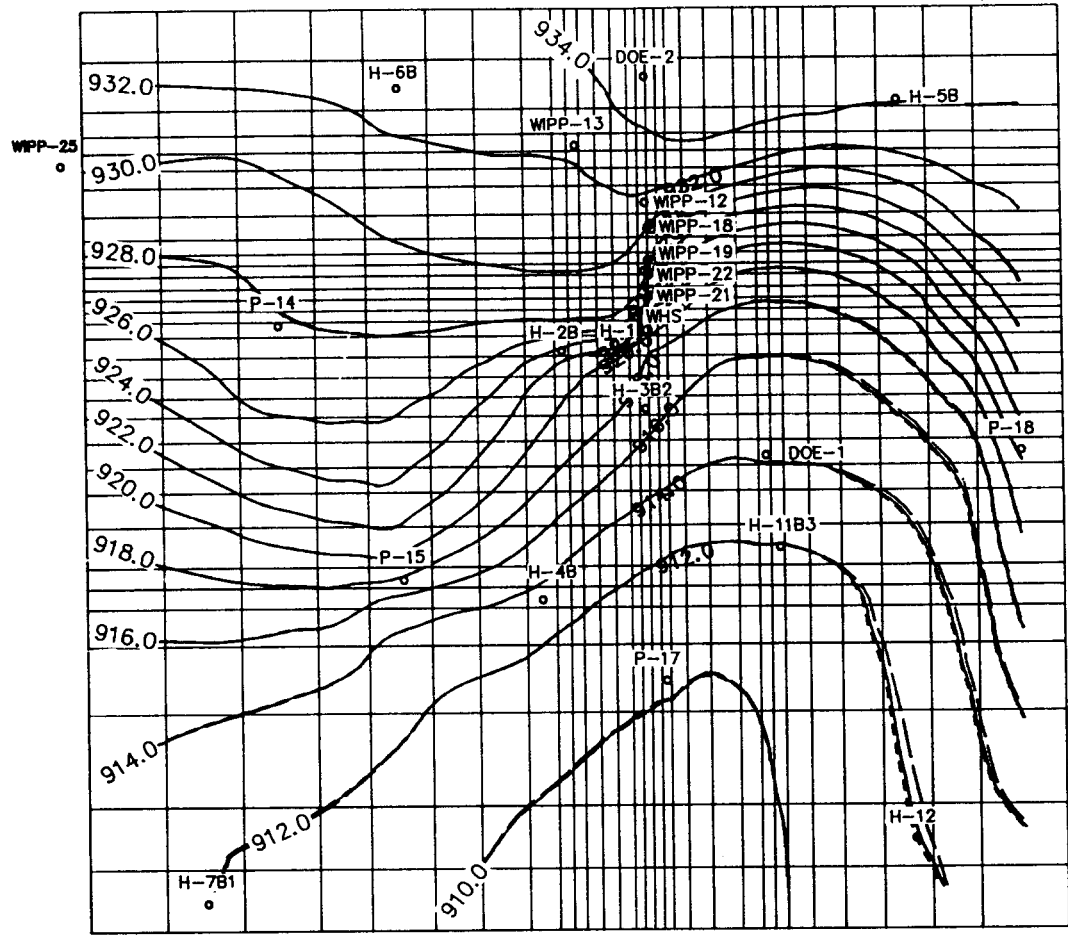
Figure 4.7



Drawn by	Date
Checked by	Date
Revisions	Date

**Pressure-Calibrated Steady-State Model:  
 Difference Between the Calculated and the  
 Measured Formation-Water Densities**

MODEL GR.D 1.2



- Observation Well
- Freshwater Heads in m a.s.l.
- Contour Scale: Linear
- Contour Interval: 2m
- - - Long. Dispersivity = 10m
- Long. Dispersivity = 50m
- · - · Long. Dispersivity = 200m

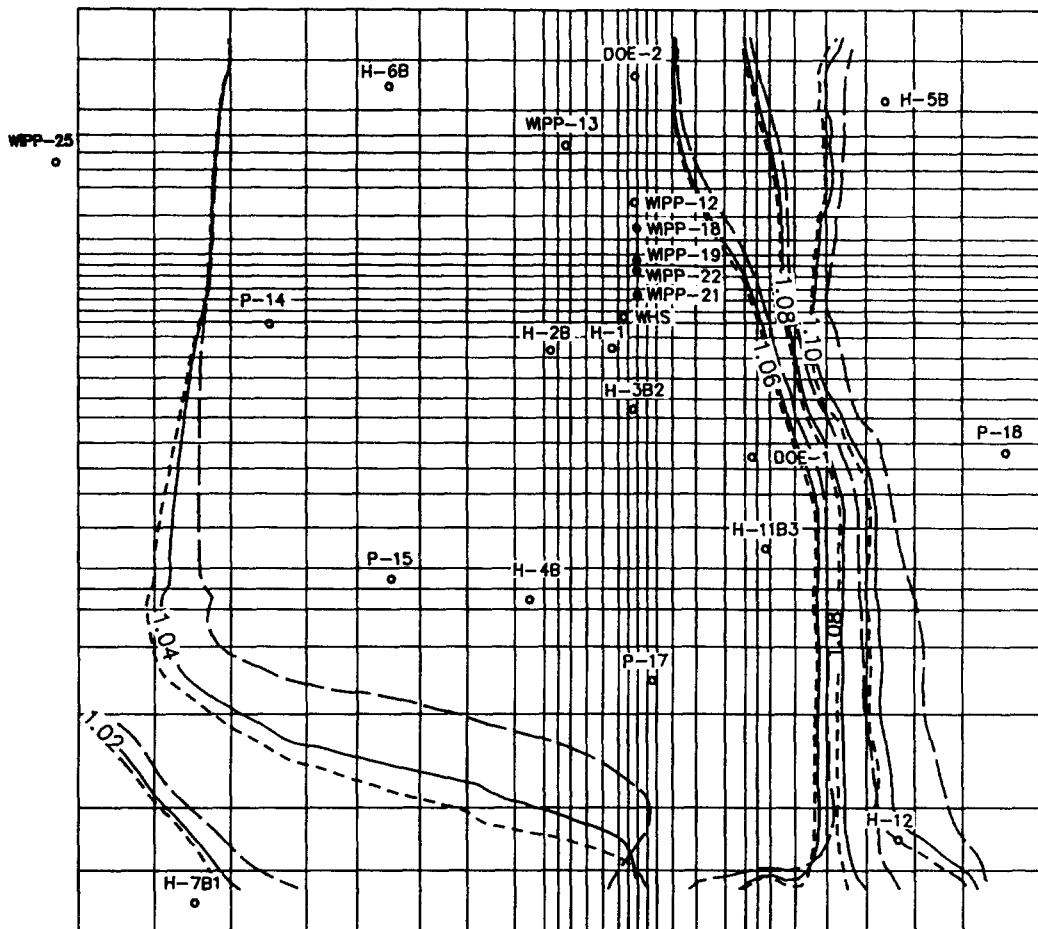
Drawn by	Date
Checked by	Date
Revisions	Date

Sensitivity Analysis for Dispersivity:  
Variation of the Calculated Freshwater Heads

**INTERA** Technologies

Figure 4.9

MODEL GRID 1.2



○ Observation Well

Formation-Water Densities in  $g/cm^3$

Contour Scale: Linear

Contour Interval:  $0.02 g/cm^3$

--- Long. Dispersivity = 10m

— Long. Dispersivity = 50m

- - - Long. Dispersivity = 200m



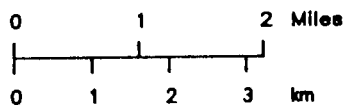
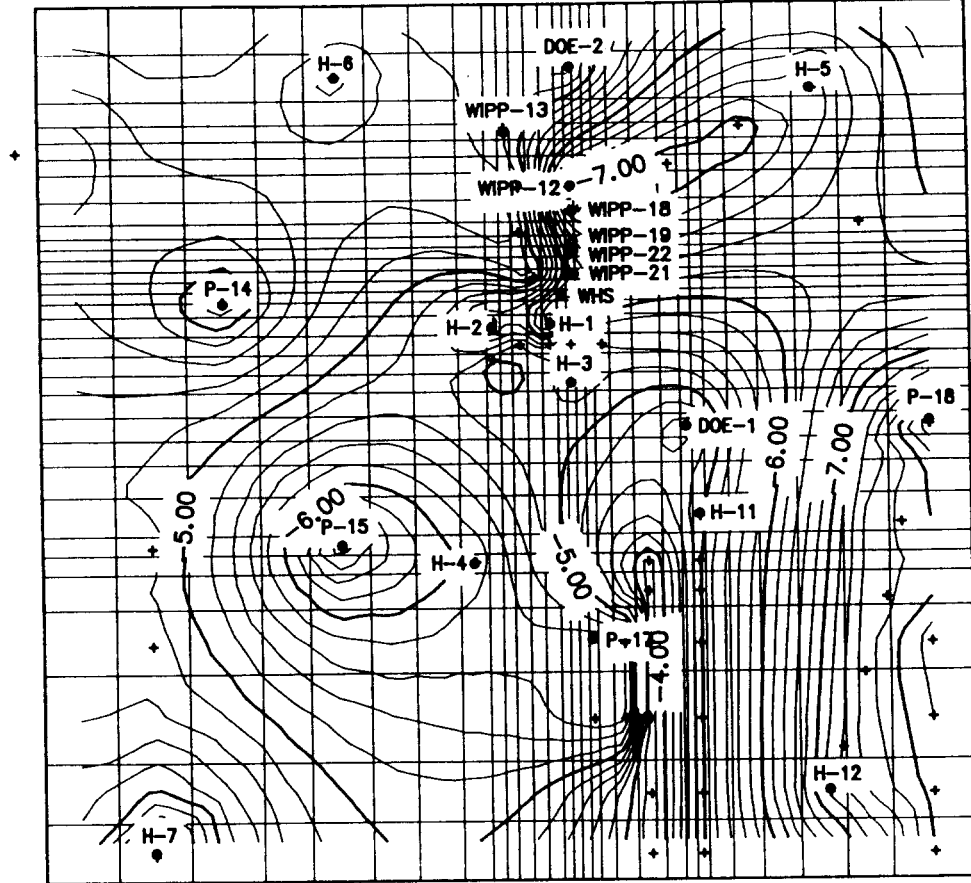
Drawn by	Date
Checked by	Date
Revisions	Date

Sensitivity Analysis for Dispersivity:  
Variation of the Calculated Fluid Densities

**INTERA** Technologies

Figure 4.10

MODEL AREA



+ Data Point  
 o Observation Well  
 Transmissivities in sqm/s  
 Contour Scale: Logarithmic  
 Contour Interval: 0.2 log sqm/s

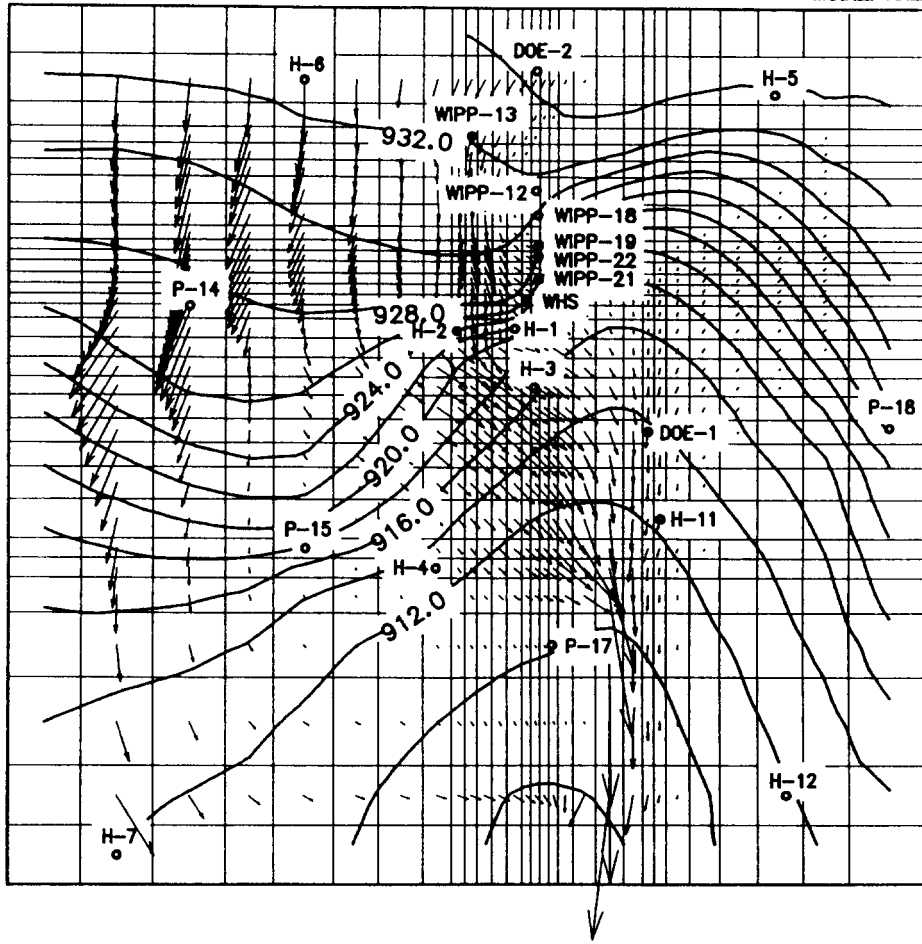
Drawn by	Date
Checked by	Date
Revisions	Date

The Density-Calibrated Steady-State Transmissivities

**INTERA** Technologies

Figure 4.11

MODEL AREA



→ Darcy Velocity Vector:  $1.E-8$  m/s  
(Linear Scale)



o Observation Well

Freshwater Heads in m a.s.l.

Contour Scale: Linear

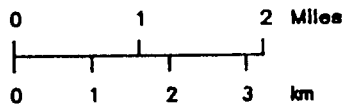
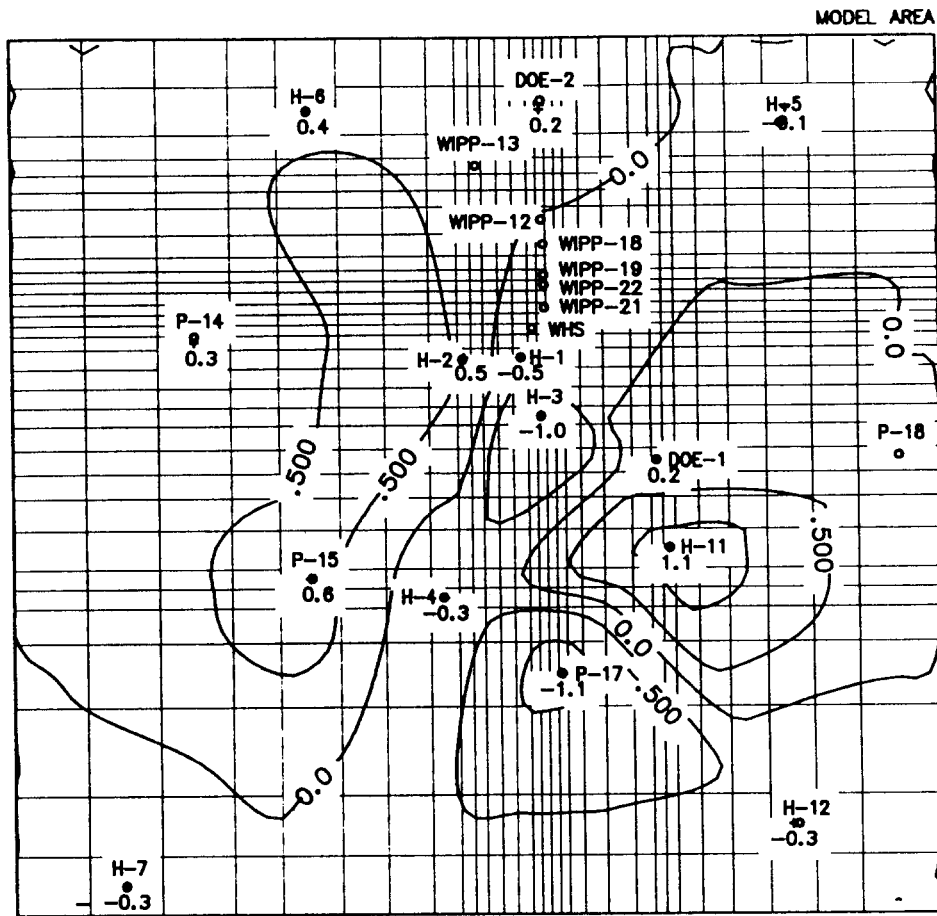
Contour Interval: 2 m

Drawn by	Date
Checked by	Date
Revisions	Date

The Calculated Freshwater Heads of the Density-Calibrated Steady-State Model

**INTERA** Technologies

Figure 4.12



- + Data Point
- o Observation Well

Freshwater-Head Differences in m  
 Contour Scale: Linear  
 Contour Interval: 0.5 m

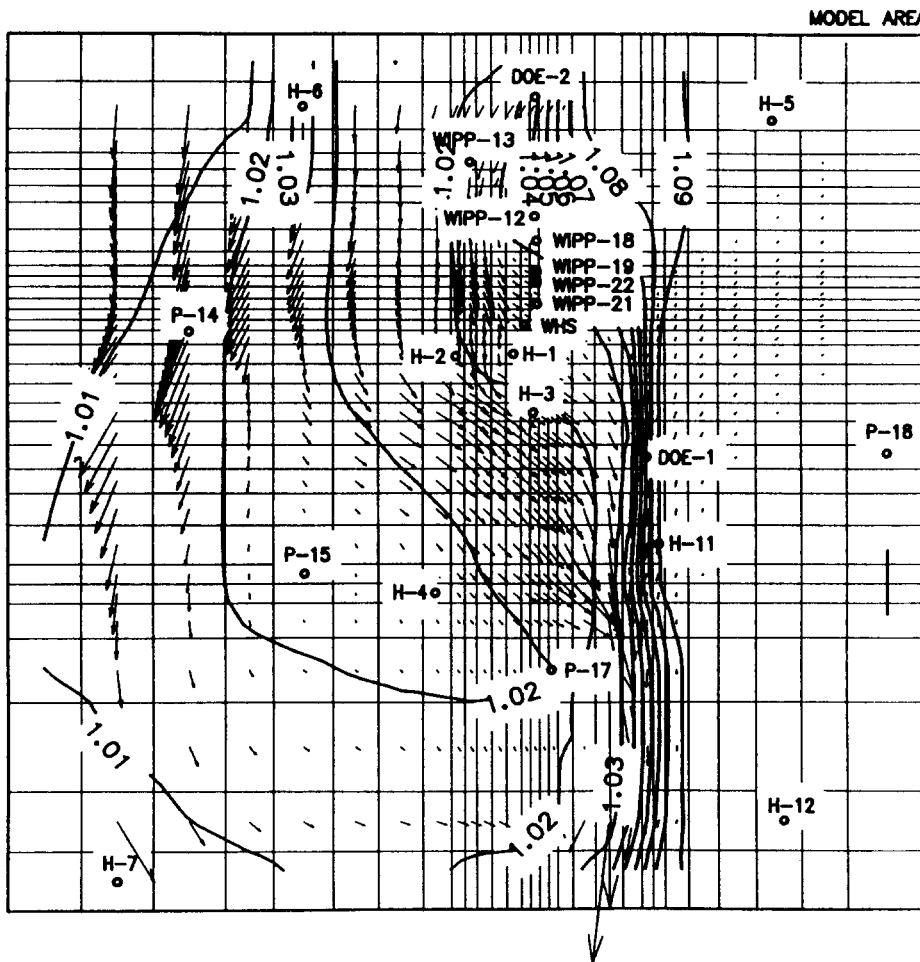
Drawn by	Date
Checked by	Date
Revisions	Date

**Density-Calibrated Steady-State Model:  
 Difference Between the Calculated and the  
 Measured Freshwater Heads**

**INTERA Technologies**

Figure 4.13





→ Darcy Velocity Vector: 1.E-8 m/s  
(Linear Scale)



o Observation Well

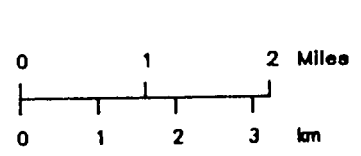
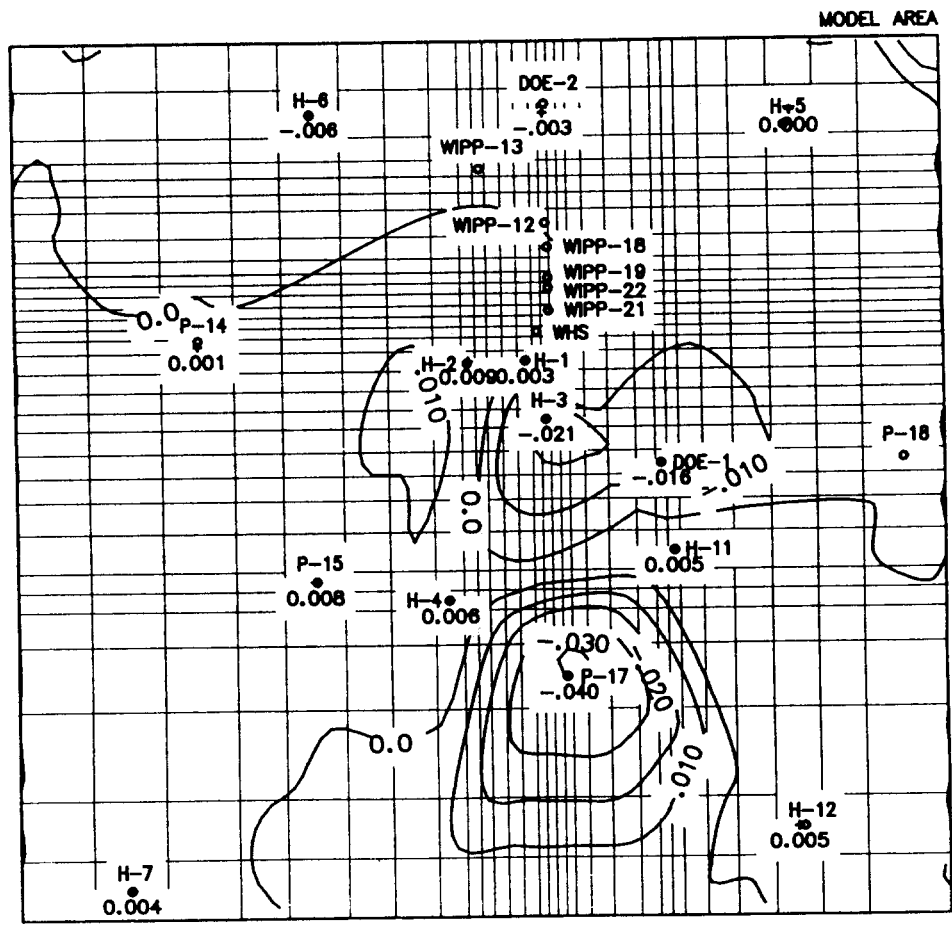
Formation-Water Densities in g/ccm

Contour Scale: Linear

Contour Interval: 0.01 g/ccm

Drawn by	Date
Checked by	Date
Revisions	Date

The Calculated Formation-Water Densities  
of the Density-Calibrated Steady-State Model



+ Data Point  
 o Observation Well  
 Formation-Water Density Differences in g/ccm  
 Contour Scale: Linear  
 Contour Interval: 0.01 g/ccm

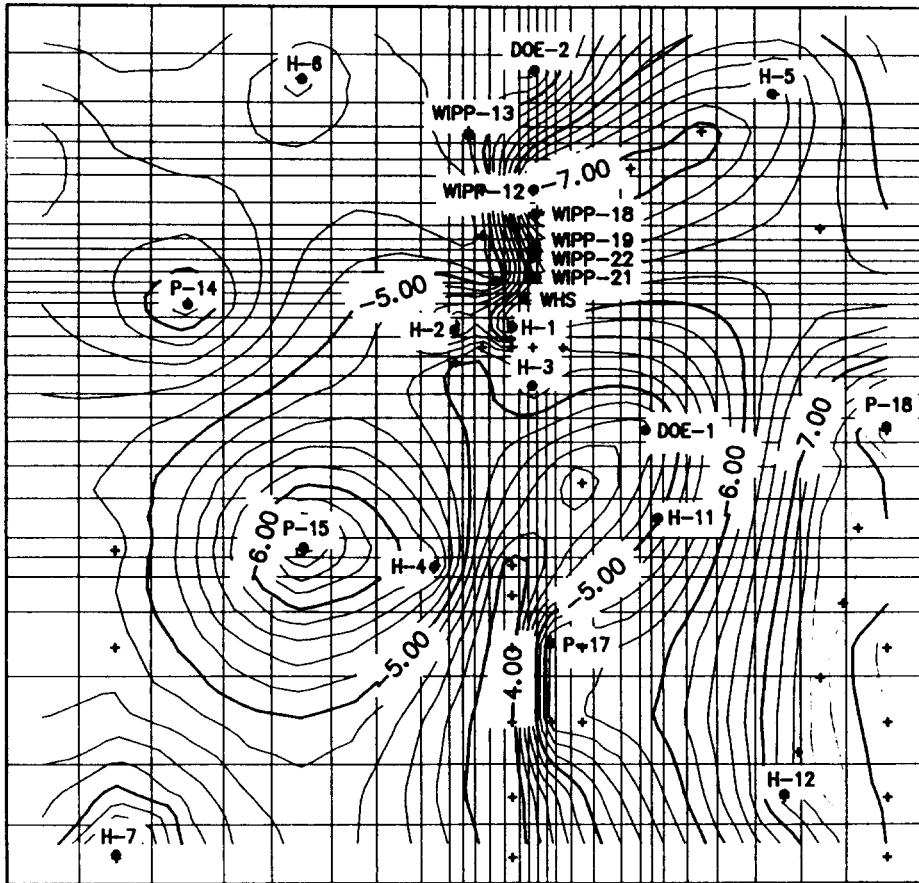
Drawn by	Date
Checked by	Date
Revisions	Date

Density-Calibrated Steady-State Model:  
 Difference Between the Calculated and the  
 Measured Formation-Water Densities

**INTERA** Technologies

Figure 4.15

MODEL AREA



+ Data Point  
 o Observation Well  
 Transmissivities in sqm/s  
 Contour Scale: Logarithmic  
 Contour Interval: 0.2 log sqm/s

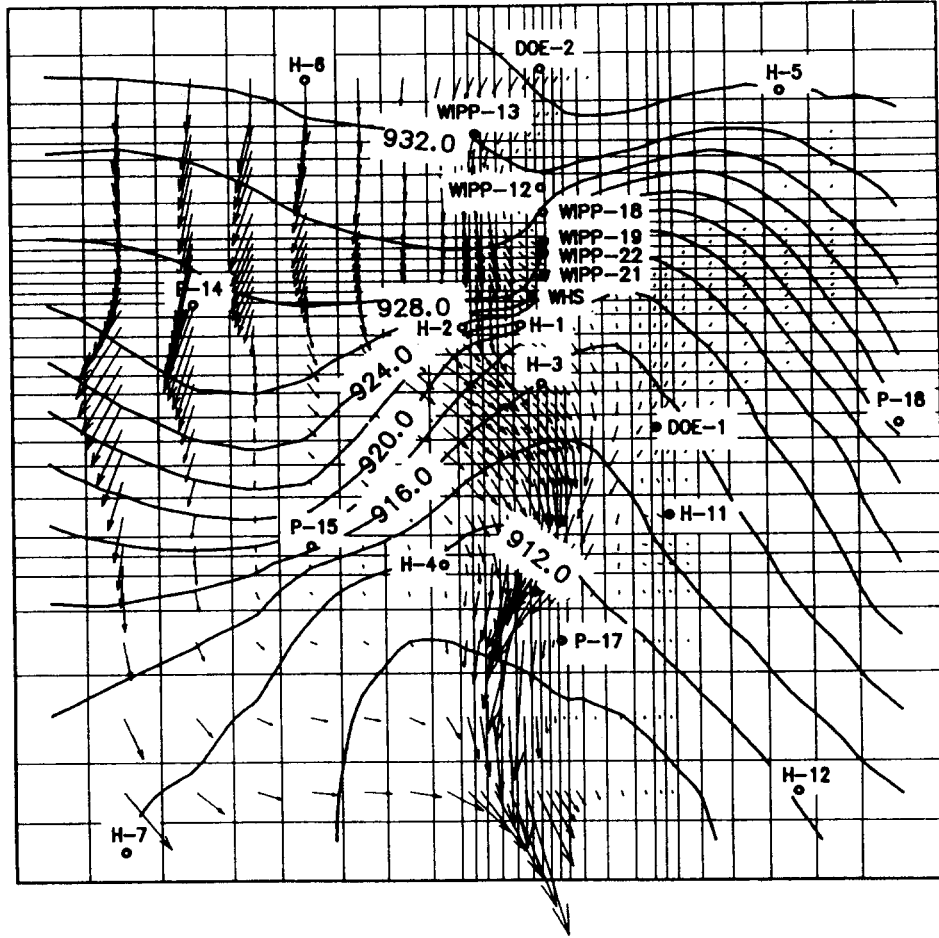
Drawn by	Date
Checked by	Date
Revisions	Date

The Transmissivities of the Model with a High Transmissivity Zone Between H-4 and P-17

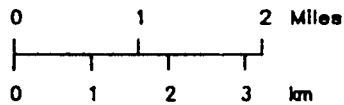
**INTERA** Technologies

Figure 4.16

MODEL AREA



→ Darcy Velocity Vector:  $1.E-8$  m/s  
(Linear Scale)



○ Observation Well

Freshwater Heads in m a.s.l.

Contour Scale: Linear

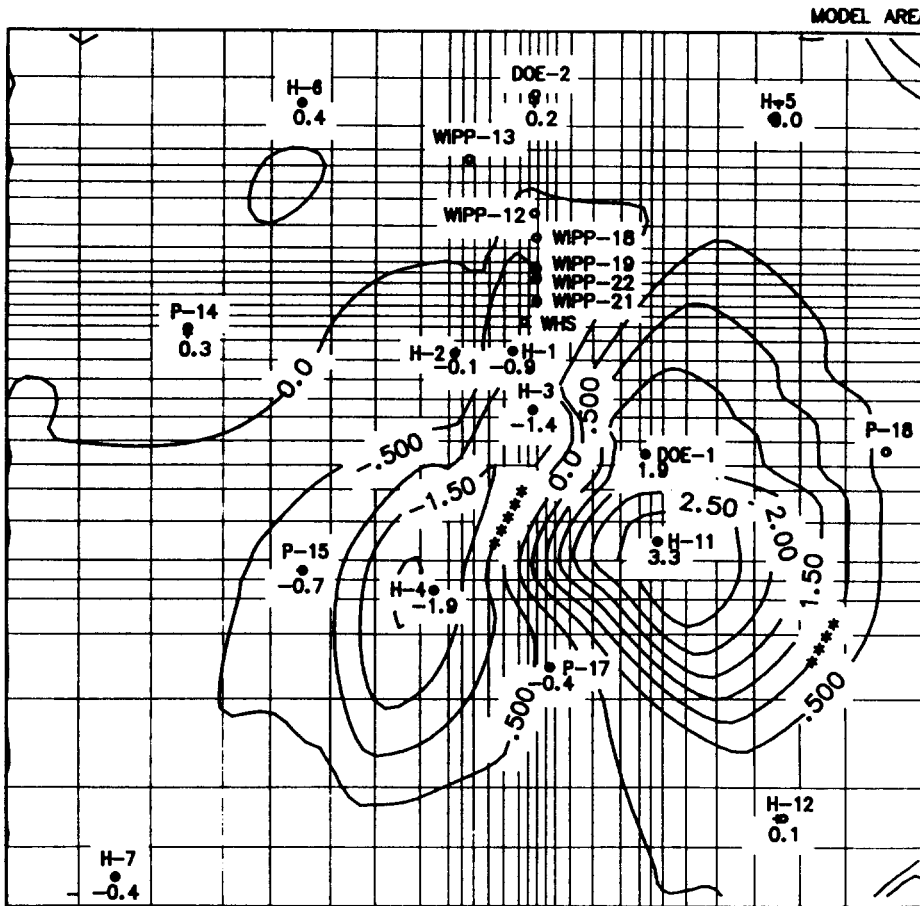
Contour Interval: 2 m

Drawn by	Date
Checked by	Date
Revisions	Date

The Calculated Freshwater Heads of the Steady-State Model with a High-Transmissivity Zone Between H-4 and P-17

**INTERA** Technologies

Figure 4.17



+ Data Point  
 o Observation Well  
 Freshwater—Head Differences In m  
 Contour Scale: Linear  
 Contour Interval: 0.5 m

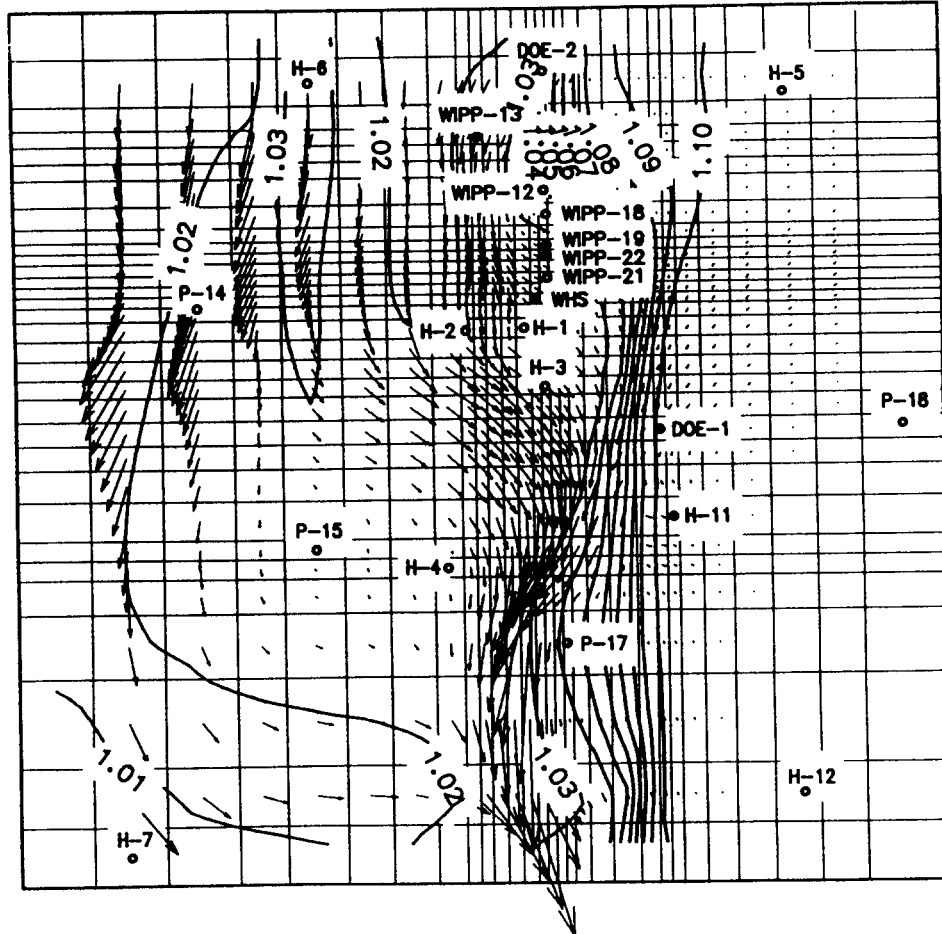
Drawn by	Date
Checked by	Date
Revisions	Date

Steady-State Model with a High-Transmissivity Zone Between H-4 and P-17: Difference Between the Calculated and the Measured Freshwater Heads

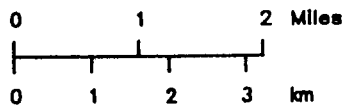
**INTERA** Technologies

Figure 4.18

MODEL AREA



→ Darcy Velocity Vector:  $1.E-8$  m/s  
(Linear Scale)



o Observation Well

Formation-Water Densities in g/ccm

Contour Scale: Linear

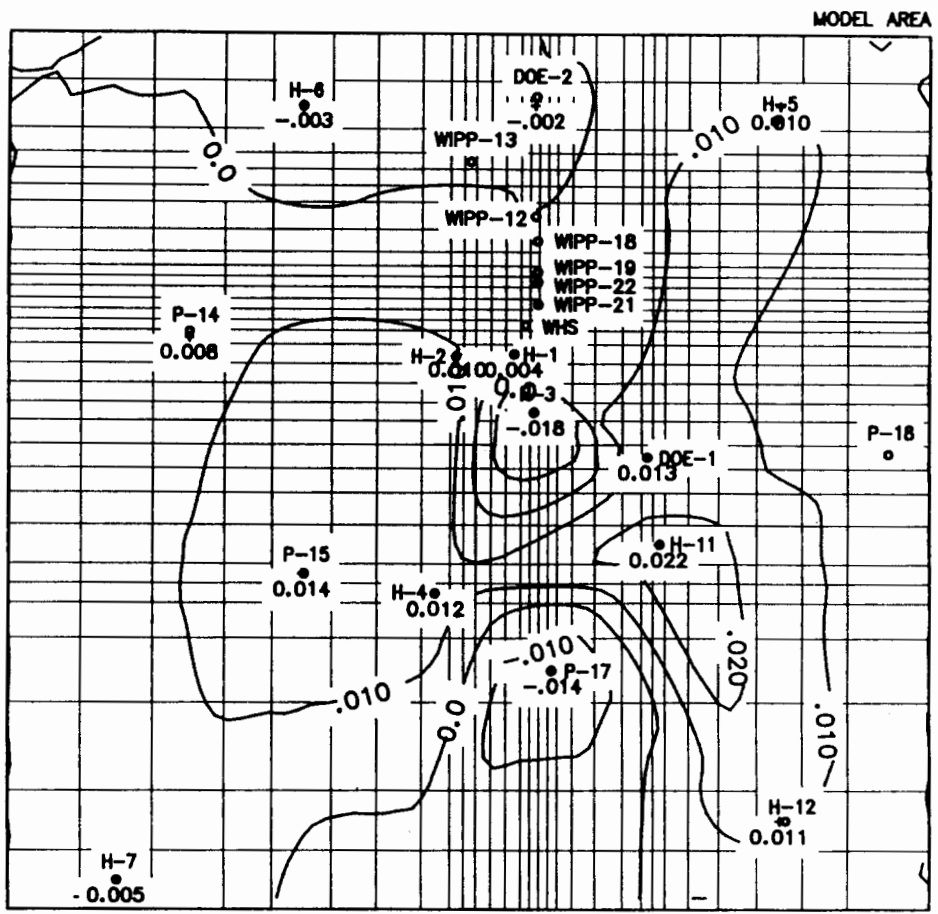
Contour Interval: 0.01 g/ccm

Drawn by	Date
Checked by	Date
Revisions	Date

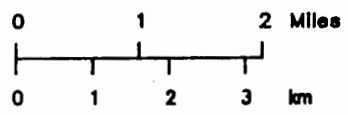
The Calculated Formation-Water Densities of the Steady-State Model with a High-Transmissivity Zone Between H-4 and P-17

**INTERA** Technologies

Figure 4.19



+ Data Point  
 o Observation Well  
 Formation-Water Density Differences in g/ccm  
 Contour Scale: Linear  
 Contour Interval: 0.01 g/ccm

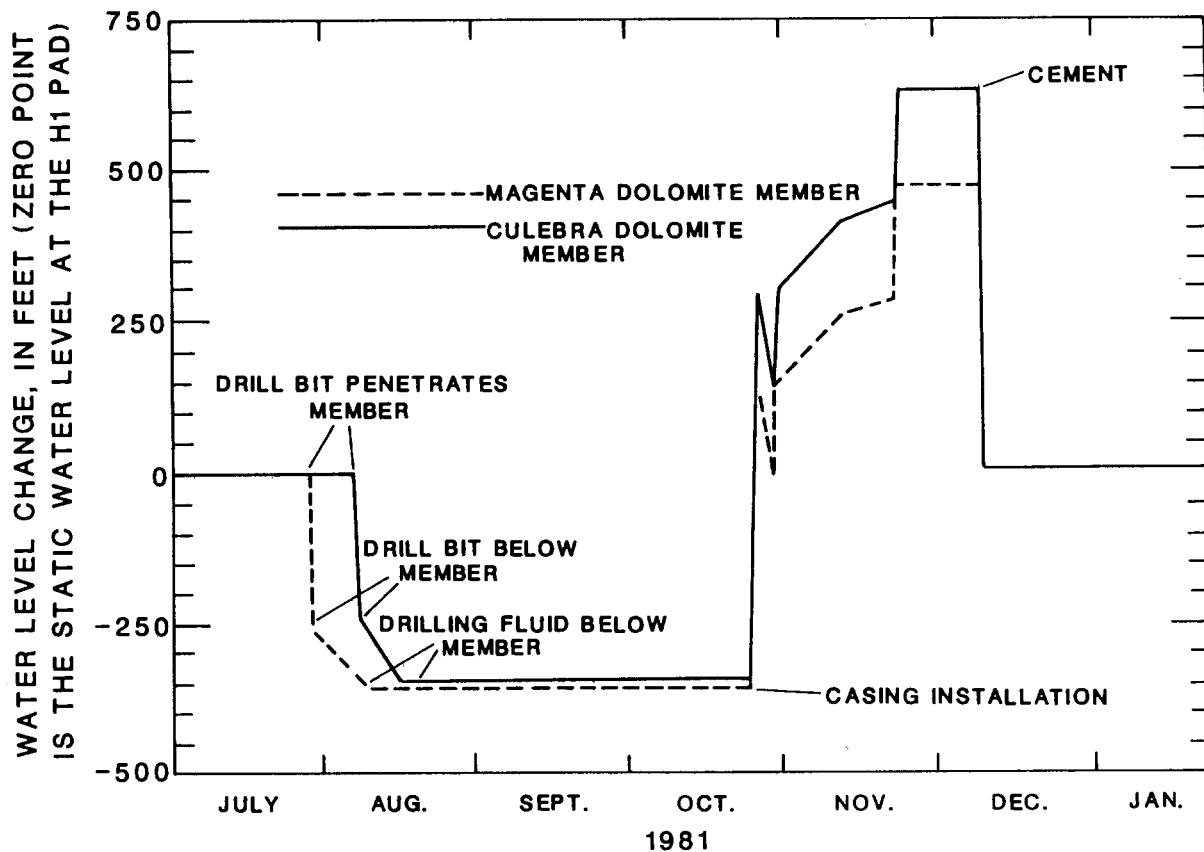


Drawn by	Date
Checked by	Date
Revisions	Date

Steady-State Model with a High-Transmissivity Zone between H-4 and P-17: Difference Between the Calculated and the Measured Formation-Water Densities

**INTERA Technologies**

Figure 4.20



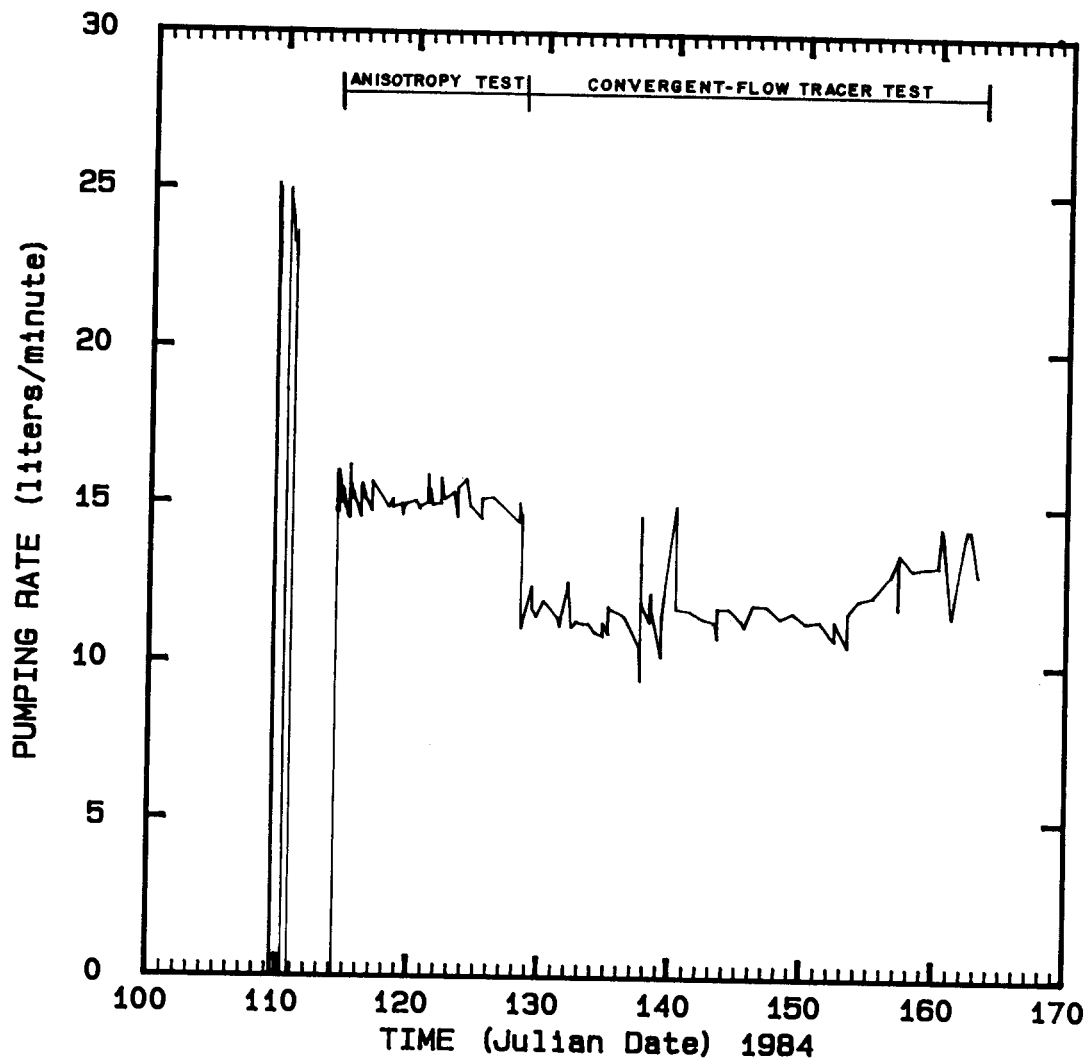
Drawn by	Date
Checked by	Date
Revisions	Date

The Exploratory Shaft Simulated Stresses in the Magenta and Culebra Dolomite Members (from Stevens & Beyeler, 1985)

**INTERA** Technologies

Figure 5.1



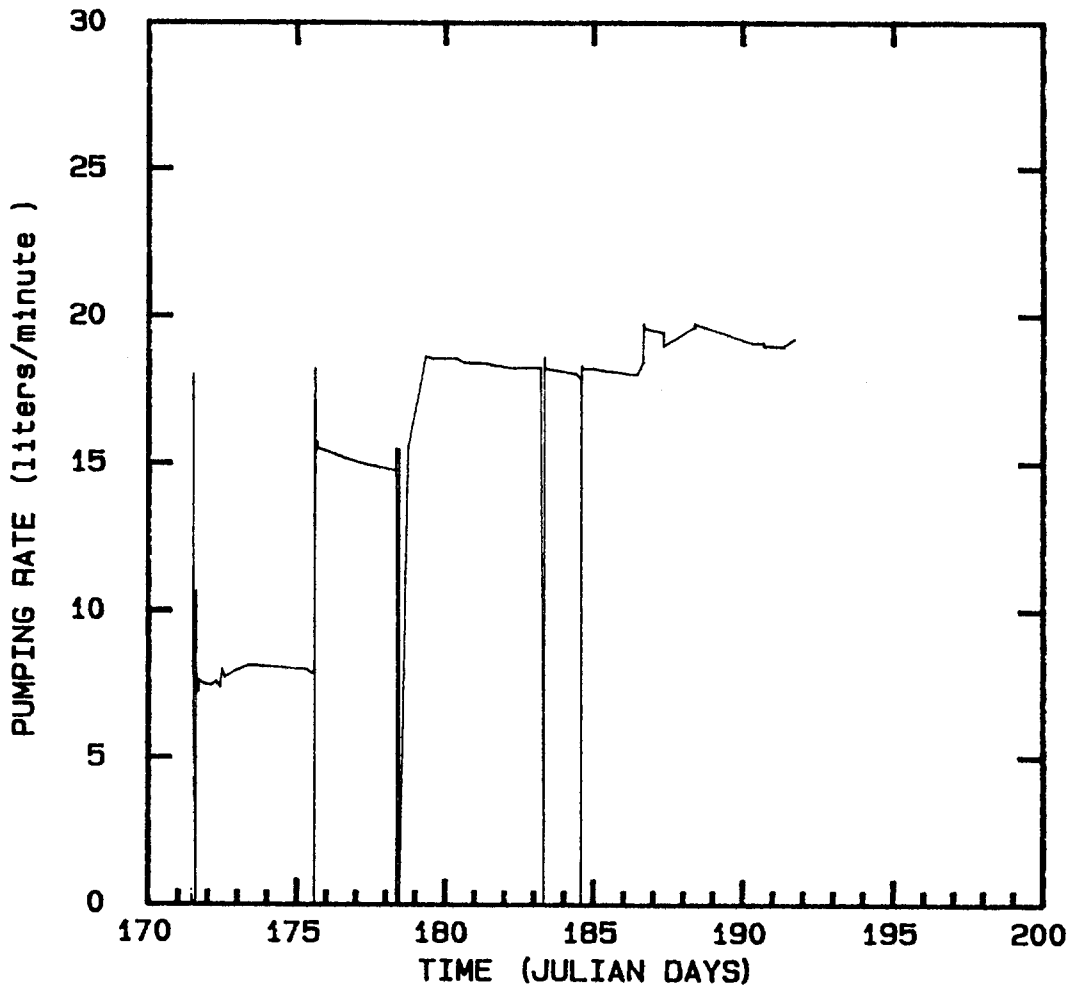


Drawn by	Date
Checked by	Date
Revisions	Date

The H-3b2 Anisotropy and Convergent-Flow Tracer Test: Recorded Pump Rates

**INTERA** Technologies

Figure 5.2



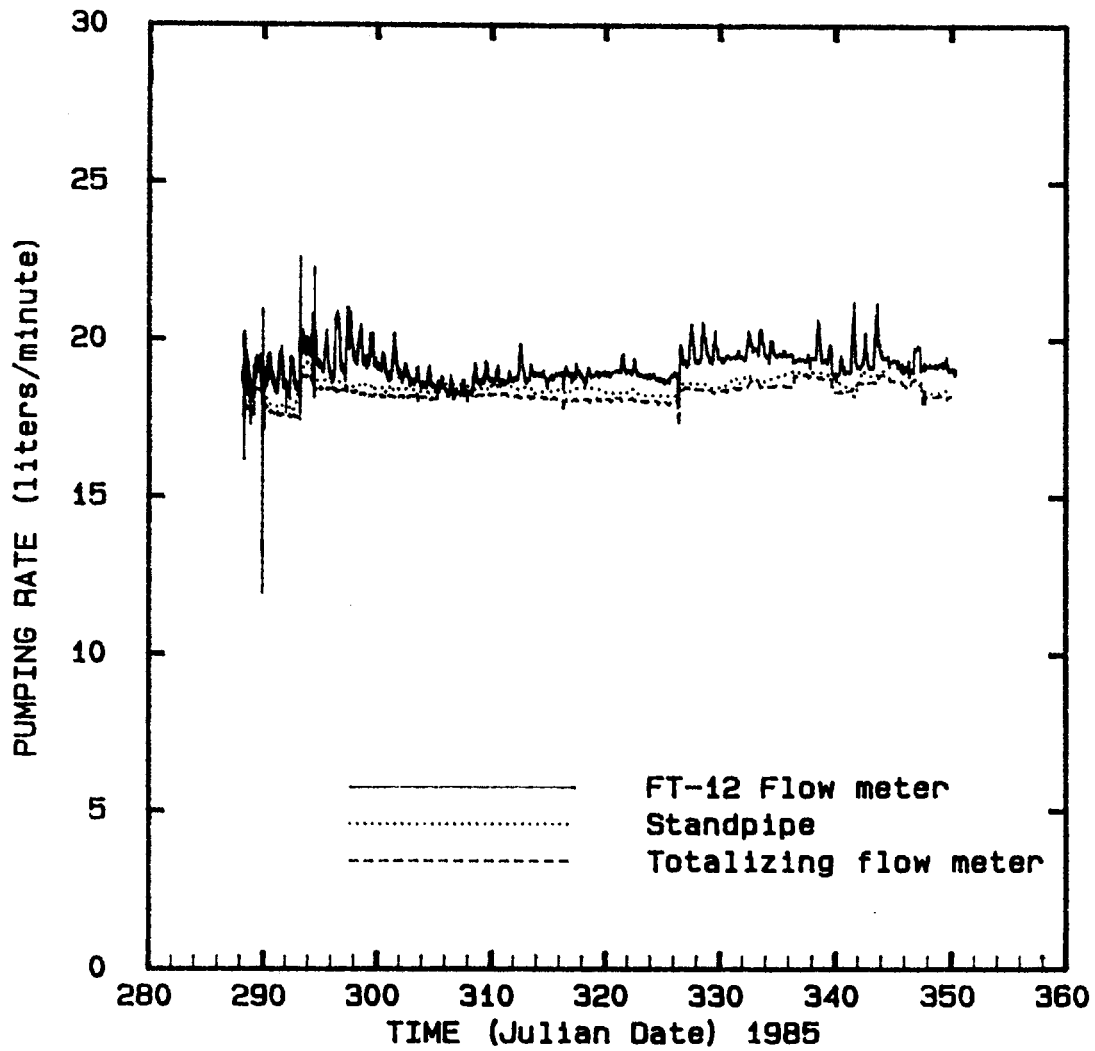
TEST PERIOD  
 JUNE 20 - JULY 10, 1985

Drawn by	Date
Checked by	Date
Revisions	Date

The H-3b2 Step-Drawdown Test:  
 Recorded Pump Rates

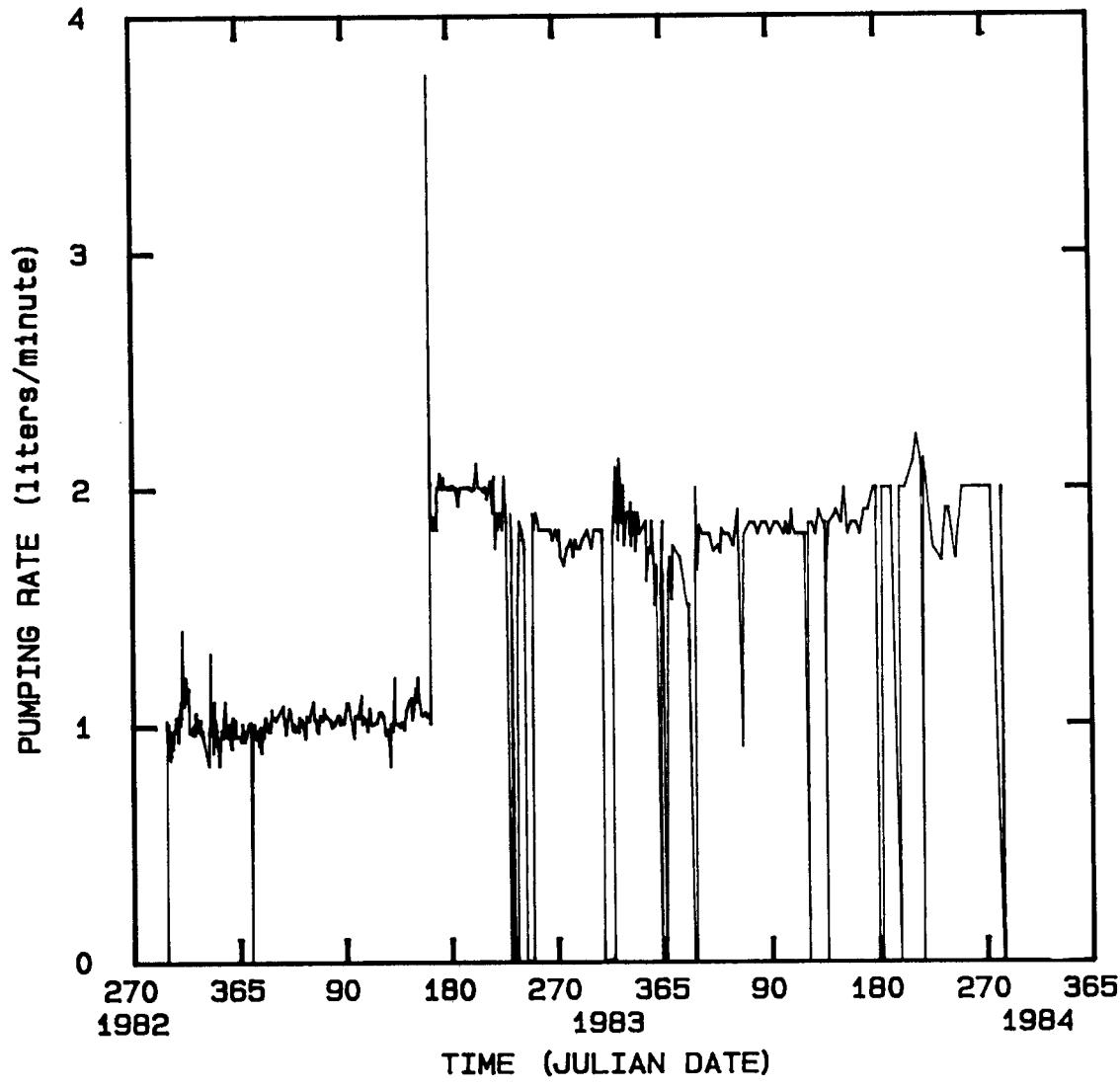
**INTERA** Technologies

Figure 5.3



Drawn by	Date
Checked by	Date
Revisions	Date

The H-3b2 Multipad Pumping Test:  
Recorded Pump Rates



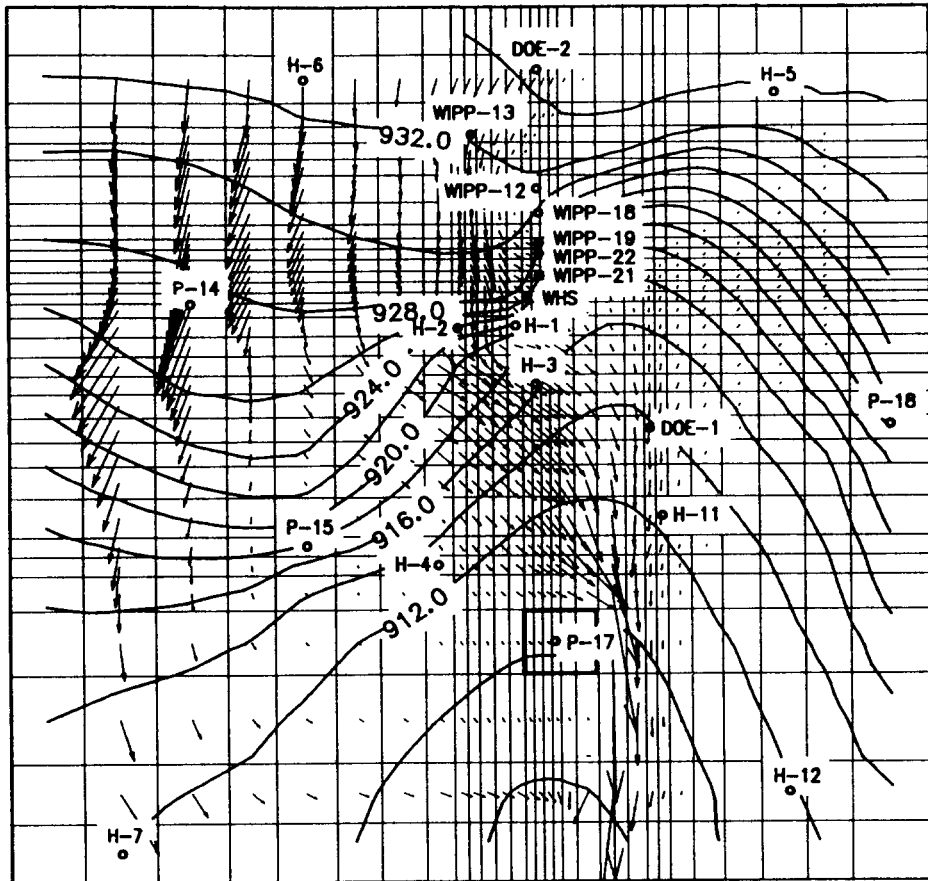
Drawn by	Date
Checked by	Date
Revisions	Date

The H-4c Convergent-Flow Tracer Test:  
Recorded Pump Rates

**INTERA** Technologies

Figure 5.5

MODEL AREA



→ Darcy Velocity Vector:  $1.E-8$  m/s  
(Linear Scale)

 Area with Vertical Flux

○ Observation Well

0 1 2 Miles

Freshwater Heads in m a.s.l.

Contour Scale: Linear

Contour Interval: 2 m

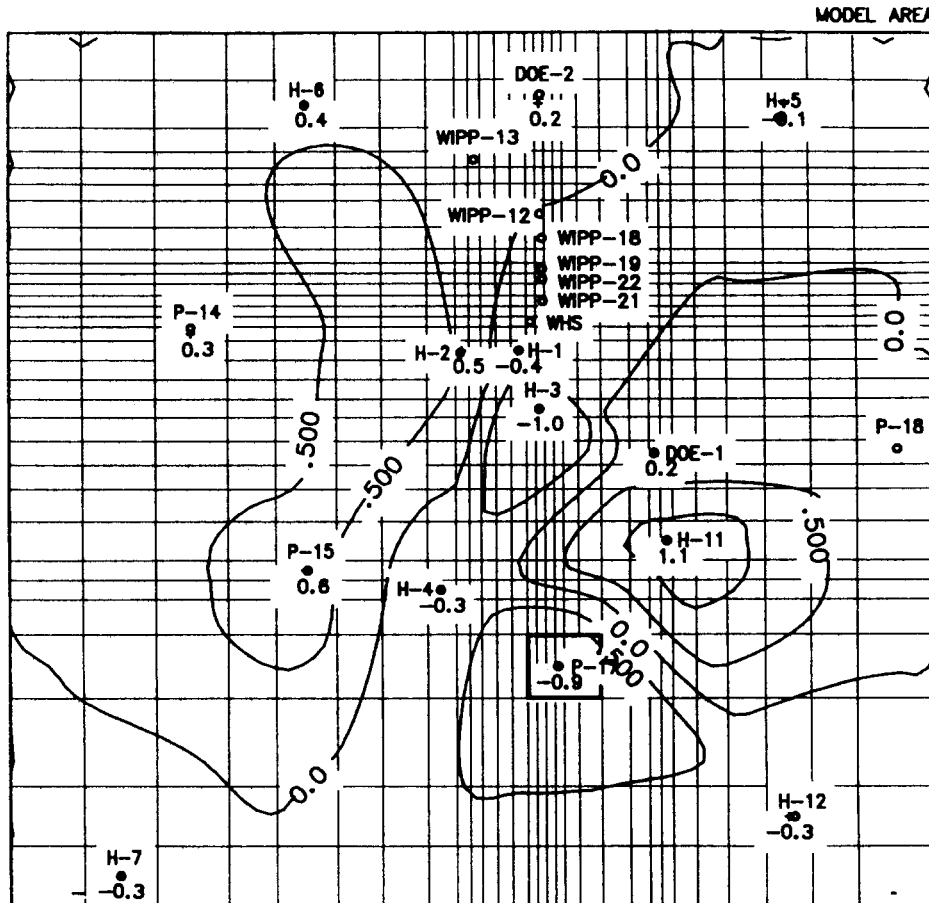
0 1 2 3 km

Drawn by	Date
Checked by	Date
Revisions	Date

The Calculated Freshwater Heads of the Density-Calibrated Steady-State Model with a Vertical Flux at P-17



**INTERA** Technologies

Figure 6.1



 Area with  
Vertical Flux

+ Data Point  
 o Observation Well

0 1 2 Miles  
  
 0 1 2 3 km  


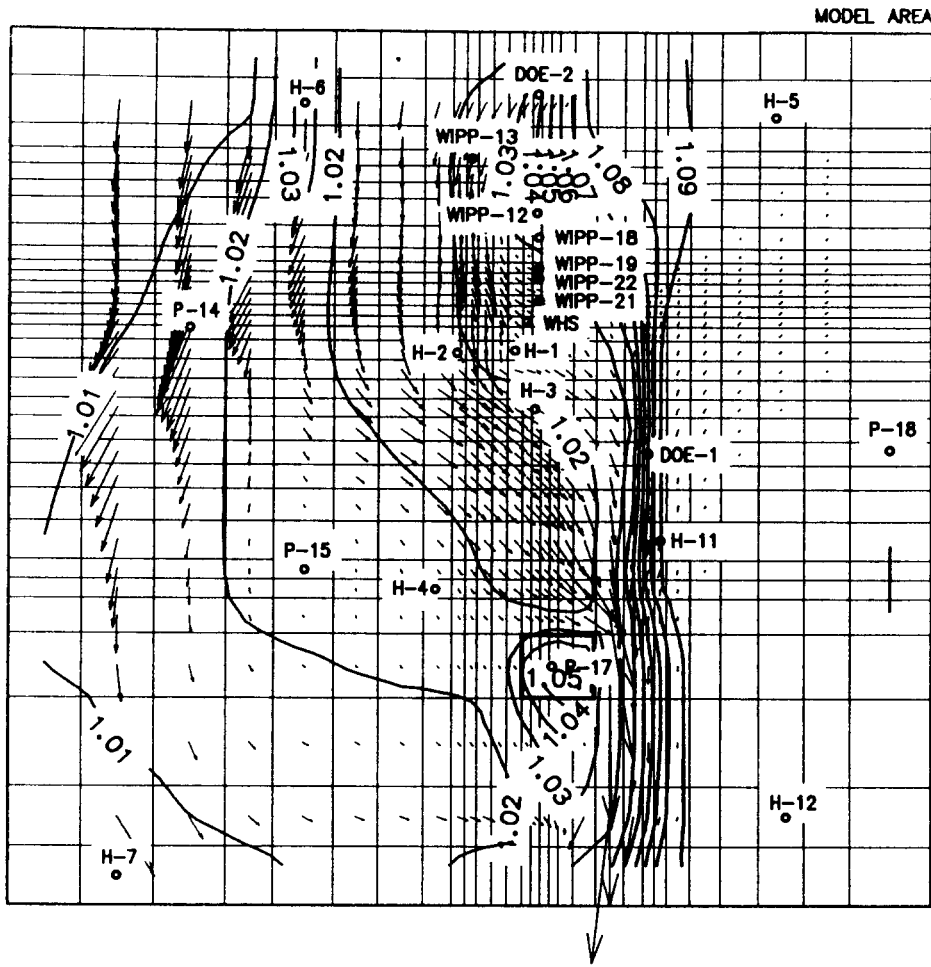
Freshwater-Head Differences in m  
 Contour Scale: Linear  
 Contour Interval: 0.5 m

Drawn by	Date
Checked by	Date
Revisions	Date

Density-Calibrated Steady-State Model with a Vertical Flux at P-17: Difference Between the Calculated and the Measured Freshwater Heads

**INTERA** Technologies

Figure 6.2



→ Darcy Velocity Vector: 1.E-8 m/s  
(Linear Scale)

□ Area with Vertical Flux

○ Observation Well

0 1 2 Miles

Formation-Water Densities in g/ccm

Contour Scale: Linear

0 1 2 3 km

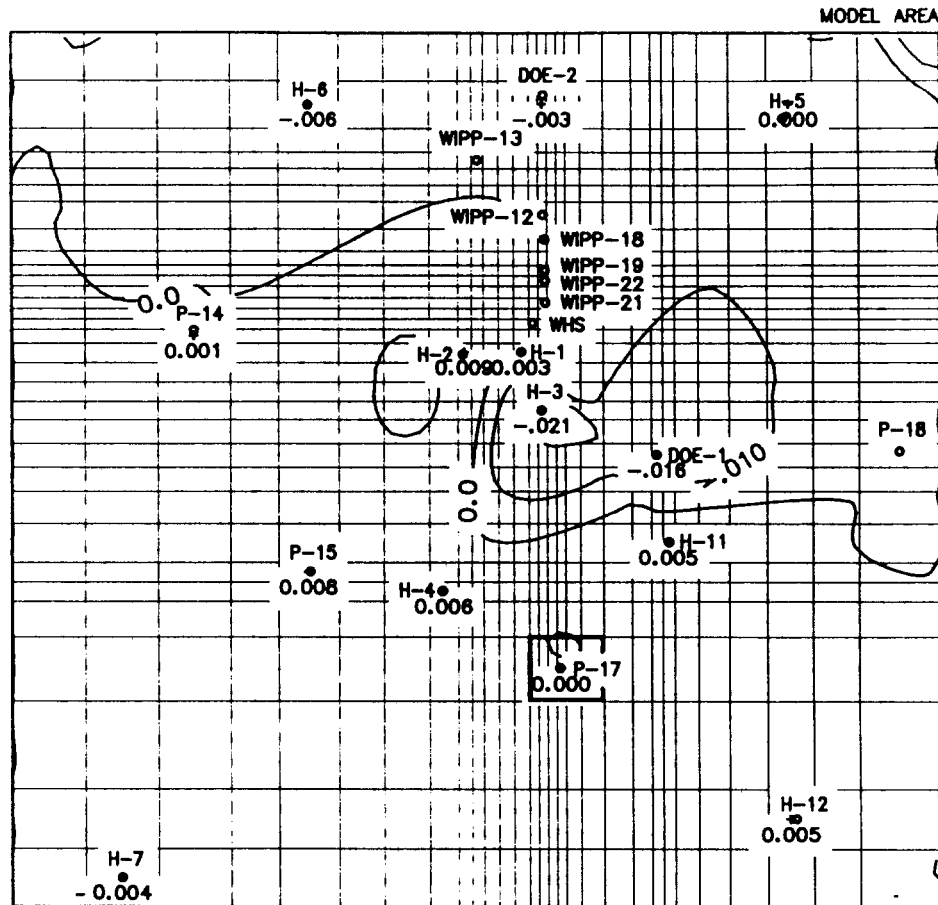
Contour Interval: 0.01 g/ccm

Drawn by	Date
Checked by	Date
Revisions	Date

The Calculated Formation-Water Densities of the Density-Calibrated Steady-State Model with a Vertical Flux at P-17

**INTERA** Technologies

Figure 6.3



Area with Vertical Flux

+ Data Point  
o Observation Well

0 1 2 Miles  
  
0 1 2 3 km

Formation-Water Density Differences in g/ccm  
Contour Scale: Linear  
Contour Interval: 0.01 g/ccm

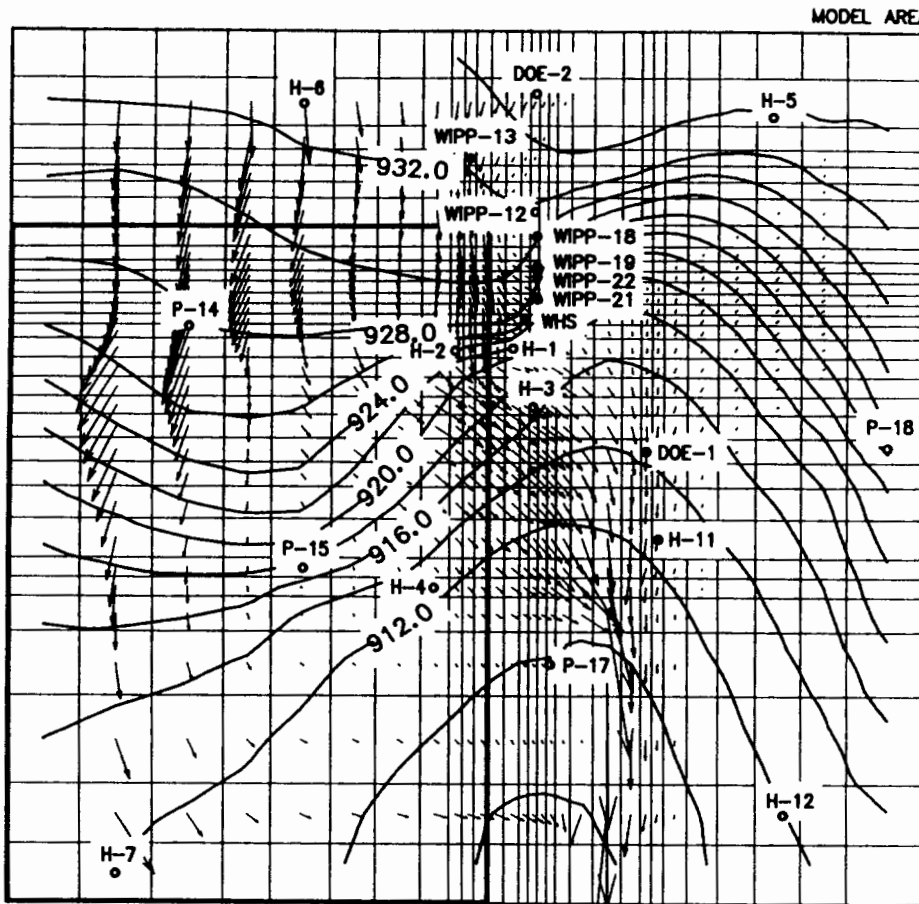
Drawn by	Date
Checked by	Date
Revisions	Date

Density-Calibrated Steady-State Model with a Vertical Flux at P-17: Difference Between the Calculated and the Measured Formation-Water Densities

**INTERA** Technologies

Figure 6.4





→ Darcy Velocity Vector:  $1.E-8$  m/s  
(Linear Scale)

Area with Vertical Flux

○ Observation Well

0 1 2 Miles

Freshwater Heads in m a.s.l.

Contour Scale: Linear

Contour Interval: 2 m

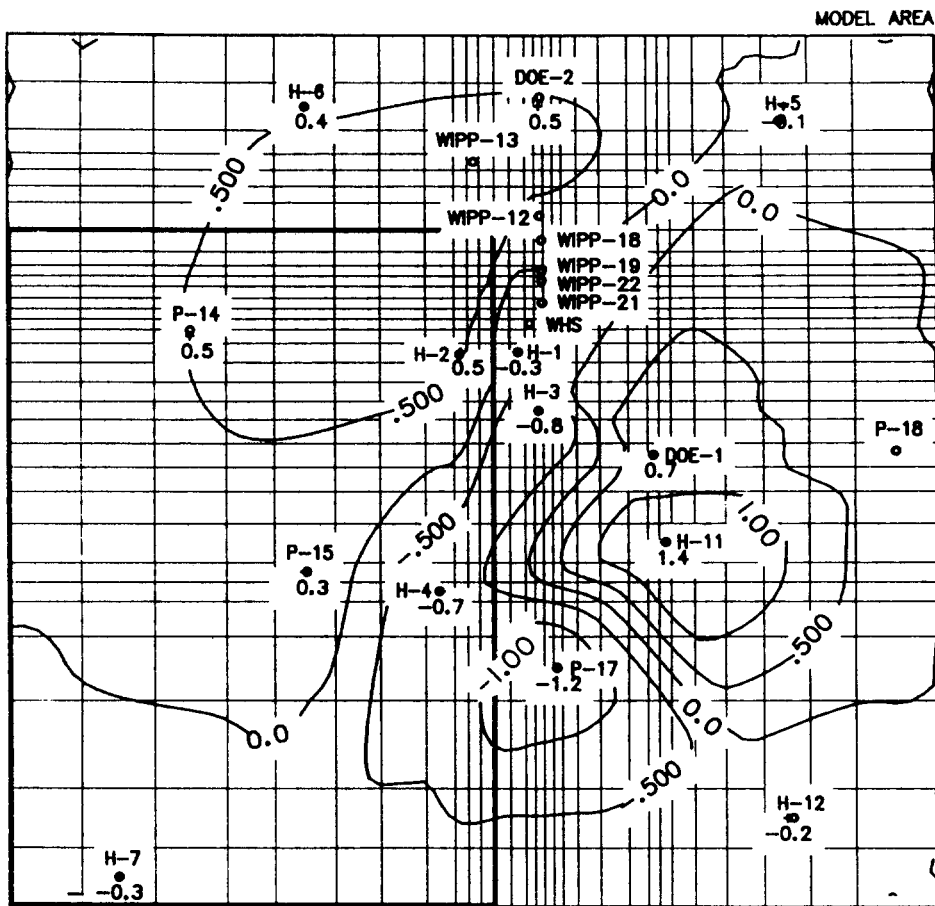
0 1 2 3 km

Drawn by	Date
Checked by	Date
Revisions	Date

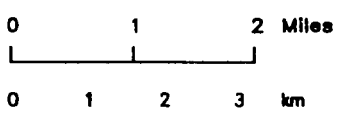
The Calculated Freshwater Heads of the Steady-State Model with No Vertical Flux

**INTERA** Technologies

Figure 6.5



Area with  
Vertical Flux



+ Data Point  
 o Observation Well

Freshwater-Head Differences In m  
 Contour Scale: Linear  
 Contour Interval: 0.5 m

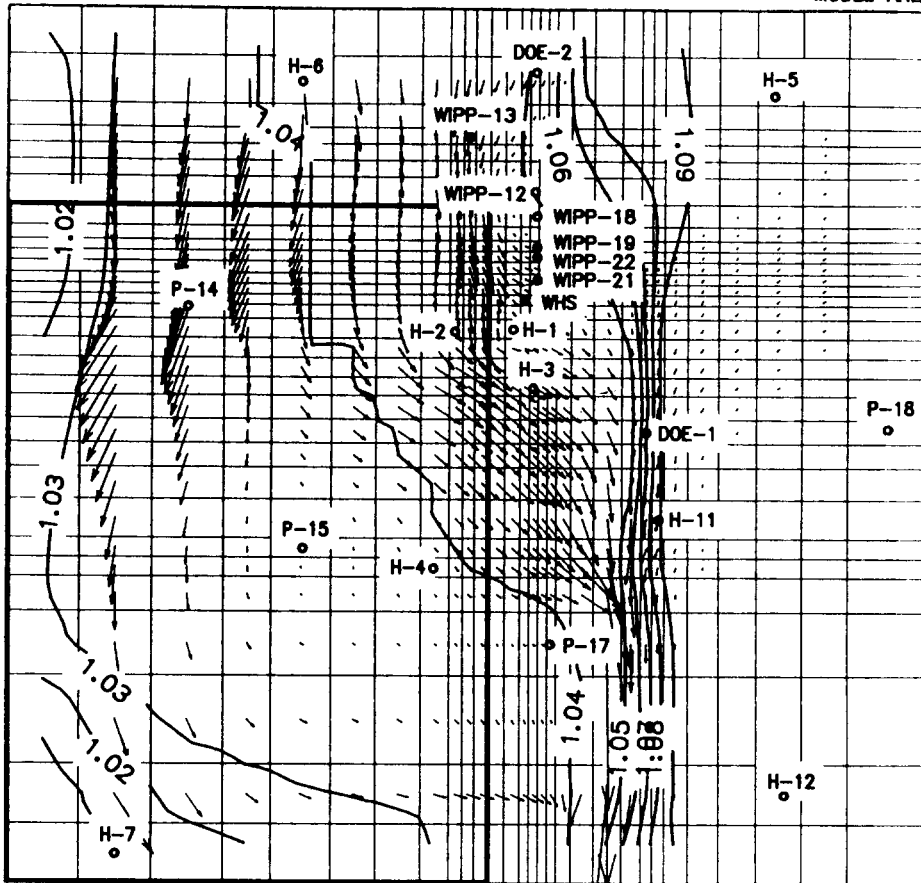
Drawn by	Date
Checked by	Date
Revisions	Date

Steady-State Model with No Vertical Flux:  
 Difference Between the Calculated and the  
 Observed Freshwater Heads

**INTERA** Technologies

Figure 6.6

MODEL AREA



→ Darcy Velocity Vector:  $1.E-8$  m/s  
(Linear Scale)

 Area with Vertical Flux

o Observation Well

0 1 2 Miles

Formation-Water Densities in g/ccm

Contour Scale: Linear

Contour Interval: 0.01 g/ccm

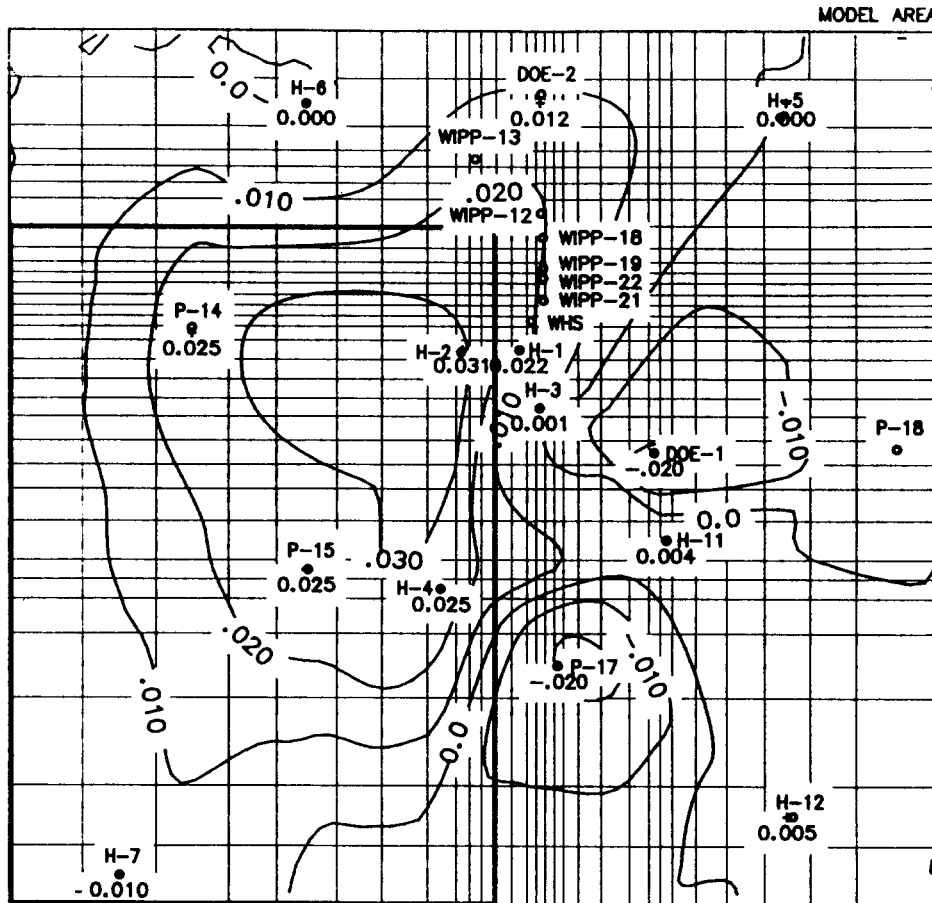
0 1 2 3 km

Drawn by	Date
Checked by	Date
Revisions	Date

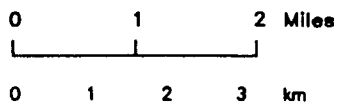
The Calculated Formation-Water Densities of the Steady-State Model with No Vertical Flux

**INTERA** Technologies

Figure 6.7



□ Area with Vertical Flux



+ Data Point  
o Observation Well

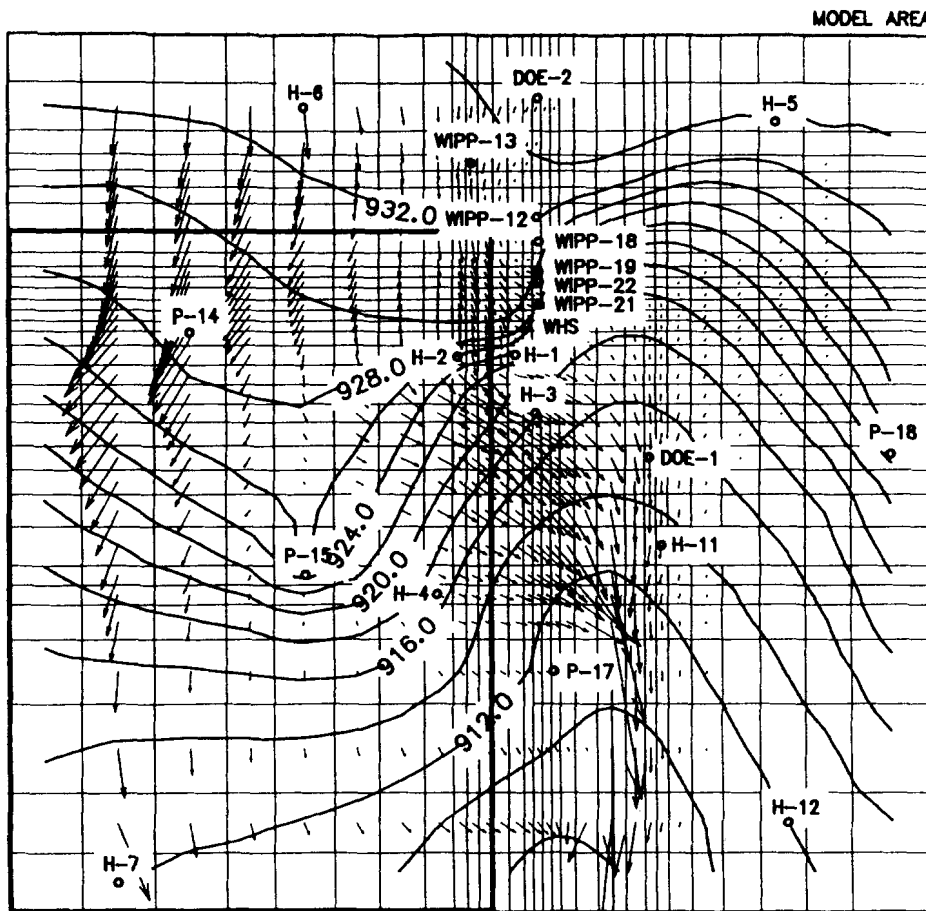
Formation-Water Density Differences in g/ccm  
Contour Scale: Linear  
Contour Interval: 0.01 g/ccm

Drawn by	Date
Checked by	Date
Revisions	Date

Steady-State Model with No Vertical Flux:  
Difference Between the Calculated and the  
Observed Formation-Water Densities

**INTERA** Technologies

Figure 6.8



→ Darcy Velocity Vector:  $1.E-8$  m/s  
(Linear Scale)

□ Area with Vertical Flux

○ Observation Well

0 1 2 Miles  
0 1 2 3 km

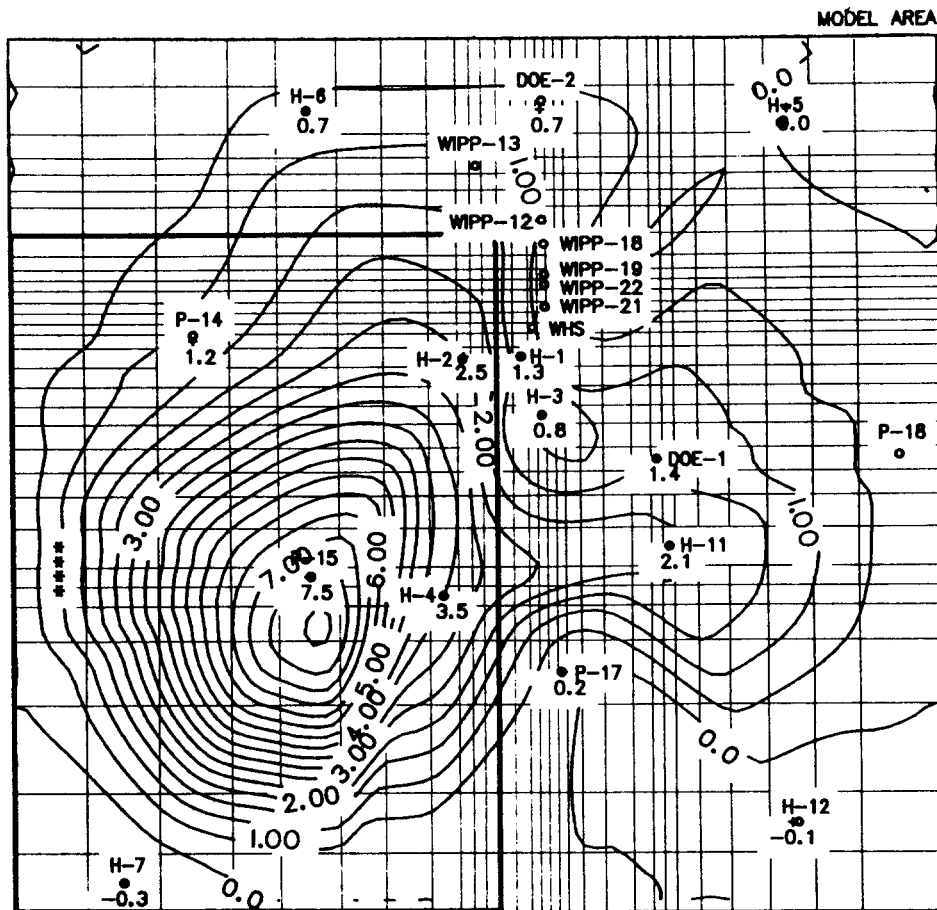
Freshwater Heads in m a.s.l.  
Contour Scale: Linear  
Contour interval: 2 m

Drawn by	Date
Checked by	Date
Revisions	Date

The Calculated Freshwater Heads of the Steady-State Model with a Vertical Flux of  $5 \times 10^{-12}$  m/s

**INTERA** Technologies

Figure 6.9



 Area with Vertical Flux



+ Data Point  
o Observation Well

Freshwater-Head Differences in m  
Contour Scale: Linear  
Contour Interval: 0.5 m

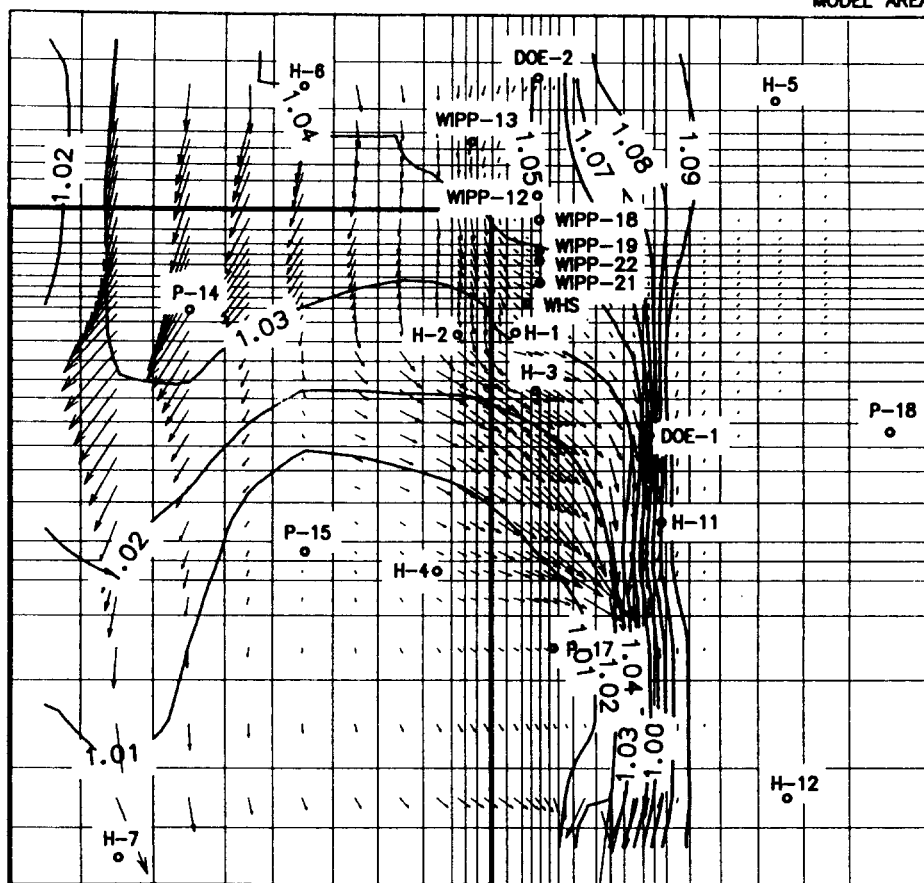
Drawn by	Date
Checked by	Date
Revisions	Date

Steady-State Model with a Vertical Flux of  $5 \times 10^{-12}$  m/s: Difference Between the Calculated and the Observed Freshwater Heads

**INTERA** Technologies

Figure 6.10

MODEL AREA



→ Darcy Velocity Vector:  $1.E-8$  m/s  
(Linear Scale)

 Area with Vertical Flux

0 1 2 Miles  
0 1 2 3 km

o Observation Well

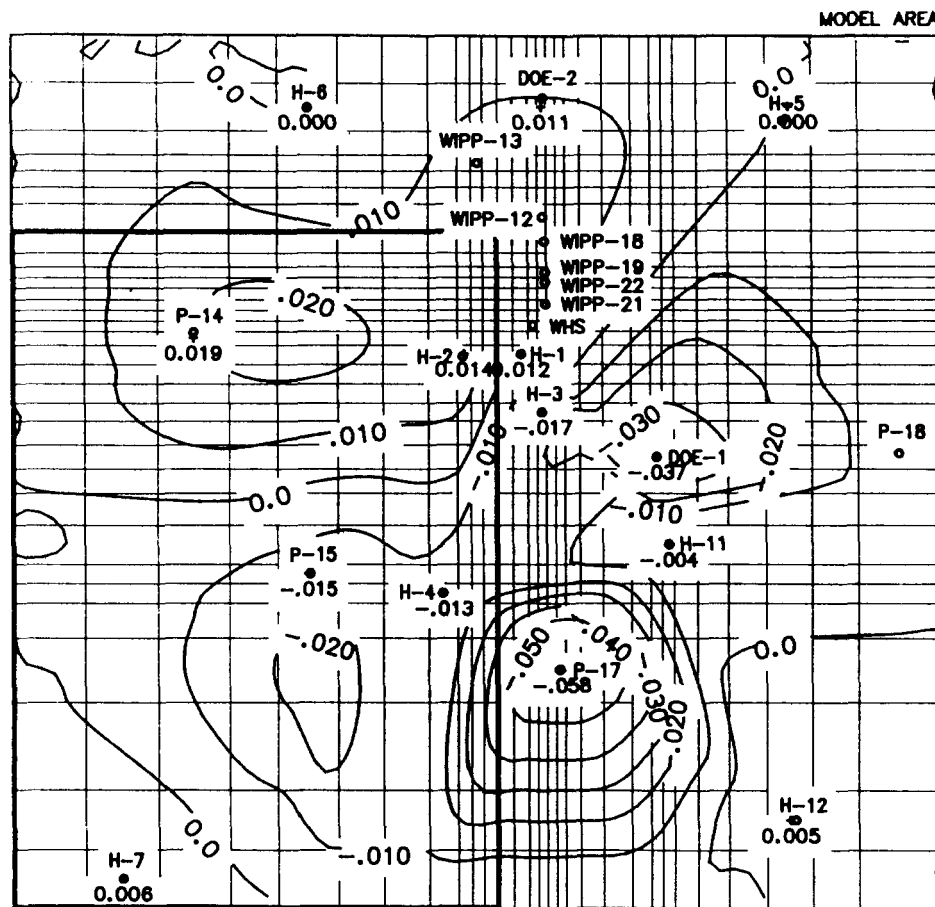
Formation-Water Densities in g/ccm  
Contour Scale: Linear  
Contour Interval: 0.01 g/ccm

Drawn by	Date
Checked by	Date
Revisions	Date

The Calculated Formation-Water Densities of the Steady-State Model with a Vertical Flux of  $5 \times 10^{-12}$  m/s

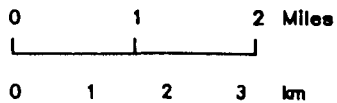
**INTERA** Technologies

Figure 6.11



Area with Vertical Flux

+ Data Point  
 o Observation Well



Formation-Water Density Differences in g/ccm  
 Contour Scale: Linear  
 Contour Interval: 0.01 g/ccm

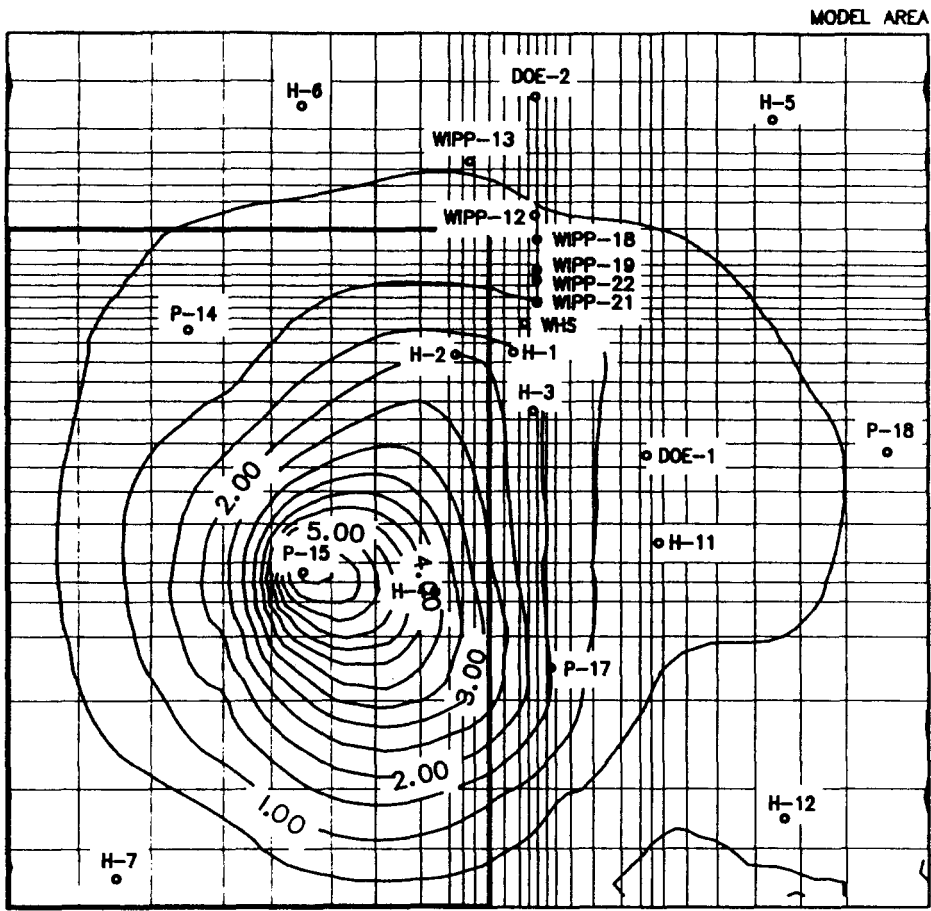
Drawn by	Date
Checked by	Date
Revisions	Date

Steady-State Model with a Vertical Flux of  $5 \times 10^{-12}$  m/s: Difference Between the Calculated and the Observed Formation-Water Densities

**INTERA** Technologies

Figure 6.12





Area with Vertical Flux

0      1      2 Miles  
 ───────────  
 0      1      2      3 km

+ Data Point  
 o Observation Well

Freshwater-Head Differences in m  
 Contour Scale: Linear  
 Contour Interval: 0.5 m

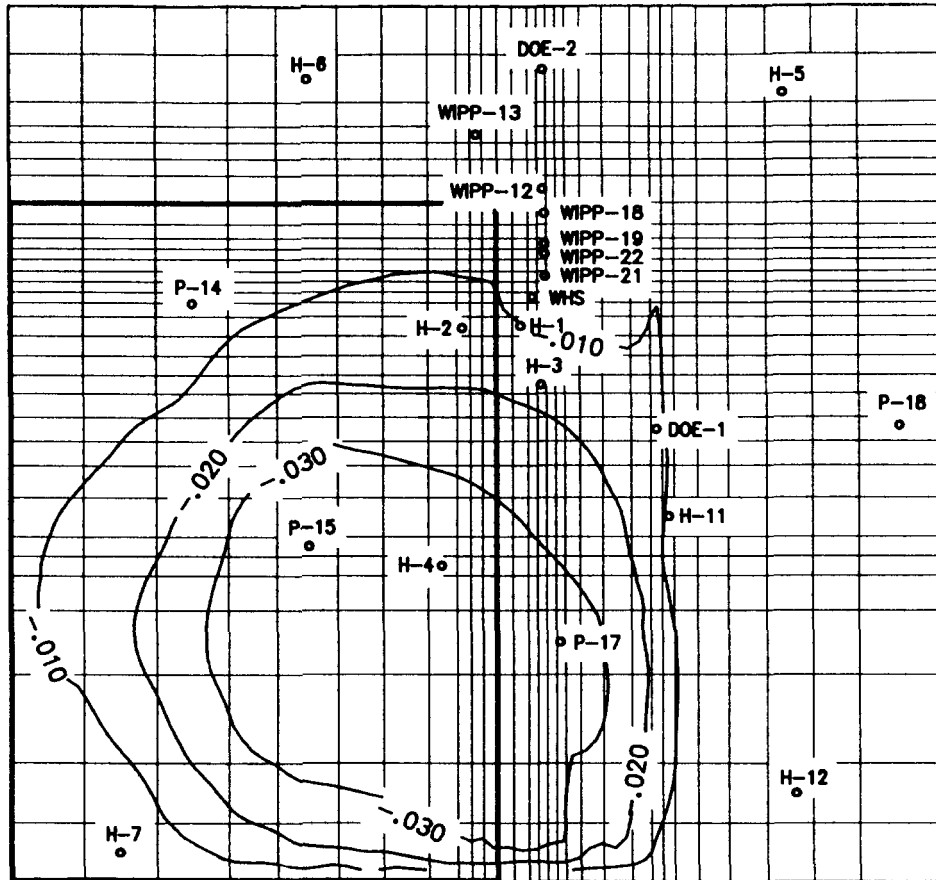
Drawn by	Date
Checked by	Date
Revisions	Date

The Freshwater-Head Differences Caused by a Vertical Flux of  $5 \times 10^{-12}$  m/s

**INTERA** Technologies

Figure 6.13

MODEL AREA



 Area with Vertical Flux

+ Data Point  
o Observation Well

0 1 2 Miles  
0 1 2 3 km

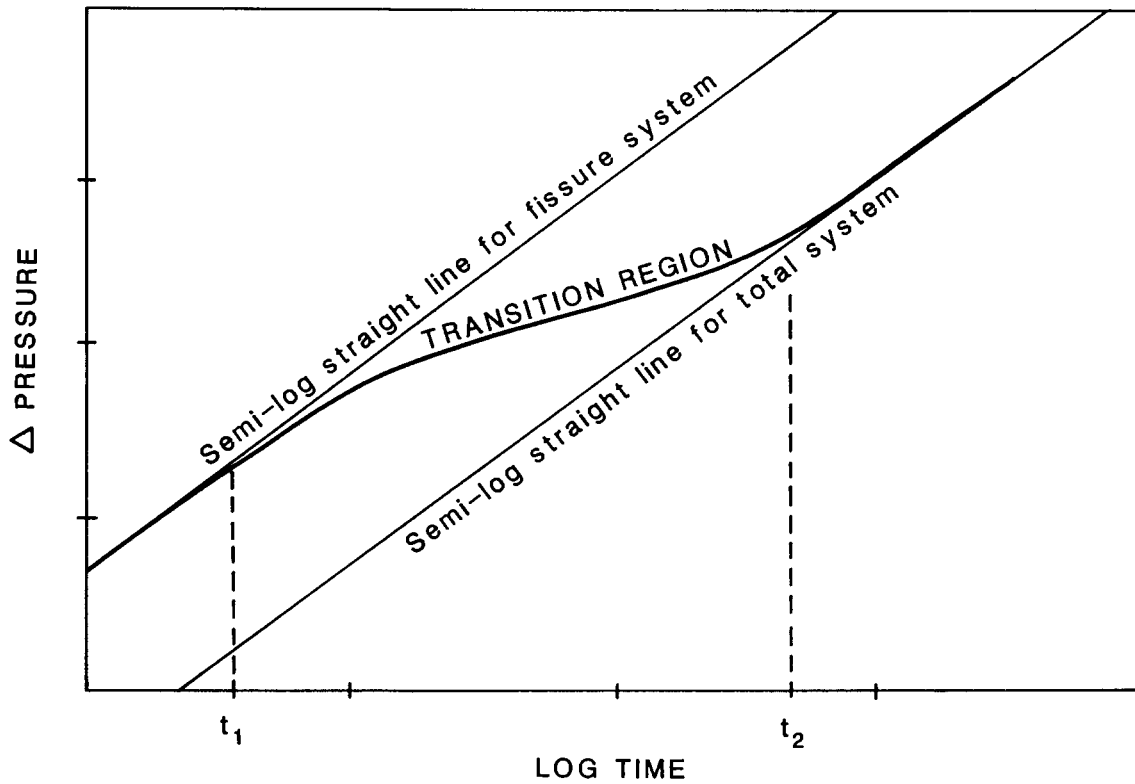
Formation-Water Density Differences in g/ccm  
Contour Scale: Linear  
Contour Interval: 0.01 g/ccm

Drawn by	Date
Checked by	Date
Revisions	Date

The Formation-Water Density Differences Caused by a Vertical Flux of  $5 \times 10^{-12}$  m/s

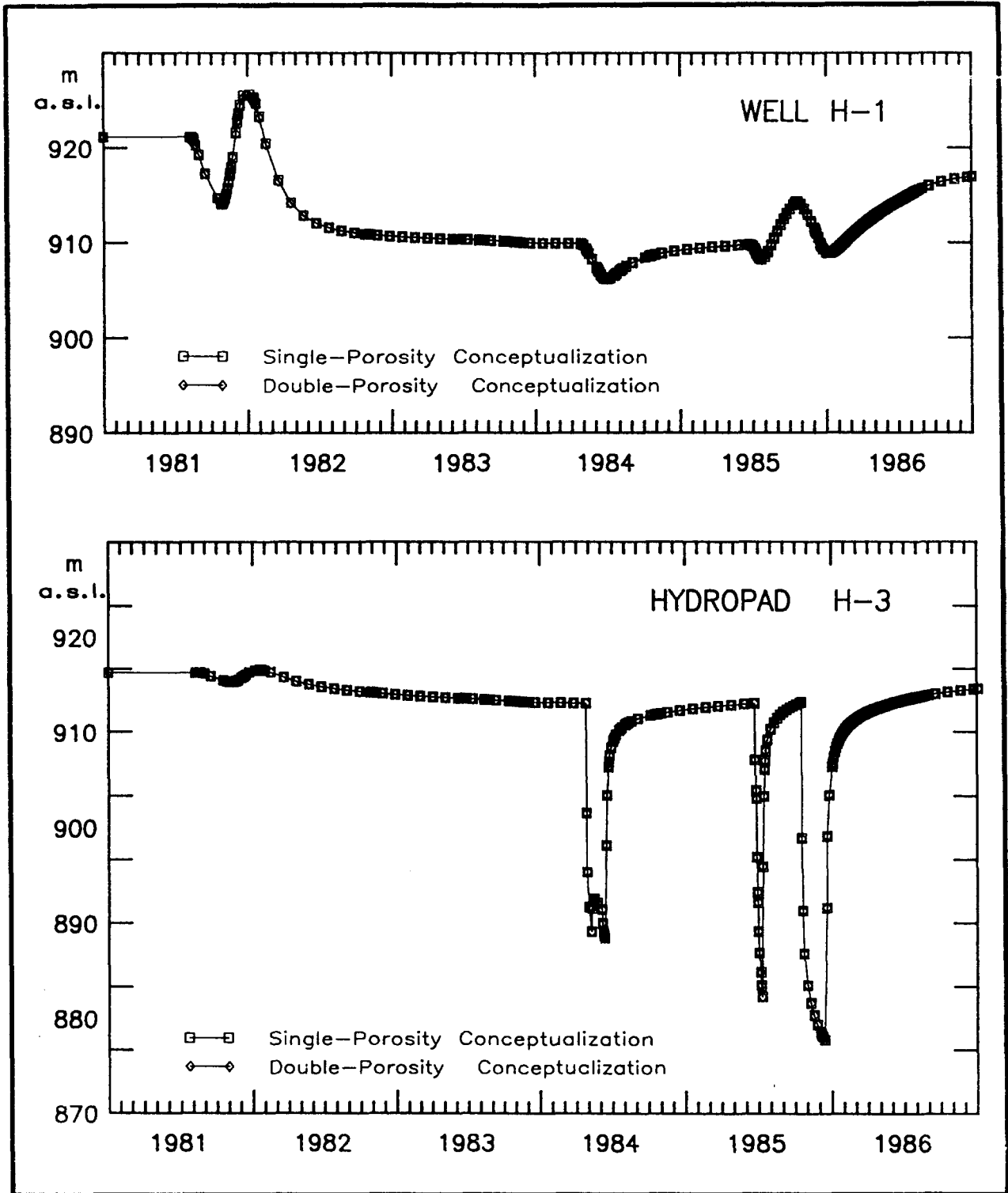
**INTERA** Technologies

Figure 6.14



Drawn by	Date
Checked by	Date
Revisions	Date

Pressure Response in a Double-Porosity Medium  
(after Warren and Root, 1963)



Drawn by	Date
Checked by	Date
Revisions	Date

Comparison Between Single- and Double-Porosity Simulation Results at Selected Hydropads

**INTERA Technologies**

Figure 7.2

Well	UTM Coordinates		Derived from		Closest Sat. Surveyed Well
	m North	m East	Sat. Survey 1984	Sandia Basic Data Report	
H-1	35 81 672	6 13 427	X		
H-2b	35 81 642	6 12 653		X	H-1
H-2c	35 81 660	6 12 668		X	H-1
H-3b1	35 80 892	6 13 723		X	H-1
H-3b2	35 80 894	6 13 693		**	H-1
H-3b3	35 80 866	6 13 705		**	H-1
H-4b	35 78 480	6 12 377	X		
H-4c	35 78 496	6 12 403		X	H-4b
H-5b	35 84 809	6 16 867		X	H-5a
H-6b	35 84 989	6 10 600		X	H-6c
H-7b1	35 74 648	6 08 126		X	H-7a
H-7c	35 74 639	6 08 097		X	H-7a
H-7b2					
H-8b	35 63 557	6 08 666	X		

\*\* based on field measurements relative to H-3b1 (INTERA)

Drawn by	Date	Borehole Coordinates
Checked by	Date	
Revisions	Date	

<b>INTERA Technologies</b>	Table 3.1a
----------------------------	------------

Well	UTM Coordinates		Derived from Sat. Survey 1984	Derived from Sandia Basic Data Report	Closest Sat. Surveyed Well
	m North	m East			
H-9a					
H-9b	35 68 265	6 13 990	X		
H-9c					
H-10b	35 72 476	6 22 979	X		
H-11b3	35 79 134	6 15 360	X		
H-12	35 75 442	6 17 018	X		
DOE-1	35 80 298	6 15 196	X		
DOE-2	35 85 119	6 13 720	X		
P-14	35 81 972	6 09 084	X		
P-15	35 78 739	6 10 625	X		
P-17	35 77 453	6 13 927		X	H-4b
P-18	35 80 349	6 18 376	X		
WIPP-12	35 83 520	6 13 711		X	H-1
WIPP-13	35 84 245	6 12 844		X	H-1
WIPP-18	35 83 191	6 13 736		X	H-1
WIPP-19	35 82 776	6 13 740		X	H-1
WIPP-21	35 82 339	6 13 746		X	H-1
WIPP-22	35 82 641	6 13 742		X	H-1

Drawn by	Date	Borehole Coordinates
Checked by	Date	
Revisions	Date	

<b>INTERA Technologies</b>	Table 3.1b
----------------------------	------------

Well	UTM Coordinates		Derived from Sat. Survey 1984	Sandia Basic Data Report	Closest Sat. Surveyed Well
	m North	m East			
WIPP-25	35 84 025	6 06 387	X		
WIPP-26	35 81 041	6 03 995	X		
WIPP-27	35 93 077	6 04 433	X		
WIPP-28	35 94 682	6 11 266		X	WIPP-30
WIPP-29	35 78 773	5 96 941	X		
WIPP-30	35 89 707	6 13 717	X		
WHS *	35 82 066	6 13 581		X	H-1

\* Waste-Handling Shaft

Drawn by	Date	Borehole Coordinates
Checked by	Date	
Revisions	Date	
<b>INTERA Technologies</b>		Table 3.1c

UTM Coordinates of the model-area corners:

South-west corner:	35 74 260 mN	6 06 680 mE
South-east corner:	35 74 260 mN	6 18 920 mE
North-east corner:	35 85 960 mN	6 18 920 mE
North-west corner:	35 85 960 mN	6 06 680 mE

Dimensions of the model area:

East - West:	12.24 km
North - South:	11.70 km
Area:	143.21 km <sup>2</sup>

Grid block dimensions (m):

From West to East: 960, 960, 960, 640, 800,  
 600, 600, 380, 180, 160,  
 200, 200, 200, 120, 120,  
 120, 120, 200, 300, 370,  
 250, 150, 160, 310, 400,  
 500, 600, 600, 1080.

From South to North: 780, 800, 1180, 860, 470,  
 260, 260, 520, 430, 320,  
 320, 320, 240, 260, 260,  
 260, 190, 140, 140, 140,  
 160, 140, 140, 190, 300,  
 360, 220, 220, 220, 320,  
 640, 640.

Drawn by	Date	Coordinates and Dimensions of the Model Area and the Grid Blocks
Checked by	Date	
Revisions	Date	
<b>INTERA Technologies</b>		Table 3.2



Well	Elevation Of The Culebra Dolomite			Thickness Of The Culebra Dolomite* [m]
	Bottom* [m a.s.l.]	Top* [m a.s.l.]	Center* [m a.s.l.]	
H-1	822.3	829.3	825.8	7.0
H-2a	832.4	839.1	835.8	6.7
H-2b	832.6	839.3	836.0	6.7
H-2c	830.5	839.0	834.8	8.5
H-3b1	821.3	828.5	824.9	7.3
H-3b2	819.5	826.8	823.2	7.3
H-3b3	820.3	827.3	823.8	7.0
H-4a	856.8	864.0	860.4	7.3
H-4b	857.9	865.9	861.9	7.9
H-4c	858.2	866.1	862.1	7.9
H-5a	788.2	795.2	791.7	7.0
H-5b	788.1	795.1	791.6	7.0
H-5c	787.0	794.6	790.8	7.6
H-6a	828.7	835.7	832.2	7.0
H-6b	828.8	835.8	832.3	7.0
H-6c	828.9	835.9	832.4	7.0
H-7a	880.4	891.7	886.1	11.3

\* Note: Last figure of reported values is rounded.

Drawn by	Date	Elevation and Thickness of the Culebra Dolomite
Checked by	Date	
Revisions	Date	
<b>INTERA Technologies</b>		Table 3.3a

Well	Elevation Of The Culebra Dolomite			Thickness Of The Culebra Dolomite* [m]
	Bottom* [m a.s.l.]	Top* [m a.s.l.]	Center* [m a.s.l.]	
H-7b	880.4	891.7	886.1	11.3
H-7b2	880.4	891.7	886.1	11.3
H-8b	858.6	866.6	862.6	7.9
H-9a	831.3	840.5	835.9	9.1
H-9b	831.4	840.5	836.0	9.1
H-9c	831.5	840.6	836.0	9.1
H-10b	699.9	709.3	704.6	9.4
H-11b3	807.5	815.2	811.4	7.6
H-12	784.5	792.7	788.6	8.2
DOE-1	798.6	805.6	802.1	7.0
DOE-2	784.0	790.8	787.4	6.8
P-1	847.4	855.6	851.5	8.2
P-2	791.4	799.3	795.4	7.9
P-3	828.3	835.3	831.8	7.0
P-4	802.2	810.4	806.3	8.2
P-5	805.8	812.8	809.3	7.0
P-6	851.6	858.6	855.1	7.0

\* Note: Last figure of reported values is rounded.

Drawn by	Date	Elevation and Thickness of the Culebra Dolomite
Checked by	Date	
Revisions	Date	
<b>INTERA Technologies</b>		Table 3.3b

Well	Elevation Of The Culebra Dolomite			Thickness Of The Culebra Dolomite* [m]
	Bottom* [m a.s.l.]	Top* [m a.s.l.]	Center* [m a.s.l.]	
P-7	856.5	864.4	860.5	7.9
P-8	838.4	846.0	842.2	7.6
P-9	809.1	816.1	812.6	7.0
P-10	777.9	785.8	781.9	7.9
P-11	782.1	790.0	786.1	7.9
P-12	828.4	835.4	831.9	7.0
P-13	828.5	835.5	832.0	7.0
P-14	842.8	849.6	846.2	6.7
P-15	876.1	882.9	879.5	6.7
P-16	851.9	858.9	855.4	7.0
P-17	838.6	846.2	842.4	7.6
P-18	773.5	782.4	777.9	8.8
P-19	776.6	785.8	781.2	9.2
P-20	784.5	792.4	788.5	7.9
WIPP-11	780.0	787.0	783.5	7.0
WIPP-12	803.6	811.2	807.4	7.6
WIPP-13	816.7	823.7	820.2	7.0

\* Note: Last figure of reported values is rounded.

Drawn by	Date	Elevation and Thickness of the Culebra Dolomite
Checked by	Date	
Revisions	Date	
<b>INTERA Technologies</b>		Table 3.3c

Well	Elevation Of The Culebra Dolomite			Thickness Of The Culebra Dolomite* [m]
	Bottom* [m a.s.l.]	Top* [m a.s.l.]	Center* [m a.s.l.]	
WIPP-14	790.3	796.1	793.2	5.8
WIPP-18	807.9	814.6	811.2	6.7
WIPP-19	808.7	816.6	812.6	7.9
WIPP-21	812.6	819.9	816.3	7.3
WIPP-22	811.3	818.0	814.7	6.7
WIPP-25	834.2	843.4	838.8	9.1
WIPP-26	896.6	904.2	900.4	7.6
WIPP-27	870.0	879.2	874.6	9.1
WIPP-28	884.2	892.2	888.2	7.9
WIPP-29	893.7	904.4	899.0	10.7
WIPP-30	844.6	851.6	848.1	7.0
WIPP-33	836.7	845.3	841.0	8.6
WIPP-34	784.0	792.2	788.1	8.2
ERDA-6	853.9	861.8	857.9	7.9
ERDA-9	817.3	824.3	820.8	7.0
CABIN BABY	865.8	871.4	868.6	5.6
AEC-7	843.6	852.3	847.9	8.7
AEC-8	813.2	820.8	817.0	7.6

\* Note: Last figure of reported values is rounded.

Drawn by	Date	Elevation and Thickness of the Culebra Dolomite
Checked by	Date	
Revisions	Date	
<b>INTERA Technologies</b>		Table 3.3d

Fluid Properties

Compressibility of Water	:	$4.53 \times 10^{-10} \text{ m}^2/\text{N}$ (25°C)
Thermal expansion factor of water	:	$2.07 \times 10^{-4} \text{ 1/}^\circ\text{C}$
Heat Capacity of water	:	$4.18 \times 10^3 \text{ J/kg}^\circ\text{C}$
Fluid densities: "water"	:	$1000 \text{ kg/m}^3$
"brine"	:	$2000 \text{ kg/m}^3$
Fluid viscosity:	:	$1 \times 10^{-3} \text{ Pas}$

Rock Properties

Porosity	:	0.2
Compressibility of the pore structure	:	$7.57 \times 10^{-10} \text{ m}^2/\text{N}$
Heat capacity of the rock	:	$8.0 \times 10^2 \text{ J/kg}^\circ\text{C}$
Rock density	:	$2500 \text{ kg/m}^3$

Transport Parameters

Longitudinal dispersivity factor	:	50 m
Transverse dispersivity factor	:	2.5 m
Molecular diffusivity in the porous medium (includes porosity and tortuosity)	:	$2 \times 10^{-10} \text{ m}^2/\text{s}$

Drawn by	Date	Physical Model Constants
Checked by	Date	
Revisions	Date	
<b>INTERA Technologies</b>		Table 3.4

Transmissivity of the Culebra Dolomite

Observation Well	[m <sup>2</sup> /s]	log [m <sup>2</sup> /s]
H-1	7.5 x 10 <sup>-8</sup>	-7.125
H-2	6.0 x 10 <sup>-7</sup>	-6.222
H-3	4.0 x 10 <sup>-6</sup>	-5.398
H-4a	1.4 x 10 <sup>-6</sup>	-5.854
H-4b	1.0 x 10 <sup>-6</sup>	-6.000
H-4c	1.1 x 10 <sup>-6</sup>	-5.959
H-5a	1.8 x 10 <sup>-7</sup>	-6.745
H-5b	2.1 x 10 <sup>-7</sup>	-6.678
H-5c	1.1 x 10 <sup>-7</sup>	-6.959
H-6a	7.8 x 10 <sup>-5</sup>	-4.108
H-6b	8.1 x 10 <sup>-5</sup>	-4.092
H-6c	7.8 x 10 <sup>-5</sup>	-4.108
H-7b	1.2 x 10 <sup>-3</sup>	-2.921
H-8b	7.2 x 10 <sup>-6</sup>	-5.143
H-9b	1.8 x 10 <sup>-4</sup>	-3.745
H-10b	7.5 x 10 <sup>-8</sup>	-7.125
H-11b3	1.1 x 10 <sup>-5</sup>	-4.959
H-12	4.5 x 10 <sup>-8</sup>	-7.347
DOE-1	3.6 x 10 <sup>-5</sup>	-4.444
DOE-2	3.9 x 10 <sup>-5</sup>	-4.409
P-14	2.5 x 10 <sup>-4</sup>	-3.602
P-15	8.9 x 10 <sup>-8</sup>	-7.051
P-17	1.8 x 10 <sup>-6</sup>	-5.745
P-18	2.1 x 10 <sup>-9</sup>	-8.678

Drawn by	Date	Transmissivity of the Culebra Dolomite
Checked by	Date	
Revisions	Date	
<b>INTERA Technologies</b>		Table 3.5a

Transmissivity Of The Culebra Dolomite

Observation Well	[m <sup>2</sup> /s]	log [m <sup>2</sup> /s]
WIPP-25	2.9 x 10 <sup>-4</sup>	-3.538
WIPP-26	1.3 x 10 <sup>-3</sup>	-2.886
WIPP-27	7.0 x 10 <sup>-4</sup>	-3.155
WIPP-28	1.9 x 10 <sup>-5</sup>	-4.721
WIPP-29	1.1 x 10 <sup>-3</sup>	-2.959
WIPP-30	3.2 x 10 <sup>-7</sup>	-6.495

Drawn by	Date
Checked by	Date
Revisions	Date

Transmissivity of the Culebra Dolomite

**INTERA** Technologies

Table 3.5b

Raw Non-Directional Semi-Variogram:

Distance interval (km)	Midpoint (km)	Number of Pairs	$\gamma$ (constant drift)
0 - 3.5	2.286	55	0.9053
3.5 - 5.0	4.355	46	2.1140
5.0 - 6.5	5.170	48	2.3138
6.5 - 10.0	7.991	104	2.3509
10.0 - 12.5	10.792	46	2.5038
12.5 - 15.0	13.595	51	3.6583
15.0 - 20.0	17.022	51	2.8385
> 20.0	22.871	28	

Theoretical Semi-Variogram:

Consistency Check:

Type : exponential  
 :  $\gamma(h = 0) = 0$   
 :  $\gamma(h > 0) = \omega(1 - e^{-h/a}) + c$   
 $\omega$  : 2.05  
 a : 1.30 km  
 c : 0.0

Kriged Average Error : 0.066  
 Kriged Mean Square Error : 1.403  
 Reduced Mean Square Error: 1.007

Range : 3.9 km (3a)  
 Sill : 2.05 ( $\omega + c$ )  
 Nugget: 0.0 (c)

Drawn by	Date	Results of the Semi-Variogram Analysis (Culebra Transmissivities)
Checked by	Date	
Revisions	Date	
<b>INTERA Technologies</b>		Table 3.6



Observation Well	Elevation Of The Culebra Dolomite Center [m.a.s.l.]	Freshwater Head [m.a.s.l.]
H-1	825.8	921.6
H-2b	836.0	923.6
H-3b1	824.9	917.3
H-4b	861.9	913.2
H-5b	791.6	934.4
H-6b	832.3	932.2
H-7b	886.1	912.3
H-8b	862.6	911.5
H-9b	836.0	906.9
H-10b	704.6	920.0
H-11*	811.7	911.1
H-12	788.6	912.0
DOE-1	802.1	913.7
DOE-2	787.4	934.0
P-14	846.2	927.4
P-15	879.5	917.4
P-17	842.4	911.2
WIPP-25	838.8	930.3
WIPP-26	900.4	918.8
WIPP-27	874.6	940.7
WIPP-28	888.2	933.2
WIPP-29	899.0	905.6
WIPP-30	848.1	929.4

\* Average values from H-11b1, H-11b2, and H-11b3

Drawn by	Date	Best Estimate of the Undisturbed Freshwater Heads in the Culebra Dolomite
Checked by	Date	
Revisions	Date	
<b>INTERA Technologies</b>		Table 3.7

Well Or Hydropad	Density [g/cm <sup>3</sup> ]
H-1	1.020
H-2	1.010
H-3	1.040
H-4	1.015
H-5	1.100
H-6	1.040
H-7	1.000
H-8	1.000
H-9	1.000
H-10	1.045
H-11	1.085
H-12	1.095
DOE-1	1.090
DOE-2	1.040
P-14	1.015
P-15	1.015
P-17	1.060
P-18	1.090
WIPP-25	1.010
WIPP-26	1.010
WIPP-27	1.090
WIPP-28	1.035
WIPP-29	1.215
WIPP-30	1.020

Drawn by	Date	Best Estimate of the Undisturbed Formation- Water Densities in the Culebra Dolomite
Checked by	Date	
Revisions	Date	
<b>INTERA Technologies</b>		Table 3.8

Grid Block Index*	Grid Block Elevation** [m a.s.l.]	Freshwater Head [m a.s.l.]	Density [g/cm <sup>3</sup> ]	Formation Pressure [kPa]	Brine Concentration ***
1, 1	889.0	912.2	1.000	328.8	0.000
2, 1	884.5	911.8	1.000	369.0	0.000
3, 1	884.0	911.2	1.010	368.1	0.010
4, 1	884.0	910.9	1.010	365.1	0.010
5, 1	884.0	910.3	1.020	359.2	0.020
6, 1	879.0	909.7	1.030	402.4	0.030
7, 1	869.0	909.3	1.040	496.5	0.040
8, 1	861.0	909.0	1.050	572.0	0.050
9, 1	856.0	908.8	1.050	619.1	0.050
10, 1	853.0	908.6	1.050	646.6	0.050
11, 1	850.0	908.4	1.060	674.0	0.060
12, 1	846.0	908.2	1.060	711.3	0.060
13, 1	843.0	908.0	1.060	738.8	0.060
14, 1	840.0	908.0	1.060	768.2	0.060
15, 1	838.0	907.9	1.070	786.8	0.070
16, 1	836.0	907.9	1.070	806.4	0.070
17, 1	834.0	907.9	1.070	826.0	0.070
18, 1	832.0	907.9	1.070	845.6	0.070
19, 1	829.0	908.0	1.070	876.0	0.070
20, 1	824.0	908.8	1.080	932.9	0.080
21, 1	820.0	909.2	1.080	976.1	0.080
22, 1	817.0	909.8	1.080	1011.4	0.080
23, 1	814.0	910.0	1.090	1042.8	0.090
24, 1	810.0	910.2	1.090	1083.9	0.090
25, 1	804.0	910.4	1.090	1144.7	0.090
26, 1	799.0	910.7	1.090	1196.7	0.090
27, 1	789.0	911.0	1.100	1297.7	0.100
28, 1	779.0	911.5	1.105	1400.7	0.105
29, 1	767.0	912.0	1.105	1523.3	0.105
1,32	849.0	934.2	1.020	936.8	0.020

\* Grid Block 1,1: South-west Corner  
Grid Block 29,1: South-east Corner

\*\* Corresponds to the center of the grid blocks

\*\*\* See explanation for model calculation of formation-water densities (section 5.3.1)

Drawn by	Date	Initial Boundary Conditions
Checked by	Date	
Revisions	Date	
<b>INTERA Technologies</b>		Table 3.9a

Grid Block Index	Grid Block Elevation [m a.s.l.]	Freshwater Head [m a.s.l.]	Density [g/cm <sup>3</sup> ]	Formation Pressure [kPa]	Brine Concentration
2,32	843.0	934.5	1.030	998.6	0.030
3,32	842.0	934.8	1.040	1011.4	0.040
4,32	841.0	934.5	1.040	1018.2	0.040
5,32	833.0	934.0	1.040	1091.8	0.040
6,32	828.0	933.8	1.040	1138.9	0.040
7,32	819.0	933.8	1.040	1227.1	0.040
8,32	810.0	934.2	1.040	1319.3	0.040
9,32	806.0	934.3	1.040	1359.5	0.040
10,32	802.0	934.4	1.040	1399.7	0.040
11,32	798.0	934.5	1.040	1439.9	0.040
12,32	794.0	934.6	1.040	1480.1	0.040
13,32	792.0	934.7	1.040	1500.7	0.040
14,32	790.0	934.8	1.040	1521.3	0.040
15,32	788.0	934.9	1.050	1541.9	0.050
16,32	788.0	935.0	1.050	1542.9	0.050
17,32	788.0	935.0	1.050	1542.9	0.050
18,32	788.0	935.0	1.050	1542.9	0.050
19,32	787.0	935.0	1.060	1552.7	0.060
20,32	787.0	935.0	1.060	1552.7	0.060
21,32	787.0	935.0	1.070	1552.7	0.070
22,32	787.0	935.0	1.070	1552.7	0.070
23,32	787.0	935.0	1.080	1552.7	0.080
24,32	788.0	935.0	1.080	1542.9	0.080
25,32	789.0	935.0	1.090	1533.1	0.090
26,32	793.0	935.0	1.090	1493.9	0.090
27,32	798.0	935.0	1.100	1444.8	0.100
28,32	806.0	935.0	1.105	1366.4	0.105
29,32	813.0	935.0	1.105	1297.7	0.105
1, 2	889.0	913.7	1.000	343.5	0.000
1, 3	894.0	914.4	1.000	301.4	0.000
1, 4	894.0	915.2	1.000	309.2	0.000
1, 5	894.0	916.0	1.010	317.1	0.010
1, 6	893.0	916.5	1.010	331.8	0.010

Drawn by	Date	Initial Boundary Conditions
Checked by	Date	
Revisions	Date	
<b>INTERA Technologies</b>		Table 3.9b

Grid Block Index	Grid Block Elevation [m a.s.l.]	Freshwater Head [m a.s.l.]	Density [g/cm <sup>3</sup> ]	Formation Pressure [kPa]	Brine Concentration
1, 7	893.0	917.0	1.010	336.7	0.010
1, 8	892.0	917.5	1.010	351.4	0.010
1, 9	891.0	918.4	1.010	370.0	0.010
1,10	890.0	919.0	1.010	385.7	0.010
1,11	889.0	919.7	1.010	402.4	0.010
1,12	886.0	920.8	1.010	442.6	0.010
1,13	883.0	922.0	1.010	483.8	0.010
1,14	881.0	923.0	1.010	513.2	0.010
1,15	879.0	923.8	1.010	540.7	0.010
1,16	876.0	924.3	1.010	575.0	0.010
1,17	874.0	925.5	1.010	606.4	0.010
1,18	872.0	925.8	1.010	628.9	0.010
1,19	870.0	926.2	1.010	652.5	0.010
1,20	868.0	926.8	1.010	678.0	0.010
1,21	866.0	927.0	1.010	699.5	0.010
1,22	864.0	927.3	1.010	722.1	0.010
1,23	862.0	927.6	1.010	744.6	0.010
1,24	859.0	928.0	1.010	778.0	0.010
1,25	855.0	928.5	1.010	822.1	0.010
1,26	849.0	929.0	1.010	885.8	0.010
1,27	844.0	929.6	1.010	940.8	0.010
1,28	843.0	930.3	1.010	957.4	0.010
1,29	843.0	930.7	1.010	961.4	0.010
1,30	843.0	931.3	1.020	967.2	0.020
1,31	844.0	932.5	1.020	969.2	0.020
29, 2	768.0	914.0	1.105	1533.1	0.105
29, 3	770.0	916.0	1.105	1533.1	0.105
29, 4	774.0	918.0	1.105	1513.5	0.105
29, 5	777.0	920.0	1.105	1503.7	0.105
29, 6	777.0	921.0	1.105	1513.5	0.105
29, 7	778.0	921.5	1.105	1508.6	0.105
29, 8	778.0	923.0	1.105	1523.3	0.105
29, 9	778.0	924.0	1.105	1533.1	0.105

Drawn by	Date	Initial Boundary Conditions
Checked by	Date	
Revisions	Date	

<b>INTERA</b> Technologies	Table 3.9c
----------------------------	------------

Grid Block Index	Grid Block Elevation [m a.s.l.]	Freshwater Head [m a.s.l.]	Density [g/cm <sup>3</sup> ]	Formation Pressure [kPa]	Brine Concentration
29,10	778.0	925.0	1.105	1542.9	0.105
29,11	777.5	925.5	1.105	1552.7	0.105
29,12	777.0	926.5	1.105	1567.4	0.105
29,13	777.0	927.0	1.105	1572.3	0.105
29,14	776.0	927.5	1.105	1587.0	0.105
29,15	776.0	928.2	1.105	1593.9	0.105
29,16	777.0	928.8	1.105	1599.8	0.105
29,17	777.0	929.2	1.105	1593.9	0.105
29,18	777.0	929.6	1.105	1597.8	0.105
29,19	777.0	930.0	1.105	1601.7	0.105
29,20	778.0	930.3	1.105	1594.9	0.105
29,21	778.0	930.7	1.105	1598.8	0.105
29,22	779.0	931.0	1.105	1591.9	0.105
29,23	779.0	931.3	1.105	1594.9	0.105
29,24	780.0	931.8	1.105	1590.0	0.105
29,25	783.0	932.4	1.105	1566.4	0.105
29,26	786.0	933.0	1.105	1542.9	0.105
29,27	788.0	933.8	1.105	1531.1	0.105
29,28	790.0	934.1	1.105	1514.4	0.105
29,29	792.0	934.2	1.105	1495.8	0.105
29,30	796.0	934.3	1.105	1457.6	0.105
29,31	802.0	934.5	1.105	1400.7	0.105

Drawn by	Date	Initial Boundary Conditions
Checked by	Date	
Revisions	Date	
<b>INTERA Technologies</b>		Table 3.9d

Observation Well	Elevation Of The Culebra Dolomite Center [m.a.s.l.]	Freshwater Head October 1985 [m.a.s.l.]	Difference To Undisturbed Heads [m]
H-1	825.8	909.4	-12.2
H-2b2	835.4	916.5	-7.1*
H-3b1	824.9	909.2	-8.1
H-4b	861.9	911.9	-1.3
H-5b**	791.6	934.4	±0.0
H-6c	832.4	932.3	+0.1***
H-7b	886.1	912.2	-0.1
H-8b	862.6	911.5	±0.0
H-9b	836.0	906.3	-0.6
H-10b	no data available from October 1985		
H-11****	811.7	910.7	-0.4
H-12	788.6	910.9	-1.1
DOE-1	802.1	910.6	-3.1
DOE-2	no data available from October 1985		
P-14	846.2	927.4	±0.0
P-15	879.5	916.8	-0.6
P-17	842.4	910.3	-0.9
WIPP-25	838.8	930.3	±0.0
WIPP-26	900.4	918.7	-0.1
WIPP-27	874.6	940.7	±0.0
WIPP-28	888.2	933.2	±0.0
WIPP-29	899.0	905.6	±0.0
WIPP-30	848.1	929.1	-0.3

\* Difference in freshwater head compared to H-2b (Table 3.7).

\*\* H-5b water-level measurement taken prior to water-quality sampling (August 20-28, 1985) was utilized

\*\*\* Difference in freshwater head compared to H-6b

\*\*\*\* Average values from H-11b1, H-11b2, and H-11b3

Drawn by	Date	Freshwater Heads in the Culebra Dolomite in October 1985
Checked by	Date	
Revisions	Date	
<b>INTERA Technologies</b>		Table 3.10

Observation Well	Observed Freshwater Head [m a.s.l.]	Calculated Freshwater Head [m a.s.l.]	Difference [m]	Squared Difference [m <sup>2</sup> ]
H-1	921.6	926.35	+4.75*	22.56*
H-2b	923.6	927.94	+4.34	18.83
H-3	917.3	923.26	+5.96	35.48
H-4b	913.2	917.78	+4.58	20.94
H-5b	934.4	934.28	-0.12	0.02
H-6b	932.2	933.00	+0.80	0.64
H-7b	912.3	911.95	-0.36	0.13
H-11	911.1	921.97	+10.87	118.20
H-12	912.0	914.46	+2.46	6.03
DOE-1	913.7	923.64	+9.94	98.73
DOE-2	934.0	934.56	+0.57	0.32
P-14	927.4	928.37	+0.97	0.94
P-15	917.4	919.12	+1.72	2.96
P-17	911.2	916.06	+4.86	23.60
SUM :			+51.32	349.36
MEAN :			+3.67	24.95

\* Note: Last figure of reported values is rounded. Therefore, the square root of the squared difference does not exactly equal the reported difference.

Drawn by	Date	The Difference Between the Calculated and the Measured Freshwater Heads for the Initial Steady-State Model Under Undisturbed Conditions
Checked by	Date	
Revisions	Date	
<b>INTERA Technologies</b>		Table 4.1



Observation Well	Observed Freshwater Head [m a.s.l.]	Calculated Freshwater Head [m a.s.l.]	Difference [m]	Squared Difference [m <sup>2</sup> ]
H-1	921.6	921.45	-0.15*	0.02*
H-2b	923.6	924.10	+0.50	0.25
H-3	917.3	917.14	-0.16	0.03
H-4b	913.2	913.33	+0.13	0.02
H-5b	934.4	934.37	-0.03	0.01
H-6b	932.2	932.66	+0.46	0.21
H-7b1	912.3	911.96	-0.34	0.11
H-11	911.1	911.98	+0.88	0.77
H-12	912.0	911.85	-0.15	0.02
DOE-1	913.7	914.22	+0.52	0.27
DOE-2	934.0	934.58	+0.58	0.33
P-14	927.4	927.91	+0.51	0.26
P-15	917.4	917.89	+0.49	0.24
P-17	911.2	910.26	-0.94	0.89
SUM :			+2.30	3.43
MEAN :			+0.16	0.25

\* Note: Last figure of reported values is rounded. Therefore, the square root of the squared difference does not exactly equal the reported difference.

Drawn by	Date	The Difference Between the Calculated and the Measured Freshwater Heads for the Pressure-Calibrated Steady-State Model Under Undisturbed Conditions
Checked by	Date	
Revisions	Date	
<b>INTERA Technologies</b>		Table 4.2

Grid Block Index*	Grid Block Elevation** [m a.s.l.]	Freshwater Head [m a.s.l.]	Density [g/cm <sup>3</sup> ]	Formation Pressure [kPa]	Brine Concentration ***
1, 1	889.0	912.2	1.000	328.8	0.000
2, 1	884.5	911.8	1.000	369.0	0.000
3, 1	884.0	911.2	1.010	368.1	0.010
4, 1	884.0	910.9	1.010	365.1	0.010
5, 1	884.0	910.3	1.020	359.2	0.020
6, 1	879.0	909.7	1.030	402.4	0.030
7, 1	869.0	909.3	1.040	496.5	0.040
8, 1	861.0	909.0	1.050	572.0	0.050
9, 1	856.0	908.7	1.050	618.1	0.050
10, 1	853.0	908.3	1.050	643.6	0.050
11, 1	850.0	908.0	1.060	670.1	0.060
12, 1	846.0	907.7	1.060	706.4	0.060
13, 1	843.0	907.3	1.060	731.9	0.060
14, 1	840.0	907.0	1.060	758.4	0.060
15, 1	838.0	907.0	1.070	778.0	0.070
16, 1	836.0	907.0	1.070	797.6	0.070
17, 1	834.0	907.0	1.070	817.2	0.070
18, 1	832.0	907.0	1.070	836.8	0.070
19, 1	829.0	907.0	1.070	866.2	0.070
20, 1	824.0	907.5	1.080	920.2	0.080
21, 1	820.0	908.0	1.080	964.3	0.080
22, 1	817.0	908.5	1.080	998.6	0.080
23, 1	814.0	909.0	1.090	1032.9	0.090
24, 1	810.0	909.5	1.090	1077.1	0.090
25, 1	804.0	910.0	1.090	1140.8	0.090
26, 1	799.0	910.5	1.090	1194.8	0.090
27, 1	789.0	911.0	1.100	1297.7	0.100
28, 1	779.0	911.5	1.100	1400.7	0.100
29, 1	767.0	912.0	1.100	1523.3	0.100
1, 32	849.0	934.2	1.005	936.8	0.005

\* Grid Block 1,1: South-west Corner

Grid Block 29,1: South-east Corner

\*\* Corresponds to the center of the grid blocks

\*\*\* See explanation for model calculation of formation-water densities (section 3.3.1)

Drawn by	Date	Density-Calibrated Boundary Conditions
Checked by	Date	
Revisions	Date	
<b>INTERA Technologies</b>		Table 4.3a

Grid Block Index	Grid Block Elevation [m a.s.l.]	Freshwater Head [m a.s.l.]	Density [g/cm <sup>3</sup> ]	Formation Pressure [kPa]	Brine Concentration
2,32	843.0	934.5	1.005	998.6	0.005
3,32	842.0	934.8	1.007	1011.4	0.007
4,32	841.0	934.5	1.007	1018.2	0.007
5,32	833.0	934.0	1.039	1091.8	0.039
6,32	828.0	933.8	1.007	1138.9	0.007
7,32	819.0	933.8	1.007	1227.1	0.007
8,32	810.0	934.2	1.017	1319.3	0.017
9,32	806.0	934.3	1.017	1359.5	0.017
10,32	802.0	934.4	1.017	1399.7	0.017
11,32	798.0	934.5	1.017	1439.9	0.017
12,32	794.0	934.6	1.017	1480.1	0.017
13,32	792.0	934.7	1.017	1500.7	0.017
14,32	790.0	934.8	1.017	1521.3	0.017
15,32	788.0	934.9	1.017	1541.9	0.017
16,32	788.0	935.0	1.017	1542.9	0.017
17,32	788.0	935.0	1.035	1542.9	0.035
18,32	788.0	935.0	1.060	1542.9	0.060
19,32	787.0	935.0	1.085	1552.7	0.085
20,32	787.0	935.0	1.085	1552.7	0.085
21,32	787.0	935.0	1.085	1552.7	0.085
22,32	787.0	935.0	1.085	1552.7	0.085
23,32	787.0	935.0	1.085	1552.7	0.085
24,32	788.0	935.0	1.085	1542.9	0.085
25,32	789.0	935.0	1.085	1533.1	0.085
26,32	793.0	935.0	1.085	1493.9	0.085
27,32	798.0	935.0	1.100	1444.8	0.100
28,32	806.0	935.0	1.100	1366.4	0.100
29,32	813.0	935.0	1.100	1297.7	0.000
1, 2	889.0	913.7	1.000	343.5	0.000
1, 3	894.0	914.4	1.000	301.4	0.000
1, 4	894.0	915.2	1.000	309.2	0.000
1, 5	894.0	916.0	1.000	317.1	0.000
1, 6	893.0	916.5	1.000	331.8	0.000

Drawn by	Date	Density-Calibrated Boundary Conditions
Checked by	Date	
Revisions	Date	
<b>INTERA Technologies</b>		Table 4.3b

Grid Block Index	Grid Block Elevation [m a.s.l.]	Freshwater Head [m a.s.l.]	Density [g/cm <sup>3</sup> ]	Formation Pressure [kPa]	Brine Concentration
1, 7	893.0	917.0	1.000	336.7	0.000
1, 8	892.0	917.5	1.000	351.4	0.000
1, 9	891.0	918.4	1.000	370.0	0.000
1,10	890.0	919.0	1.000	385.7	0.000
1,11	889.0	919.7	1.000	402.4	0.000
1,12	886.0	920.8	1.000	442.6	0.000
1,13	883.0	922.0	1.000	483.8	0.000
1,14	881.0	923.0	1.000	513.2	0.000
1,15	879.0	923.8	1.000	540.7	0.000
1,16	876.0	924.3	1.000	575.0	0.000
1,17	874.0	925.5	1.000	606.4	0.000
1,18	872.0	925.8	1.000	628.9	0.000
1,19	870.0	926.2	1.000	652.5	0.000
1,20	868.0	926.8	1.000	678.0	0.000
1,21	866.0	927.0	1.000	699.5	0.000
1,22	864.0	927.3	1.000	722.1	0.000
1,23	862.0	927.6	1.000	744.6	0.000
1,24	859.0	928.0	1.000	778.0	0.000
1,25	855.0	928.5	1.000	822.1	0.000
1,26	849.0	929.0	1.000	885.8	0.000
1,27	844.0	929.6	1.000	940.8	0.000
1,28	843.0	930.3	1.000	957.4	0.000
1,29	843.0	930.7	1.000	961.4	0.000
1,30	843.0	931.3	1.000	967.2	0.000
1,31	844.0	932.5	1.000	969.2	0.000
29, 2	768.0	914.0	1.100	1533.1	0.100
29, 3	770.0	916.0	1.100	1533.1	0.100
29, 4	774.0	918.0	1.100	1513.5	0.100
29, 5	777.0	920.0	1.100	1503.7	0.100
29, 6	777.0	921.0	1.100	1513.5	0.100
29, 7	778.0	921.5	1.100	1508.6	0.100
29, 8	778.0	923.0	1.100	1523.3	0.100
29, 9	778.0	924.0	1.100	1533.1	0.100

Drawn by	Date	Density-Calibrated Boundary Conditions
Checked by	Date	
Revisions	Date	
<b>INTERA Technologies</b>		Table 4.3c

Grid Block Index	Grid Block Elevation [m a.s.l.]	Freshwater Head [m a.s.l.]	Density [g/cm <sup>3</sup> ]	Formation Pressure [kPa]	Brine Concentration
29,10	778.0	925.0	1.100	1542.9	0.100
29,11	777.5	925.5	1.100	1552.7	0.100
29,12	777.0	926.5	1.100	1567.4	0.100
29,13	777.0	927.0	1.100	1572.3	0.100
29,14	776.0	927.5	1.100	1587.0	0.100
29,15	776.0	928.2	1.100	1593.9	0.100
29,16	776.0	928.8	1.100	1599.8	0.100
29,17	777.0	929.2	1.100	1593.9	0.100
29,18	777.0	929.6	1.100	1597.8	0.100
29,19	777.0	930.0	1.100	1601.7	0.100
29,20	778.0	930.3	1.100	1594.9	0.100
29,21	778.0	930.7	1.100	1598.8	0.100
29,22	779.0	931.0	1.100	1591.9	0.100
29,23	779.0	931.3	1.100	1594.9	0.100
29,24	780.0	931.8	1.100	1590.0	0.100
29,25	783.0	932.4	1.100	1566.4	0.100
29,26	786.0	933.0	1.100	1542.9	0.100
29,27	788.0	933.8	1.100	1531.1	0.100
29,28	790.0	934.1	1.100	1514.4	0.100
29,29	792.0	934.2	1.100	1495.8	0.100
29,30	796.0	934.3	1.100	1457.6	0.100
29,31	802.0	934.5	1.100	1400.7	0.100

Drawn by	Date	Density-Calibrated Boundary Conditions
Checked by	Date	
Revisions	Date	
<b>INTERA Technologies</b>		Table 4.3d

Observation Well	Observed Freshwater Head [m a.s.l.]	Calculated Freshwater Head [m a.s.l.]	Difference [m]	Squared Difference [m <sup>2</sup> ]
H-1	921.6	921.14	-0.46*	0.21*
H-2b	923.6	924.08	+0.48	0.23
H-3	917.3	917.34	-0.97	0.93
H-4b	913.2	913.92	-0.28	0.07
H-5b	934.4	934.29	-0.11	0.01
H-6b	932.2	932.57	+0.37	0.13
H-7b1	912.3	911.96	-0.34	0.12
H-11	911.1	912.17	+1.08	1.16
H-12	912.0	911.71	-0.29	0.08
DOE-1	913.7	913.93	+0.23	0.05
DOE-2	934.0	934.21	+0.21	0.05
P-14	927.4	927.67	+0.27	0.07
P-15	917.4	917.96	+0.56	0.32
P-17	911.2	910.13	-1.065	1.14
SUM :			-0.31	4.57
MEAN :			+0.02	0.33

\* Note: Last figure of reported values is rounded. Therefore, the square root of the squared difference does not exactly equal the reported difference.

Drawn by	Date	The Difference Between the Calculated and the Measured Freshwater Heads for the Density-Calibrated Steady-State Model Under Undisturbed Conditions
Checked by	Date	
Revisions	Date	
<b>INTERA Technologies</b>		Table 4.4

Well	Freshwater Heads* in the Magenta Dolomite [m.a.s.l.]	the Culebra Dolomite [m.a.s.l.]	Head Difference [m]	Thickness* of the Tamarisk Member [m]	Hydraulic** Gradient [m/m]
H-1	962.6	920.5	42.1	26.5	1.6
H-2	959.5	924.5	35.0	24.4	1.4
H-3	961.6	914.4	47.2	26.8	1.8
H-4	959.2	913.2	46.0	29.3	1.6
H-6	932.4	933.0	-0.06	28.3	-0.002
WIPP-25	931.2	929.9	1.3	36.3	0.036

\* Data taken from Mercer, 1983.

\*\* Assuming constant density.

Drawn by	Date
Checked by	Date
Revisions	Date

The Hydraulic Gradient in the Tamarisk  
Member in the Western Model Area

**INTERA** Technologies

Table 6.1

Well	Depth (m)	Helium Porosity Initial Value %	Rerun Value %	Grain Density (g/cm <sup>3</sup> )	Horizontal Permeability (md)	Vertical Permeability (md)
H-2b	192.0	14.1		2.80	0.02	0.02
H-2b	192.0	11.5			<0.1; Klp= 0.008	
H-2b	192.0	6.6	(7.3)*			0.02; Klp=0.0085
H-2b	193.8-193.9	16.5	(14.2)	2.78	0.07	0.01
H-2b	194.3	11.8		2.81		
H-2b	195.0-195.1	7.0	(13.6)	2.78	0.19	0.37
H-3b2	207.6	18.8	(20.2)	2.84		4.2 (4.5)
H-3b2	210.1	16.8	(11.3)	2.79		3.3 (4.1)
H-3b3	204.6-204.7	18.5	(17.4)	2.83	10.0	
H-3b3	204.7-204.8	20.9	(19.5)	2.82		1.2
H-3b3	210.1	24.4	(24.1)	2.82		0.53 (0.47)
H-3b3	210.3-210.5	21.3	(19.6)	2.84	2.1	0.56
H-4b	156.4	29.7		2.85		53.0
H-4b	157.6-157.7	19.5	(22.0)	2.84		5.3
H-6b	187.2-187.3	10.8		2.83	0.05	
H-6b	187.4-187.5	11.6		2.83	0.08	0.07
H-6b	187.8	10.7		2.83	0.04	0.05
H-6b	**191.4-195.1	25.5	(20.4)	2.86		1.7 (1.6)

\* All numbers in parentheses refer to rerun values and samples as presented in Core Laboratories (1986b)

\*\* Exact depth unknown due to core loss. Sample depth shows range of possible depths

Klp= Klinkenberg permeability determination

Drawn by	Date	Summary Table of Porosity and Permeability as Determined By Core Laboratories for Selected Samples From the WIPP Site.
Checked by	Date	
Revisions	Date	
<b>INTERA Technologies</b>		Table 7.1



Parameter	Tracer			
	m-TFMB		PFB	
Solute free-water diffusion coefficient (m <sup>2</sup> /s) (includes porosity and tortuosity)	7.4 x 10 <sup>-10</sup>		7.2 x 10 <sup>-10</sup>	
Tortuosity	0.15	0.45	0.15	0.45
Matrix-block length (m)	1.2	2.1	0.25	0.44
Longitudinal dispersivity (m)	3.0		1.5	
Fracture porosity	1.9 x 10 <sup>-3</sup>		1.9 x 10 <sup>-3</sup>	
Matrix porosity	0.2		0.2	

Drawn by	Date	Summary of Best-Fit Input Parameters for m-TFMB and PFB Breakthrough Curves at the H-3 Hydropad (after Kelley and Pickens, 1986)
Checked by	Date	
Revisions	Date	
<b>INTERA Technologies</b>		Table 7.2

Well	T(m <sup>2</sup> /s)	S	λ	ω	Reference
H-3b1	1.94 x 10 <sup>-6</sup>	-7.7	2.4 x 10 <sup>-7</sup>	0.25	Beauheim, in preparation
*H-3b2	1.83 x 10 <sup>-6</sup>	-8.1	1.1 x 10 <sup>-7</sup>	0.03	
H-3b3	1.94 x 10 <sup>-6</sup>	-8.1	1.1 x 10 <sup>-7</sup>	0.03	
H-3b1	3.23 x 10 <sup>-6</sup>	-7.3	4.6 x 10 <sup>-7</sup>	0.25	Beauheim, in preparation
H-3b2	3.23 x 10 <sup>-6</sup>	-7.6	2.5 x 10 <sup>-7</sup>	0.25	
*H-3b3	3.12 x 10 <sup>-6</sup>	-7.8	1.7 x 10 <sup>-7</sup>	0.071	
*DOE-2		-4.7	8.27 x 10 <sup>-8</sup>	0.10	Beauheim, 1986

\* Pumping well during test

T = Transmissivity

S = Wellbore skin

λ = Interporosity flow coefficient

ω = Dimensionless secondary storativity coefficient

Drawn by	Date	Summary of Double-Porosity Hydraulic Parameters for the Culebra Dolomite at the WIPP Site
Checked by	Date	
Revisions	Date	
<b>INTERA Technologies</b>		Table 7.3

Primary Medium

Hydraulic Conductivity :  $2.63 \times 10^{-10}$  m/s  
Porosity : 0.2  
Compressibility :  $6.81 \times 10^{-10}$  m<sup>2</sup>/N  
Matrix Block Length : 2 m

Secondary Medium

Porosity :  $2 \times 10^{-3}$   
Compressibility :  $7.57 \times 10^{-9}$  m<sup>2</sup>/N  
Fracture Spacing : 2 m

Drawn by	Date	Base Case SWIFT II Double-Porosity Model Input Parameters
Checked by	Date	
Revisions	Date	
<b>INTERA Technologies</b>		Table 7.4

		$\tau_e$ (s)		
		$\phi_m$		
		0.1	0.2	0.3
	0.5	2775	5550	8325
$\frac{1}{2}L_m$	1.0	11100	22201	33299
(m)	2.0	44399	88802	133195
	4.0	177596	355208	532779

Matrix porosity range  $\phi_m = 0.1$  to  $0.3$

Matrix block length range  $L_m = 1$  to  $8$  m

Calculations assume:

Hydraulic conductivity of the matrix =  $2.63 \times 10^{-10}$  m/s

Average reservoir fluid density =  $1.05$  g/cm<sup>3</sup>

Drawn by	Date	Calculation of Matrix Time Constants for a Range of Matrix Porosities and Block Half Lengths
Checked by	Date	
Revisions	Date	
<b>INTERA Technologies</b>		Table 7.5

		$\tau_e$ (s)			
		$K_m$ (m/s)			
		$2.6 \times 10^{-10}$	$2.6 \times 10^{-9}$	$2.6 \times 10^{-8}$	$2.6 \times 10^{-7}$
	0.5	5550	555	55	5
	1	22201	2220	222	22
$\frac{1}{2}L_m$	2	88802	8880	888	89
(m)	4	355208	35521	3552	355

Matrix hydraulic conductivity range  $K_m = 2.6 \times 10^{-10}$  to  $2.6 \times 10^{-7}$  m/s  
Matrix block length range  $L_m = 1$  to  $8$  m

Calculations assume:

Matrix porosity = 0.2  
Average reservoir fluid density =  $1.05 \text{ g/cm}^3$

Drawn by	Date
Checked by	Date
Revisions	Date

Calculation of Matrix Time Constants  
for a Range of Matrix Hydraulic  
Conductivities and Block Half Lengths

**INTERA Technologies**

Table 7.6

		$\tau_e$ (s)		
		$C_r'$		
		$6.8 \times 10^{-11}$	$6.8 \times 10^{-10}$	$6.8 \times 10^{-9}$
	0.5	2550	5550	35546
$\frac{1}{2}L_m$	1.0	10201	22201	142183
(m)	2.0	40805	88802	568731
	4.0	163219	355208	2274925

Primary-medium compressibility range  $C_r' = 6.8 \times 10^{-11}$  to  $6.8 \times 10^{-9} \text{ m}^2/\text{N}$

Matrix block length range  $L_m = 1$  to  $8 \text{ m}$

Calculations assume:

Hydraulic conductivity of the matrix =  $2.63 \times 10^{-10} \text{ m/s}$

Average reservoir fluid density =  $1.05 \text{ g/cm}^3$

Drawn by	Date	Calculation of Matrix Time Constants for a Range of Primary-Medium Compressibilities and Matrix Block Half Lengths
Checked by	Date	
Revisions	Date	
<b>INTERA Technologies</b>		Table 7.7



## APPENDIX A: NOTATION FOR SECTION 3.1

### A.1 ROMAN SYMBOLS

$B$	viscosity parameter
$c_C$	coefficient for increase in fluid density with increasing brine content
$c_p$	specific heat of the fluid
$c_{pR}$	specific heat of the rock (single porosity) or of the fracture-fill material (dual porosity)
$c'_{pR}$	specific heat of the rock matrix
$c_R$	compressibility of the pores (single porosity) or of the fractures (dual porosity)
$c'_R$	compressibility of the matrix porosity
$c_T$	coefficient of thermal expansion
$c_W$	compressibility of the fluid
$C'$	concentration of a given component within the rock matrix
$\hat{C}$	concentration of inert contaminant
$\hat{C}'$	concentration of inert contaminant within the rock matrix
$\hat{C}_I$	injected brine concentration
$C_r$	concentration of radioactive (trace) components



- $C'_r$  concentration for radioactive (tracer) components for local (matrix) system
- $D$  dispersion/diffusion coefficient
- $\underline{D}$  dispersion/diffusion tensor
- $D'$  dispersion coefficient within the rock matrix
- $D_m$  molecular diffusion
- $D'_m$  molecular diffusion within the rock matrix
- $D'_{mo}$  molecular diffusion within the rock matrix at the reference temperature
- $\underline{E}_X$  dispersion or conduction/dispersion tensor for heat ( $X = H$ ), brine ( $X = C$ ) or radionuclide ( $X = C$ ) within the global system
- $E'_X$  dispersion or conduction/dispersion coefficient for heat ( $X = H$ ), brine ( $X = C$ ) or radionuclide ( $X = C$ ) within the local (rock-matrix) system
- $g$  acceleration of gravity
- $g_c$  units conversion factor equal to  $g$  for the English system and equal to unity for the SI system
- $H$  fluid enthalpy
- $H'$  fluid enthalpy within the rock matrix
- $H_I$  enthalpy of injected fluid
- $i, j$  x, y or z Cartesian coordinate indices

$\underline{I}$	unit tensor
$\underline{k}$	permeability tensor for the global system
$k'$	permeability coefficient for the local (matrix) system
$k'_{dr}$	equilibrium adsorption distribution coefficient for the rock matrix and radionuclide r
$k_{rs}$	product of branching ratio and daughter-parent mass fraction
$K_m$	heat conductivity
$\underline{K}_m$	heat conductivity tensor for fluid and rock (single porosity) or fluid and fracture-fill material (dual porosity)
$K'_m$	heat conductivity of fluid and rock for the rock matrix
$K'_r$	equilibrium retardation factor for the matrix and radionuclide r
$N$	number of radionuclide parent components
$p$	pressure
$p'$	pressure in the local (matrix) system
$P_0$	reference pressure for system, initial pressure for the unsteady-state aquifer model and aquifer boundary condition for the steady-state aquifer model
$q$	rate of fluid withdrawal

$q_X$  sink/source other than a well for fluid ( $X = W$ ), heat ( $X = H$ ),  
 brine ( $X = C$ ) and radionuclide ( $X = r$ )

$q_{wr}$  radionuclide source due to waste leaching

$r$  subscript for radionuclide

$R$  subscript for rock

$R_C$  brine source rate due to salt dissolution

$R'_C$  fluid source rate due to salt dissolution

$t$  time

$T$  temperature

$T'$  temperature within the rock matrix

$T_R$  reference temperature

$T_O$  reference temperature of system, interface temperature between  
 system and over/underburden and surface temperature for  
 radiation model

$\underline{u}$  Darcy flux vector

$u$  magnitude of  $\underline{u}$

$\underline{u}'$  Darcy flux vector for the local (matrix) system

$u'$  magnitude of  $\underline{u}'$

$U'$  mass-specific internal energy of the fluid within the rock  
 matrix

$U_R$  mass-specific internal energy of the rock (single porosity) or of the fracture-fill material (dual porosity)

$U'_R$  mass-specific internal energy of the rock matrix (dual porosity)

$U_O$  mass-specific internal energy of the fluid at reference fluid conditions

$W$  solid-phase concentration of component

$W_r$  solid-phase concentration of radionuclide  $r$

$x,y,z$  Cartesian coordinates

## A.2 GREEK SYMBOLS

$\alpha_L$	longitudinal dispersivity
$\alpha'_L$	longitudinal dispersivity for the rock matrix
$\alpha_T$	transverse dispersivity
$\Gamma_X$	total loss to the rock matrix for fluid (X = W), heat (X = H), brine (X = C) or radionuclide (X = r)
$\Gamma'_X$	source to the rock-matrix unit for fluid (X = W), heat (X = H), brine (X = C) and radionuclide (X = r)
$\delta'$	fractional change in molecular diffusivity per degree rise in temperature
$\delta_{ij}$	Kronecker delta
$\eta$	Freundlich isotherm parameter
$\kappa$	Freundlich isotherm parameter
$\lambda$	decay constant
$\mu$	viscosity
$\mu'$	viscosity of fluid within the rock matrix
$\mu_R$	viscosity parameter
$\rho$	fluid density
$\rho'$	density of fluid within the rock matrix

- $\rho_I$  fluid density at reference temperature and pressure and unit brine concentration
- $\rho_N$  fluid density at reference temperature and pressure and zero brine concentration
- $\rho_R$  formation density
- $\rho_O$  fluid density for the initial conditions
- $\phi$  porosity
- $\phi'$  porosity of rock matrix
- $\phi_O$  porosity at the reference pressure
- $\phi'_O$  porosity of rock matrix at the reference temperature

### A.3 SUBSCRIPTS

C brine

H heat or enthalpy

r radioactive component

s parent radionuclide component

W water or fluid

X generalized subscript denoting fluid, heat, brine or radionuclide

APPENDIX B: CONVERSION FACTORS

Variable	Metric Unit	Divide by	to Obtain English Unit
Area	m <sup>2</sup>	0.0929	ft <sup>2</sup>
Compressibility	1/Pa	1.4504 E-4	1/psi
Component mass flow rate	kg/s	5.2498 E-6	lb/d
Component transmissibility	kg/s	5.2498 E-6	lb/d
Concentration	fraction	1.0	fraction
Darcy velocity	m/s	3.5278 E-6	ft/d
Density	kg/m <sup>3</sup>	16.018	lb/ft <sup>3</sup>
Diffusivity	m <sup>2</sup> /s	1.0753 E-6	ft <sup>2</sup> /d
Dispersivity	m	0.3048	ft
Distribution coefficient	m <sup>3</sup> /kg	6.2430 E-2	ft <sup>3</sup> /lb
Enthalpy	J	1054.6	Btu
Fluid transmissibility	kg/s	5.2498 E-6	lb/d
Fluid heat capacity	J/kg-°C	4185.0	Btu/lb-°F
Fluid mass flow rate	kg/s	5.2498 E-6	lb/d
Half-life	s	3.1536 E+7	yr
Heat flow rate	J/s	1.2206 E-6	Btu/d
Hydraulic conductivity	m/s	3.5278 E-6	ft/d
Length	m	0.3048	ft
	m	1609.344	mi
Mass	kg	0.45359	lb
Porosity	fraction	1.0	fraction
Pressure	Pa	6894.6	psi
	bar	68.946 E-3	psi
	m (water)	0.7031	psi
Rock heat capacity	J/m <sup>3</sup> -°C	67037.0	Btu/ft <sup>3</sup> -°F
Salt dissolution product	1/s	1.1574 E-5	1/d
Temperature	°C +17.78	0.5556	°F
Thermal conductivity	J/m-s-°C	0.7208	Btu/ft-d-°F
Thermal expansion	1/°C	1.800	1/°F
Thermal transmissibility	J/s-°C	0.4004	Btu/d-°F



Variable	Divide Metric Unit	by	to Obtain English Unit
Time	s	86400	d
Transmissivity	m <sup>2</sup> /s	1.0753 E-6	ft <sup>2</sup> /d
Viscosity	Pa-s	0.001	cp (centipoise)
Volume	m <sup>3</sup>	0.02832	ft <sup>3</sup>
Waste concentration	kg/m <sup>3</sup>	16.018	lb/ft <sup>3</sup>
Well flow rate	m <sup>3</sup> /s	3.2774 E-7	ft <sup>3</sup> /d
	l/min	3.7854	gal/min
	l/s	15.850	gal/min
Well index	m <sup>2</sup> /s	1.0753 E-6	ft <sup>2</sup> /d

APPENDIX C: TRANSMISSIVITIES OF THE CULEBRA DOLOMITE  
(By G. J. Saulnier and A. Haug)

Well	Test Type	Reported Value [m <sup>2</sup> /s]	Source or Reference	Value used for the model [m <sup>2</sup> /s]
H-1	Not Reported	8.6 x 10 <sup>-8</sup>	Seward (1982)	7.5 x 10 <sup>-8</sup>
	Slug	7.5 x 10 <sup>-8</sup>	Mercer (1983)	
H-2	Not Reported	5.4 x 10 <sup>-7</sup>	Seward (1982)	6.0 x 10 <sup>-7</sup>
	Slug	4.3 x 10 <sup>-7</sup>	Mercer (1983)	
	Recirc. Tracer	7.5 x 10 <sup>-7</sup>	Hydro Geo Chem (unpub. estimate)	
H-3	Not Reported	7.5 x 10 <sup>-7</sup>	Seward (1982)	4.0 x 10 <sup>-6</sup>
	Slug	2.0 x 10 <sup>-5</sup>	Mercer (1983)	
	Pumping	1.8 x 10 <sup>-6</sup> - 3.2 x 10 <sup>-6</sup>	Beauheim (in prep.)	
H-4a	Pumping	9.7 x 10 <sup>-7</sup> - 1.8 x 10 <sup>-6</sup>	Gonzalez (1983)	1.4 x 10 <sup>-6</sup>
H-4b	Not Reported	9.2 x 10 <sup>-7</sup>	Seward (1982)	1.0 x 10 <sup>-6</sup>
	Slug	9.7 x 10 <sup>-7</sup>	Mercer (1983)	
	Pumping	3.2 x 10 <sup>-7</sup> - 1.9 x 10 <sup>-6</sup>	Gonzalez (1983)	
H-4c	Pumping	4.3 x 10 <sup>-7</sup> - 1.8 x 10 <sup>-6</sup>	Gonzalez (1983)	1.1 x 10 <sup>-6</sup>
H-5a	Pumping	1.2 x 10 <sup>-7</sup> - 2.1 x 10 <sup>-7</sup>	Gonzalez (1983)	1.8 x 10 <sup>-7</sup>
H-5b	Slug	2.1 x 10 <sup>-7</sup>	Mercer (1983)	2.1 x 10 <sup>-7</sup>
	Pumping	1.3 x 10 <sup>-7</sup> - 2.6 x 10 <sup>-7</sup>	Gonzalez (1983)	
H-5c	Pumping	4.3 x 10 <sup>-8</sup> - 1.7 x 10 <sup>-7</sup>	Gonzalez (1983)	1.1 x 10 <sup>-7</sup>

Well	Test Type	Reported Value [m <sup>2</sup> /s]	Source or Reference	Value used for the model [m <sup>2</sup> /s]
H-6a	Pumping	7.2 x 10 <sup>-5</sup> - 9.3 x 10 <sup>-5</sup>	Gonzalez (1983)	7.8 x 10 <sup>-5</sup>
H-6b	Pumping	7.8 x 10 <sup>-5</sup>	Mercer (1983)	8.1 x 10 <sup>-5</sup>
	Pumping	6.7 x 10 <sup>-5</sup> - 9.5 x 10 <sup>-5</sup>		
H-6c	Pumping	7.5 x 10 <sup>-5</sup> - 8.3 x 10 <sup>-5</sup>	Gonzalez (1983)	7.8 x 10 <sup>-5</sup>
H-7b	Pumping	1.1 x 10 <sup>-3</sup>	Mercer (1983)	1.2 x 10 <sup>-3</sup>
H-7	Pumping	1.2 x 10 <sup>-3</sup>	INTERA (unpub. estimate)	
H-8	Pumping	7.2 x 10 <sup>-6</sup>	INTERA (unpub. estimate)	7.2 x 10 <sup>-6</sup>
H-9	Pumping	2.5 x 10 <sup>-4</sup>	Mercer (1983)	1.8 x 10 <sup>-4</sup>
	Pumping	1.2 x 10 <sup>-4</sup>	INTERA (unpub. estimate)	
H-10b	Slug	7.5 x 10 <sup>-8</sup>	Mercer (1983)	7.5 x 10 <sup>-8</sup>
H-11	Pumping	8.7 x 10 <sup>-6</sup> - 6.6 x 10 <sup>-5</sup>	INTERA (unpub. estimate)	1.1 x 10 <sup>-5</sup>
H-12	Pumping	4.5 x 10 <sup>-8</sup>	INTERA (unpub. estimate)	4.5 x 10 <sup>-8</sup>
DOE-1	Pumping	2.7 x 10 <sup>-5</sup> - 3.6 x 10 <sup>-5</sup>	Gonzalez and Hydro Geo Chem (unpub. data)	3.6 x 10 <sup>-5</sup>
DOE-2	Pumping	3.9 x 10 <sup>-5</sup> *	Beauheim (1986)	3.9 x 10 <sup>-5</sup>

\* preliminary result of interpretation of a 1985 pumping test (available during compilation of transmissivity data base). Evaluation of a pumping test conducted in 1986 indicates a higher value (9.6 x 10<sup>5</sup> m<sup>2</sup>/s).

Well	Test Type	Reported Value [m <sup>2</sup> /s]	Source or Reference	Value used for the model [m <sup>2</sup> /s]
P-14	Pumping Slug	1.5 x 10 <sup>-4</sup> 3.5 x 10 <sup>-4</sup>	Mercer (1983) Hydro Geo Chem (1983, unpub. data)	2.5 x 10 <sup>-4</sup>
P-15	Not Reported Slug	1.1 x 10 <sup>-7</sup> 7.5 x 10 <sup>-8</sup>	Seward (1983) Mercer (1983)	8.9 x 10 <sup>-8</sup>
P-17	Slug	1.1 x 10 <sup>-6</sup> 1.4 x 10 <sup>-6</sup> - 3.2 x 10 <sup>-6</sup>	Mercer (1983) Hydro Geo Chem (1983, unpub. data)	1.8 x 10 <sup>-6</sup>
P-18	Slug Pulse	1.1 x 10 <sup>-9</sup> 3.2 x 10 <sup>-9</sup>	Mercer (1983) Hydro Geo Chem (1983, unpub. data)	2.1 x 10 <sup>-9</sup>
WIPP-25	Pumping	2.9 x 10 <sup>-4</sup>	Mercer (1983)	2.9 x 10 <sup>-4</sup>
WIPP-26	Pumping	1.3 x 10 <sup>-3</sup>	Mercer (1983)	1.3 x 10 <sup>-3</sup>
WIPP-27	Pumping	7.0 x 10 <sup>-4</sup>	Mercer (1983)	7.0 x 10 <sup>-4</sup>
WIPP-28	Pumping	1.9 x 10 <sup>-5</sup>	Mercer (1983)	1.9 x 10 <sup>-5</sup>
WIPP-29	Pumping	1.1 x 10 <sup>-3</sup>	Mercer (1983)	1.1 x 10 <sup>-3</sup>
WIPP-30	Slug Pumping	3.2 x 10 <sup>-7</sup> 2.2 x 10 <sup>-8</sup>	Mercer (1983) Gonzalez (1983)	3.2 x 10 <sup>-7</sup>

References :

Beauheim, R.L., 1986. Hydraulic-Test Interpretations for Well DOE-2 at the Waste Isolation Pilot Plant (WIPP) site; Sandia National Laboratories, SAND 86-1364.

Beauheim, R.L., in preparation. Analysis of Pumping Tests of the Culebra Dolomite Conducted at the H-3 Hydropad at the Waste Isolation Pilot Plant (WIPP) Site. Sandia National Laboratories, SAND86-2311.

Gonzalez, D. D., 1983. Groundwater Flow in the Rustler Formation, Waste Isolation Pilot Plant (WIPP), Southeast New Mexico (SENM): Interim Report. Sandia National Laboratories, SAND 82-1012.

INTERA: Interpretation of data published in:

- Hydro Geo Chem, Inc. 1985. Hydrologic Data Report #1. Sandia National Laboratories, Contractor Report SAND 85-7206.
  
- INTERA Technologies, Inc., and Hydro Geo Chem, Inc., 1985. Hydrologic Data Report #2. Sandia National Laboratories, Contractor Report SAND 85-7263.
  
- INTERA Technologies, Inc., 1986. Hydrologic Data Report #3. Sandia National Laboratories, Contractor Report SAND 86-7103.

Mercer, J. W., 1983. Geohydrology of the Proposed Waste Isolation Pilot Plant Site, Los Medanos Area, Southeastern New Mexico. U.S. Geological Survey Water-Resources Investigation Report 83-4016, 113 p.

Seward, P.D., 1982. Abridged Borehole Histories for the Waste Isolation Pilot Plant (WIPP) Studies. Sandia National Laboratories, SAND 82-0080.



## APPENDIX D: EQUIVALENT FRESHWATER ELEVATIONS

(By G. A. Freeze)

Freshwater heads are useful in identifying hydraulic gradients in aquifers of variable density such as those existing at the WIPP site. Freshwater head at a given point is defined as the height of a column of freshwater that will balance the existing pressure at that point (Luszczynski, 1961). The freshwater column exerts a pressure,  $p$ , at that point equivalent to:

$$p = \rho_f g h_f \quad (D.1)$$

where  $\rho_f$  = density of the freshwater;  
 $h_f$  = freshwater head.

In this report, freshwater heads are indicative of heads above the center of the Culebra dolomite and freshwater elevations are indicative of elevations above mean sea level. Freshwater elevation and freshwater head are related by:

$$Z_f = h_f + Z_c \quad (D.2)$$

where  $Z_f$  = freshwater elevation above mean sea level;  
 $h_f$  = freshwater head;  
 $Z_c$  = elevation of the center of the Culebra dolomite above mean sea level.

Measured water-level data can be converted to equivalent freshwater head from knowledge of the density of the borehole fluid. The fluid pressure in a borehole above a given datum is:

$$p = \rho g h \quad (D.3)$$



where  $\rho$  = average density of the borehole fluid;  
 $h$  = fluid column height above the datum.

Combining equations D.1 and D.3 yields:

$$h_f = \frac{\rho h}{\rho_f} \quad (D.4)$$

If the freshwater density is assumed to be 1.000 g/cm<sup>3</sup>, then the equivalent freshwater head is equal to the fluid column height the average borehole fluid density.

Water-level data have been collected at the WIPP site in two forms: depths to water below top of casing measured by steel tape or electronic sounding device, and pressure measured by downhole transducers. These data have been collected since 1977 by the U.S. Geological Survey, Hydro Geo Chem Inc. (HGC) and INTERA Technologies, Inc.

Depth-to-water data were converted to equivalent freshwater elevation as follows:

$$Z_f = (d_w - d_c) \frac{\rho}{\rho_f} + Z_c \quad (D.5)$$

where  $d_w$  = measured depth to water;  
 $d_c$  = depth to the center of the Culebra dolomite;  
 $\rho$  = average density of the borehole fluid.

Detailed fluid-density logs are required for calculating the exact average borehole-fluid density. Because such density logs were not available for most of the wells at the WIPP site, estimated average density values were used to calculate the freshwater elevations.

Transducer pressure data were converted to equivalent freshwater elevation as follows:

$$Z_f = \frac{p}{g\rho_f} + (d_t - d_c) \frac{\rho}{\rho_f} + Z_c \quad (D.6)$$

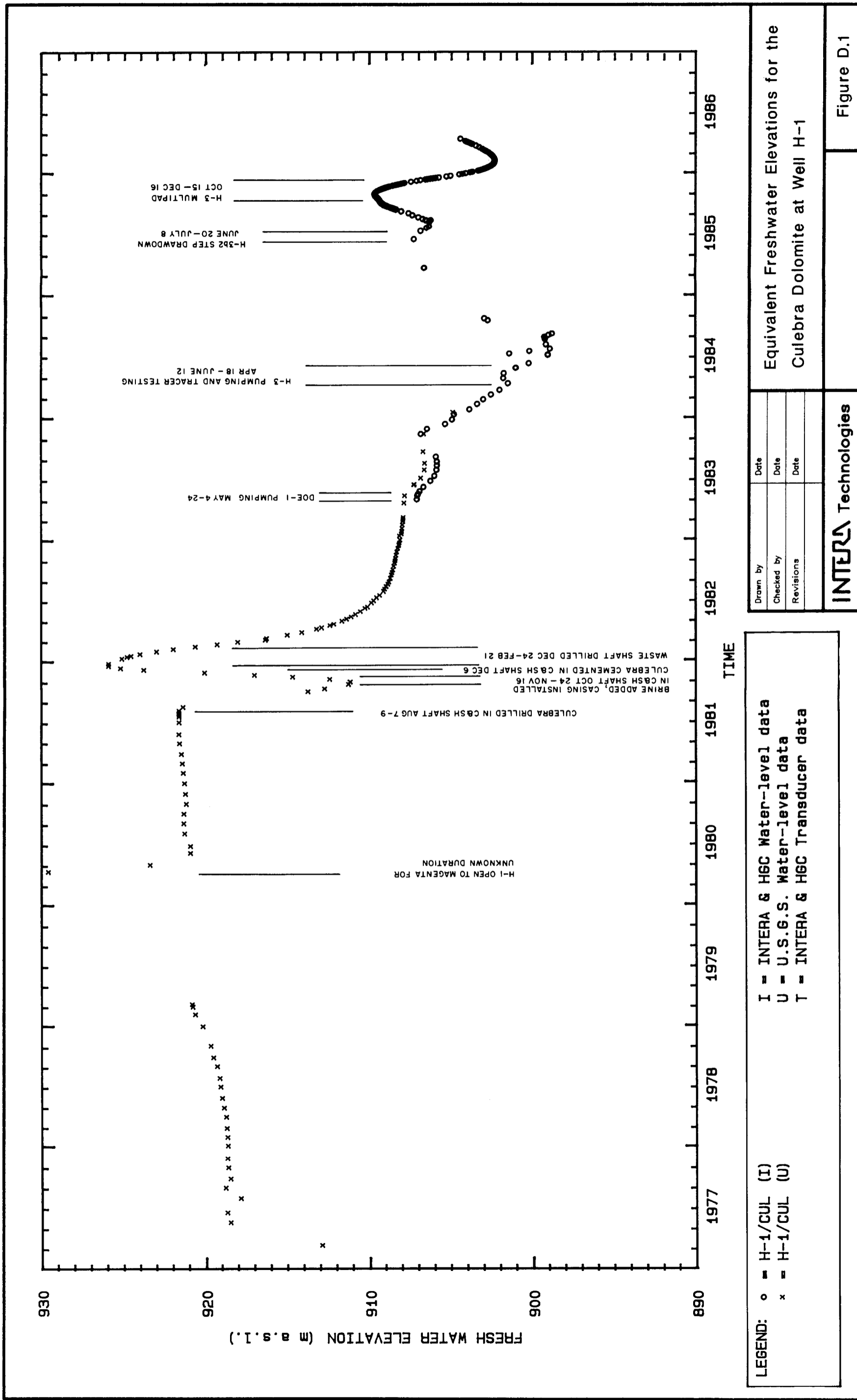
where  $p$  = measured transducer pressure;  
 $d_t$  = depth to transducer;  
 $\rho$  = average density of the borehole fluid.

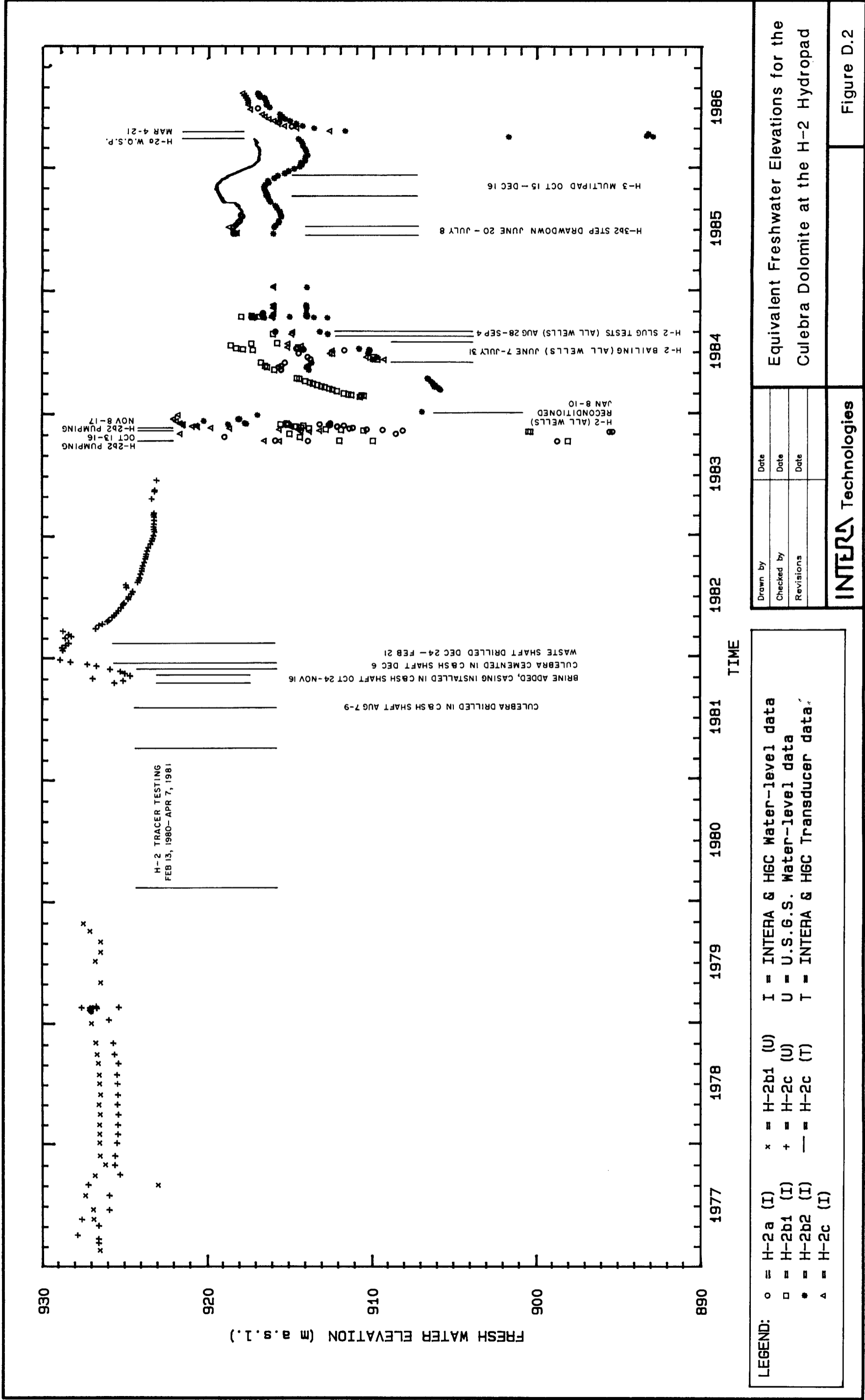
Equivalent freshwater elevations were calculated for all water-level data and the results are plotted in Figures D.1 through D.31. Plots of wells in close proximity to the H-3 hydropad have been annotated. The annotations indicate testing periods that may have influenced water levels and should aid in the interpretation of the freshwater elevations.

#### REFERENCE

Luszczynski, N.J., 1961. Head and flow of ground water of variable density, *Journal of Geophysical Research*, Vol. 66, No. 12, p. 4247-4256.







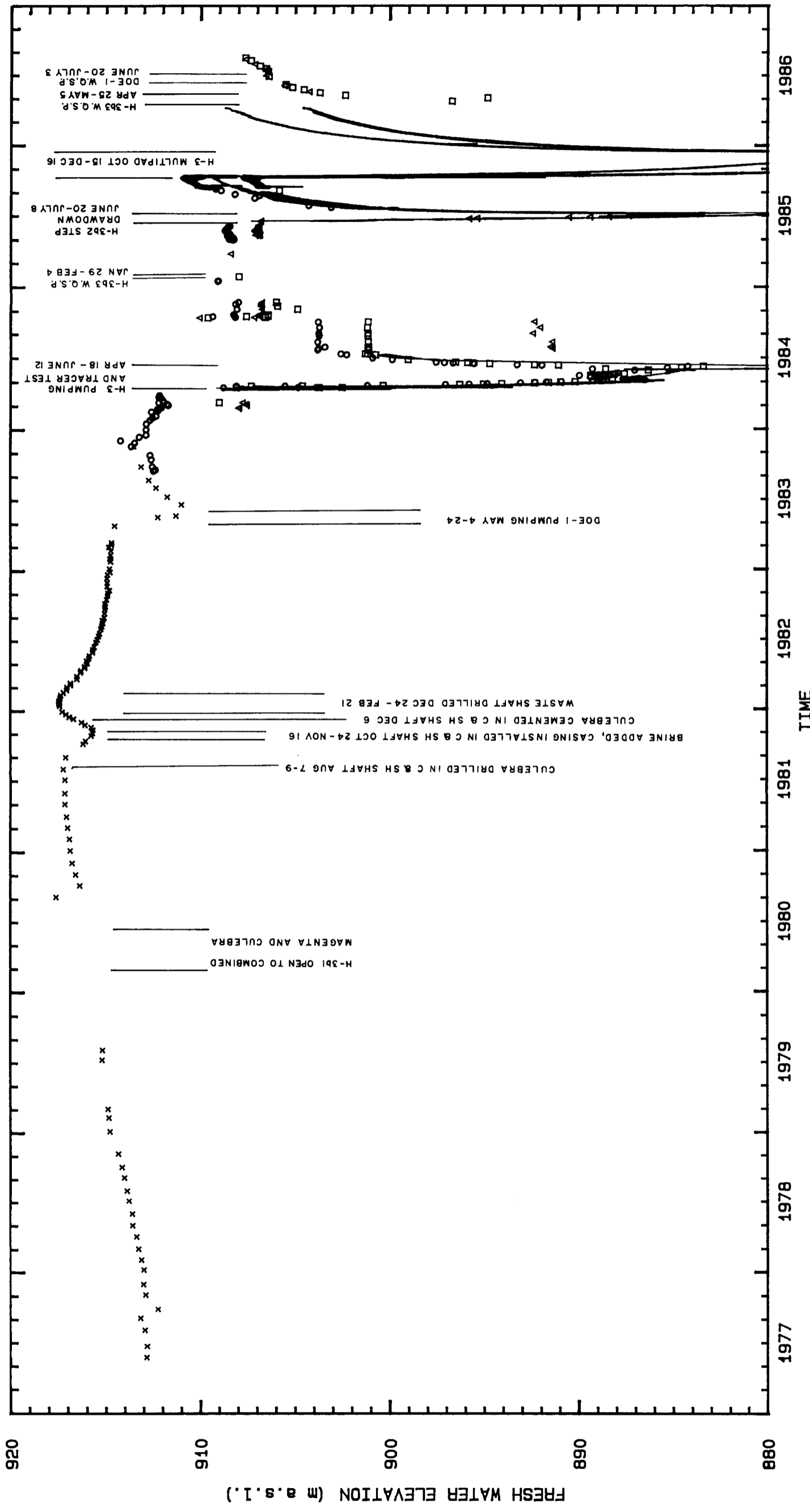
Equivalent Freshwater Elevations for the Culebra Dolomite at the H-2 Hydropad

Figure D.2

Drawn By	Date
Checked By	Date
Revisions	Date

**INTERA Technologies**

LEGEND: ○ = H-2a (I) □ = H-2b1 (I) ● = H-2b1 (U) △ = H-2b2 (I)  
 x = H-2b1 (U) + = H-2c (U) — = H-2c (T) I = INTERA & HGC Water-level data  
 U = U.S.G.S. Water-level data T = INTERA & HGC Transducer data



**LEGEND:**

- = H-3b1 (I)
- = H-3b2 (I)
- △ = H-3b3 (I)
- x = H-3b1 (U)
- = H-3b1 (T)
- = H-3b2 (T)
- = H-3b3 (T)

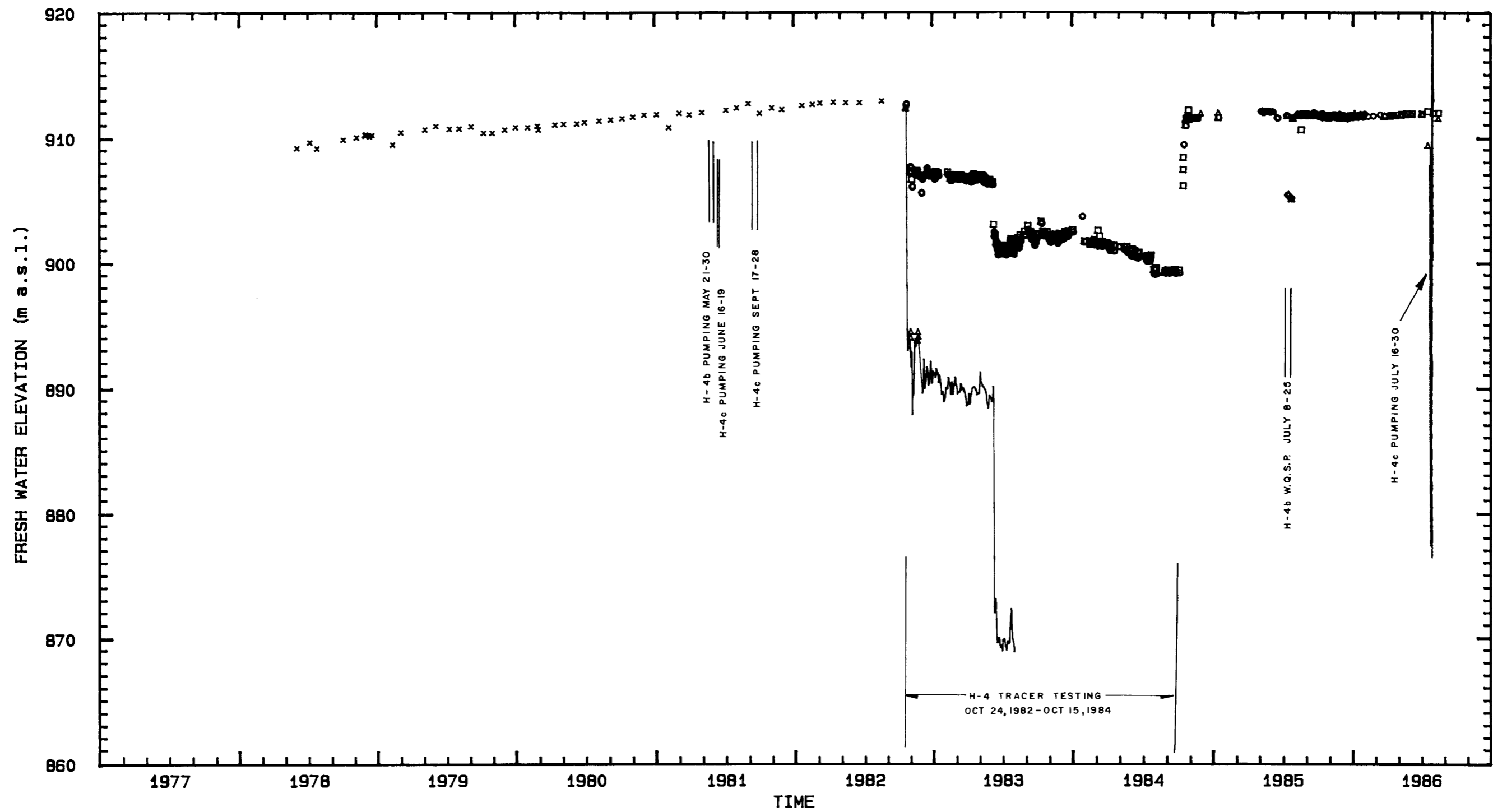
I = INTERA & HGC Water-level data  
 U = U.S.G.S. Water-level data  
 T = INTERA & HGC Transducer data

Drawn by	Date
Checked by	Date
Revisions	Date

**INTERA Technologies**

Equivalent Freshwater Elevations for the Culebra Dolomite at the H-3 Hydropad

Figure D.3



**LEGEND:**

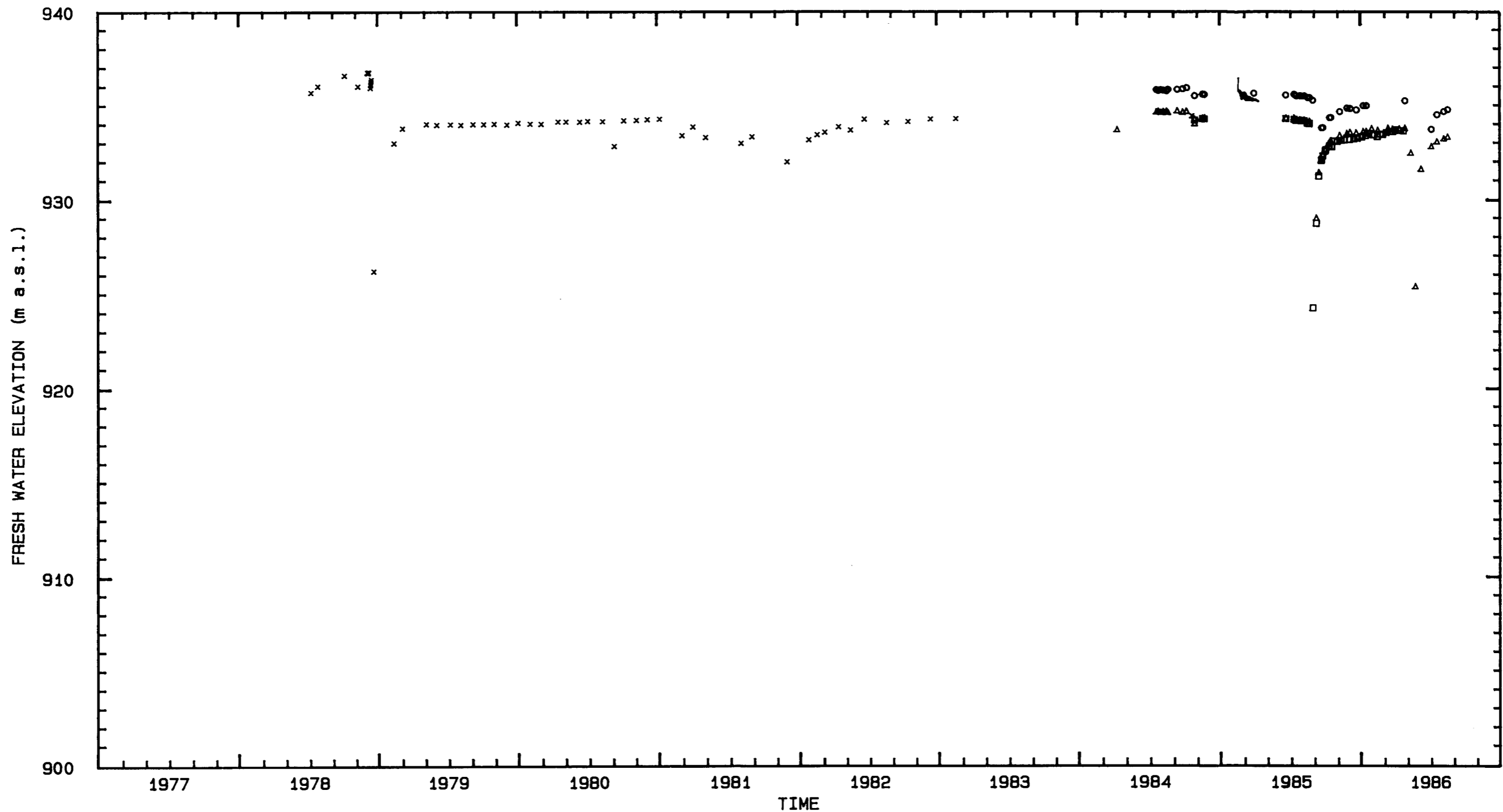
○ = H-4a (I)	— = H-4b (T)	I = INTERA & HGC Water-level data
□ = H-4b (I)	— = H-4c (T)	U = U.S.G.S. Water-level data
△ = H-4c (I)		T = INTERA & HGC Transducer data
x = H-4b (U)		

Drawn by	Date
Checked by	Date
Revisions	Date

Equivalent Freshwater Elevations for the Culebra Dolomite at the H-4 Hydropad

**INTERA** Technologies

Figure D.4



**LEGEND:**    ○ = H-5a (I)    — = H-5b (T)    I = INTERA & HGC Water-level Data  
                  □ = H-5b (I)                                    U = U.S.G.S. Water-level Data  
                  △ = H-5c (I)                                    T = INTERA & HGC Transducer Data  
                  × = H-5b (U)

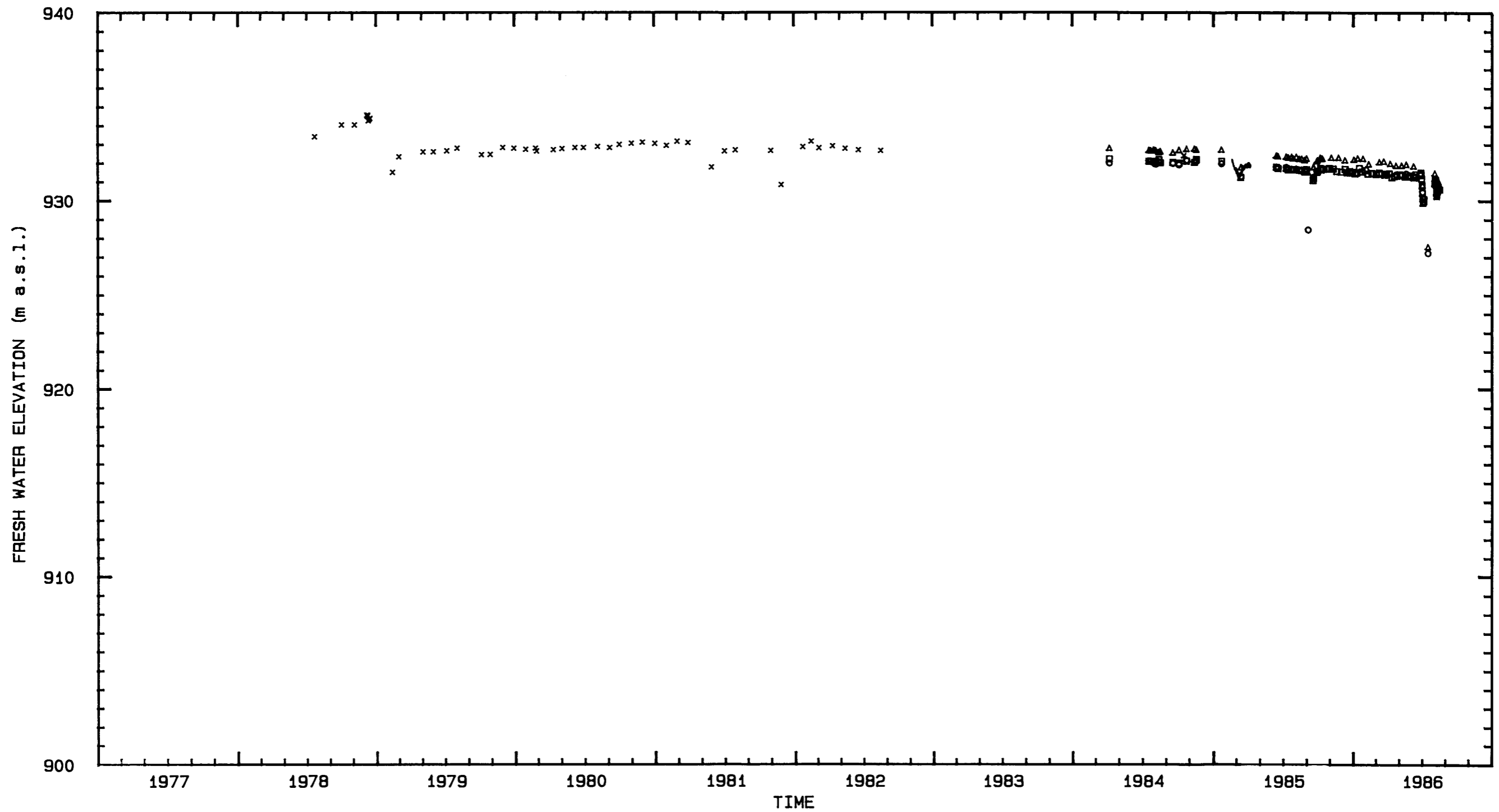
Drawn by	Date
Checked by	Date
Revisions	Date

Equivalent Freshwater Elevations for the  
 Culebra Dolomite at the H-5 Hydropad

**INTERA Technologies**

Figure D.5





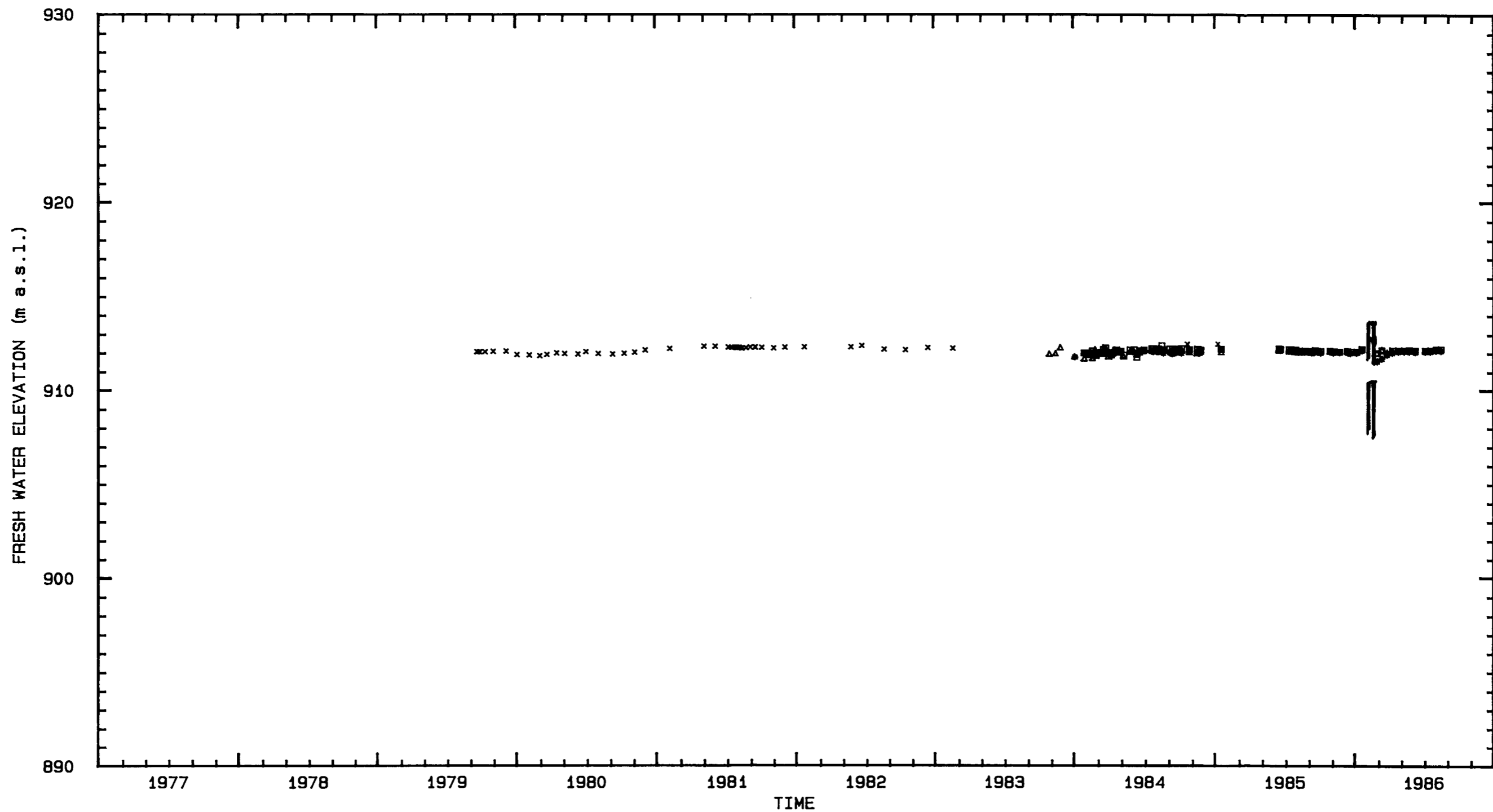
**LEGEND:** ○ = H-6a (I)    — = H-6b (T)    I = INTERA & HGC Water-level Data  
 □ = H-6b (I)                                    U = U.S.G.S. Water-level Data  
 △ = H-6c (I)                                    T = INTERA & HGC Transducer Data  
 × = H-6b (U)

Drawn by	Date
Checked by	Date
Revisions	Date

Equivalent Freshwater Elevations for the  
 Culebra Dolomite at the H-6 Hydropad

**INTERA** Technologies

Figure D.6



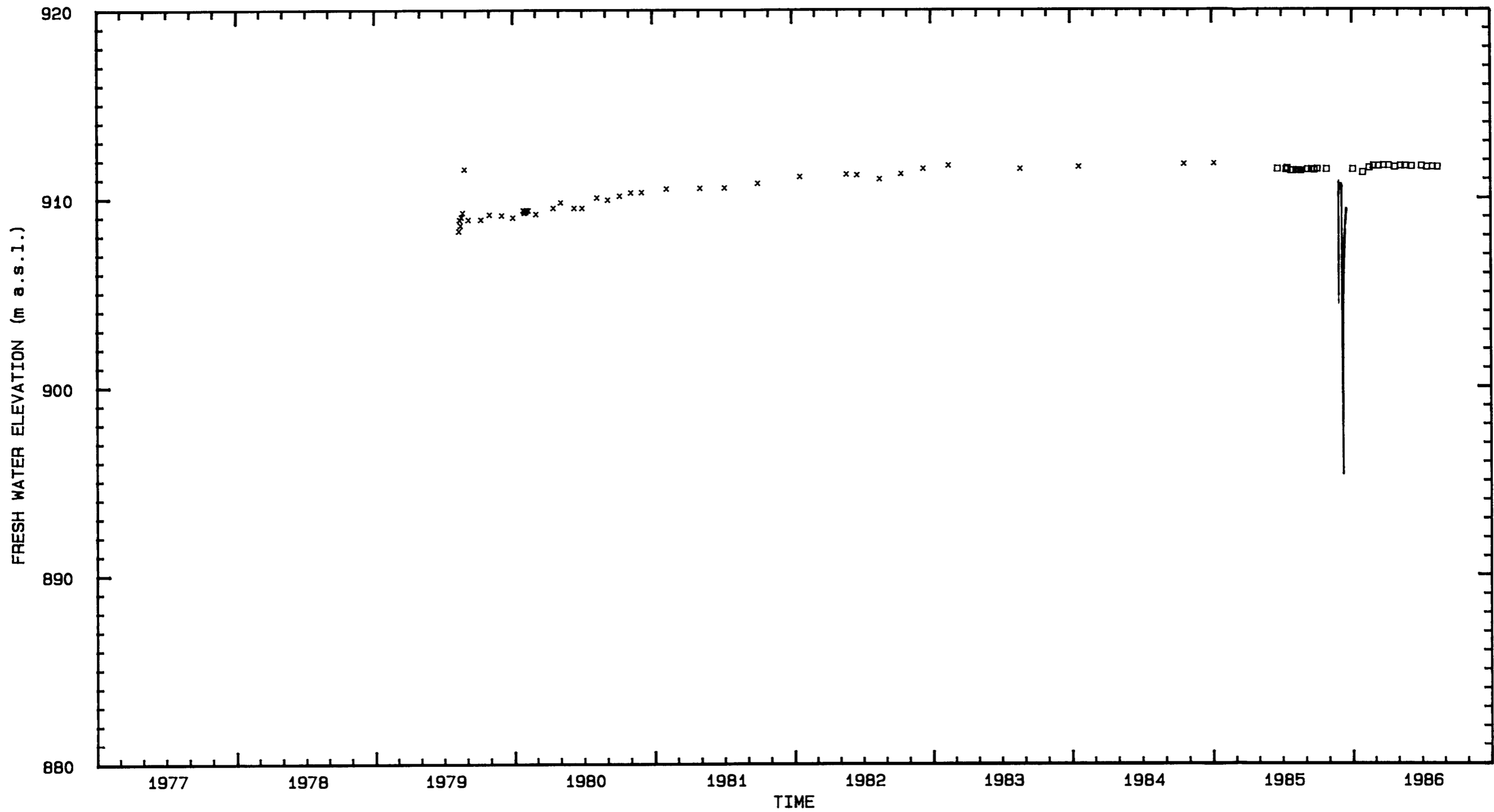
LEGEND: □ = H-7b (I)    — = H-7b (T)    I = INTERA & HGC Water-level Data  
 \* = H-7b2 (I)    — = H-7b2 (T)    U = U.S.G.S. Water-level Data  
 △ = H-7c (I)    — = H-7c (T)    T = INTERA & HGC Transducer Data  
 x = H-7b2 (U)

Drawn by	Date
Checked by	Date
Revisions	Date

Equivalent Freshwater Elevations for the  
 Culebra Dolomite at the H-7 Hydropad

**INTERA** Technologies

Figure D.7



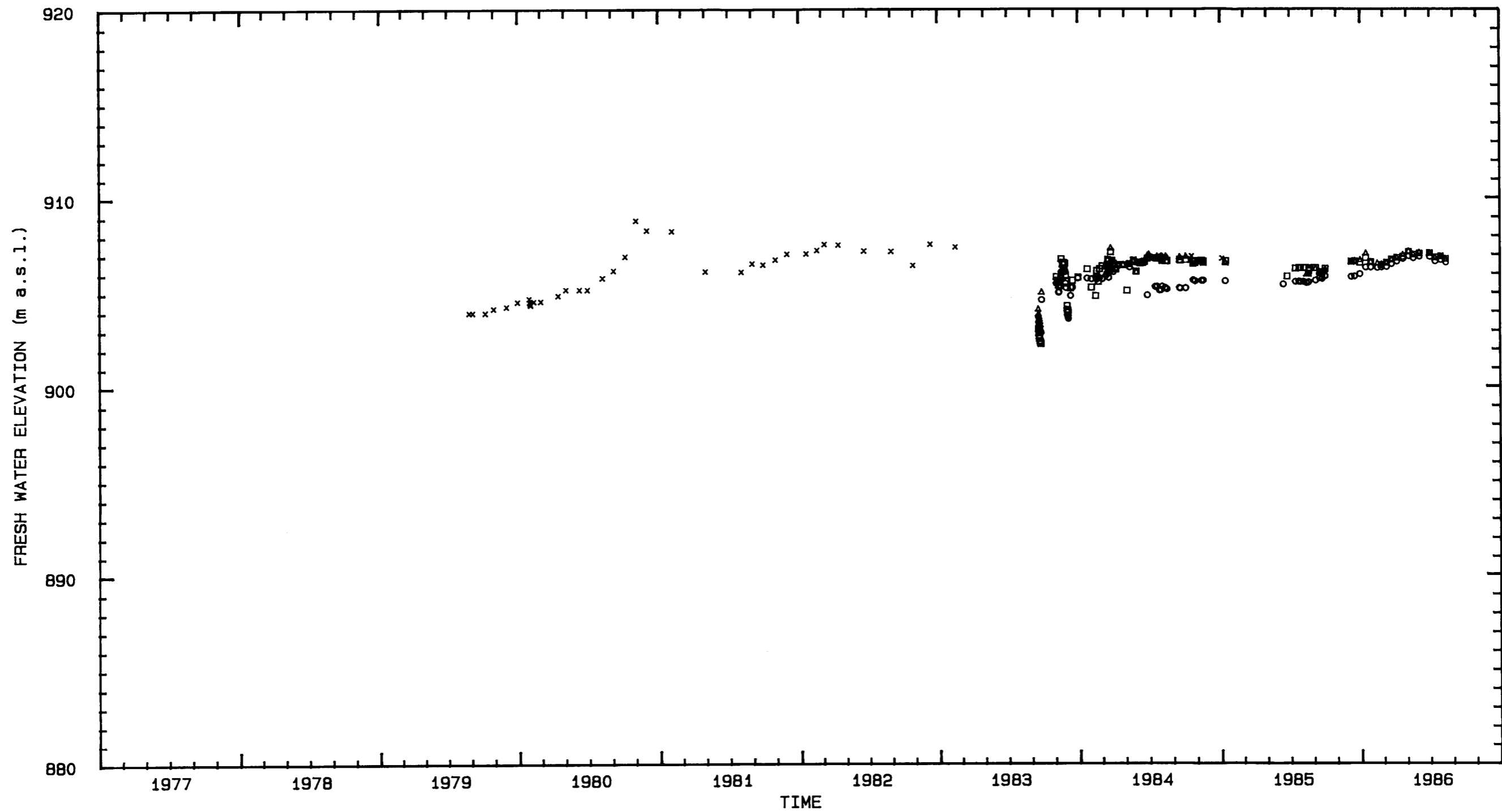
LEGEND: □ = H-8b (I)      I = INTERA & HGC Water-level Data  
 × = H-8b (U)      U = U.S.G.S. Water-level Data  
 — = H-8b (T)      T = INTERA & HGC Transducer Data

Drawn by	Date
Checked by	Date
Revisions	Date

Equivalent Freshwater Elevations for the  
 Culebra Dolomite at the H-8 Hydropad

**INTERA** Technologies

Figure D.8



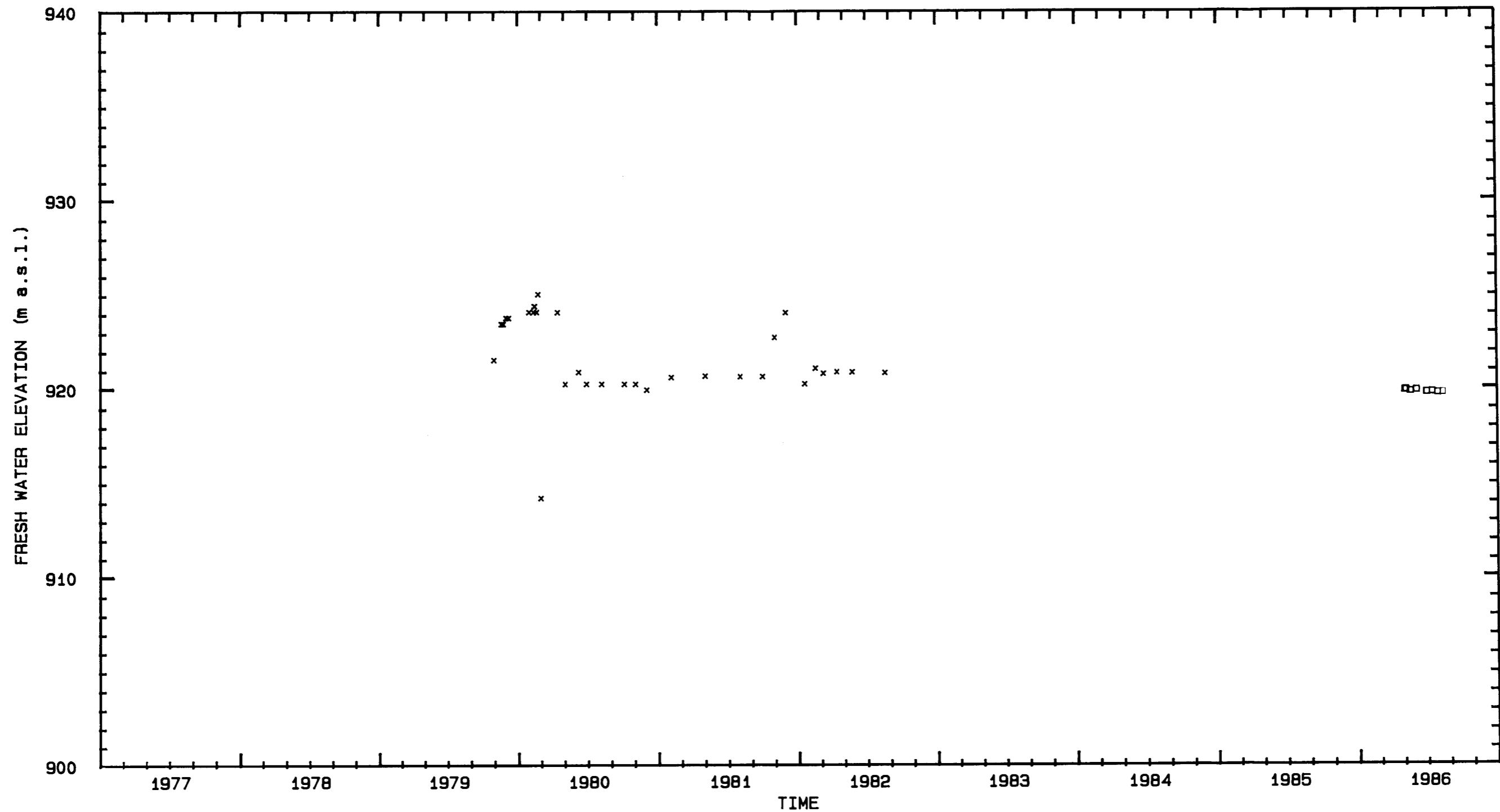
**LEGEND:**  
 ○ = H-9a (I)  
 □ = H-9b (I)  
 △ = H-9c (I)  
 × = H-9b (U)  
 I = INTERA & HGC Water-level Data  
 U = U.S.G.S. Water-level Data  
 T = INTERA & HGC Transducer Data

Drawn by	Date
Checked by	Date
Revisions	Date

Equivalent Freshwater Elevations for the Culebra Dolomite at the H-9 Hydropad

**INTERA** Technologies

Figure D.9



LEGEND: □ = H-10b (I)  
 x = H-10b (U)

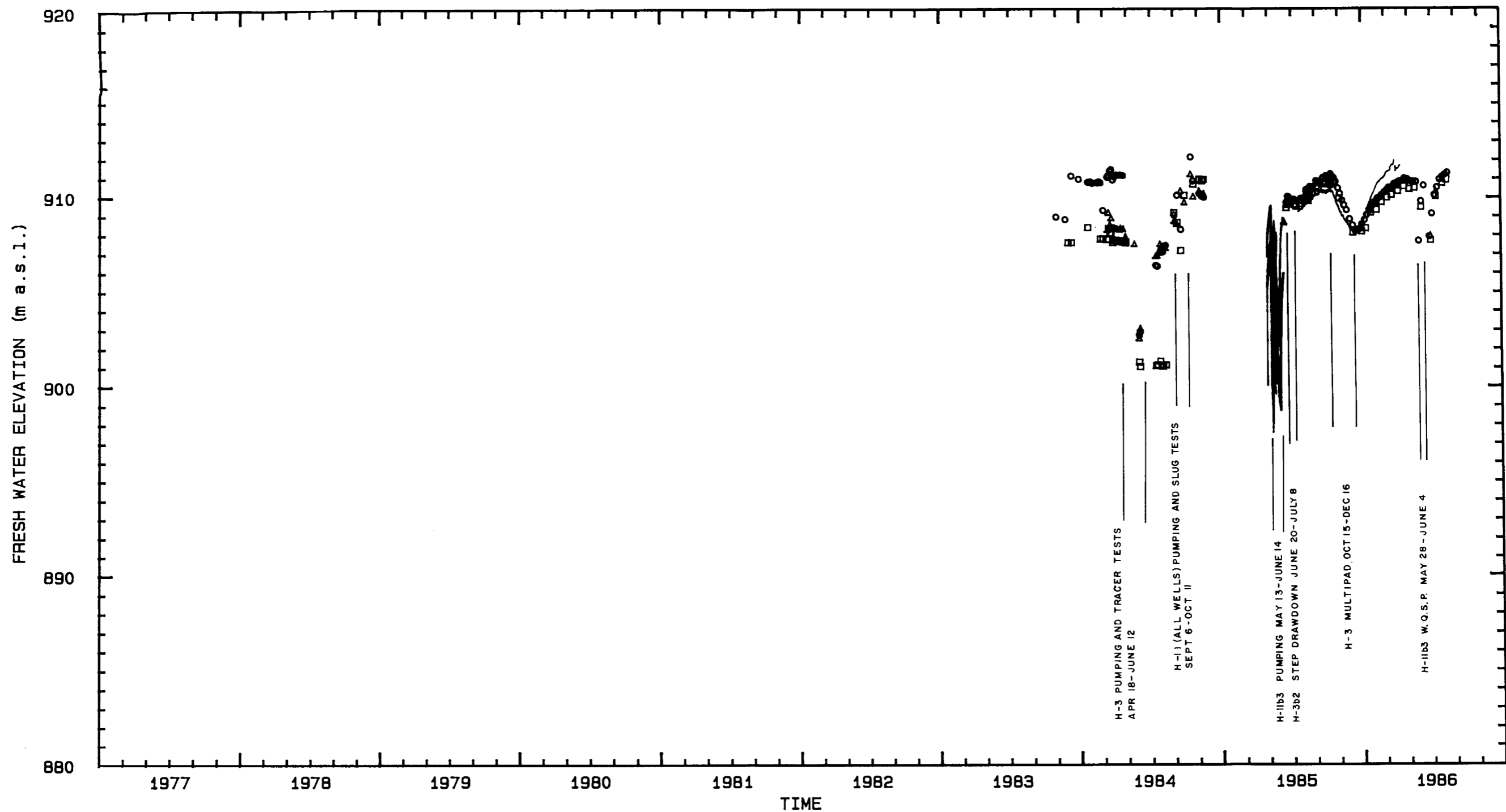
I = INTERA & HGC Water-level Data  
 U = U.S.G.S. Water-level Data  
 T = INTERA & HGC Transducer Data

Drawn by	Date
Checked by	Date
Revisions	Date

Equivalent Freshwater Elevations for the  
 Culebra Dolomite at the H-10 Hydropad

**INTERA** Technologies

Figure D.10



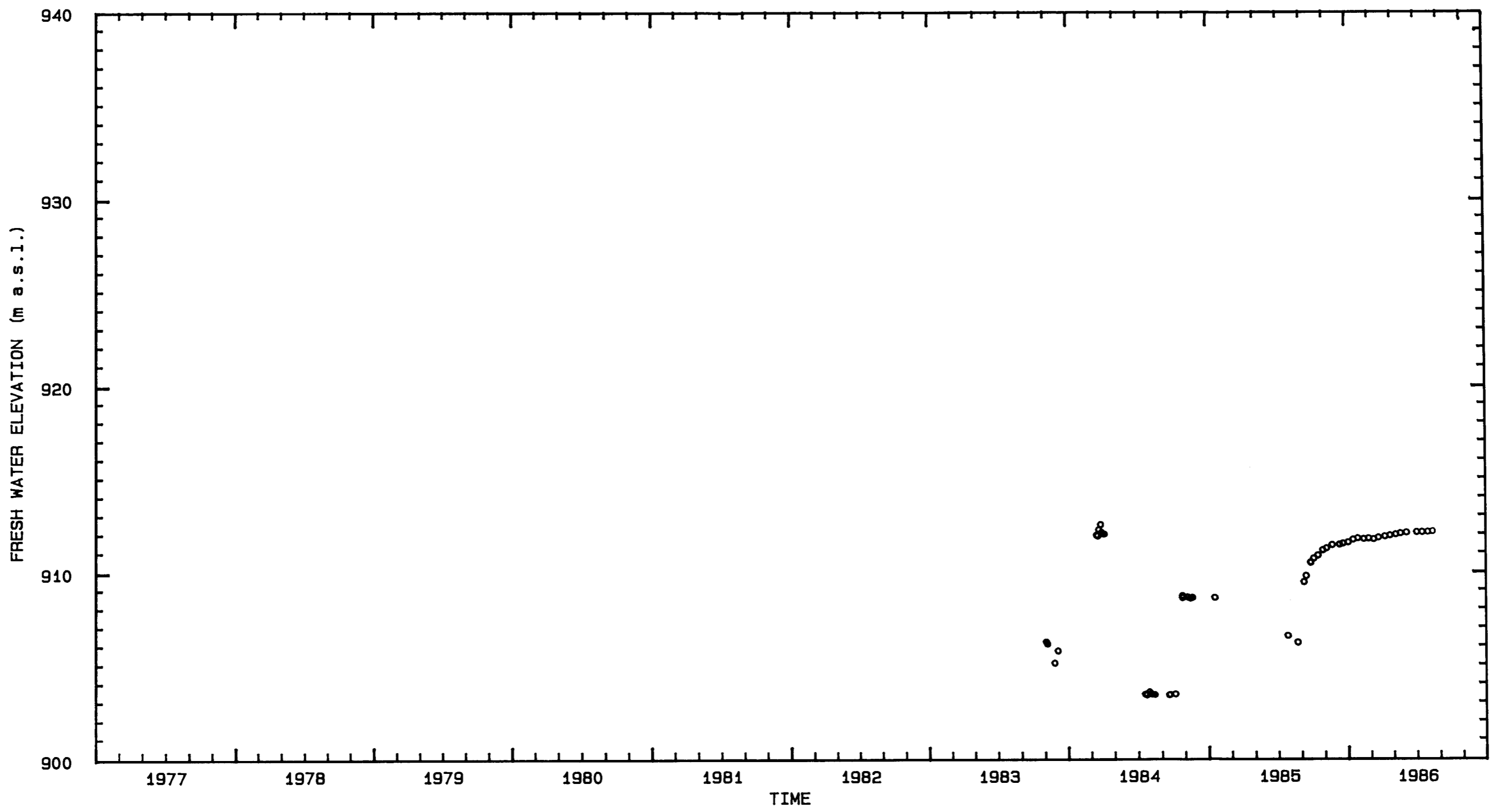
LEGEND: ○ = H-11b1 (I) — = H-11b1 (T) I = INTERA & HGC Water-level data  
 □ = H-11b2 (I) — = H-11b2 (T) U = U.S.G.S. Water-level data  
 △ = H-11b3 (I) — = H-11b3 (T) T = INTERA & HGC Transducer data

Drawn by	Date
Checked by	Date
Revisions	Date

Equivalent Freshwater Elevations for the Culebra Dolomite at the H-11 Hydropad

**INTERA** Technologies

Figure D.11



LEGEND: ○ = H-12 (I)

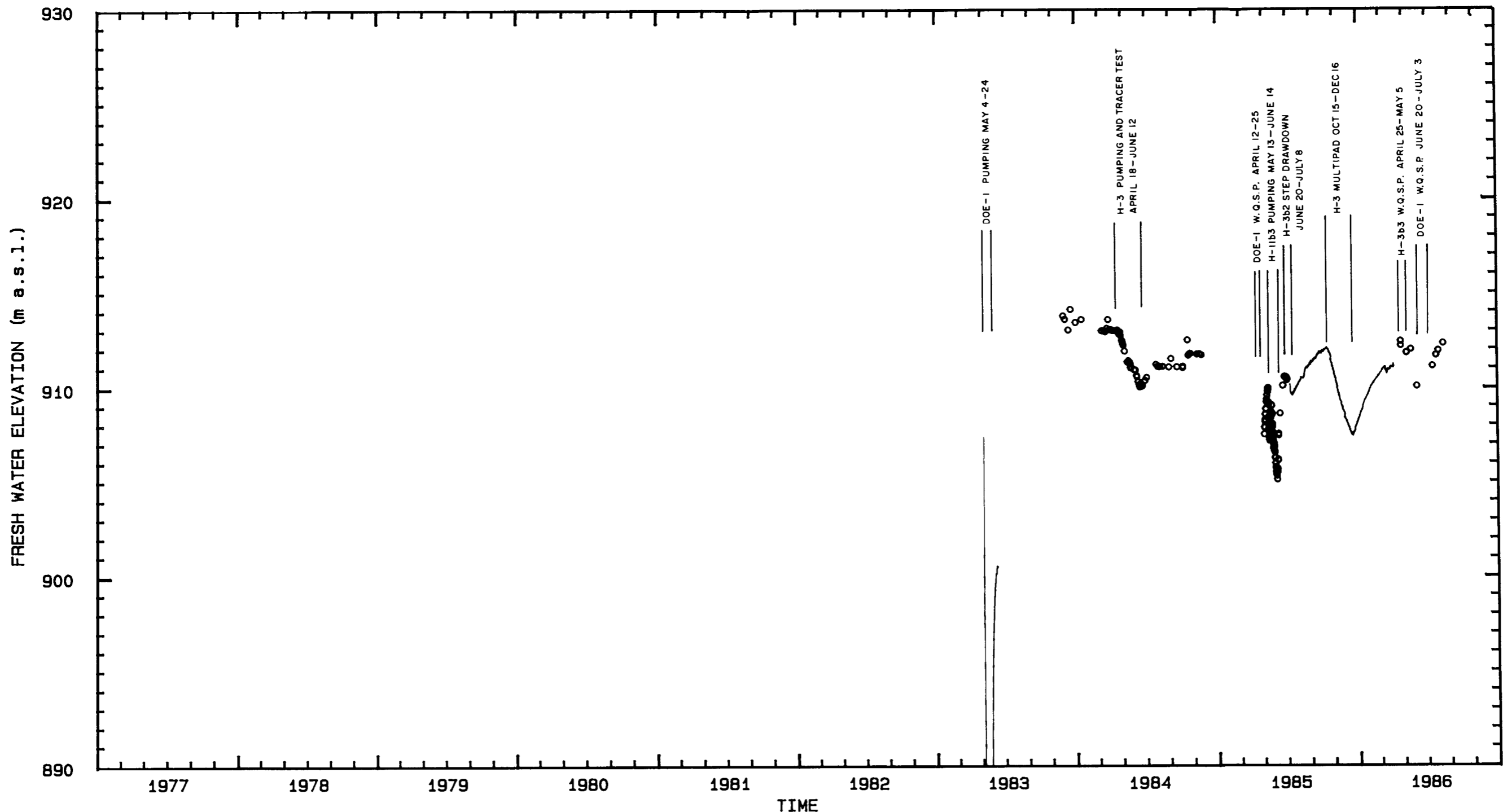
I = INTERA & HGC Water-level data  
 U = U.S.G.S. Water-level data  
 T = INTERA & HGC Transducer data

Drawn by	Date
Checked by	Date
Revisions	Date

Equivalent Freshwater Elevations for the  
 Culebra Dolomite at Well H-12

**INTERA** Technologies

Figure D.12



LEGEND: ○ = DOE-1 (I)      I = INTERA & HGC Water-level data  
 — = DOE-1 (T)      U = U.S.G.S. Water-level data  
                              T = INTERA & HGC Transducer data

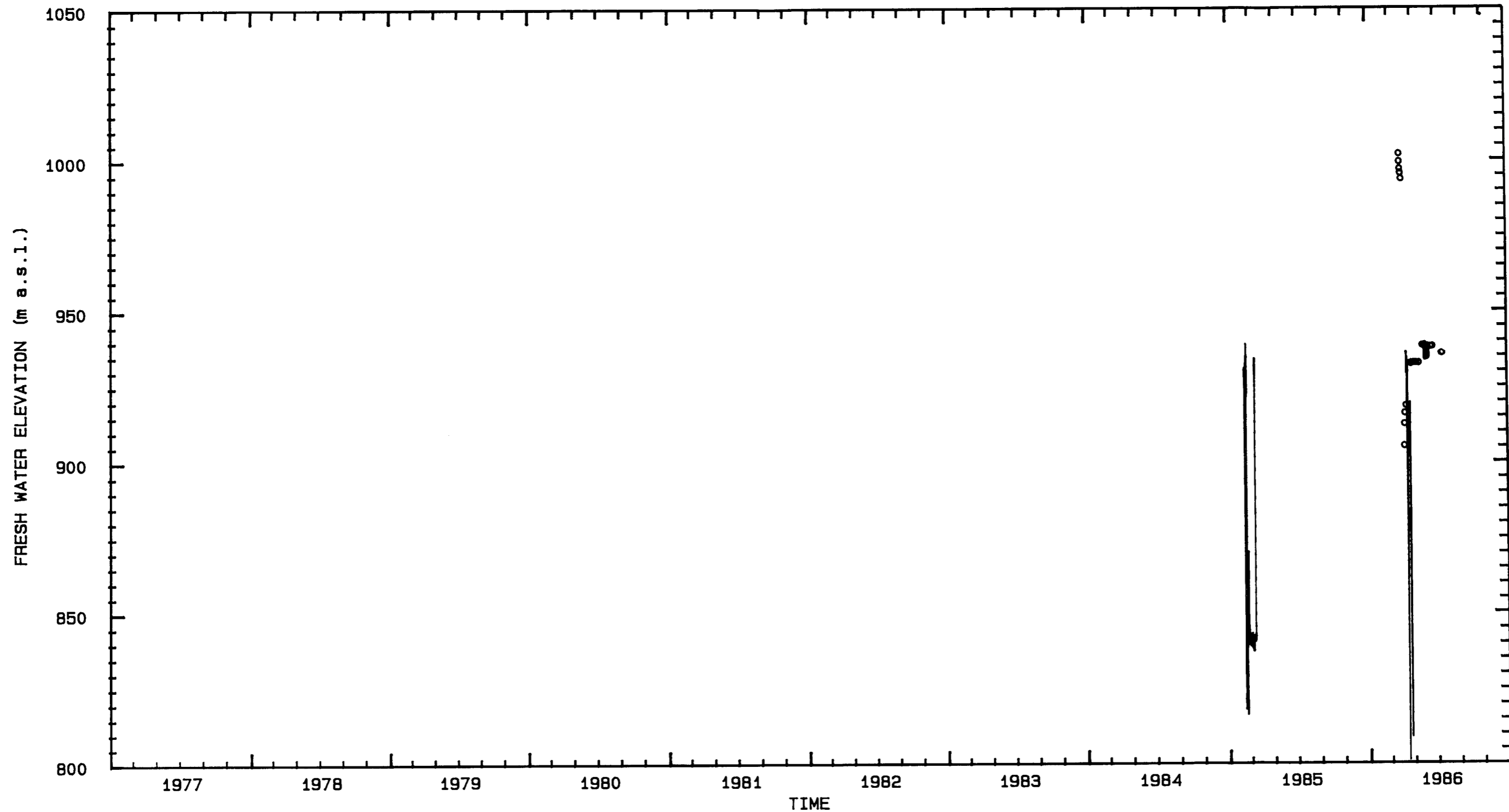
Drawn by	Date
Checked by	Date
Revisions	Date

Equivalent Freshwater Elevations for the  
 Culebra Dolomite at Well DOE-1

**INTERA** Technologies

Figure D.13





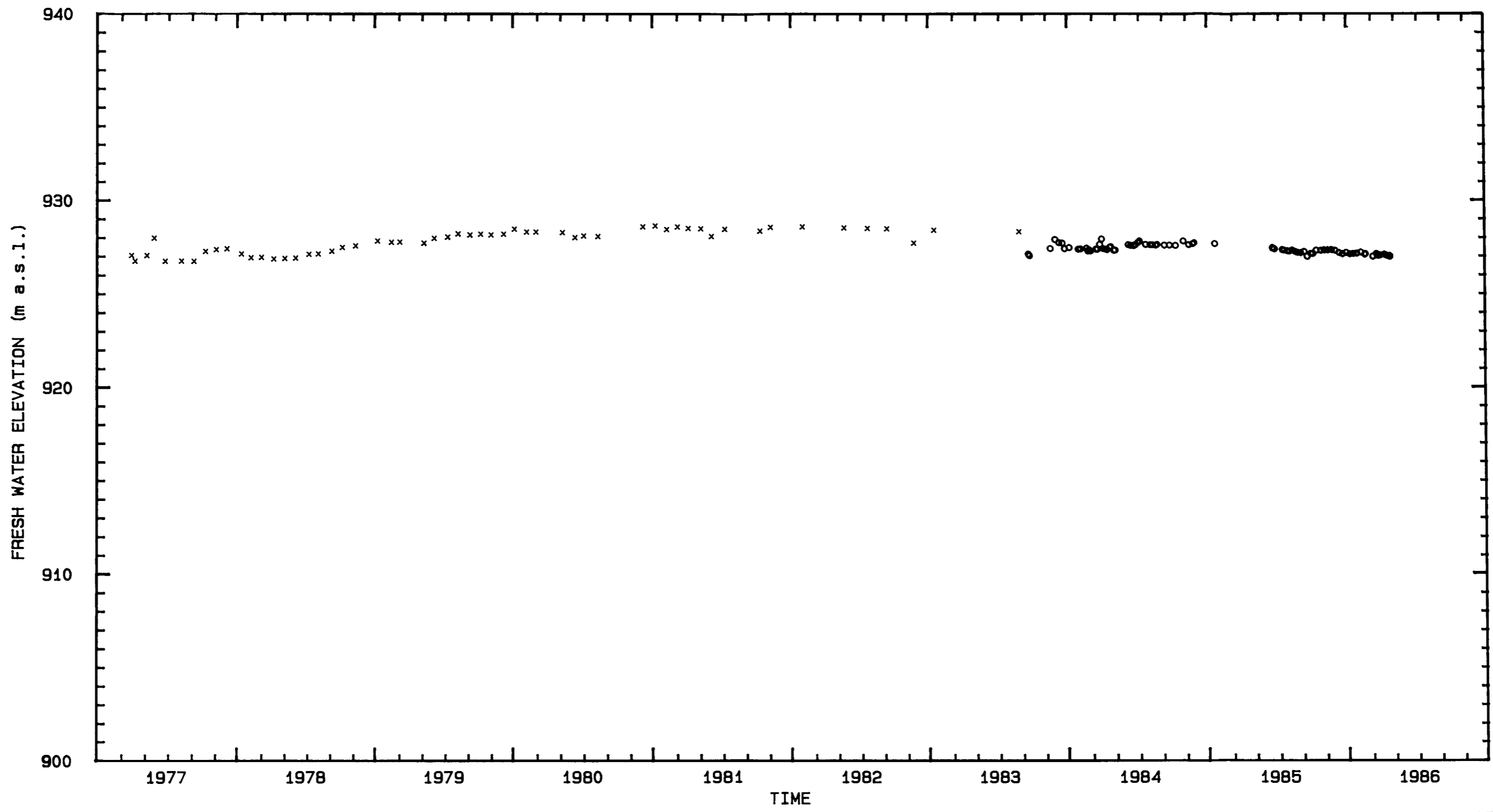
LEGEND: ○ = DOE-2 (I)      I = INTERA & HGC Water-level data  
 — = DOE-2 (T)      U = U.S.G.S. Water-level data  
                                  T = INTERA & HGC Transducer data

Drawn by	Date
Checked by	Date
Revisions	Date

Equivalent Freshwater Elevations for the  
 Culebra Dolomite at Well DOE-2

**INTERA** Technologies

Figure D.14



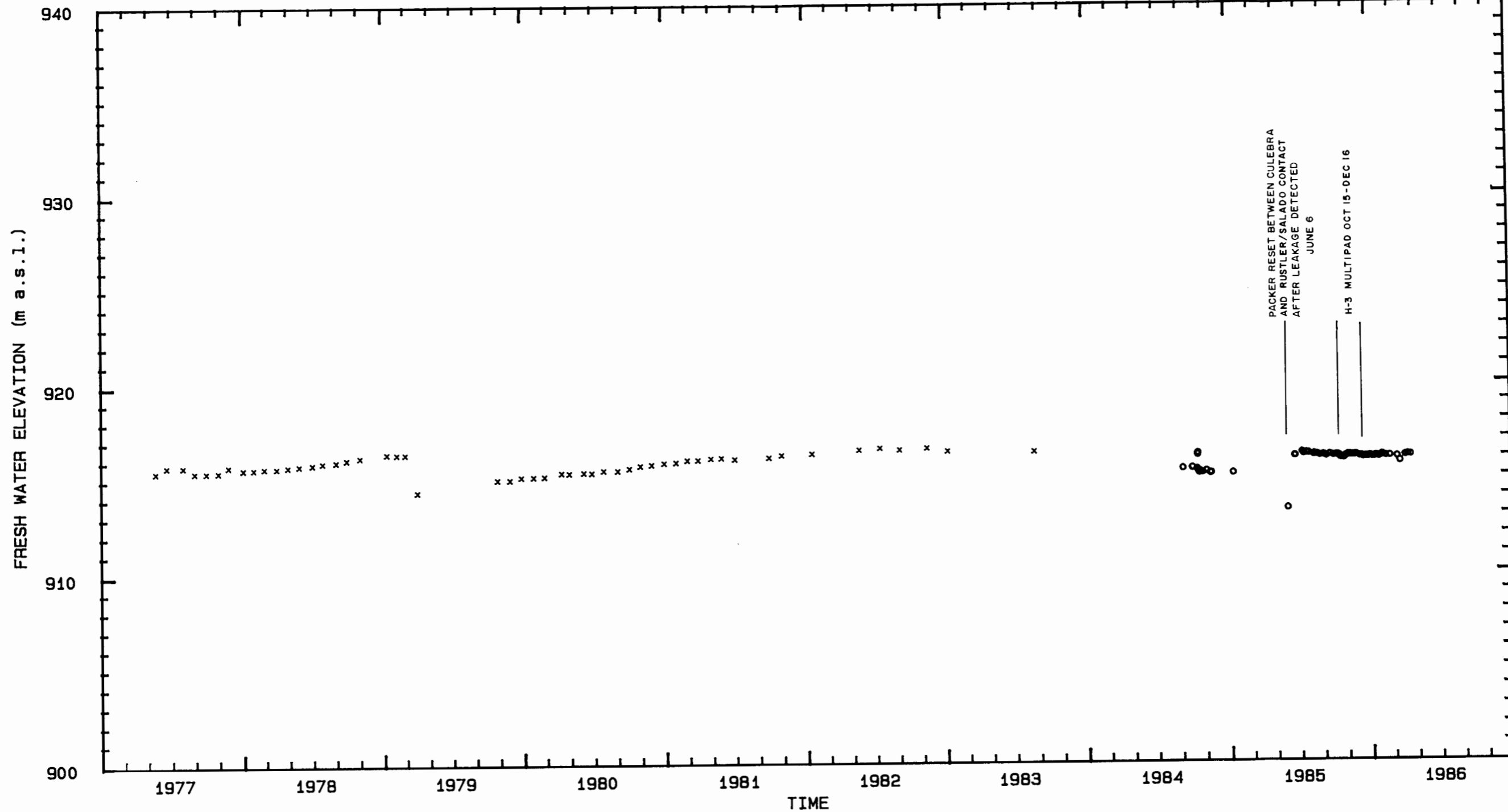
**LEGEND:**  
 o = P-14 (I)  
 x = P-14 (U)  
 I = INTERA & HGC Water-level Data  
 U = U.S.G.S. Water-level Data  
 T = INTERA & HGC Transducer Data

Drawn by	Date
Checked by	Date
Revisions	Date

Equivalent Freshwater Elevations for the Culebra Dolomite at Well P-14

**INTERA** Technologies

Figure D.15



LEGEND: ○ = P-15 (I)  
 × = P-15 (U)

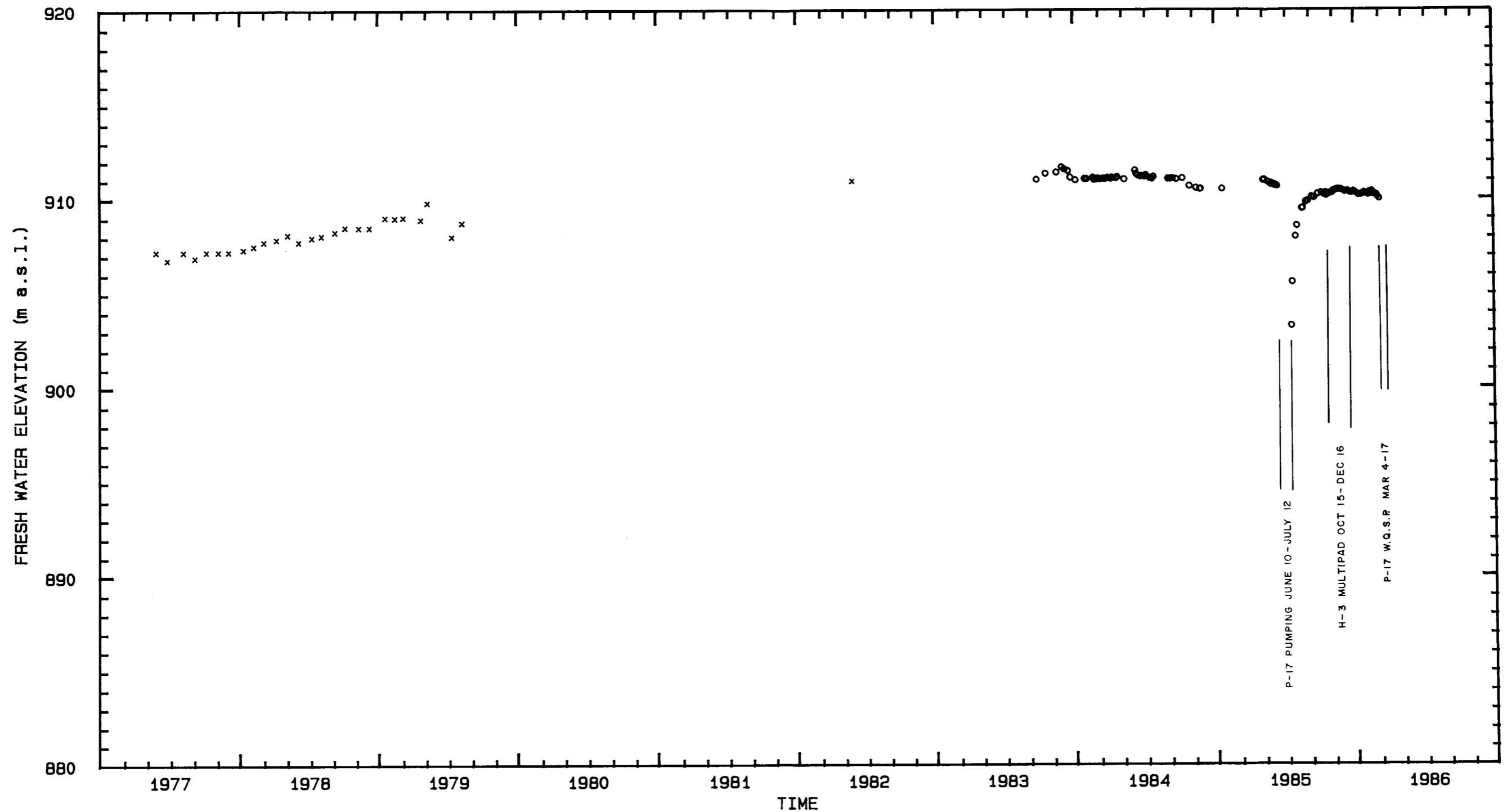
I = INTERA & HGC Water-level data  
 U = U.S.G.S. Water-level data  
 T = INTERA & HGC Transducer data

Drawn by	Date
Checked by	Date
Revisions	Date

Equivalent Freshwater Elevations for the  
 Culebra Dolomite at Well P-15

**INTERA** Technologies

Figure D.16



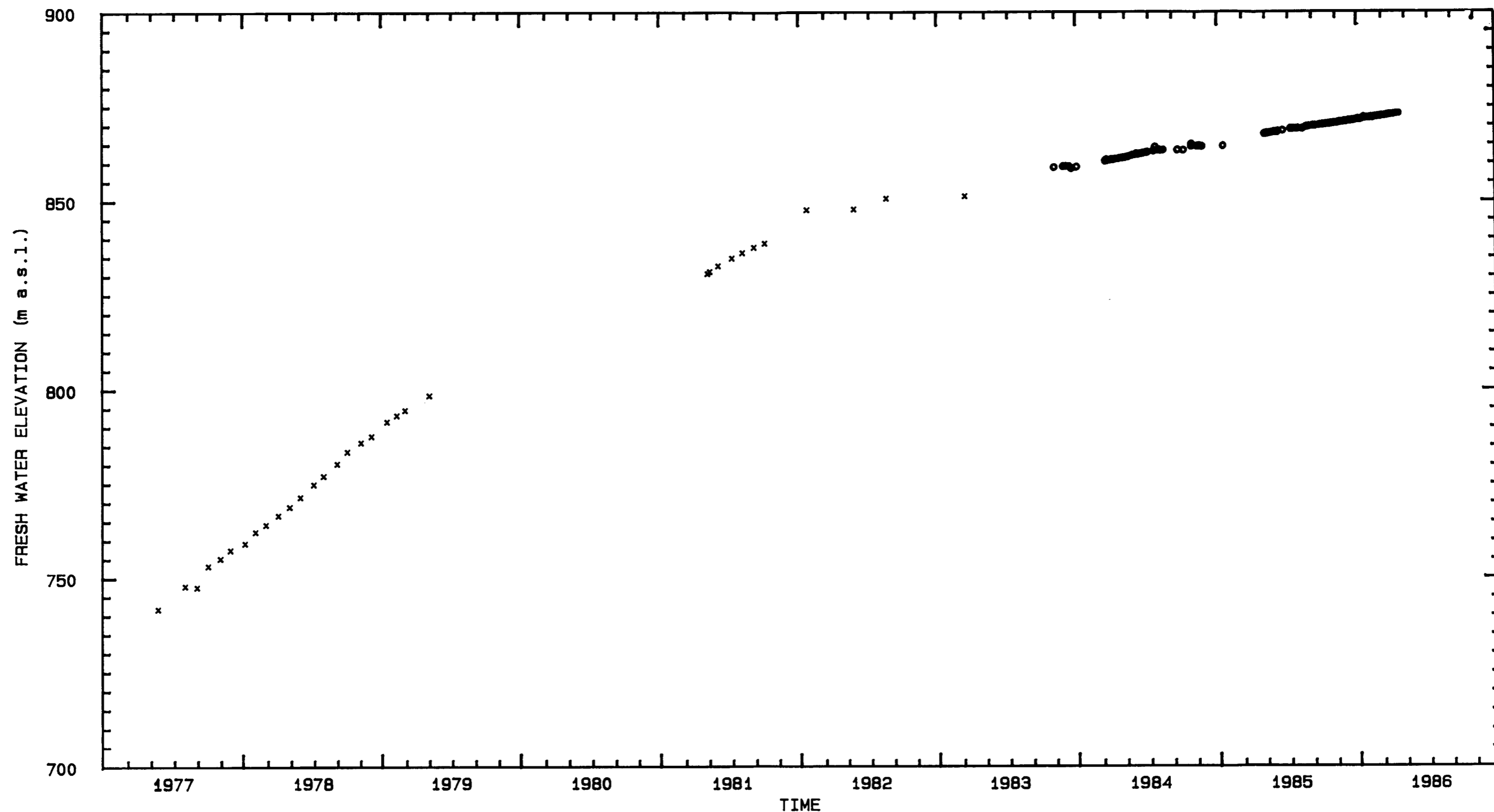
LEGEND:    o = P-17 (I)                    I = INTERA & HGC Water-level Data  
               x = P-17 (U)                    U = U.S.G.S. Water-level Data  
     T = INTERA & HGC Transducer Data

Drawn by	Date
Checked by	Date
Revisions	Date

Equivalent Freshwater Elevations for the  
 Culebra Dolomite at Well P-17

**INTERA** Technologies

Figure D.17



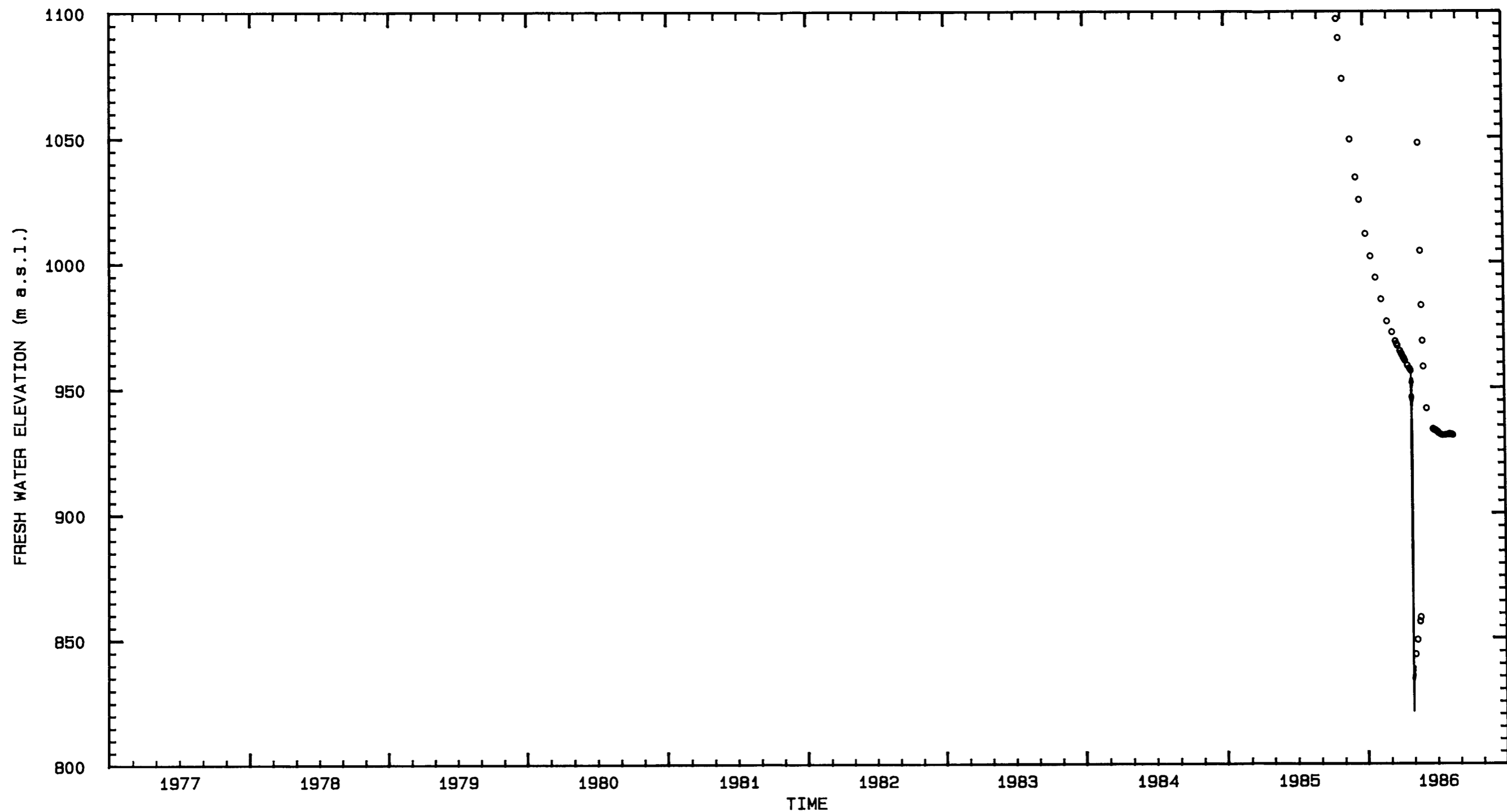
LEGEND: o = P-18 (I)      I = INTERA & HGC Water-level data  
 x = P-18 (U)      U = U.S.G.S. Water-level data  
                          T = INTERA & HGC Transducer data

Drawn by	Date
Checked by	Date
Revisions	Date

Equivalent Freshwater Elevations for the  
 Culebra Dolomite at Well P-18

**INTERA** Technologies

Figure D.18



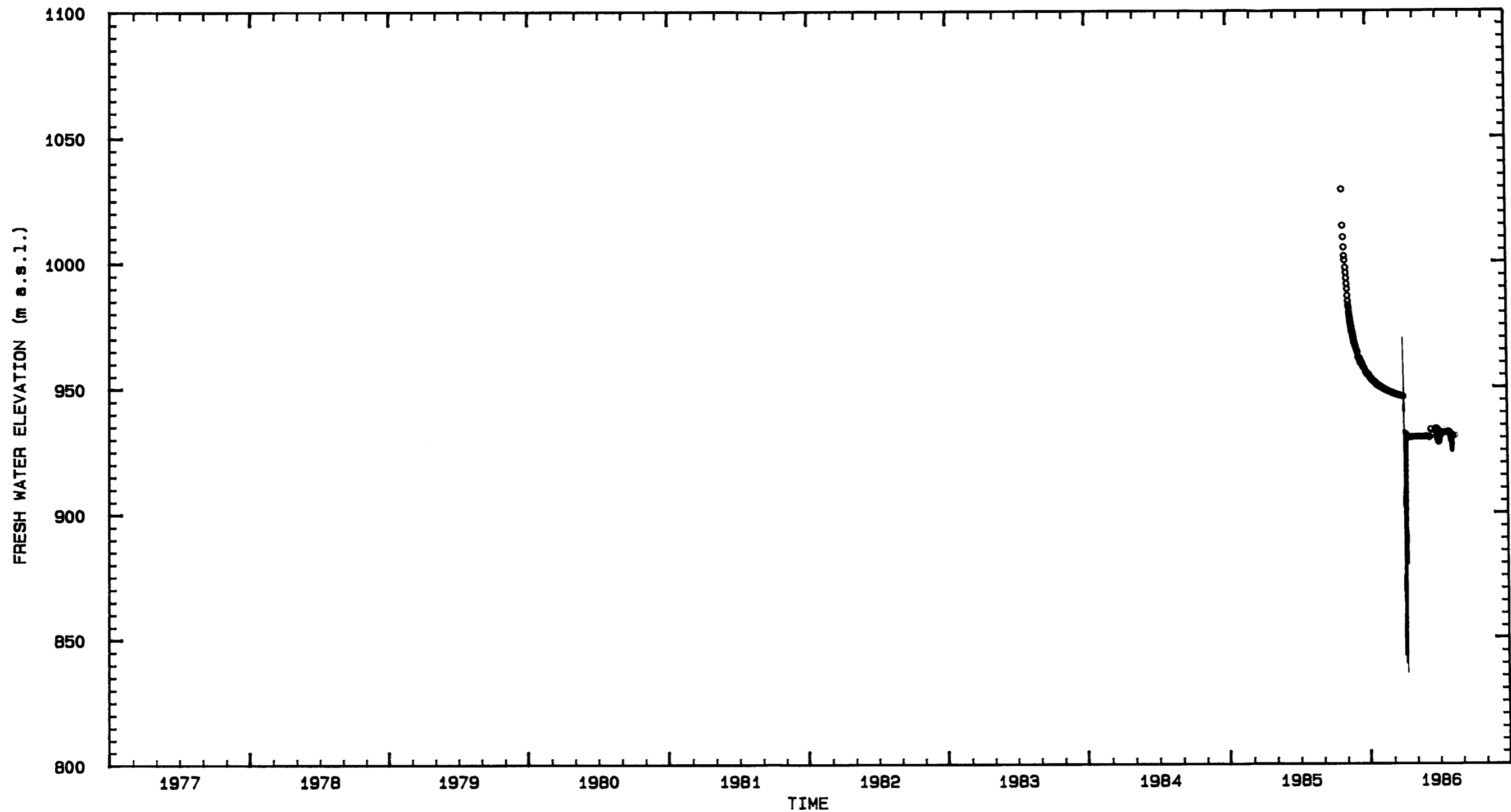
LEGEND: ○ = WIPP-12 (I) I = INTERA & HGC Water-level data  
 — = WIPP-12 (T) U = U.S.G.S. Water-level data  
 T = INTERA & HGC Transducer data

Drawn by	Date
Checked by	Date
Revisions	Date

Equivalent Freshwater Elevations for the Culebra Dolomite at Well WIPP-12

**INTERA** Technologies

Figure D.19



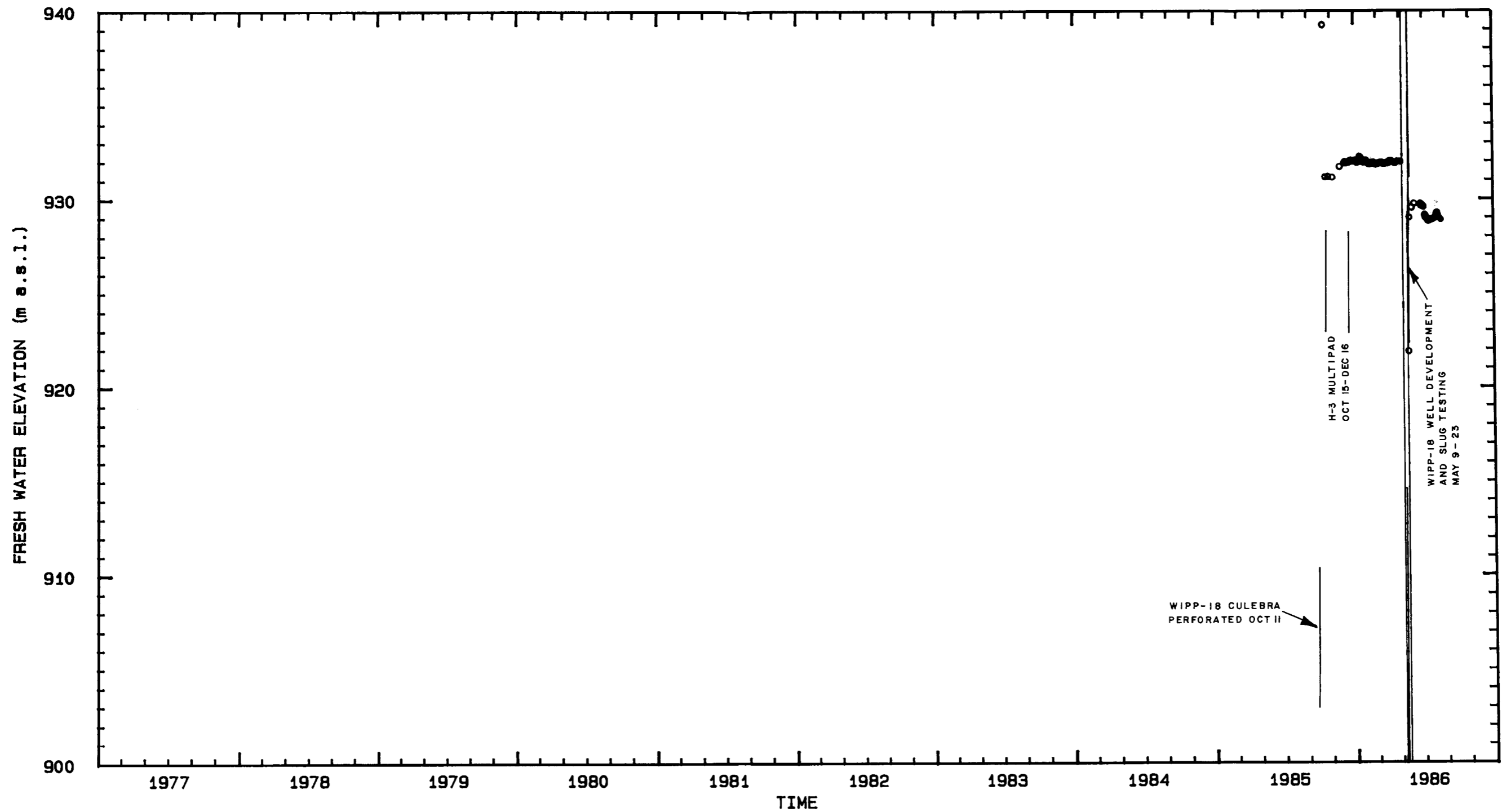
LEGEND: ○ = WIPP-13 (I)      I = INTERA & HGC Water-level data  
 — = WIPP-13 (T)      U = U.S.G.S. Water-level data  
                                  T = INTERA & HGC Transducer data

Drawn by	Date
Checked by	Date
Revisions	Date

Equivalent Freshwater Elevations for the  
 Culebra Dolomite at Well WIPP-13

**INTERA** Technologies

Figure D.20



**LEGEND:** ○ = WIPP-18 (I)      I = INTERA & HGC Water-level data  
 — = WIPP-18 (T)      U = U.S.G.S. Water-level data  
    T = INTERA & HGC Transducer data

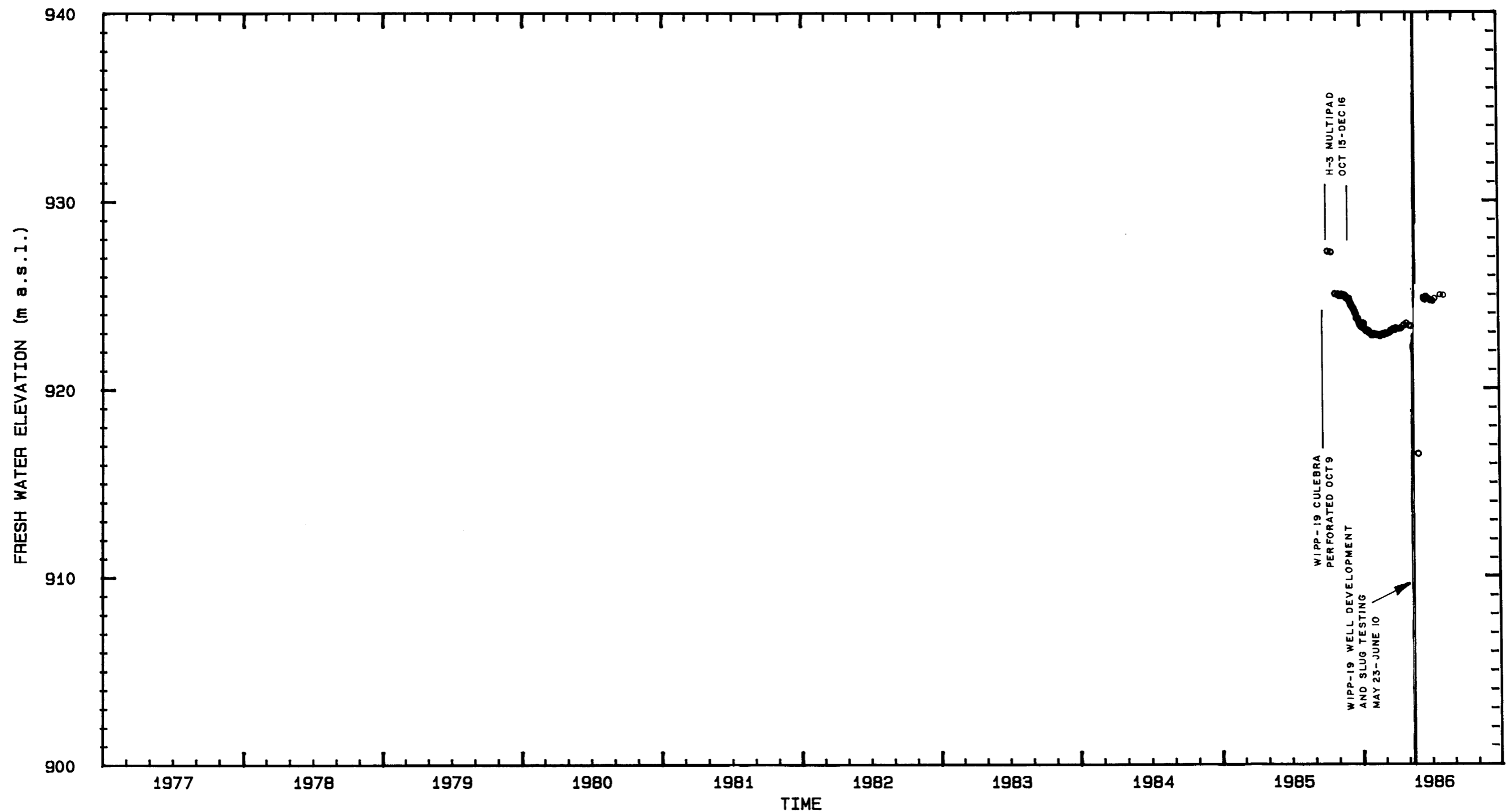
Drawn by	Date
Checked by	Date
Revisions	Date

Equivalent Freshwater Elevations for the  
 Culebra Dolomite at Well WIPP-18

**INTERA Technologies**

Figure D.21





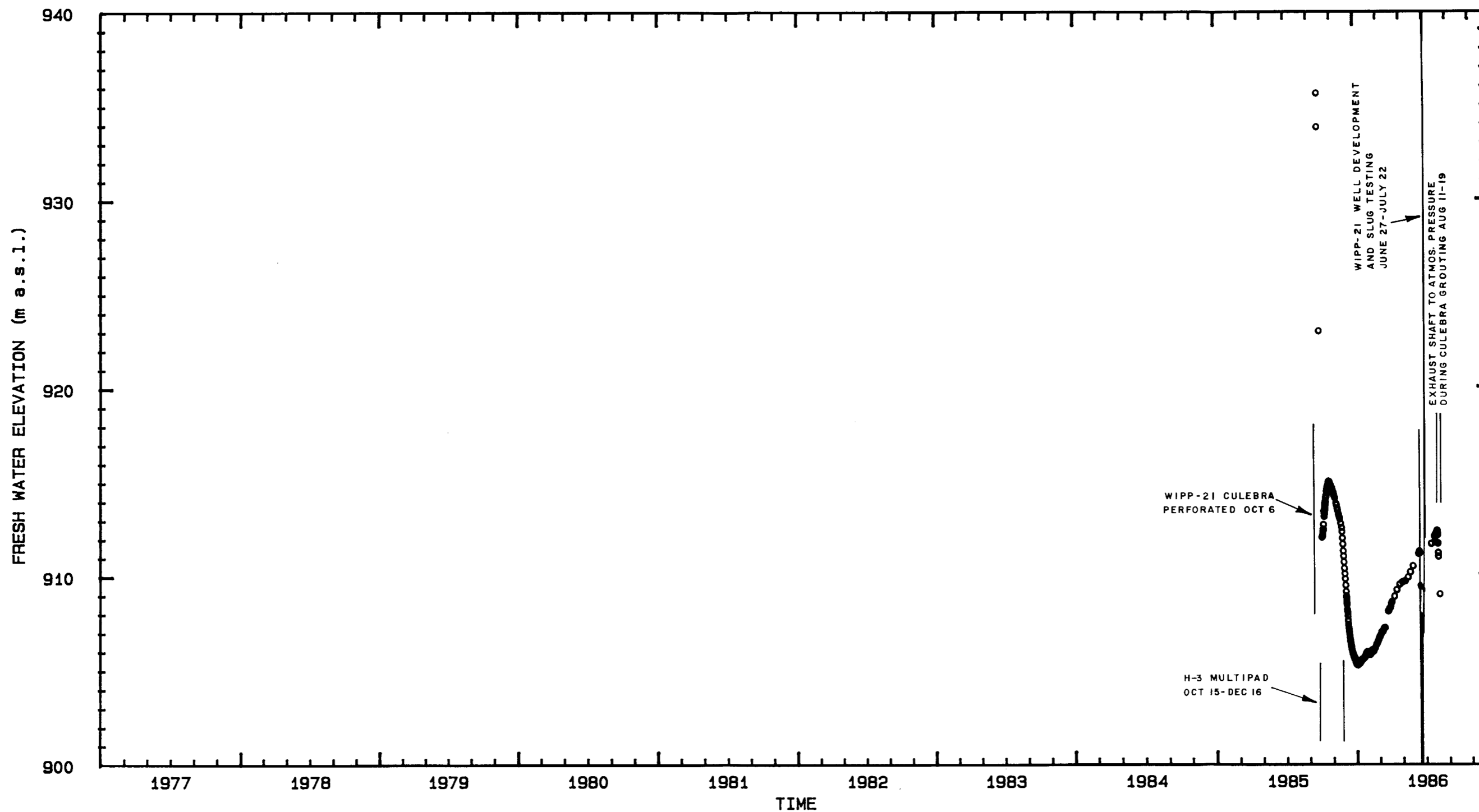
LEGEND: ○ = WIPP-19 (I)      I = INTERA & HGC Water-level data  
 — = WIPP-19 (T)      U = U.S.G.S. Water-level data  
                              T = INTERA & HGC Transducer data

Drawn by	Date
Checked by	Date
Revisions	Date

Equivalent Freshwater Elevations for the Culebra Dolomite at Well WIPP-19

**INTERA Technologies**

Figure D.22



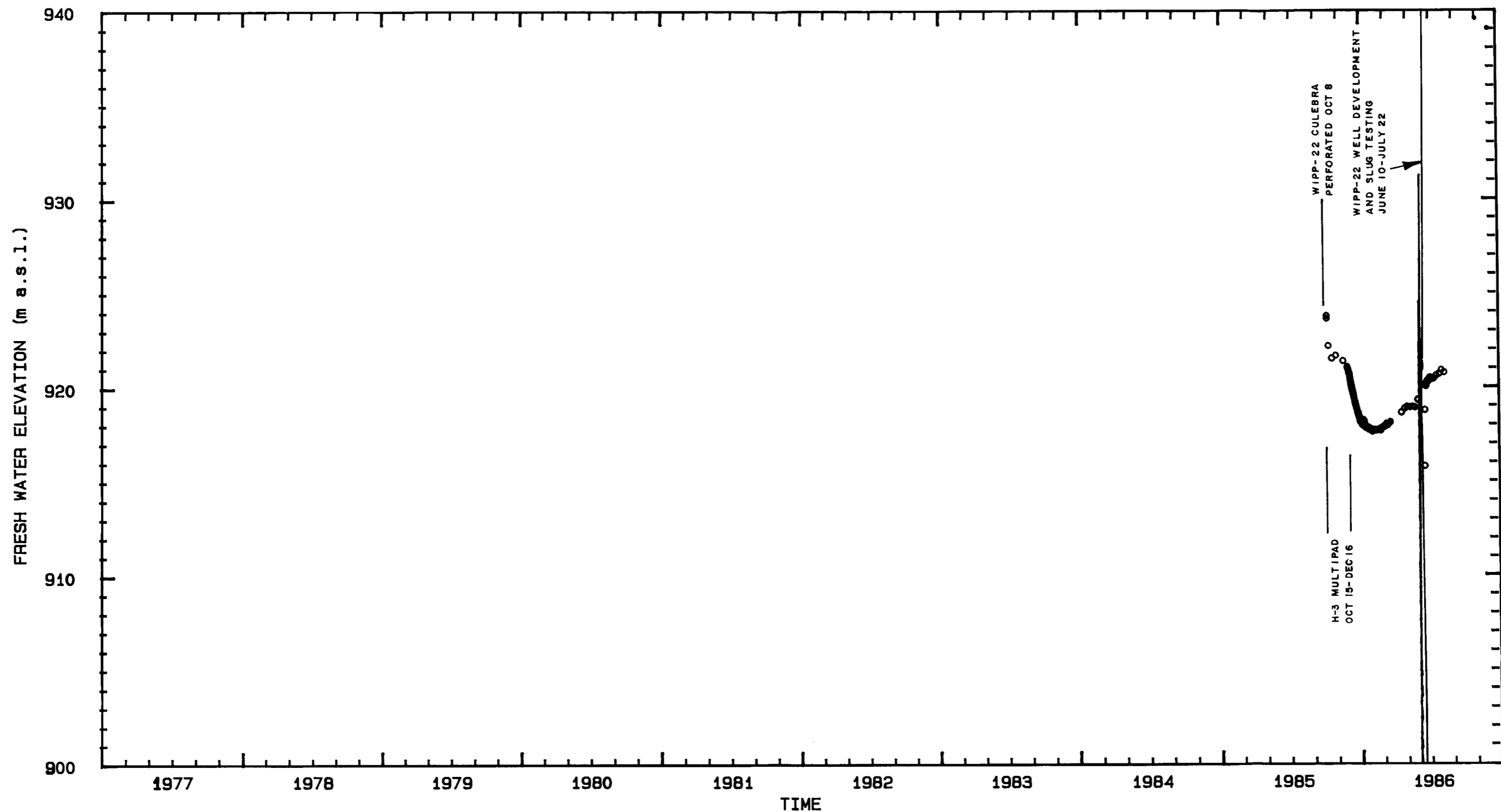
LEGEND: ○ = WIPP-21 (I)      I = INTERA & HGC Water-level data  
 — = WIPP-21 (T)      U = U.S.G.S. Water-level data  
                                  T = INTERA & HGC Transducer data

Drawn by	Date
Checked by	Date
Revisions	Date

Equivalent Freshwater Elevations for the Culebra Dolomite at Well WIPP-21

**INTERA Technologies**

Figure D.23



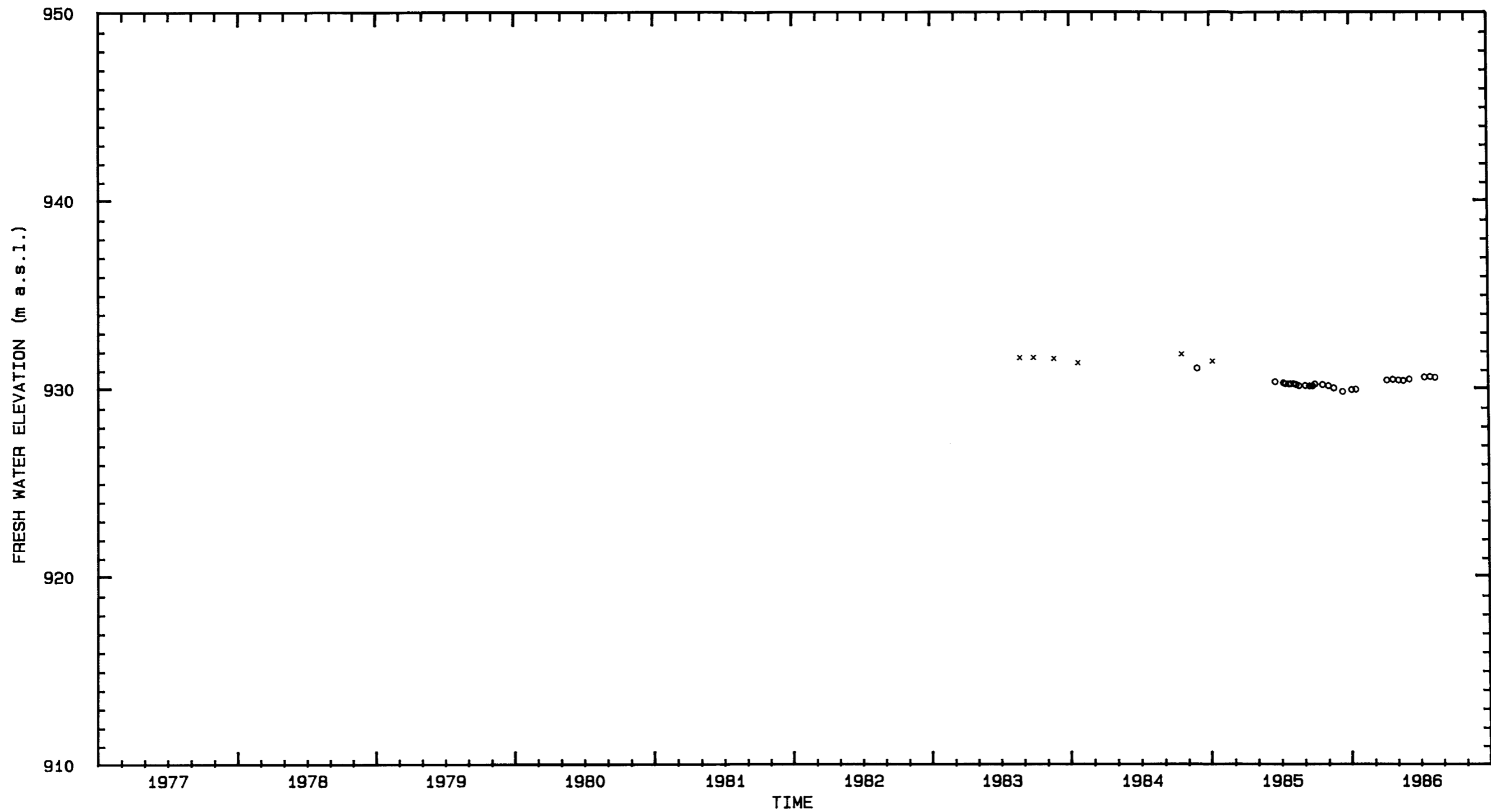
LEGEND: ○ = WIPP-22 (I) I = INTERA & HGC Water-level data  
 — = WIPP-22 (T) U = U.S.G.S. Water-level data  
 T = INTERA & HGC Transducer data

Drawn by	Date
Checked by	Date
Revisions	Date

Equivalent Freshwater Elevations for the Culebra Dolomite at Well WIPP-22

**INTERA** Technologies

Figure D.24



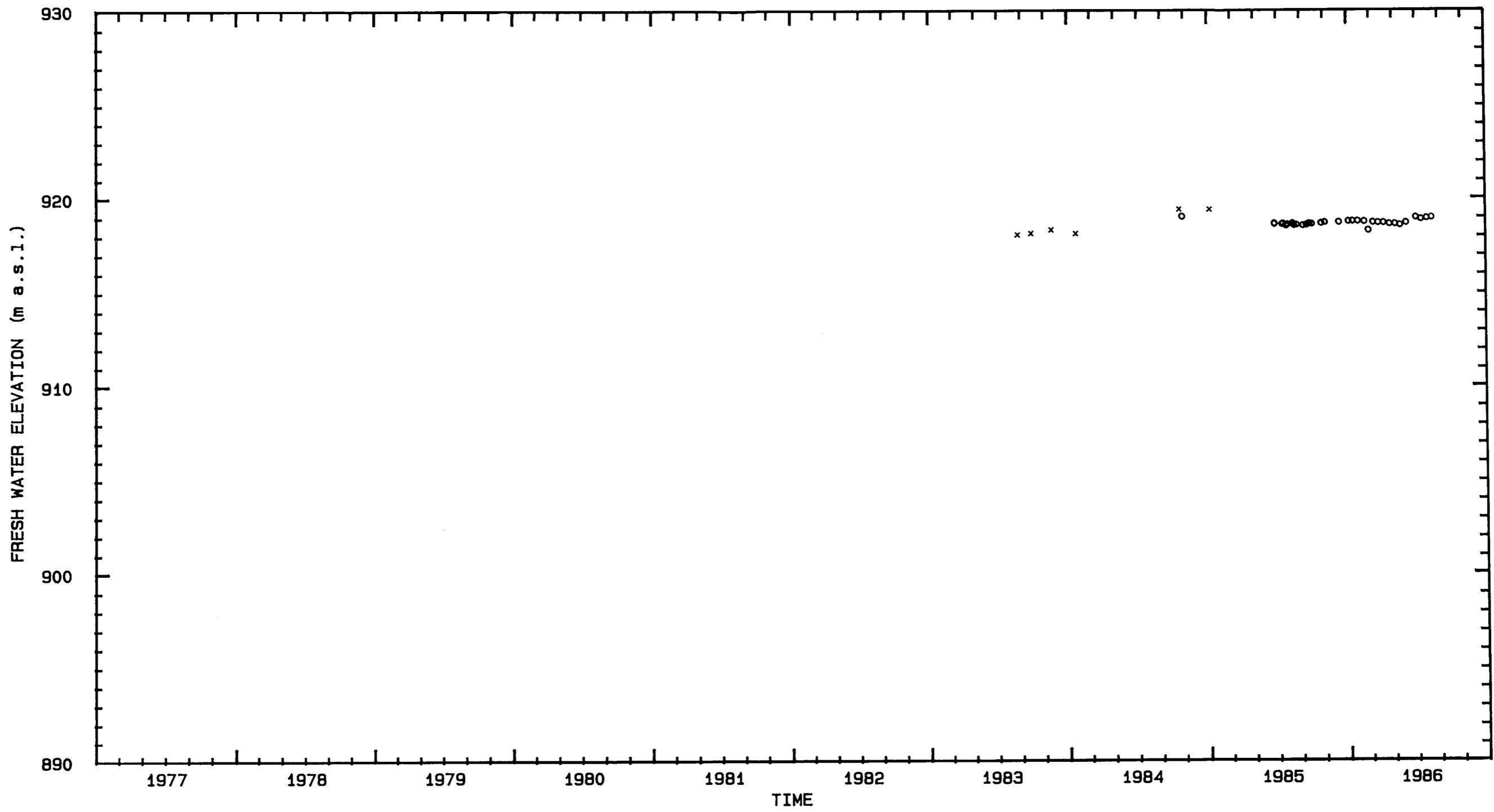
LEGEND: o = WIPP-25 (I)      I = INTERA & HGC Water-level Data  
 x = WIPP-25 (U)      U = U.S.G.S. Water-level Data  
    T = INTERA & HGC Transducer Data

Drawn by	Date
Checked by	Date
Revisions	Date

Equivalent Freshwater Elevations for the  
 Culebra Dolomite at Well WIPP-25

**INTERA** Technologies

Figure D.25



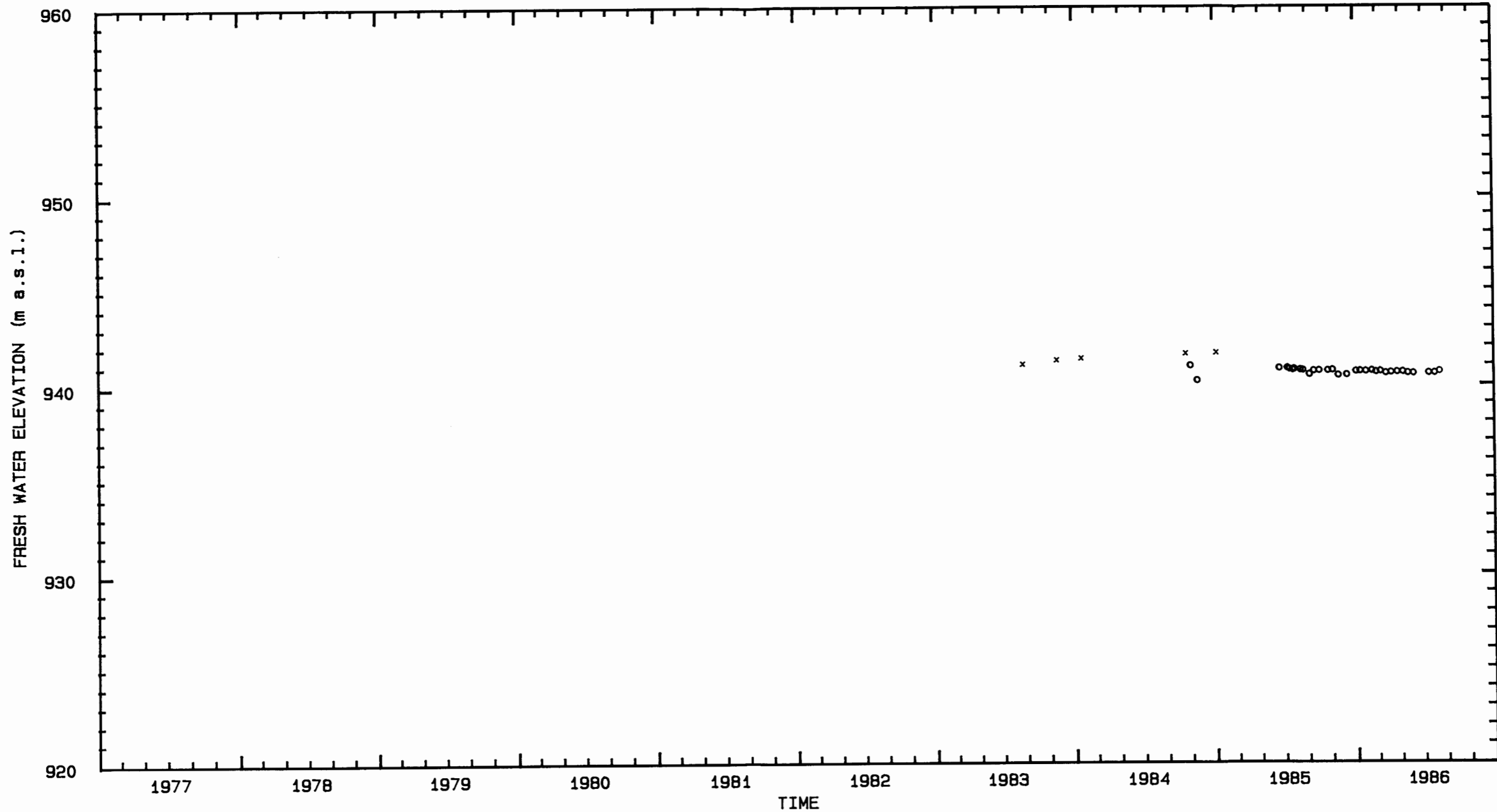
**LEGEND:** o = WIPP-26 (I)      I = INTERA & HGC Water-level Data  
 x = WIPP-26 (U)            U = U.S.G.S. Water-level Data  
    T = INTERA & HGC Transducer Data

Drawn by	Date
Checked by	Date
Revisions	Date

Equivalent Freshwater Elevations for the  
 Culebra Dolomite at Well WIPP-26

**INTERA** Technologies

Figure D.26



LEGEND: ○ = WIPP-27 (I)  
 × = WIPP-27 (U)

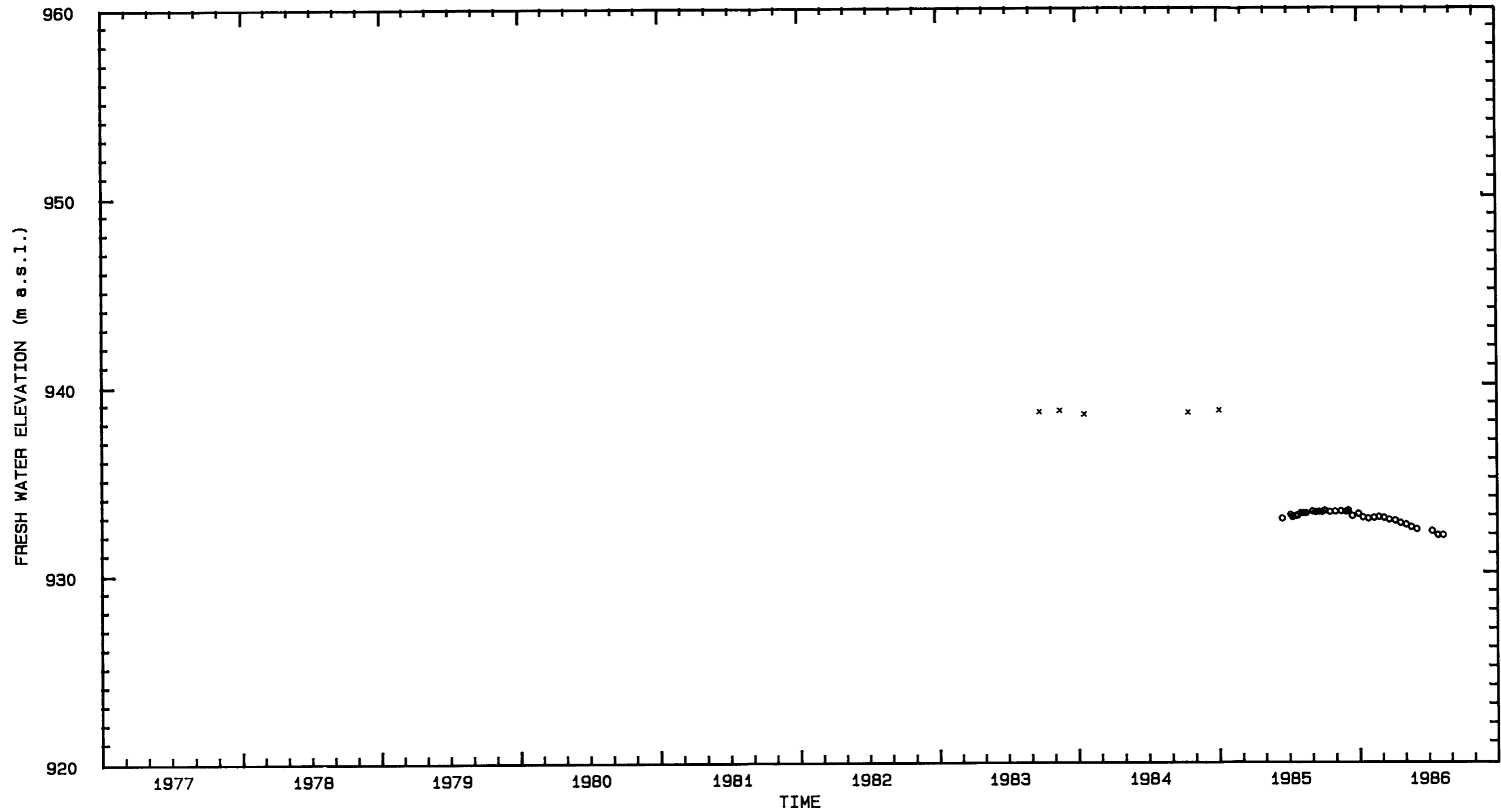
I = INTERA & HGC Water-level Data  
 U = U.S.G.S. Water-level Data  
 T = INTERA & HGC Transducer Data

Drawn by	Date
Checked by	Date
Revisions	Date

Equivalent Freshwater Elevations for the  
 Culebra Dolomite at Well WIPP-27

**INTERA** Technologies

Figure D.27



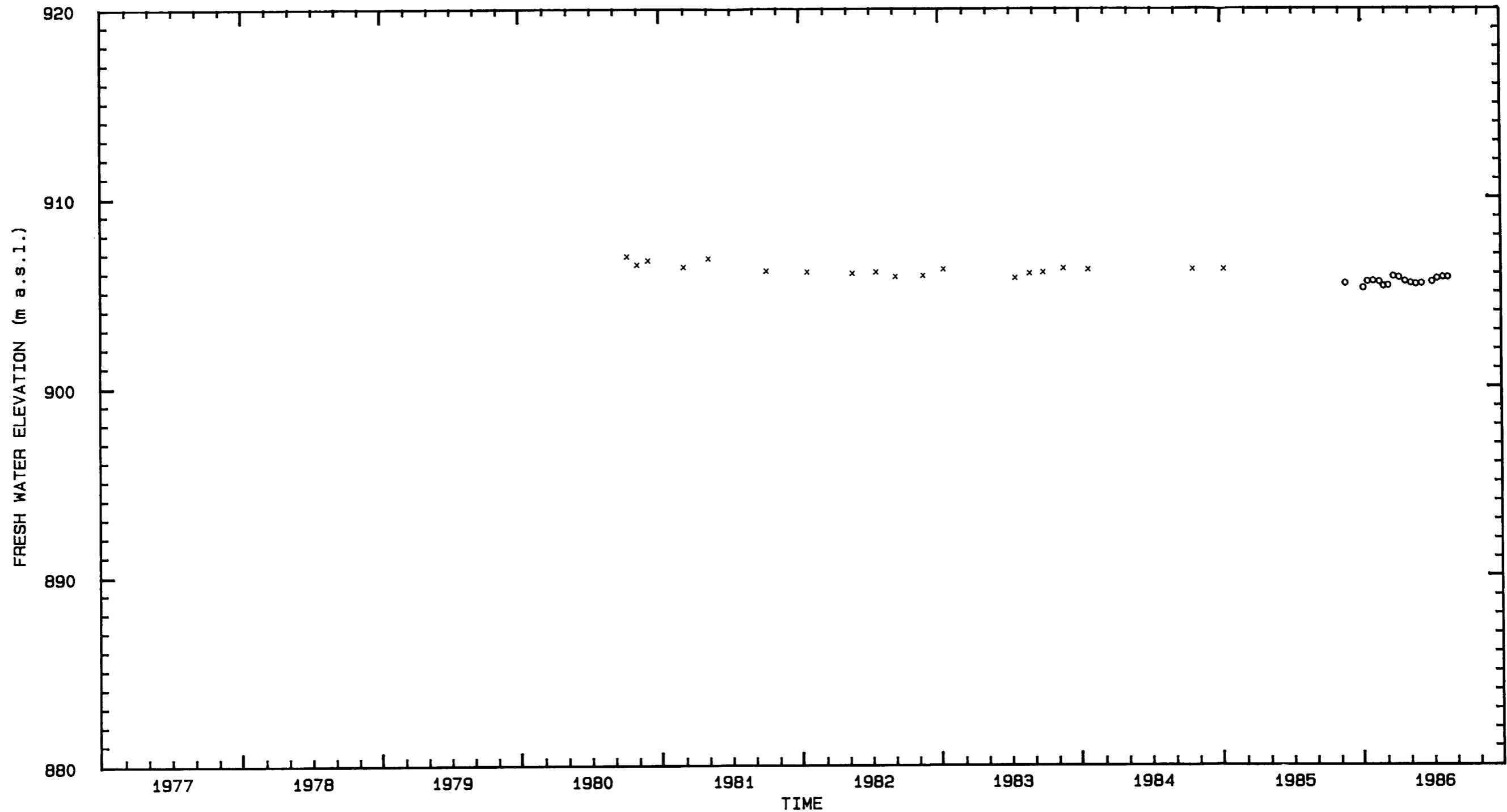
**LEGEND:** ○ = WIPP-28 (I)      I = INTERA & HGC Water-level Data  
 × = WIPP-28 (U)      U = U.S.G.S. Water-level Data  
    T = INTERA & HGC Transducer Data

Drawn by	Date
Checked by	Date
Revisions	Date

Equivalent Freshwater Elevations for the Culebra Dolomite at Well WIPP-28

**INTERA Technologies**

Figure D.28



LEGEND: ○ = WIPP-29 (I)      I = INTERA & HGC Water-level Data  
 × = WIPP-29 (U)      U = U.S.G.S. Water-level Data  
    T = INTERA & HGC Transducer Data

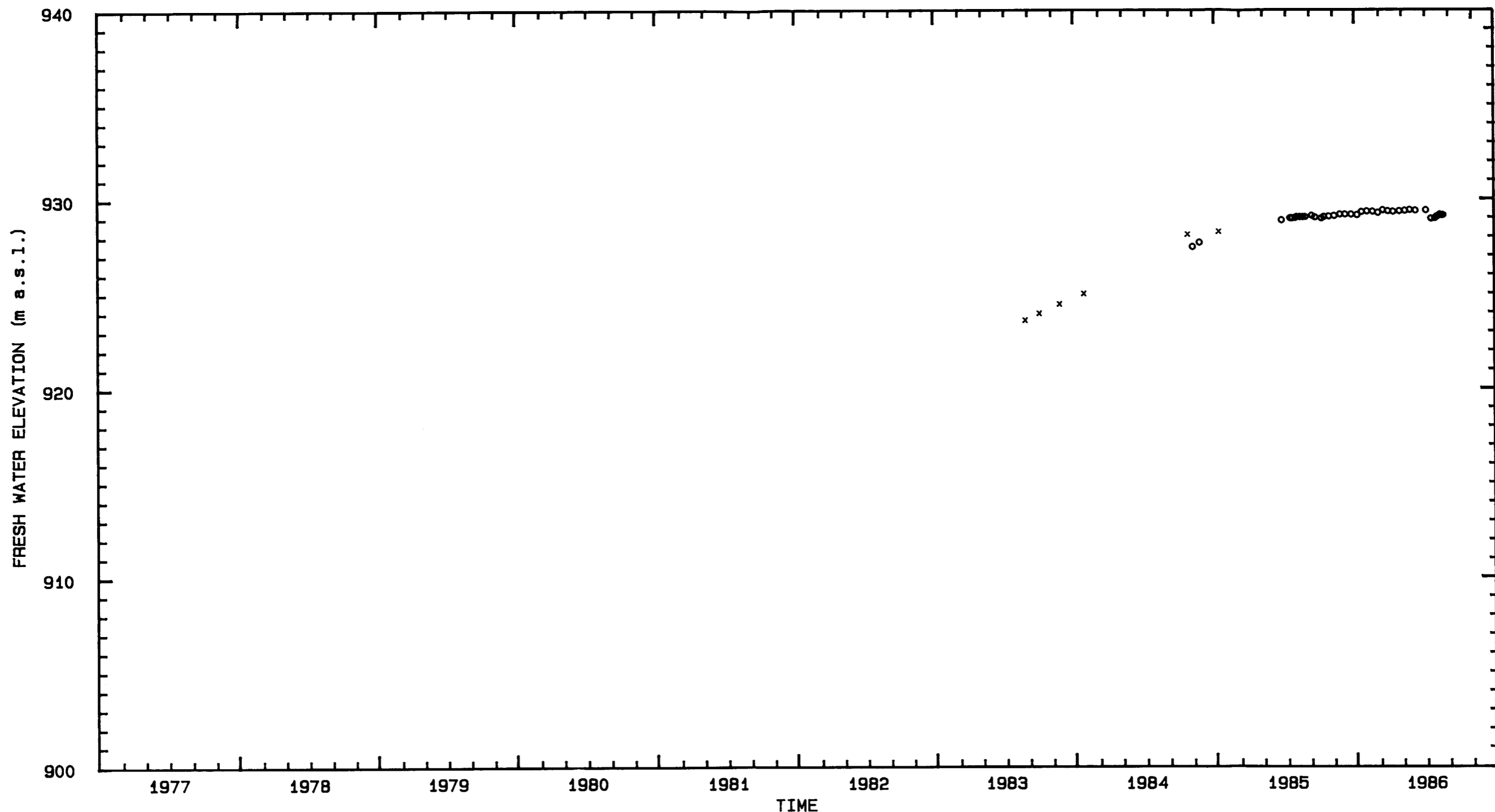
Drawn by	Date
Checked by	Date
Revisions	Date

Equivalent Freshwater Elevations for the  
 Culebra Dolomite at Well WIPP-29

**INTERA** Technologies

Figure D.29





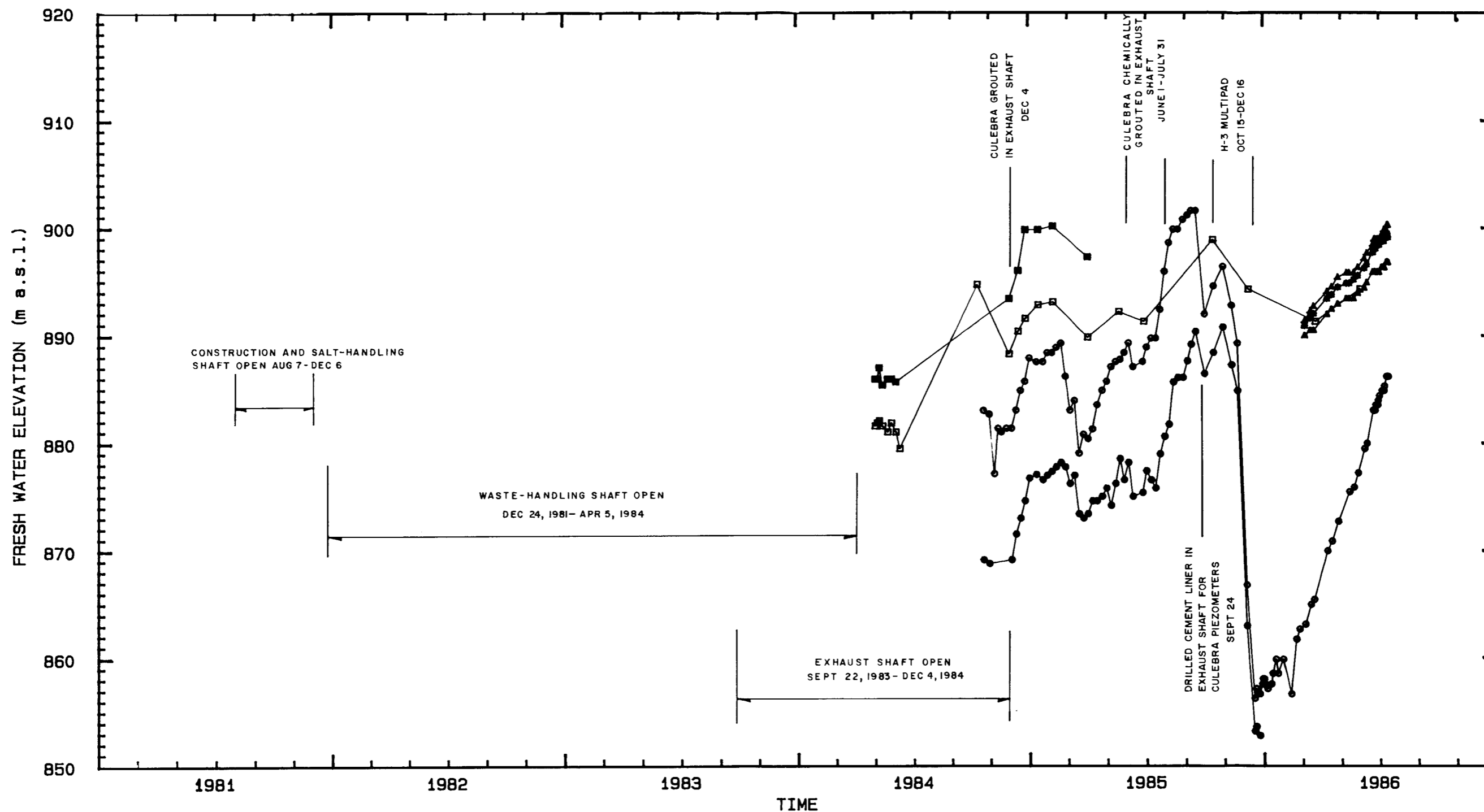
LEGEND: o = WIPP-30 (I)      I = INTERA & HGC Water-level Data  
 x = WIPP-30 (U)      U = U.S.G.S. Water-level Data  
 T = INTERA & HGC Transducer Data

Drawn by	Date
Checked by	Date
Revisions	Date

Equivalent Freshwater Elevations for the  
 Culebra Dolomite at Well WIPP-30

**INTERA** Technologies

Figure D.30



LEGEND: ● WASTE SHAFT #207    □ C&SH SHAFT #207    ▲ EXHAUST SHAFT #210  
 ○ WASTE SHAFT #208    ■ C&SH SHAFT #208    ▲ EXHAUST SHAFT #211  
 ● EXHAUST SHAFT #212

Drawn by	Date
Checked by	Date
Revisions	Date

Equivalent Freshwater Elevations for the Culebra Dolomite in the Construction and Salt-Handling Shaft, Waste-Handling Shaft, and Exhaust Shaft.

**INTERA** Technologies

Figure D.31

APPENDIX E: CONSISTENCY OF DENSITIES AND CHEMICAL COMPOSITIONS  
OF WATER SAMPLES FROM THE CULEBRA DOLOMITE

(By A. J. Meijer, J. L. Lolcama, and F. J. Pearson)

To interpret ground-water hydraulic and geochemical data, water density data are required. Densities of water standing in boreholes are needed to convert measured water levels to formation pressures or to fresh-water heads. Densities of formation waters are necessary to support ground-water flow modeling and to calculate molal (mol/kg H<sub>2</sub>O) concentrations of dissolved constituents from analyzed values. Water analyses are usually reported as milligrams per liter (mg/l) solution, while molal concentrations are required for geochemical equilibrium calculations.

The densities of water samples from boreholes open to a given formation will be the same as the densities of the formation water only if the samples are not contaminated. Contamination can result from the mixing of formation water with drilling fluids, with fluids used in borehole construction, and with water from other formations. Knowledge of the extent of such contamination, if any, is required to evaluate the composition and density of formation fluids for geochemical purposes, to estimate formation pressures, and for flow-path validation to support ground-water modeling.

Density and chemical analytical data on Culebra samples have been evaluated for their internal consistency and for indications of how well they may represent the density and chemistry of Culebra formation waters. The evaluation procedures and conclusions are described in the remainder of this appendix.

## E.1 Densities of Culebra Water Samples

Table E.1 is a summary of measured and calculated data for water samples from the Culebra.

The chemical analytical data are from Mercer (1983, Table 2) and from Robinson (SAND86-0917, in preparation). Additional density data on 1980 samples from the WIPP wells 25 to 30 are from Lambert and Robinson (1984). The 1984 and 1985 samples were taken as part of the WIPP Ecological Monitoring Program, and their pH values, conductivities, and densities are as given in Figure 10.6 of Westinghouse Electric Corporation (1985). Undated density data were taken from field notes and data collected for Sandia National Laboratories by Hydro Geo Chem, Inc.

Two values for total dissolved solids are given in Table E.1. The first is the residue on evaporation of the sample as reported by the analytical laboratory. The second is the sum of the analyzed concentrations of individual dissolved species. Both measures of total dissolved solids should be nearly the same in an internally consistent analysis.

The charge balances given in Table E-1 were calculated using:

$$\text{Balance (\%)} = 100 \frac{(\sum \text{ meq Cations } - \sum \text{ meq Anions })}{(\sum \text{ meq Cations } + \sum \text{ meq Anions })}$$

where meq is millequivalents per liter solution. Because solutions are electrically neutral, the more closely the balance of an analysis approaches zero, the more reliable the analysis. Analyses with balances worse than 10% (5% for the most recently collected samples) should be used with caution.

The reliability of densities derived from specific gravity measurements made on water samples from the Culebra Dolomite has been evaluated by comparing them with densities calculated on the basis of the concentrations of dissolved constituents in the same waters as reported in laboratory analyses.

The approach used here in calculating densities is based on a paper by Kumar (1986) which in turn is based on the Pitzer theory of activity coefficients in electrolyte solutions (Pitzer, 1979). Given the appropriate constants and coefficients, the Pitzer formalism allows the calculation of densities of solutions of single and mixed electrolytes.

As shown in the inset in Figure E.1, the densities of pure solutions of various salts (Weast, 1983) at a given mass concentration are not equal. The densities of chloride solutions show the following density order  $KCl < NaCl < MgCl_2 < CaCl_2$  for the same mass concentration. For pure sulfate solutions, the cation order is the same. However, because of gypsum saturation, the maximum concentration of pure  $CaSO_4$  solutions is limited to approximately 1350 mg/l. The  $CaSO_4$  curve shown in Figure E.1 has been extrapolated to higher concentrations by maintaining a constant ratio to the  $MgSO_4$  curve.

The density of mixed-electrolyte solutions can be approximated by combining the densities of pure salt solutions in proportion to their molal or molar concentrations to arrive at densities that are generally within 1.0 percent of measured densities. To obtain better agreement, the interactions among ions in solutions must be considered. The Pitzer formalism can be used to model these interactions. Kumar (1986) has shown that this approach allows densities to be calculated to within 0.04 percent for chloride brines.

Kumar (1986) has presented the constants and Pitzer coefficients for brines composed of  $NaCl$ ,  $KCl$ ,  $MgCl_2$ , and  $CaCl_2$  at 20 to 40 degrees

centigrade and 1 bar. The constants and Pitzer coefficients for the sulfate salts are not presently available.

The apparent densities of the chloride components of the formation waters in the Culebra at the WIPP site were calculated using Kumar's (1986) constants and coefficients and molalities of the chloride salts reflecting the molal cation proportions in the waters with  $\text{Na}^+$  added or subtracted to achieve charge balance. These densities were "corrected" for the sulfate components by a linear combination of densities of pure sulfate solutions weighted by the appropriate cation molalities in the same proportions as used for the chloride components. The results of these calculations are plotted against total dissolved solids in Figure E.1.

The densities plotted in Figure E.1 are for the temperature measured for a given sample at the WIPP site at the time of sample collection. Most of the points plot within 0.1 percent of the regression curve drawn in Figure E.1. The slope of the hand-fitted curve decreases with increasing total dissolved solids reflecting the changing proportions of salts in the solutions. At low TDS values ( $\leq 20$  g/l), the sulfate component is dominant and generates a relatively steep slope starting from a Y-intercept of  $0.9977 \text{ g/cm}^3$ . From 20 up to approximately 160 g/l, the slope is nearly constant, presumably reflecting the dominance of the NaCl component and the nearly constant slope of the NaCl curve over this range (Figure E.1). Above 160 g/l the slope further decreases in parallel with the NaCl curve. The rather limited deviation of individual points from a smooth curve reflects the fact that the densities of pure potassium-salt solutions are less than pure sodium-salt solutions, while the densities of the magnesium and calcium solutions are greater, thus tending to cancel or balance the effects of the non-sodium salts. Some of the deviation (up to 0.12 percent) of points from a smooth curve results from the range of temperature over which the samples were collected.

A comparison of calculated and measured densities is shown graphically in Figure E.2. Again, the density values plotted are for temperatures measured in the field. Overall, there is a good correlation between calculated and measured densities. However, multiple samples from various wells show substantial data scatter with the most recently determined densities lying closest to the equiline. The scatter of the data points from the equiline could reflect: (1) errors in the specific-gravity measurements made in the field; (2) differences in the compositions of the sample on which the specific-gravity measurement was made and the sample which was chemically analyzed; (3) errors in the chemical analysis; (4) errors in the temperature measurements; (5) uncertainties in the densities of the chloride and sulfate components in mixed-electrolyte solutions; and (6) calculation and/or transcription errors.

The 1985 and 1986 samples generally plot within 0.3 percent of the equiline. As noted previously, up to 0.12 percent of this deviation could be due to errors in the temperature measurement ( $\pm 5^\circ\text{C}$ ). Errors in the chemical analyses are clearly indicated by the charge imbalances shown in Table E.1. In the density calculations, these imbalances were attributed to errors in the analysis of  $\text{Na}^+$ . However, errors in the analyses of the other components (e.g.,  $\text{Cl}^-$ ) could also explain the charge imbalances. The effect of errors in chemical analyses is largest in the most concentrated brines (WIPP-27 and WIPP-29). Up to 4.0 g/l of  $\text{Na}^+$  had to be added to achieve charge balance in these samples. According to the curve shown in Figure E.1, this error in chemical analysis equates to an error in the density calculation of approximately 0.2 percent.

Uncertainties in the densities of the chloride and sulfate components in mixed-electrolyte solutions are estimated to result in errors in the density calculation of less than 0.25 percent. Kumar (1986) has shown that the densities of chloride solutions can be calculated to within 0.04 percent. Uncertainties in the sulfate densities are limited by the

sulfate concentrations in the solutions and pure-salt density data to less than 0.2 percent.

Overall, the maximum error associated with factors 3 through 5 is in the range of 0.5 to 0.6 percent. The remaining differences between measured and calculated densities are presumed to be due to field-measurement and/or sample-collection errors.

The preferred density values listed in Table E.1 were selected on the following basis: (1) for wells with multiple samples, the most recent density value rounded to the nearest 0.005 was selected; (2) for wells with only one sample, the measured density rounded to the nearest 0.005 was selected if it fell within 0.3 percent of the equiline, otherwise the calculated density rounded to the nearest 0.005 was selected.

## E.2 Reliability of Samples as Representative of Culebra Formation Water Chemistry

The preceding section examined how well the analytical data represent the density of the waters sampled. This section describes further examination of how well the water samples collected and analyzed represent the chemistry of water in the Culebra.

From knowledge of the mineralogy and petrology of an aquifer and the principles of aqueous geochemistry, it is possible to predict certain properties of water from that formation. The Culebra can be grossly characterized as a gypsum-bearing dolomite with trace quantities of halite (Core Laboratories, 1986). Formations of this type are not uncommon and a number of studies have been made on the geochemistry of the waters they contain. Aquifers studied include:



- The Floridan aquifer, described by Hanshaw et al. (1965) and by Rightmire et al. (1974).
- The Edwards aquifer of central Texas, described by Pearson and Rettman (1976).
- The Muschelkalk aquifer of northern Switzerland, described by Schmassmann et al. (1984) and by Pearson (1985).
- The Gipskeuper of northern Switzerland, described by Pearson and Lolcama (in preparation).

From these studies it appears that waters in aquifers of this type are characterized by :

- Saturation with respect to calcite, even if the residence time of the water being sampled is as short as a few years;
- Saturation with respect to dolomite, if the residence time of the water sampled is several hundred years or more;
- Saturation with respect to gypsum. In formations in which there has been limited freshwater circulation, allowing plentiful gypsum to remain, gypsum saturation can occur in waters with residence times of only a few tens of years. Thus, in the Edwards aquifer (Pearson and Rettman, 1976) and in the Gipskeuper of northern Switzerland (Pearson and Lolcama, in preparation), waters saturated with calcite and gypsum but undersaturated with dolomite have been found. Some of these waters contain tritium and cannot have residence times of more than a few tens of years.

Near the outcrop, however, ground-water circulation is commonly extensive enough to dissolve much of the readily-available gypsum.

Remaining gypsum is shielded from actively-circulating ground water by other minerals. While this gypsum may continue to dissolve, it does so only slowly, at a rate determined by diffusion through micro-cracks in the shielding minerals, for example. Water in such an aquifer must have a considerable residence time before it reaches gypsum saturation. This gives rise to the calcite- and dolomite-saturated but gypsum-undersaturated waters typical of the near-outcrop Edwards aquifer and in most of the Floridan aquifer.

- Saturation with respect to celestite, common in waters saturated with gypsum. Strontium analyses are not as frequently made on water samples as are calcium analyses. Where they are available, as in the studies of the Muschelkalk and Edwards aquifers mentioned above, they show that gypsum and celestite are generally both at saturation.
- General undersaturation with respect to halite. This probably occurs because halite is so very soluble and dissolves so rapidly that even a limited amount of ground-water circulation would remove readily-accessible halite from a formation. Thus, higher chloride concentrations in waters from such formations tend to be present in waters taken at points distant from outcrops and recharge areas or in areas which for other reasons have limited ground-water circulation rates.

Calculations have been carried out to assess the state of saturation of water samples from the Culebra with respect to calcite, dolomite, gypsum, and celestite. The calculations were carried out with the geochemical computer program PHREEQE (Parkhurst et al., 1980; INTERA Environmental Consultants, 1983).

The PHREEQE code uses the ion-pair model of solution behavior to calculate the distribution of dissolved species from the chemical

analysis of a solution. It calculates dissolved-ion activity products and compares them with equilibrium constants for selected minerals to calculate saturation indices. To use PHREEQE or any other geochemical code satisfactorily requires that it be supported by an internally consistent thermodynamic data base appropriate for the solution species and minerals being considered. The data base used for these calculations was prepared especially for work in the Culebra and is described in Pearson et al. (in preparation). The WATEQ Debye-Huckel equation was used to calculate activity coefficients of the major ions (Truesdell and Jones 1974; Nordstrom and Munoz, 1985, Section 7.6). This semi-empirical equation reproduces mean-salt activity coefficients to within 0.01 log activity units in solutions to ionic strengths of at least 3 molal.

In the Culebra samples discussed here, a sum-of-dissolved-solids content of about 100 g/l corresponds to an ionic strength of 3 molal.

Ramey (1985) calculated saturation indices of the minerals halite, anhydrite, gypsum, calcite, and dolomite for the same pre-1984 analyses used for this report. To make these calculations, Ramey used a computer program in the WATEQ series, which embodied the same ion-pair model of solution behavior as does PHREEQE. In addition, although Ramey states (p. 26) that he used the Davies equation for activity coefficients, the equation given in his report is the same WATEQ Debye-Huckel equation as was used for the calculations reported here. Thus, if the thermodynamic data used by Ramey were the same as those adopted here, his results should agree closely with those of this report shown in Table E.1. A comparison of these is discussed below.

Calcite saturation indices calculated by Ramey (1985) are shown in his Figure 14. The average difference between Ramey's values and those given in Table E.1 is 0.06 units. This difference is not significant and could well be a result of slight differences between the two geochemical computer programs. The calcite saturation indices for sample P-15 were not used in this comparison. Ramey used a pH of 10.2

for his calculations on that sample. Mercer (1983) does not report a pH for sample P-15, and in making the calculations leading to Table E.1 a pH of 7.0 was assumed. Thus the two calculated saturation indices are not comparable.

Gypsum-saturation indices calculated by Ramey (1985) are shown in his Figure 13. The average difference between Ramey's values and those given in Table E.1 is 0.24 units. This difference is too large to be attributed only to slight differences between the computer programs used and may well reflect differences between the thermodynamic data bases used by Ramey and in preparing this report. If the solubility product for gypsum used by Ramey were 0.24 log units more negative than that used for this report, it would account for the difference between the two sets of gypsum-saturation indices. The specific thermodynamic data set used by Ramey is not readily available, but in preparing the data base used here, it was noted that the solubility product used in some versions of WATEQ was 0.27 log units more negative than the value selected. The difference between 0.27 and 0.24 could well be a result of slight differences between the computer programs used.

In summary, it appears that had Ramey's (1985) calculations been made with the same thermodynamic data as used for this report, his results would not have differed significantly from those given here.

Saturation indices of calcite, gypsum, and celestite are listed in Table E.1, and their distributions are shown as histograms in Figure E.3. Two groups of analyses are distinguished in the figure. Group 1 comprises those samples which were collected in 1985 and 1986 as part of the environmental assessment program. These samples were collected and analyzed with particular care to avoid contamination. The other samples comprise Group 2 and were collected at various times between 1975 and 1984 (Mercer, 1983, Table 2; Robinson, personal communication). Strontium analyses are available for the 1981-1986

samples but not for those collected earlier. Thus, celestite saturation indices are shown only for the more recent samples.

The saturation indices for celestite and gypsum cluster tightly around zero, suggesting these waters were indeed in equilibrium with celestite and gypsum in the Culebra. There is little difference in the spread of celestite saturation indices for the 2 groups of samples. This likely reflects the basic precision of the strontium analyses. In the case of gypsum, saturation indices for the Group 1 samples cluster more tightly around zero than the Group 2 samples. Although the calcite indices cluster around the zero point, the spread is considerably greater than those for celestite and gypsum, even among the more recent samples. This phenomenon is commonly observed and results from the difficulty in collecting ground-water samples without some loss of dissolved  $\text{CO}_2$ . This loss can occur both when water is extracted from the formation, and while it is collected and analyzed at the surface.  $\text{CO}_2$  loss makes the measured pH of the sample higher than the actual pH of the water in the formation. The high pH values are reflected as positive calcite saturation indices. This effect may be the cause of the apparent oversaturation of a number of these samples.

Sampling difficulties generally do not result in undersaturation with respect to calcite, so the samples in Table E.1 and Figure E.3 which have strongly negative calcite saturation indices must be examined. Possible reasons why a given sample may have a saturation index other than zero include the following: (1) errors in the chemical analysis or sampling procedure; (2) contamination by fluids used in well construction; (3) errors in the calculation of the saturation index including the procedure for calculating activities for ions in solution; and (4) a lack of equilibrium between the formation water and the mineral in question.

Samples 14 (H-4b, 14-Dec-78) and 21 (H-5b, 19-Dec-78) are strongly to moderately undersaturated with gypsum and calcite. These wells were resampled in 1981 and 1985 and the resulting analyses are shown in Figure E.3 as sample numbers 15 and 16, and 22 and 23, respectively. The 1981 and 1985 samples are all saturated with calcite and gypsum although the 1981 sample is significantly oversaturated with calcite, presumably as a result of CO<sub>2</sub> loss during sampling. Comparison of the 1978, 1981, and 1985 analytical results shows that while there is good agreement among most constituents, the calcium concentrations reported in 1978 are very much lower than the 1981 and 1985 values. The negative saturation indices for 1978 samples are therefore probably the result of analytical errors. They do not indicate either that the aquifer is undersaturated with gypsum and calcite or that the sample is not representative of the formation fluid at this location.

A similar situation exists for samples 25, 26, and 27 from well H-6b. Sample 25, collected on December 20, 1978, is undersaturated with respect to gypsum and somewhat oversaturated with respect to calcite. Samples 26 and 27, collected in 1981 and 1985, are very close to saturation with respect to both calcite and gypsum. The reported calcium concentration in sample 25 is about 50 percent of the concentration reported for samples 26 and 27, while the concentrations of the other components are comparable. This suggests the calcium analysis for sample 25 is in error.

Samples 56, 57, and 58 from the WIPP-29 well are undersaturated with respect to both calcite and gypsum. Although this could be due to analytical or calculational errors, Lambert (1978) has argued on the basis of isotopic data that waters from this well may be locally derived and not representative of Culebra formation waters. They will, therefore, not be discussed further.

Samples 59 and 60 are from the WIPP-30 well. Sample 59 is under-saturated with gypsum and calcite, while sample 60 is saturated with gypsum and strongly oversaturated with calcite. These samples are very different from each other in total dissolved solids contents and chemical composition.

The sampling of WIPP-30 is described by Lambert and Robinson (1984, p. 30 and Fig. 4.3). Before sampling the Culebra, a more saline sample from the Rustler/Salado contact was collected in mid-July. During the following pumping test of the Culebra in mid-August, it was noticed that the salinity of the fluid produced was increasing with time. A packer separating the Culebra from the Rustler/Salado Contact zone was removed and found to be leaking because of a missing shear plug. When the packer was replaced and the pumping resumed, a decrease in conductivity in the sample fluid was noted corresponding to the removal of the more saline Rustler/Salado water which had invaded the Culebra. The less saline and lower density water of sample 60 is probably more representative of Culebra formation water than is that from sample 59 which probably represents a mixture of Culebra and deeper, more saline water from the Rustler/Salado contact. The oversaturation of sample 60 with calcite presumably reflects loss of CO<sub>2</sub> during sampling.

The same type of sampling procedure was used on the other WIPP wells (25 to 30) listed in Table E.1. First, a sample was collected from the highly saline Rustler/Salado contact zone. Then a packer was emplaced so as to isolate the Culebra. A sample was collected and a pumping test carried out. During the pumping test, conductivity and other chemical parameters were monitored (Lambert and Robinson, 1984). During the pumping of WIPP-25, WIPP-28, and WIPP-29, decreases in the density, conductivity, and/or bicarbonate content of the discharge were noted. In these wells, the initial samples collected for analyses (46 and possibly 47 from WIPP-25; 54 from WIPP-28; and 56 from WIPP-29) may well have included some component of the more saline Rustler/Salado waters.

During pumping of WIPP-26 and WIPP-27, there was little change in the chemistry of the discharge and thus the samples from these wells do not contain as obvious a component of Rustler/Salado water.

Sample 40, taken from well P-14 in March 14, 1977, is undersaturated with calcite and nearly saturated with gypsum. Sample 41, taken from the same well on February 26, 1986, is saturated with both calcite and gypsum. The main difference in the chemistry of the two samples is a much higher NaCl content of sample 40. Because P-14 was cased and sequentially perforated in first, the Rustler/Salado Contact, and, second, the Culebra, these differences may reflect a sampling problem similar to that observed for the WIPP wells previously discussed. Alternatively, it may reflect contamination resulting from drilling or well-construction fluids.

Additional samples which are significantly undersaturated with respect to calcite and/or gypsum include samples 13, 35, 36, 37, 42, 45, and 52. The results of calculations presented by Siegel (1986) suggest that the use of the Pitzer approach to calculation of activity coefficients in brines may resolve the problems with samples 13, 36, 52, and possibly 45. This explanation does not apply to the apparent undersaturation of samples 35, 37, and 42 from wells H-11b3, DOE-1, and P-15. Because only one analysis is available for each of these wells, pinpointing the problem with each of these analyses will be difficult.

### E.3 Summary and Conclusions

Densities were calculated for water samples from wells at the WIPP site and the surrounding area based on the chemical compositions of these samples. Calculated densities compare favorably with measured densities for the samples most recently (1984-85) obtained as part of the Environmental Monitoring Program. Samples taken prior to 1984 show greater variations between calculated and measured densities. Those



samples showing variations greater than 0.5 percent are listed in Table E.2. Most of the pre-1984 samples listed in Table E.2 are from wells that were sampled more recently with better results. Those wells for which adequate density data are not available are listed in Table E.3. For these wells, the calculated densities rounded to the nearest 0.005 are the recommended values.

The extent to which the water samples represent Culebra formation waters has been evaluated by calculating the degree to which the waters are saturated with mineral phases known to be present in the Culebra. The corresponding saturation indices should be close to zero if the waters have equilibrated with the minerals in the formation. Most of the samples are close to saturation ( $\pm 0.1$ ) with celestite ( $\text{SrSO}_4$ ), gypsum ( $\text{CaSO}_4 \cdot 2\text{H}_2\text{O}$ ), and calcite ( $\text{CaCO}_3$ ). Of those samples undersaturated with calcite and/or gypsum, most are older samples from wells for which more recent samples show saturation or oversaturation in these mineral phases. This suggests the older samples did not represent Culebra waters. Samples undersaturated with calcite and/or gypsum from wells with only a single sample are listed in Table E.3. These samples probably do not adequately represent Culebra waters. Resampling of these wells may resolve the discrepancies. The WIPP-29 well is also listed in Table E.3 because both the chemical and density data for this well are suspect. As Lambert (1985) has pointed out, water from this well likely represents local infiltration and does not represent Culebra water.

## REFERENCES

- Core Laboratories, Inc., 1986. A Complete Petrographic Study of Various Samples from the Rustler Formation. Prepared for INTERA Technologies, Austin, Texas, as contractor to Sandia National Laboratories, Albuquerque, New Mexico.
- Hanshaw, B.B., W. Back, and M. Rubin, 1965. Carbonate equilibria and radiocarbon distribution related to groundwater flow in the Floridan Limestone Aquifer, U.S.A.. In, Hydrology of Fractured Rocks, Proceedings of the Dubrovnik Symposium, October, 1986, International Association of Scientific Hydrology-UNESCO, Vol. 1, 601-614 p.
- INTERA Environmental Consultants, Inc., 1983. PHREEQE: A Geochemical Speciation and Mass Transfer Code Suitable for Nuclear Waste Performance Assessment. ONWI-435, prepared for Battelle Memorial Institute, Office of Nuclear Waste Isolation, Columbus, Ohio, 304 p.
- Kumar, A., 1986. Prediction of densities of concentrated brines by Pitzer Theory. J. Chemical Engineering Data, Vol. 31, p 19-20.
- Lambert, S.J. and K.L. Robinson, 1984. Field Geochemical Studies of Groundwaters in Nash Draw Southeastern New Mexico. Sandia National Laboratories, SAND83-1122, 38 p.
- Lambert, S.J., 1978. Stable-Isotope Studies of Groundwaters in Southeastern New Mexico. Sandia National Laboratories, SAND85-1978C, 22 p.
- Mercer, J.W., 1983. Geohydrology of the Proposed Waste Isolation Pilot Plant Site Los Medanos, Southeastern New Mexico. U.S. Geological Survey Water-Resources Investigations Report 83-4016, 113 p.

- Nordstrom, D.K., and J.L. Munoz, 1985. Geochemical Thermodynamics. The Benjamin/Cummings Publishing Co., Inc., Menlo Park California, 447 p.
- Parkhurst, D.L., D.C. Thorstenson, and L.N. Plummer, 1980. PHREEQE - A Computer Program for Geochemical Calculations. U.S. Geological Survey Water-Resources Investigations 80-96, 210 p.
- Pearson, F.J., 1985. Sondierbohrung Boettstein - Results of Hydrogeochemical Investigations: Analysis and Interpretation. Nagra, Baden, Switzerland, Technischer Bericht NTB85-05, 116 p.
- Pearson, F.J., Jr. and J.L. Lolcama, in preparation. Chemistry of groundwaters in the Boettstein, Weiach, Riniken, Schafisheim, Kaisten and Leuggern Boreholes: A Hydrochemically Consistent Data Set. Nagra, Baden, Switzerland, Technischer Bericht NTB86-19, in preparation.
- Pearson, F.J., Jr. and P.L. Rettman, 1976. Geochemical and isotopic analysis of waters associated with the Edwards Limestone Aquifer, Central Texas. U.S. Geological Survey Report, published by Edwards Underground/Water District, San Antonio, Texas, 35 p.
- Pearson, F.J., Jr., V.A. Kelley, and J.F. Pickens, in preparation. Preliminary Design for a Sorbing Tracer Test in the Culebra Dolomite at the H-3 Hydropad at the Waste Isolation Pilot Plant (WIPP) Site. Sandia National Laboratories, SAND86-7177.
- Pitzer, K.S., 1979. Activity coefficients in electrolyte solutions. R.M., Ed.; CRC Press, Boca Raton, Florida, Vol.1, Chapter 7.
- Ramey, D.S., 1985, Chemistry of Rustler Fluids. Health and Environment Department, Environmental Evaluation Group, Santa Fe, NM, EEG-31, 61 p.

Rightmire, C.T., F.J. Pearson, Jr., W. Back, R.O. Rye, and B.B. Hanshaw, 1974. Distribution of sulphur isotopes of sulphates in groundwaters from the Principal Artesian Aquifer of Florida and the Edwards Aquifer of Texas, United States of America. In, Isotope Techniques in Groundwater Hydrology, 1974, International Atomic Energy Agency, Vienna, Vol.II, p. 191-207.

Robinson, K.L., in preparation. Analysis of Solutes in Groundwaters for the Rustler Formation at and Near the WIPP Site. Sandia National Laboratories, SAND86-0917.

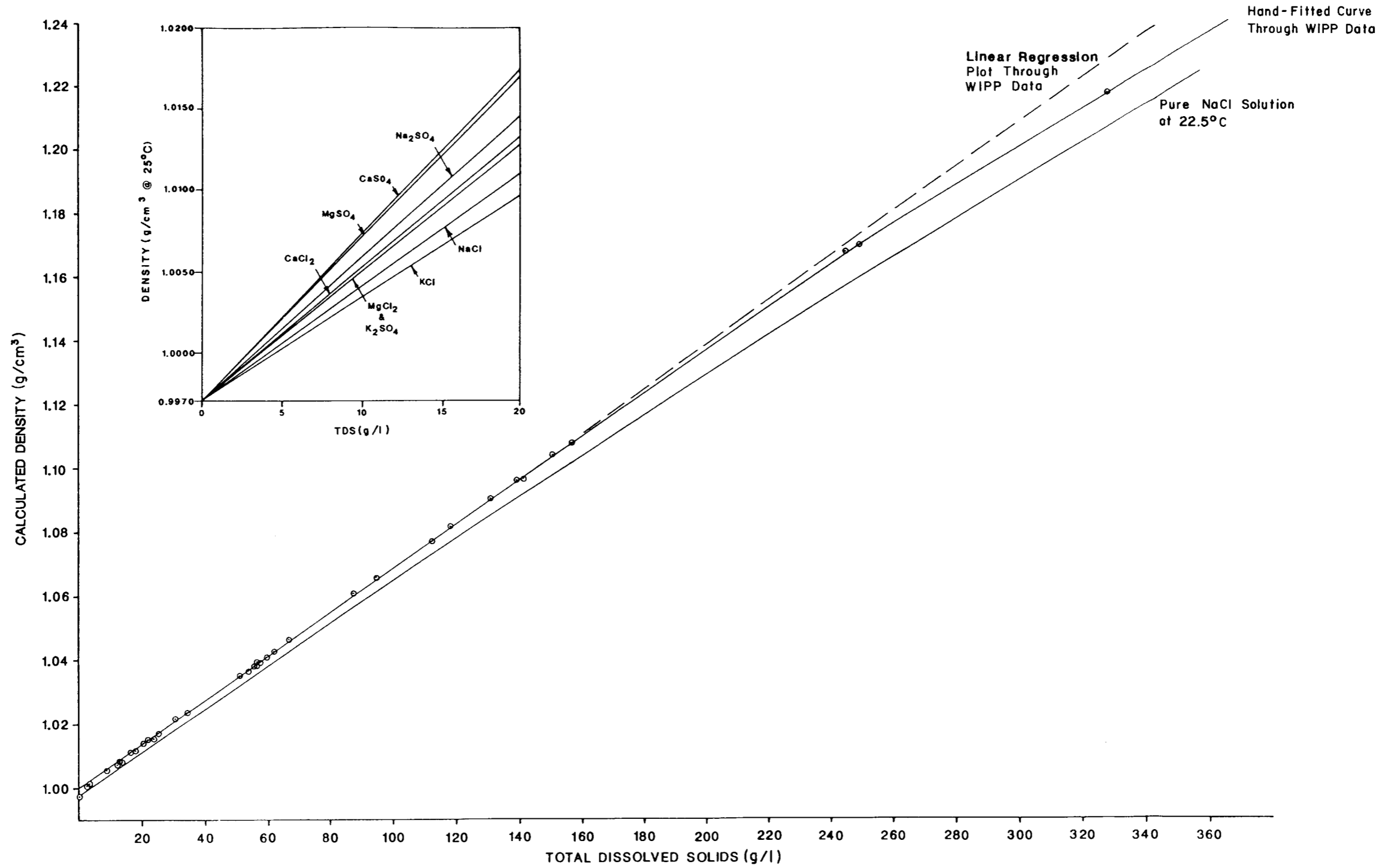
Schmassmann, H., W. Balderer, W. Kanz, and A. Pekdeger, 1984. Beschaffenheit der Tiefengrundwasser in der zentralen Nordschweiz und angrenzenden Gebieten. Nagra, Baden, Switzerland, Technischer Bericht NTB84-21, 334 p.

Siegel, M., 1986. Preliminary Notes on Calculations of Saturation Indices of Culebra Brine Samples. Sandia National Laboratories, Division 6431, Internal Memorandum, 12 p.

Truesdell, A.H. and B.F. Jones, 1974. WATEQ, A computer program for calculating equilibria of natural waters. U.S. Geological Survey Journal of Research, Vol.2, p. 233-248.

Weast, Robert C., ed., 1983. CRC Handbook of Chemistry and Physics. CRC Press, Inc., Boca Raton, Florida, 64th Edition.

Westinghouse Electric Corporation, 1985. Ecological Monitoring Program at the Waste Isolation Pilot Plant. Second Semi-annual Report Covering Data Collected January to June 1985. DOE/WIPP-85-002, Prepared for the U.S. Department of Energy, Carlsbad, New Mexico.



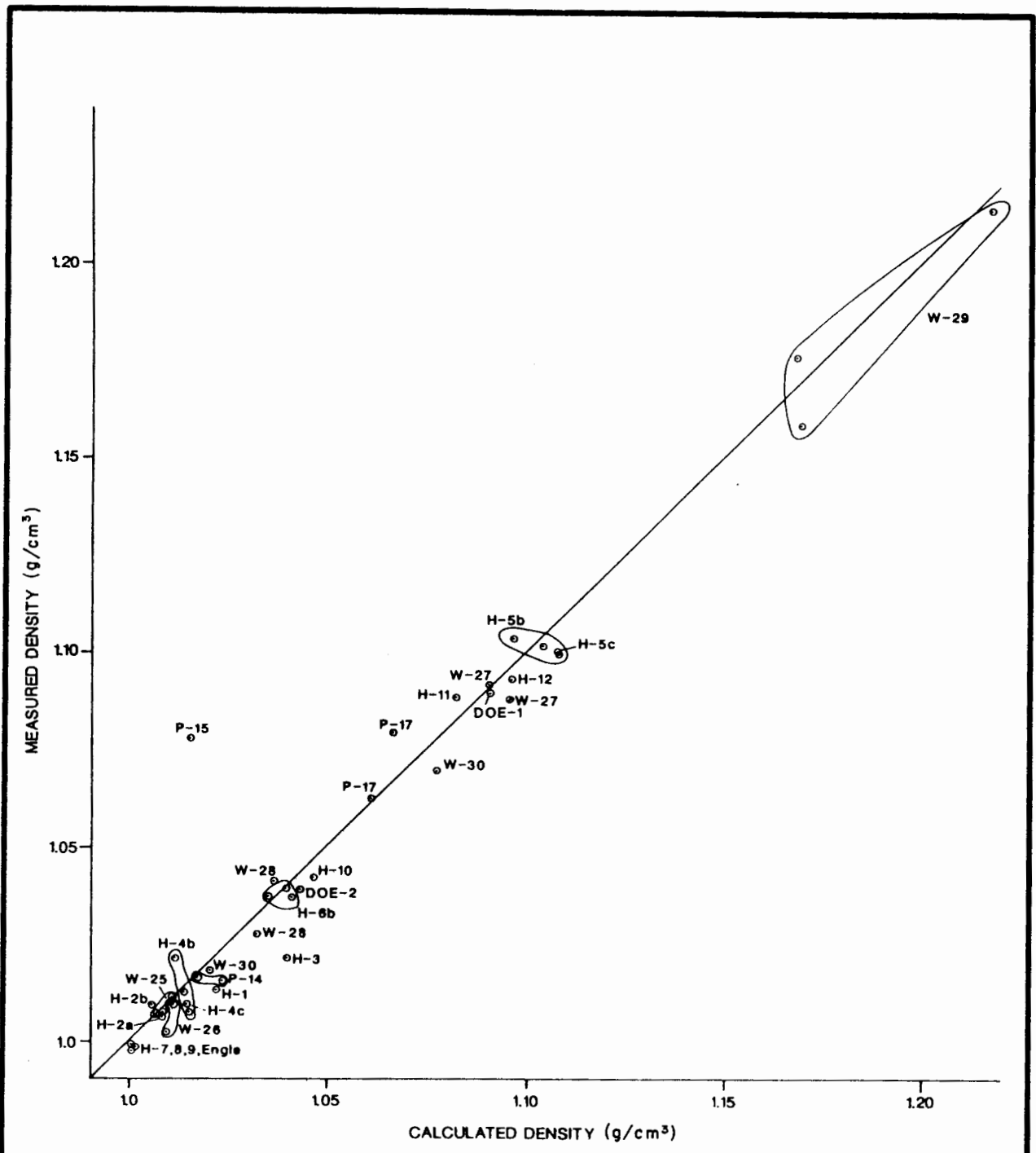
**LEGEND**  
 ○ WIPP Water Samples

Drawn by	Date
Checked by	Date
Revisions	Date

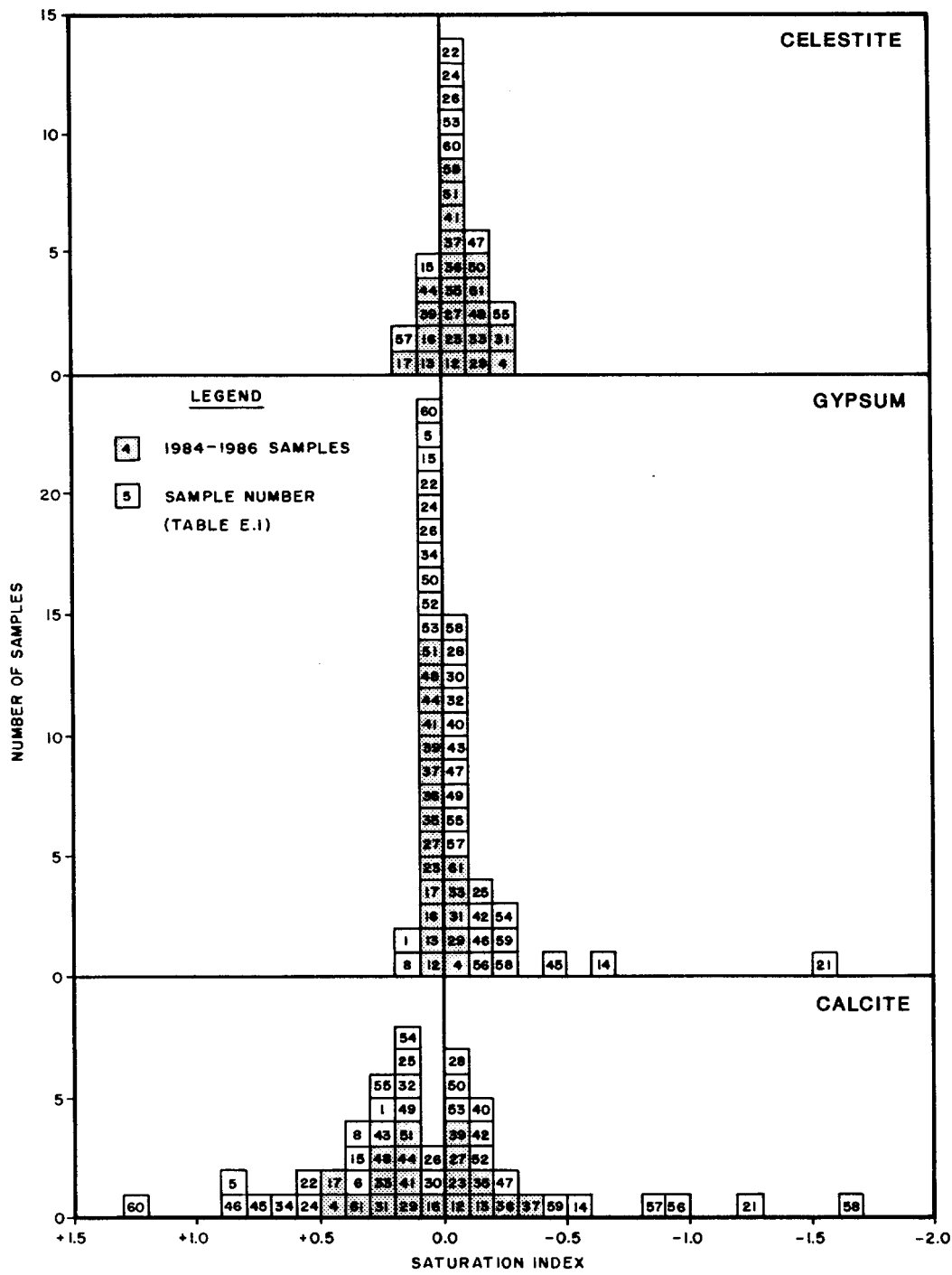
Calculated Densities Versus  
 Total Dissolved Solids for Culobra Waters

**INTERA Technologies**

Figure E.1



Drawn by	Date	Measured Densities Versus Calculated Densities
Checked by	Date	
Revisions	Date	
<b>INTERA Technologies</b>		Figure E.2



Drawn by	Date
Checked by	Date
Revisions	Date

Histogram of Saturation Indices of Celestite, Calcite, and Gypsum.

**INTERA Technologies**

Figure E.3

Smpl No.	Well Number	Date Sampled	Temp. ( C )	-----Density (kg/l)---		Charge Balance ( % )	Tot Diss Residue (g/l)	Solids Sum (g/l)	Chloride (g/l)	Sulfate (g/l)	Ratio mol Na/ mol K	---Saturation Indices---			
				Measured	Calculated							Use	Calcite	Gypsum	Celestite
1	H-1	2-Jun-76	(22.5)	1.0136	1.0218	1.020	-3.88	30.1	30.12	12	7.4	84.1	0.28	0.11	
2															
3															
4	H-2a	21-Apr-86	23.0	1.0066	1.0085	1.010	-1.97		12.98	5.31	2.98	64.9	0.50	-0.03	-0.20
5	H-2b1	22-Feb-77	22.5	1.0099	1.0058	1.010	-1.00	9.7	8.93	2.8	3	39.3	0.90	0.01	
6	H-2b2														
7	H-3b1	75/76						60		33	5.2	51.3			
8		17-Mar-77		1.0219	1.0396	1.040	1.77	62	57.27	29.6	5.7		0.39	0.11	
9			(21.5)	1.0318											
10			(21.5)	1.0378											
11	H-3b3														
12		11-Jun-84	(22.5)		1.0381	1.040	-6.12		55.16	29.5	5.13	59.8	-0.05	0.09	-0.04
13		4-Feb-85	25.0		1.0386	1.040	-2.65		56.04	30.3	4.82	72.0	-0.10	0.04	0.08
14	H-4b	14-Dec-78	(22.5)	1.0217	1.0116	1.015	1.80	18.1	18.23	7.5	4	54.8	-0.55	-0.62	
15		29-May-81	23.0	1.0076	1.0151	1.015	-4.10		21.86	7.98	6.23	49.2	0.40	0.07	0.10
16		25-Jul-85	21.5	1.0129	1.0140	1.015	-2.56		20.28	7.4	5.52	47.4	0.06	0.03	0.07
17	H-4c	10-Aug-84	(22.5)		1.0145	1.015	1.37		21.50	7.95	5.7	47.1	0.45	0.03	0.16
18			(22.5)	1.0097											
19			(22.5)	1.0097											
20			(22.5)	1.0097											
21	H-5b	19-Dec-78	(22.5)	1.1035	1.0963	1.100	2.91	144	143.70	86	0.81	64.4	-1.23	-1.58	
22		1-Jun-81	24.0	1.0971	1.1077	1.100	-4.23		154.61	89.5	7.36	68.9	0.55	0.02	0.00
23		27-Aug-85	22.5	1.1015	1.1040	1.100	1.10		152.76	85.3	7.84	68.2	-0.08	0.04	-0.02
24	H-5c	15-Oct-81	25.0	1.1000	1.1077	1.100	-4.29		154.87	89.5	7.57	68.9	0.60	0.03	0.01
25	H-6b	20-Dec-78	(22.5)	1.0376	1.0351	1.040	7.17	52.6	52.59	28	3.8	61.2	0.17	-0.14	
26		2-May-81	23.0	1.0375	1.0410	1.040	0.10		59.44	33	3.98	70.3	0.06	0.09	-0.02
27		15-Sep-85	23.5	1.0394	1.0394	1.040	-1.22		57.45	32.3	3.57	81.2	-0.07	0.04	-0.07
28	H-7b	20-Mar-80	(22.5)	0.9987	1.0015	1.000		3.61	3.29	0.35	1.9	255.8	-0.05	-0.03	
29		26-Mar-86	21.5	0.9989	1.0005	1.000	-0.56		3.22	0.32	1.85	50.3	0.13	-0.03	-0.15
30	H-8b	11-Feb-80	(22.5)	0.9977	1.0007	1.000	-4.35	3.2	2.95	0.057	2	29.7	0.02	-0.02	
31		22-Jan-86	22.0	0.9998	1.0001	1.000	-0.35		2.83	0.03	1.95	24.5	0.38	-0.03	-0.20
32	H-9b	5-Feb-80	(22.5)	0.9997	1.0049	1.000	3.36	3.59	3.49	0.32	2	2.6	0.18	-0.03	
33		14-Nov-85	22.0	0.9998	1.0006	1.000	0.83		3.07	0.193	1.9	36.2	0.29	-0.02	-0.19
34	H-10b	21-Mar-80	(22.5)	1.0426	1.0465	1.045	2.58	69.2	65.82	36	5.6	68.7	0.61	0.09	
35	H-11b3	23-May-85	22.5	1.0885	1.0819	1.085	3.12		118.12	65.9	7.18	73.1	-0.16	0.06	-0.06
36	H-12	9-Aug-85	24.0	1.0930	1.0960	1.095	-2.34		140.77	79	7.21	65.9	-0.21	0.04	-0.01

Drawn by	Date	Chemical and Physical Data on Culebra Formation-Water Samples
Checked by	Date	
Revisions	Date	
<b>INTERA Technologies</b>		Table E.1a



Smpl No.	Well Number	Date Sampled	Temp. ( C )	-----Density (kg/l)---		Charge Use	Charge Balance ( % )	Tot Diss Residue (g/l)	Solids Sum (g/l)	Chlor-ide (g/l)	Sul-fate (g/l)	Ratio mol Na/ mol K	---Saturation Indices---		
				Meas-ured	Calcul-ated								Calcite	Gypsum	Celestite
37	DOE-1	12-Apr-85	22.5	1.0895	1.0906	1.090	-8.35		131.51	73.6	7.35	70.8	-0.36	0.06	-0.05
38				1.0815											
39	DOE-2	12-Mar-85	21.5	1.0396	1.0431	1.040	0.42		60.59	34.6	3.95	76.3	-0.04	0.05	0.05
40	P-14	14-Mar-77	(22.5)	1.0159	1.0236	1.015	-3.96	38	33.67	20	1.4	21.5	-0.14	-0.07	
41		26-Feb-86	22.5	1.0167	1.0174	1.015	-1.78		25.02	14.5	1.59	195.7	0.19	0.07	-0.05
42	P-15	10-May-77	21.5	1.0778	1.0152	1.015	-6.19	24	23.72	11	3.2	6.9	-0.17	-0.12	
43	P-17	10-May-77	22.0	1.0796	1.0661	1.060	2.20	97	92.47	54	5	425.2	0.24	-0.03	
44		17-Mar-86	21.5	1.0626	1.0609	1.060	-2.34		86.76	48.2	6.02	61.5	0.13	0.05	0.02
45	P-18	10-May-77	24.5		1.0889	1.090	-6.60	420	118.70	80	0.98	2.5	0.74	-0.46	
46	WIPP-25	14-Aug-80	(22.5)	1.0117	1.0107	1.010	-5.74	22.1	17.23	8.3	2.4	9637.2	0.83	-0.11	
47		20-Aug-80	23.0	1.0076	1.0072	1.010	2.43		12.19	5.2	2.49	73.4	-0.22	-0.03	-0.18
48		12-Feb-86	21.5	1.0079	1.0086	1.010	-2.84		13.55	6.32	2.38	53.6	0.27	0.02	-0.10
49	WIPP-26	18-Aug-80	(22.5)	1.0107	1.0102	1.010	-1.11	23.8	15.75	8.2	2.3	3061.2	0.10	-0.01	
50		24-Aug-80	22.0	1.0028	1.0094	1.010	-1.68		15.17	7.2	2.48	36.2	-0.04	0.04	-0.10
51		25-Nov-85	22.0	1.0098	1.0115	1.010	-2.98		17.6	8.77	2.42	20.9	0.17	0.03	-0.09
52	WIPP-27	22-Aug-80	(22.5)	1.0915	1.0906	1.090	-14.19	186	125.83	77	3.9	92.9	-0.10	0.05	
53		5-Sep-80	(22.5)	1.0876	1.0963	1.090	-3.21		134.81	78.5	3.83	8.3	-0.09	0.05	-0.04
54	WIPP-28	21-Aug-80	(22.5)	1.0416	1.0366	1.035	-10.36	74	56.34	30	3.2	8928.6	0.19	-0.23	
55		11-Sep-80	22.5	1.0277	1.0321	1.035	-2.96		46.99	24.7	4.38	53.9	0.21	-0.04	-0.20
56	WIPP-29	20-Aug-80	(22.5)	1.1753	1.1676	1.215	8.86	239	239.05	140	13	895.7	-0.90	-0.17	
57		28-Aug-80	20.0	1.1580	1.1691	1.215	-4.60		245.57	138	14	7.8	-0.85	-0.03	0.17
58		14-Dec-85	23.0	1.2131	1.2176	1.215	-3.43		324.15	179	20.03	6.9	-1.61	-0.28	-0.07
59	WIPP-30	13-Aug-80	(22.5)	1.0696	1.0771	1.020	-6.71	110	109.32	64	5.05	70.9	-0.41	-0.22	
60		6-Sep-80	21.0	1.0184	1.0204	1.020	-5.11		29.25	14.6	4.12	58.3	1.30	0.06	-0.02
61	Engle W.	4-Mar-85	22.0		1.0009	1.000	1.80		3.26	0.23	1.99	60.7	0.38	-0.02	-0.15

Drawn by	Date	Chemical and Physical Data on Culebra Formation-Water Samples
Checked by	Date	
Revisions	Date	
<b>INTERA Technologies</b>		Table E.1b

Smpl No.	Well Number	Date Sampled	Suspect Data	Cause for Suspicion
1	H-1	2-Jun-76	Density	Difference between measured and calculated density 0.8 percent.
8	H-3b1	17-Nov-77	Density	Difference between measured and calculated density 1.7 percent.
14	H-4b	14-Dec-78	Density Chemistry	Difference between measured and calculated density 1.0 percent. Negative gypsum (-0.62) and calcite (-0.55) saturation indices.
15	H-4b	29-May-81	Density	Difference between measured and calculated density 0.7 percent.
21	H-5b	19-Dec-78	Density Chemistry	Difference between measured and calculated density 0.7 percent. Negative gypsum (-1.58) and calcite (-1.23) saturation indices.
22	H-5b	1-Jun-81	Density	Difference between measured and calculated density 1.0 percent.
25	H-6b	20-Dec-78	Chemistry	Negative gypsum saturation index (-0.14).
35	H-11b3	23-May-85	Density Chemistry	Difference between measured and calculated density 0.6 percent. Negative calcite saturation index (-0.16).
37	DOE-1	12-Apr-85	Chemistry	Negative calcite saturation index (-0.36).
40	P-14	14-Mar-77	Density Chemistry	Difference between measured and calculated density 0.75 percent. Negative calcite (-0.14) saturation index.
Drawn by		Date	Summary of Samples With Suspect Density and/or Chemical Data	
Checked by		Date		
Revisions		Date		
<b>INTERA Technologies</b>				Table E.2a

Smpl No.	Well Number	Date Sampled	Suspect Data	Cause for Suspicion
42	P-15	10-May-77	Density Chemistry	Difference between measured and calculated density 6.3 percent. Negative calcite (-0.17) and gypsum (-0.12) saturation indices.
43	P-17	10-May-77	Density	Difference between measured and calculated density 1.3 percent.
45	P-18	10-May-77	Chemistry Density	Negative gypsum saturation index (-0.46). No measured density value.
46	WIPP-25	14-Aug-80	Chemistry	Negative gypsum saturation index (-0.11).
50	WIPP-26	24-Aug-80	Density	Difference between measured and calculated density 0.7 percent.
52	WIPP-27	22-Aug-80	Chemistry	Charge balance -14.19 percent.
54	WIPP-28	21-Aug-80	Chemistry Density	Negative gypsum saturation index (-0.23). Difference between measured and calculated density 0.5 percent. Charge balance -10.36 percent.
56	WIPP-29	20-Aug-80	Chemistry Density	Negative calcite (-0.90) and gypsum (-0.17) saturation indices. Difference between measured and calculated density 0.66 percent.
57	WIPP-29	28-Aug-80	Chemistry Density	Negative calcite (-0.85) saturation index. Difference between measured and calculated density 1.0 percent.
58	WIPP-29	14-Dec-85	Chemistry	Negative calcite (-1.61) and gypsum (-0.28) saturation indices.
59	WIPP-30	13-Aug-80	Chemistry Density	Negative calcite (-0.41) and gypsum (-0.22) saturation indices. Difference between measured and calculated density 0.7 percent.
Drawn by		Date	Summary of Samples With Suspect Density and/or Chemical Data	
Checked by		Date		
Revisions		Date		
<b>INTERA Technologies</b>			Table E.2b	

Well Number	Reason(s) For Concluding That Sample Data Do Not Represent Culebra Water Properties
H-11b3	Difference between measured and calculated density 0.6 percent. Slightly negative calcite saturation index (-0.16). This well is only marginally inconsistent in water properties.
DOE-1	Negative calcite saturation index (-0.36).
P-15	Difference between measured and calculated density 6.3 percent. Negative calcite (-0.17) and gypsum (-0.12) saturation indices.
P-18	Negative gypsum saturation index (-0.46). No measured density value available.
WIPP-29	All samples from this well have negative gypsum and calcite saturation indices. Differences between measured and calculated densities for the two 1980 samples are 0.66 and 1.0 percent.

Drawn by	Date	Summary of Wells For Which No Reliable Data Are Available on the Properties of Culebra Formation Water
Checked by	Date	
Revisions	Date	
<b>INTERA Technologies</b>		Table E.3



APPENDIX F. REVIEW AND CHRONOLOGY OF KNOWN INFORMATION ON GROUND-WATER  
LEAKAGE INTO THE SHAFTS AT THE WIPP SITE. (By G. J. Saulnier)

Three deep shafts have been constructed at the WIPP site. The shafts were built as part of the development of the site as a repository for storage of defense transuranic wastes and are designed: 1) to handle waste for the repository - the waste-handling shaft; 2) to facilitate removal of excavated salt during construction of the repository - the construction and salt-handling shaft; and 3) to allow proper ventilation of the underground opening - the exhaust shaft. The relative positions and distances between the shafts are illustrated in Figure F.1. All of the shafts penetrated the entire Rustler Formation. Obvious ground-water leakage into the shafts was reported only from the Culebra. The following is a chronology of events for each shaft, highlighting information concerning the leakage or drainage of formation water from the Culebra into the three shafts.

Figure F.2 illustrates the construction and sealing history for all three shafts with a schematic representation of pressure response in the Magenta and Culebra as recorded by the piezometers installed in both the waste-handling and the construction and salt-handling shafts.

#### Waste-Handling Shaft

The waste-handling shaft was originally a bored, six-foot diameter ventilation shaft to the repository level, completed from December 1981 to February 1982. The ventilation shaft remained open to the Culebra allowing ground-water drainage from this unit prior to the shaft's excavation as the waste-handling shaft, with a nineteen-foot finished inside diameter, between November 1983 and August 1984. The additional excavation fully penetrated the Rustler Formation in February 1984. The

shaft was mapped by geologists before the shaft liner was emplaced and the following paragraph from the Quarterly Geotechnical Data Report (U.S. Department of Energy, September 1985) summarizes the observations concerning water inflow:

Of the three formations observed during geological mapping activities in the waste shaft, only the Rustler formation contained obvious fluid-bearing zones, the Magenta and the Culebra dolomite members. The Magenta exhibited few weeps and, in general, produced very little water. However, the entire Culebra section was wet, but no obvious local concentrations of water inflow were observed. Wherever a ledge was formed, a steady dripping of water was observed. The Rustler/Salado contact, often considered a fluid-producing zone, did not produce any observable fluid.

Geotechnical instruments, including pressure transducers to measure formation fluid pressure, were installed in the shaft in August and September of 1984 (Figure F.3). The pressure transducers are called piezometers by the on-site contractor and this term is used throughout the geotechnical literature concerning the WIPP site. For the sake of consistency, the term piezometer will also be used in this discussion when referring to these pressure transducers. A plot of the measurements from these piezometers is included as Figure F.4. The pressure data were collected weekly at ground surface by the Management and Operations Contractor using a datalogger. Data collection for the waste-handling shaft was discontinued in August 1986 due to construction activities in the shaft. The schedule for re-establishing measurements has not been finalized.

The following paragraph describes the sealing of the Rustler Formation as reported in the Quarterly Geotechnical Field Data Report (U. S. Department of Energy, September 1985):

Placement of the primary concrete lining of the shaft began November 30, 1983, and was completed on

April 3, 1984, to a depth of 900 ft. Both the water-bearing Magenta and Culebra dolomite members were covered with steel liner plate prior to the placement of the primary concrete lining. The required over-excavated annulus behind the steel liner plate at both water-bearing zones was backfilled with thick grout (second stage lining) after the primary concrete lining had cured. At the Magenta, the annular void was backfilled on March 8 through March 10, 1984. Second stage lining at the Culebra was completed on April 3 through April 5, 1984. After completion of the sump excavation, grouting was done to seal minor water leaks and seeps in the waste shaft lining. The shaft lining grouting program was conducted from August 11 through August 25, 1984. Prior to grouting, seepage was estimated at 0.5 gallons per minute. The seepage after grouting, measured in October 1984 from the 2-in. drain pipe connected to the three water rings, was about 0.015 gallons per minute.

The "water rings" described in the Quarterly Report are concave-upward steel rings on the bottom of indentations in the concrete-shaft wall. Leaking ground water can reach these rings by moving through cracks in the concrete wall, and flowing down the face of the shaft to the rings. The water collected by the rings is directed to a plastic pipe for drainage to the shaft sump area. The quantity of flow to the rings could be decreased by evaporation at the concrete face or by water deflected by shaft furnishings (e.g., cable support brackets, instrument boxes, etc.).

Few measurements of the amount of seepage collected by the water rings were made before 1986. In September 1985, at a time when the water-collection system inside the shaft was damaged, and all drainage went directly to the sump, the change in water level in the shaft sump was used to estimate shaft leakage. A general estimate of 0.13 gpm has been determined and reported by Mr. J. Gallerani of Bechtel National, Inc.



In January 1986, the water-collection system was repaired and all shaft drainage was directed through the plastic pipe to a 250-gallon tank. Mr. R. McKinney of IT Corporation has reported a general estimate of 0.6 gpm for the flow, but this figure is not documented in measurement records. Mr. McKinney has stated that the 250-gallon tank was emptied once per 8-hour shift, and 0.6 gpm would fill the tank in about seven hours. However, it appears that this figure is only an estimate and that the volume and time used were not exactly measured and recorded.

Mr. J. Gallerani of Bechtel National Inc. began weekly measurements of flow from the drainage system in January 1986 to establish a documented record of shaft drainage. Mr. Gallerani uses a five-gallon bucket and a stopwatch to determine the flow rates. Table F.1 lists these measurements from January through June 1986 when the plastic pipe was damaged again by construction activities. The pipe was repaired in September and two measurements were made in October 1986 by Mr. Gallerani.

An additional amount of water (small and difficult to measure) bypasses the collection rings and drips down the shaft face. The Mining Operations Section also reports a flow estimate to Mr. R. McKinney of IT Corporation. This estimate is usually about 0.1 gpm higher than Mr. Gallerani's value but the method of estimation is not well documented. (Mr. Gallerani has stated that the Mining Operations Manager times the filling of a one-gallon container that may not be calibrated.) Additional grouting of the waste-handling-shaft lining to try to stop leakage into the shaft is scheduled to begin in April 1987.

#### Construction and Salt-Handling Shaft

The history of the construction and salt-handling shaft is summarized as follows in the Quarterly Geotechnical Data Report (U.S. Department of Energy, September 1985):

The first construction activity undertaken during SPDV [Site and Preliminary Design Validation] was the excavation of the exploratory shaft, now designated the construction and salt handling shaft (C & SH Shaft). The shaft was drilled during a four-month period from July 4 to October 23, 1981. Geologic mapping was conducted during March through May 1982 ("Results of Site Validation Experiments", ref. 1-6). The shaft was outfitted with geomechanical instrumentation in April and July 1982. This included extensometers, piezometers [Figure F.2], convergence points, strain gauges and pressure cells. All instruments were read locally until October 30, 1982, when the connection was established to the datalogger located above ground.

Mr. J. Gallerani of Bechtel National Inc. has reported the existence of seepage from one of the indicator drains in the shaft key (the support buttress at the base of the upper concrete liner built through the Rustler Formation) and the observation of minor leakage at several of the piezometer connections. A water-collection ring, similar to the one in the waste-handling shaft, is built at the bottom of the construction and salt-handling-shaft key but it is not served by a plastic-pipe drainage system.

The piezometers that were placed in the Culebra in the construction and salt-handling shaft have not operated at 100% effectiveness. Since mid-1985, the surface datalogger has had no access to these instruments and they must be read individually at the Local Termination Cabinet #1 at the repository level. Work schedules involving use of the shaft allow the Management and Operations Contractor access to read these gages once every three months. Figure F.5 is a plot of the data received to date for these piezometers.

## Exhaust Shaft

The exhaust shaft was built in two stages. Initially, a 7-7/8-inch pilot hole was drilled in October and November 1983 from ground surface to a drift at the facility level in the Salado Formation. Then the pilot hole was drilled out to an 11-inch diameter in December 1983. During this period, Mr. Gallerani made two measurements of leakage from the pilot holes to the drift by catching the drain water in a plastic barrel beneath the pilot hole. On November 30, 1983, he made four measurements with a calibrated container and stopwatch and calculated an average flow rate of 0.41 gpm from the 7-7/8-inch borehole. On December 21, 1983, he calculated an average flow rate of 0.47 gpm from the 11-inch borehole. Both flow measurements were affected by a warm-air updraft from the drift which the borehole penetrated. The exhaust shaft was then raise-bored to a six-foot diameter from December 1983 to February 1984, and subsequently enlarged to fifteen feet with a final fourteen-foot finished inside diameter through the Rustler Formation from September 1984 to February 1985.

The construction of the primary concrete lining to the Salado Formation, with only steel plate covering the Magenta and Culebra, took place from July to November 1984. Backfilling behind the liner plate at the Culebra and Magenta horizons was performed in a similar fashion as that described for the waste-handling shaft. The Culebra and Magenta were grouted during the periods December 2 to 4, and December 4 to 5, 1984, respectively. J. Gallerani and J. Owens (Bethel National and Dravo, Inc., respectively, personal communication, July 1986) report that the grouting procedure did not completely seal the Culebra and Magenta at this time, and that the grouting was intended to minimize and control leakage. Construction and installation of the water-collection rings and other shaft furnishings was accomplished from December 1984 through February 1985. Water was observed seeping through the concrete lining and a flow rate of 0.35 gpm was measured at the bottom of the exhaust shaft in January 1985 by Mr. Gallerani (see also U.S. Department of Energy, September 1985). A

cement/chemical grouting and sealing of the Magenta and Culebra Members of the Rustler Formation was conducted from June 1 through July 31, 1985 to reduce water seepage through the shaft lining and to protect the integrity of the shaft key. For January 1985, before the grouting and sealing of the exhaust shaft, Mr. R. McKinney of IT Corporation reports that the estimated ground-water flow from the Rustler Formation (primarily from the Culebra Dolomite Member) was 0.6 gpm.

On September 24, 1985, the boreholes for the exhaust-shaft Culebra piezometers were drilled through the shaft liner, then capped. Piezometers were placed at the Culebra level in the exhaust shaft from November 1 to November 3, 1985. However, as of February 1986, the datalogger system was working intermittently and no readings from the exhaust-shaft piezometers were obtained. Scheduled readings began in March 1986. Figure F.6 shows the exhaust shaft pressure record along with data for the waste-handling and construction and salt-handling shafts through October 1986.

Additional chemical grouting of the Culebra and Magenta was performed in August and October 1986. The chemical grouting program consisted of the following steps:

1. On August 11, 1986, the pressure plugs in the piezometers were removed causing the piezometer pressure readings to be reduced to negative values indicating zero pressure in the piezometer sleeves. The removal of the plugs caused an unmeasured quantity of water to flow from the piezometer-access boreholes. J. Owens reports that the quantity decreased during the time the boreholes were open and virtually stopped after the chemical grouting was completed.
2. Dye-colored water was injected into the grouting holes, which are small-diameter boreholes through the liner, to determine whether there was communication between the micro-annulus behind the grout liner and the piezometer tubes. None was observed.

3. Grout was injected into the grouting holes at up to a maximum of 50 pounds per square inch over hydrostatic pressure.
4. The pressure plugs were put back on the piezometer sleeves on August 19, 1986 and data collection resumed.
5. In early October 1986, additional grouting was performed in the Culebra interval. Boreholes were drilled through the liner at level 218.5 (elevation 820.9 m a.s.l.) and water was observed to flow from these boreholes under pressure. Grout was injected into these boreholes to seal the microannulus behind the liner and reduce leakage. During the grouting, the Culebra piezometer's pressure plugs were both removed and replaced on October 1, 1986.

Figure F.6 shows the pressure response in the waste-handling shaft to the exhaust-shaft grouting and sealing activities in 1985 and 1986. The grouting and drilling exercises are noted, and can be inferred to have had a significant effect on the waste-handling shaft pressure.

#### Piezometer Installation

A brief review of the type of piezometer used and the method of installation may assist in understanding and reviewing the data (from U.S. Department of Energy, September 1985):

The piezometers are dual-component instruments containing a vibrating-wire gauge and a pneumatic gauge. The vibrating-wire gauge is the principal instrument used to measure water-pressure. The pneumatic gauge is used for initial calibration and periodic performance checks on the vibrating-wire units . . . The pneumatic units must be read manually at the instrument location.

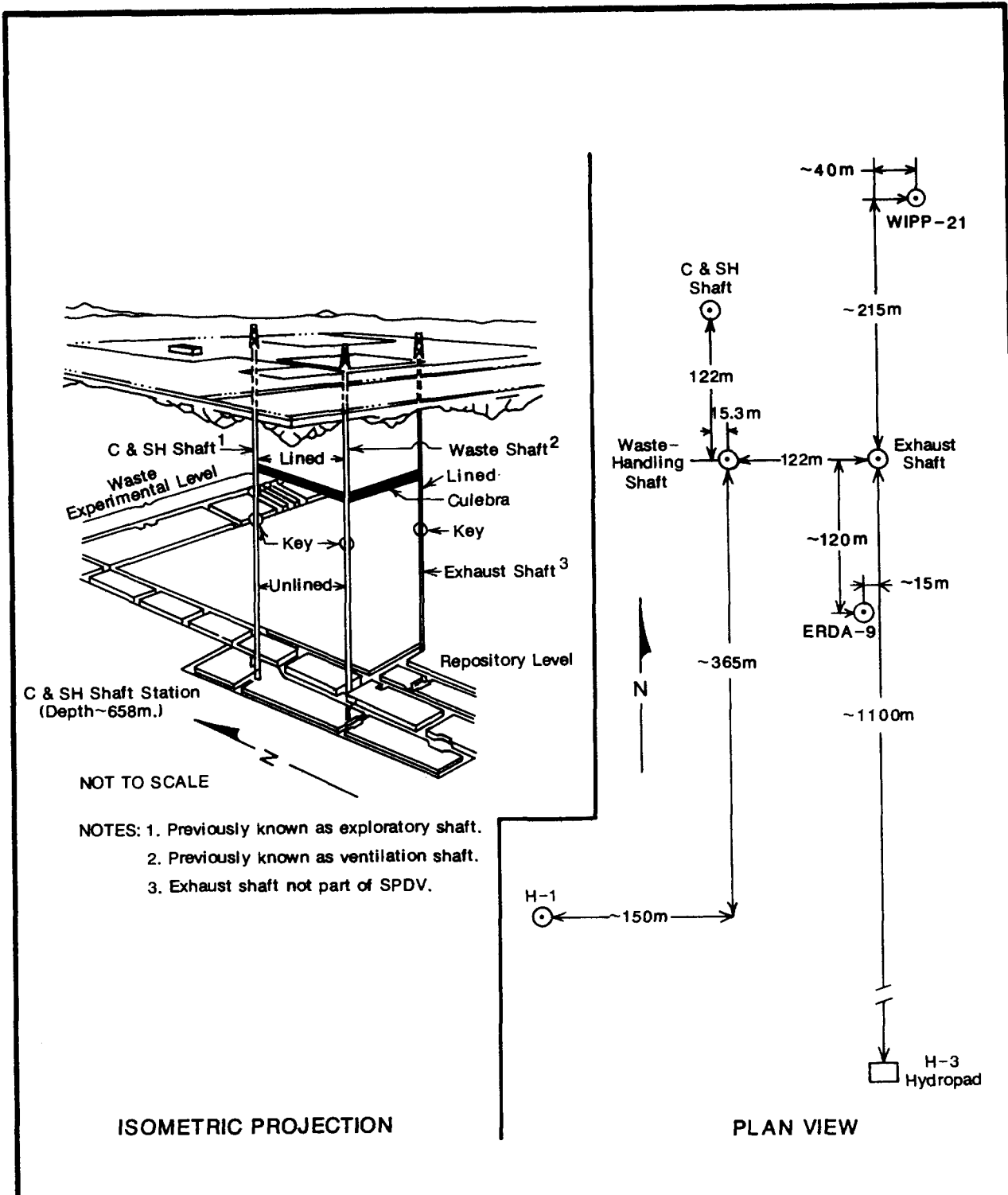
The vibrating-wire gauges are monitored at ground surface by electronic dataloggers. The electrical connections to the datalogger have been damaged in the construction and salt-handling shaft, thus requiring the downhole readings of the vibrating-wire gages as described earlier. The electrical connections for the waste-handling-shaft piezometers were removed in late August 1986 to make room for construction activities. The reconnection schedule has not yet been established.

The piezometers are installed in a four-inch pipe sleeve which passes through the concrete lining. After the concrete was poured, three-inch diameter boreholes were drilled into the bedrock at the end of the four-inch sleeves, using drilling equipment run through the sleeves. These boreholes extend a minimum of six inches into the formation and serve to access the formation for fluid-pressure measurements with the piezometers. The piezometers are set into the four-inch pipe sleeves and sealed in by a collar coupling. Figure F.7 shows construction details of the piezometer installation. The piezometers are set about one-half foot inside the collar pipe and do not reside in, and are not sealed in the three-inch boreholes in the bedrock. The piezometers can thus respond to pressure fluctuations due to cracks in the concrete liner or to any microannulus between the concrete lining and the formation, if one were to exist due to failure of the seal. If such a crack or microannulus were to connect the Magenta and Culebra, it would not only provide direct fluid-pressure communication between these two horizons, but it could also respond to a failure in the concrete liner of the shaft. In fact, data from the piezometers in the construction and salt-handling shaft were used to postulate a possible breakdown in one of the chemical seals behind the waste-handling-shaft key (the basal shaft support buttress) (U.S. Department of Energy, September 1985). Published data (U.S. Department of Energy, September 1985) show that the piezometers in the waste-handling shaft have synchronous pressure fluctuations indicating, at the least, a pressure communication between all Rustler Formation members.

The piezometers themselves are subject to damage and drift. The gages are made by IRAD Gage/Klein and GEOKON. The Management and Operations Contractor reports that readings may have an uncertainty of  $\pm 5$  psi. The gages may even show negative pressure within this  $\pm 5$  psi envelope. However, consistently negative pressures with a trend to more negative values is usually a prelude to piezometer failure. Alternatively, consistently negative pressure readings could possibly indicate an electrical polarity problem during installation and wiring. Despite these problems, the piezometers do give information that must be considered in the interpretation of the hydrogeologic system at the WIPP site. For example, WIPP-21 water levels, measured as part of the H-3 multipad pumping test, show a striking resemblance to the pressure record of the waste-handling shaft as shown on Figure F.8. The exhaust-shaft pressure record also appears to show a response to late October 1986 well-development pumping at well ERDA-9, just south of the shaft (see Figures F.1 and F.6).

#### REFERENCE

U.S. Department of Energy, 1985. Quarterly Geotechnical Field Data Report. Prepared by Bechtel National Inc., WIPP-DOE-218, September 1985.



Drawn by	Date
Checked by	Date
Revisions	Date

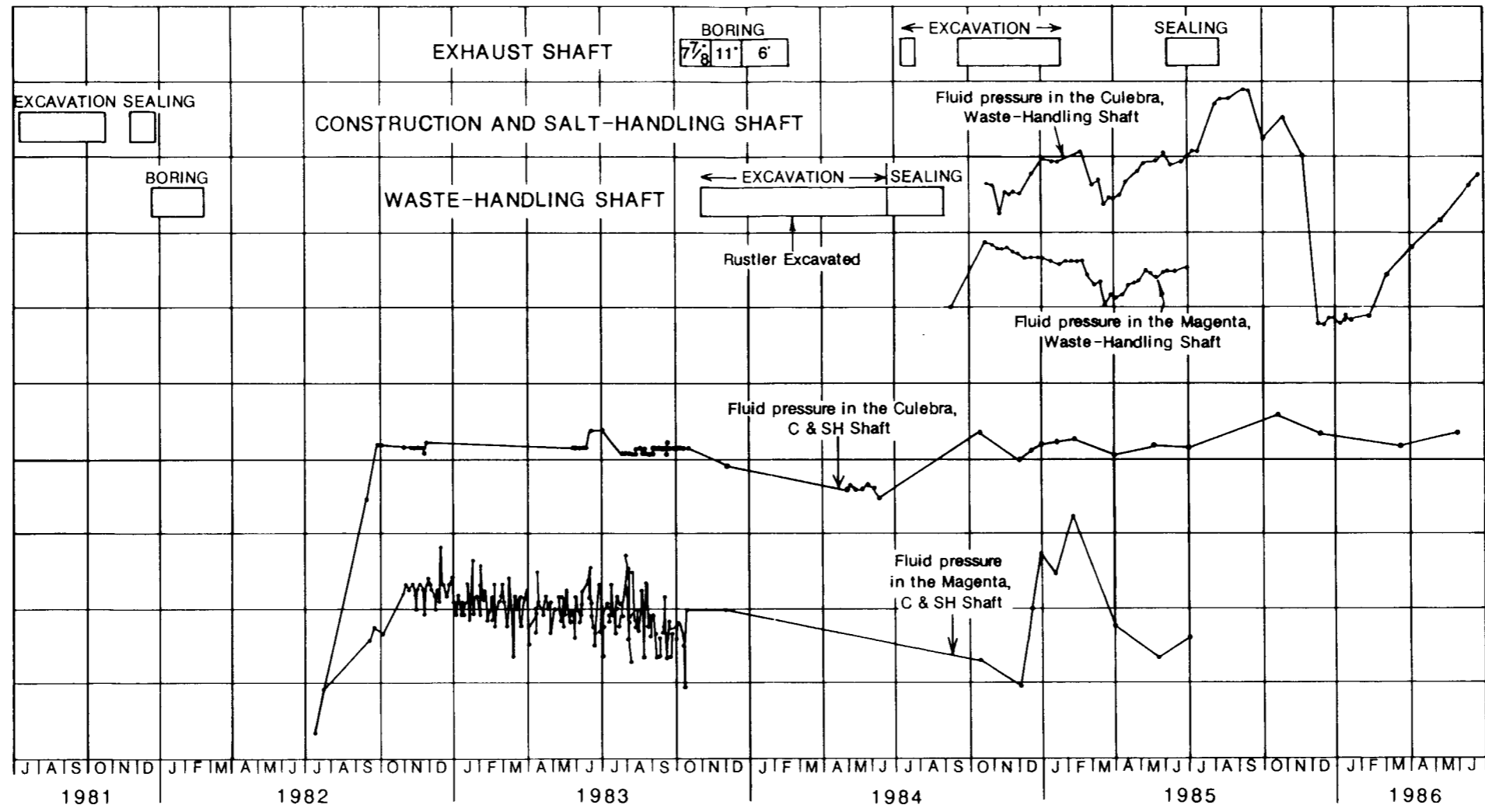
**Location of the Shafts at the WIPP Site**  
 (Modified from U.S. Department of Energy, 1985)

**INTERA Technologies**

Figure F.1

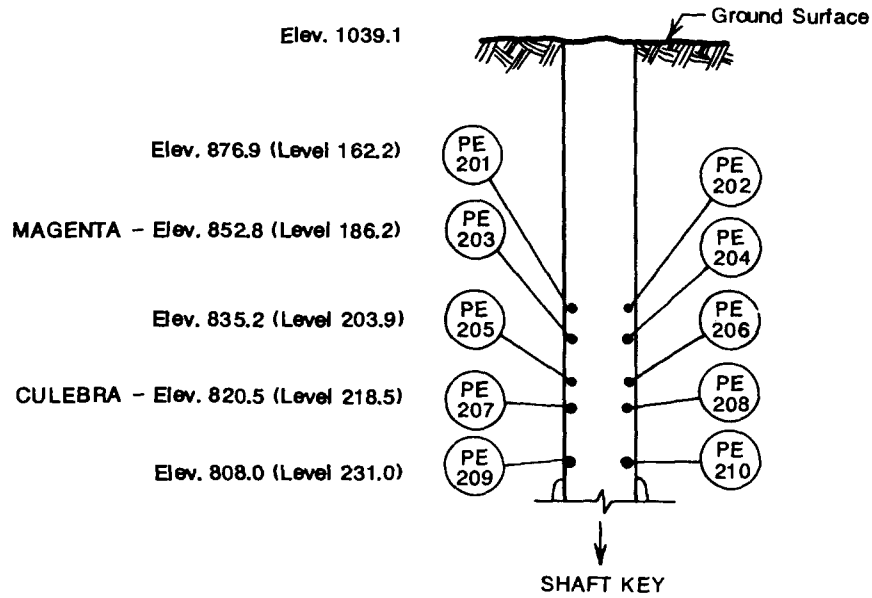




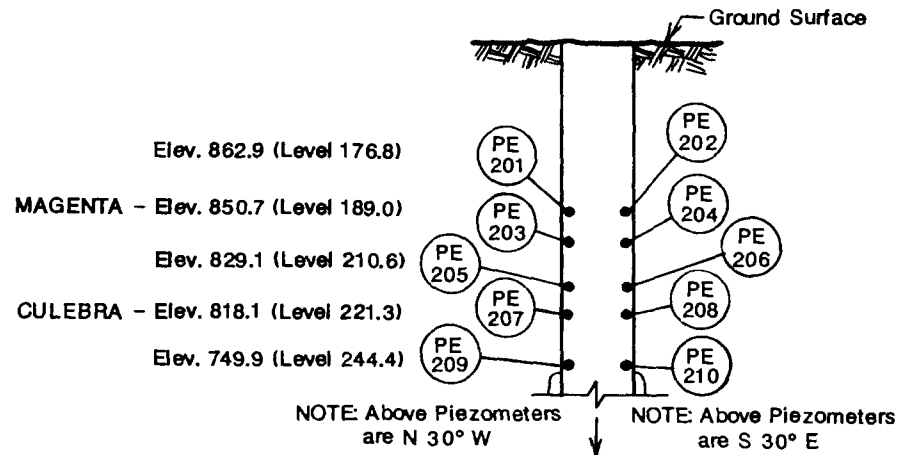


Drawn by	Date	Construction and Sealing Chronology for the Three Shafts at the WIPP Site, with Schematic Representations of Pressure Responses in the Magenta and Culebra Dolomites.
Checked by	Date	
Revisions	Date	
INTERA Technologies		Figure F.2

### WASTE-HANDLING SHAFT



### CONSTRUCTION AND SALT-HANDLING SHAFT



NOTE: Above Piezometers are N 30° W

NOTE: Above Piezometers are S 30° E

⊙ = PIEZOMETER

NOT TO SCALE

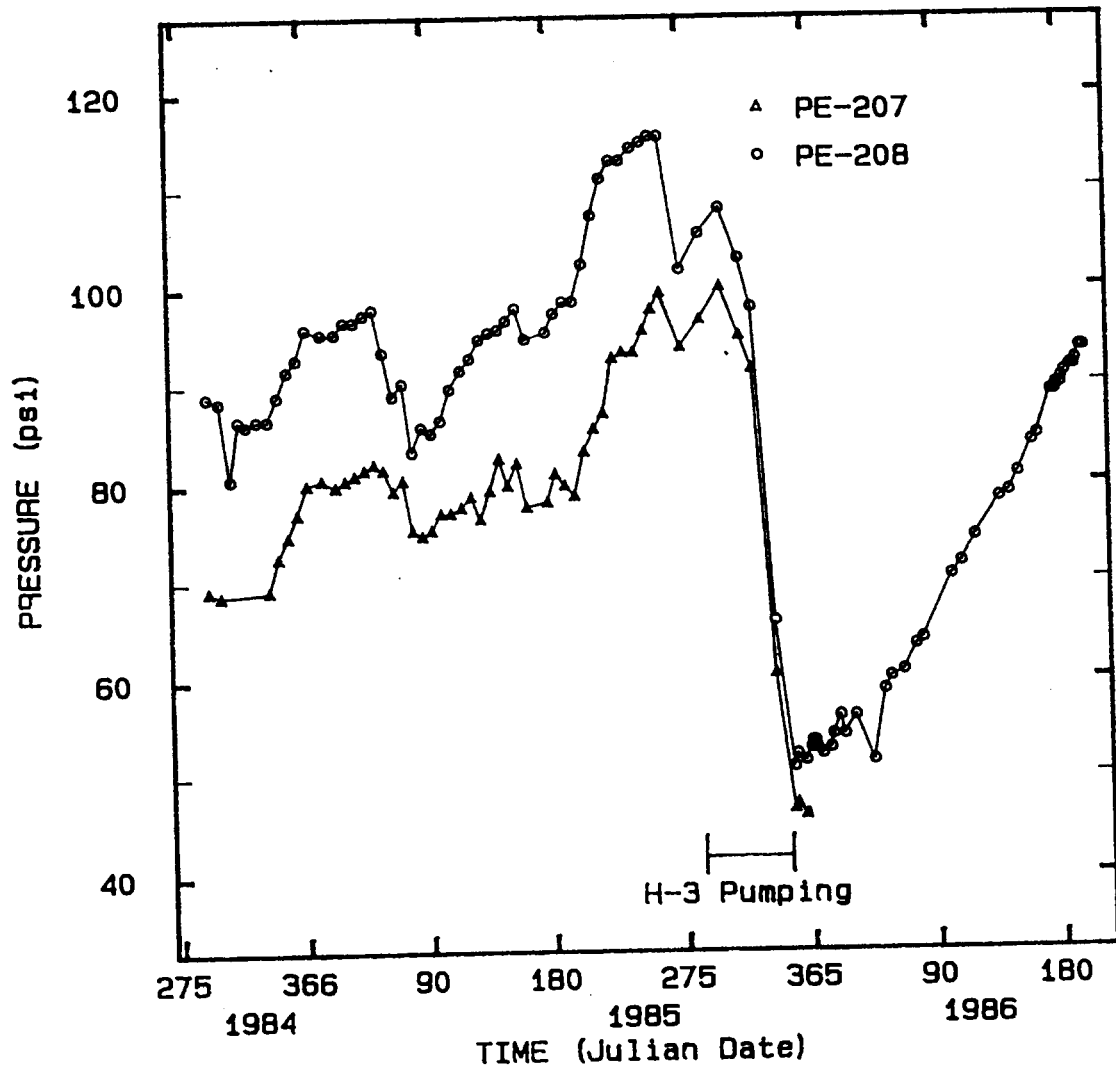
- NOTES
1. The term "Level" is an approximate depth from the top of the shaft bunton at elevation of 1039.4m msl. Elevations are from Cementation West, Inc., 1983, WIPP Shaft and Station Survey.
  2. Elevations and levels are shown in units of meters.

Drawn by	Date
Checked by	Date
Revisions	Date

Piezometer Placement in the Waste-Handling Shaft and the Construction and Salt-Handling Shaft (From U.S. Department of Energy, 1985)

**INTERA** Technologies

Figure F.3

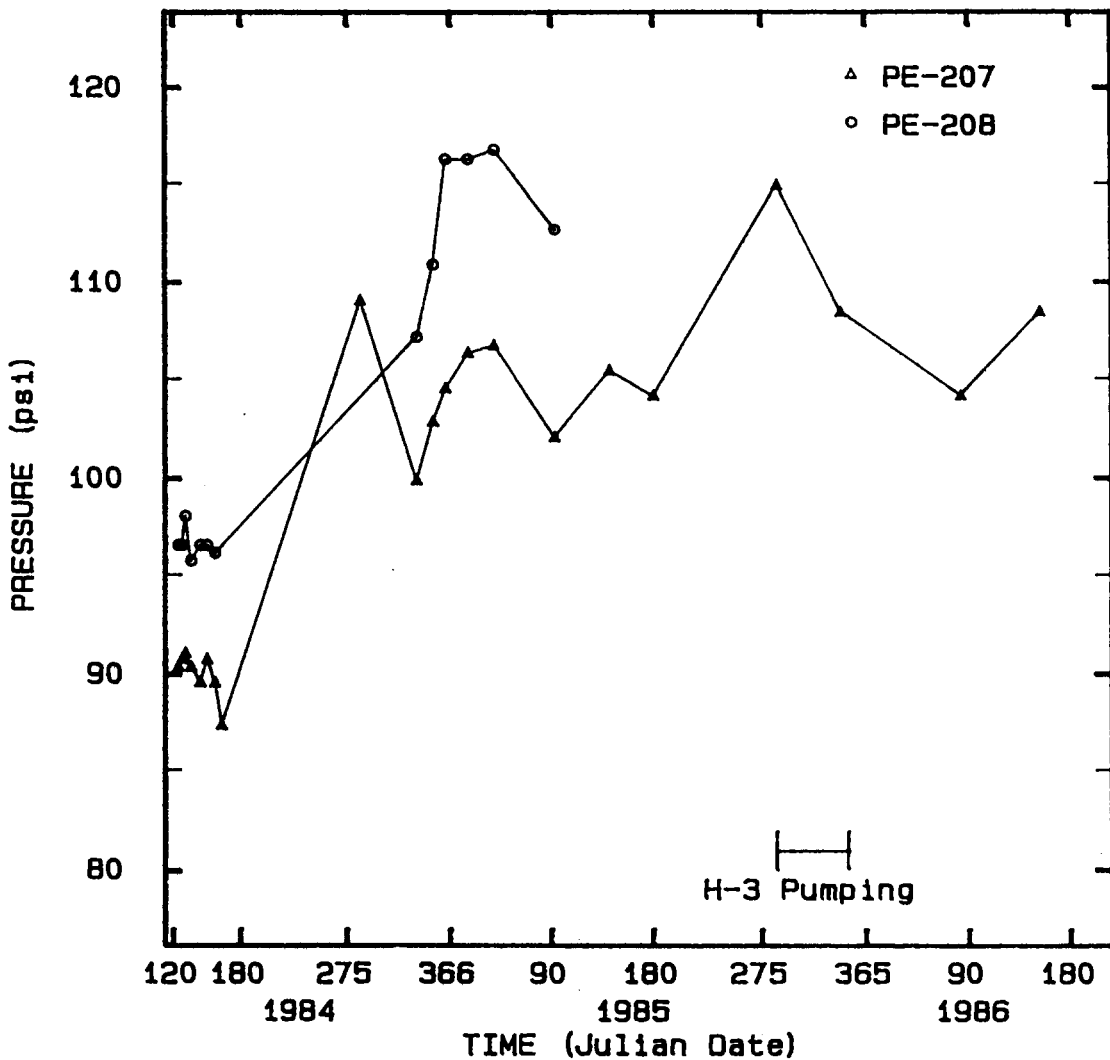


Drawn by	Date
Checked by	Date
Revisions	Date

Piezometer Measurements for the Culebra in the Waste-Handling Shaft

**INTERA Technologies**

Figure F.4



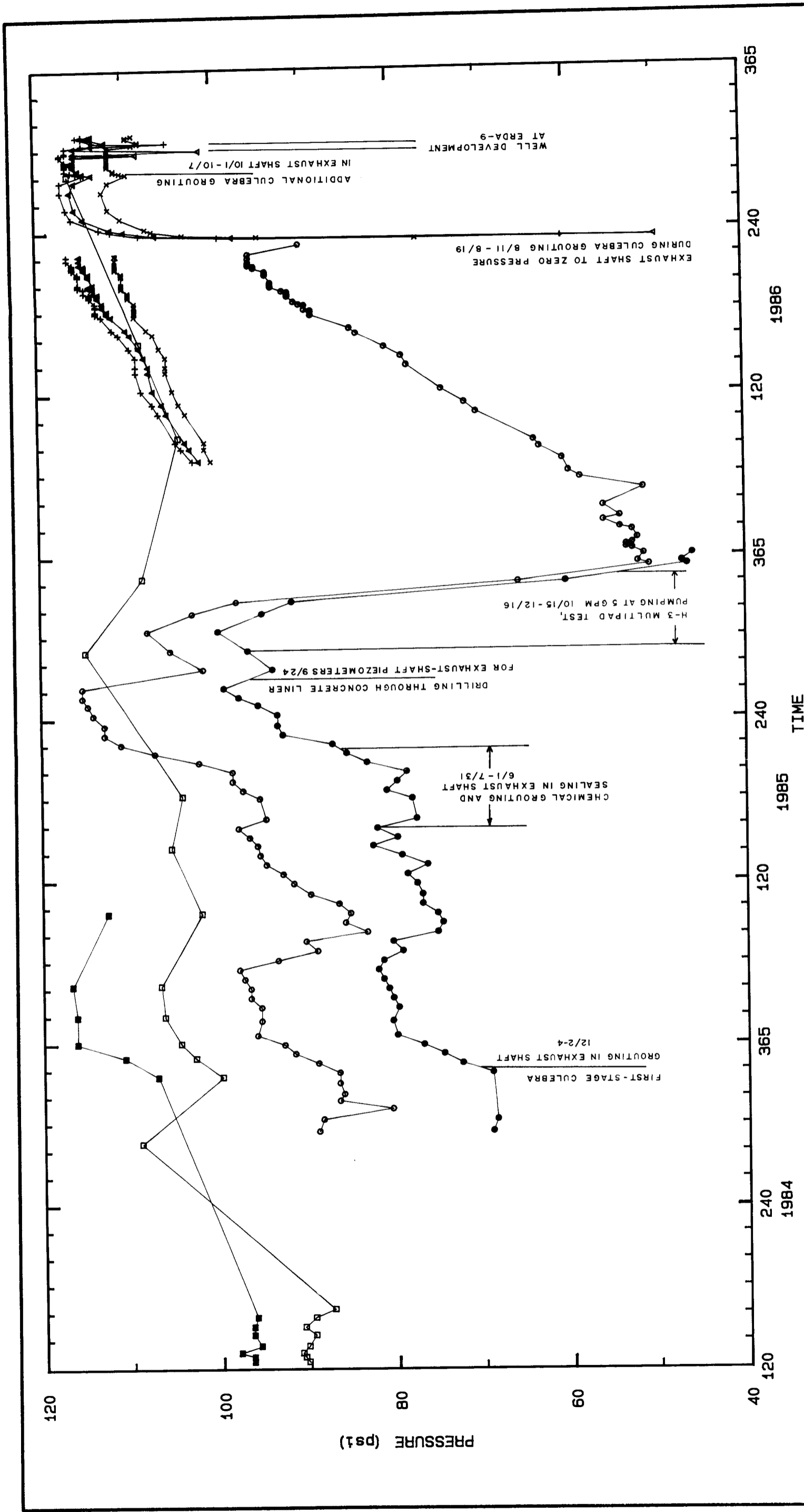
Drawn by	Date
Checked by	Date
Revisions	Date

Piezometer Measurements for the Culebra in the Construction and Salt-Handling Shaft

**INTERA Technologies**

Figure F.5





LEGEND:

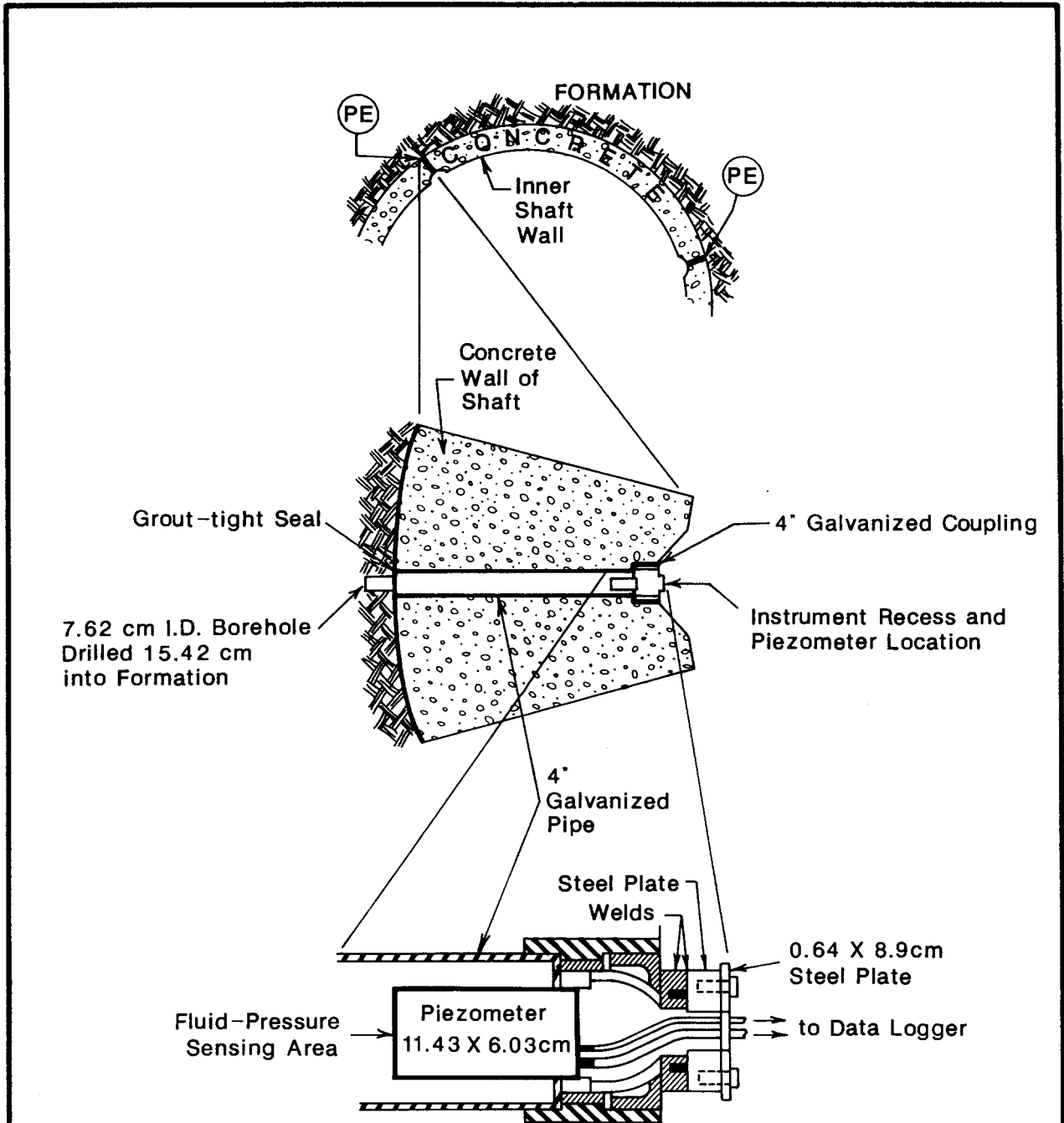
- WASTE SHAFT #207
- WASTE SHAFT #208
- C & SH SHAFT #207
- C & SH SHAFT #208
- + EXHAUST SHAFT #210
- x EXHAUST SHAFT #211
- △ EXHAUST SHAFT #212

Drawn by	Date
Checked by	Date
Revisions	Date

**INTERA Technologies**

Fluid Pressure Measured by Culebra Piezometers in the Construction and Salt-Handling Shaft, the Waste-Handling Shaft, and the Exhaust Shaft.

Figure F.6

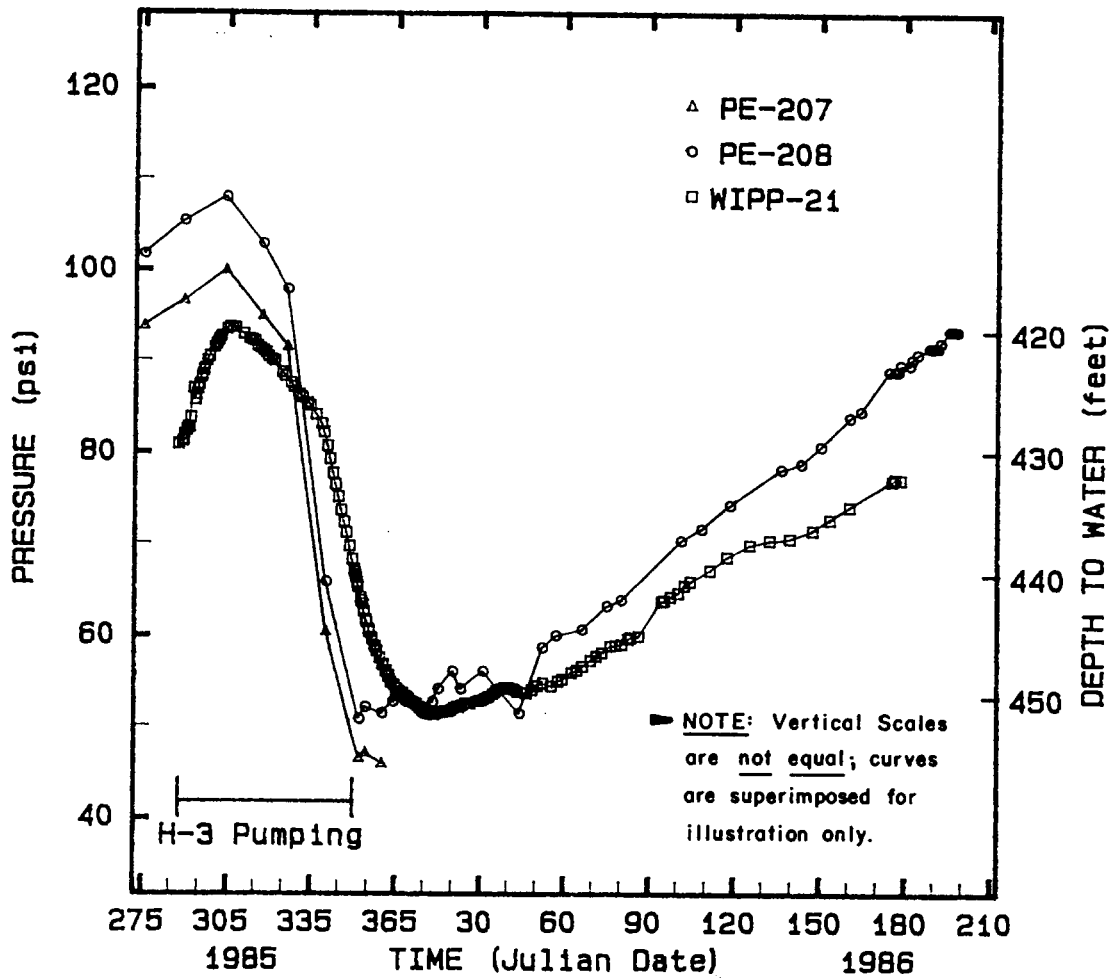


Note: Piezometer (PE) is an IRAD IM-82-6, PWC vibrating-wire and pneumatic gage with stainless-steel housing.

Drawn by	Date
Checked by	Date
Revisions	Date

Details of Piezometer Installation





Drawn by	Date
Checked by	Date
Revisions	Date

Fluid Pressure in the Waste-Handling Shaft and Water Level in WIPP-21 as Measured in the Culebra Dolomite

**INTERA Technologies**

Figure F.8

DATE	DAY	HR	MIN	DURATION (min.sec)	INFLOW (gpm)
01/23/86	23	12	0	0.00	0.47
01/30/86	30	10	0	14.46	0.36
02/05/86	36	13	0	16.07	0.33
02/20/86	51	8	45	17.30	0.30
02/28/86	59	8	45	15.50	0.33
03/07/86	66	9	45	16.00	0.33
03/13/86	72	8	25	17.25	0.30
03/18/86	77	10	30	17.10	0.30
03/26/86	85	13	0	17.05	0.30
04/02/86	92	9	15	18.13	0.29
04/15/86	105	10	30	20.00	0.26
04/25/86	115	12	30	19.10	0.27
05/15/86	135	10	30	23.30	0.22
05/19/86	139	10	35	23.10	0.22
05/22/86	142	11	40	23.20	0.22
05/28/86	148	8	30	23.00	0.23
06/02/86	153	10	30	24.30	0.21
06/06/86	157	8	30	43.00	0.12
06/06/86	157	9	30	42.30	0.12
06/12/86	163	10	20	35.00	0.15
06/19/86	170	9	15	37.30	0.14
06/24/86	175	9	30	23.30	0.22
07/01/86	182	9	30	42.00	0.13

Measurements not possible because of broken plastic pipe.

10/13/86	286	8	40	40.30	0.13
10/28/86	301	9	30	31.30	0.17

Drawn by	Date	<b>Water-Inflow Measurements for the Waste-Handling Shaft</b>
Checked by	Date	
Revisions	Date	
<b>INTERA Technologies</b>		Table F.1



**DISTRIBUTION:**

US Department of Energy (5)  
Office of Civilian Radioactive Waste Management  
Office of Geologic Repositories  
Attn: Associate Director  
    W. J. Purcell, RW-20  
    Director, Repository Coordination Div.  
    T. H. Isaacs, RW-22  
    Director, Engineering & Licensing  
    R. Stein, RW-23  
    Director, Geosciences & Technology  
    R. Stein, Actg., RW-24  
    Director, Siting Division  
    E. Burton, RW-25  
Forrestal Building  
Washington, DC 20585

US Department of Energy (3)  
Albuquerque Operations  
Attn: R. G. Romatowski  
    D. L. Krenz  
    D. G. Jackson, Director, Public Affairs Division  
PO Box 5400  
Albuquerque, NM 87185

US Department of Energy (6)  
Attn: J. Tillman,  
    WIPP Project Office (Carlsbad) (2)  
    G. Pappas, WPO (Carlsbad)  
    A. Hunt, WPO (Carlsbad)  
    R. Eastmond, WPO (Carlsbad) (2)  
PO Box 3090  
Carlsbad, NM 88221

US Department of Energy, SRPO (4)  
Office of Nuclear Waste Isolation  
Attn: J. O. Neff  
    R. Wunderlich  
    G. Appel  
    J. Sherwin  
505 King Avenue  
Columbus, OH 43201

US Department of Energy (2)  
Idaho Operations Office  
Nuclear Fuel Cycle Division  
Attn: R. M. Nelson  
    J. Whitsett  
550 Second Street  
Idaho Falls, ID 83401

US Department of Energy (2)  
Savannah River Operations Office  
Waste Management Project Office  
Attn: S. Cowan  
    W. J. Brumley  
PO Box A  
Aiken, SC 29801

US Department of Energy (3)  
Office of Defense Waste and  
Transportation Management  
Attn: J. E. Dieckhoner, DP-122  
    L. H. Harmon, DP-121  
    A. Follett, DP-121  
Washington, DC 20545

US Department of Energy  
Research & Technical Support Division  
Attn: D. E. Large  
PO Box E  
Oak Ridge, TN 37830

US Department of the Interior  
Attn: E. Roedder  
959 National Center  
Geological Survey  
Reston, VA 22092

US Nuclear Regulatory Commission (2)  
Division of Waste Management  
Attn: M. Bell  
    H. Miller  
Mail Stop 623SS  
Washington, DC 20555

US Geological Survey  
Special Projects  
Attn: R. Snyder  
MS954, Box 25046  
Denver Federal Center  
Denver, CO 80255

US Geological Survey  
Conservation Division  
Attn: W. Melton  
PO Box 1857  
Roswell, NM 88201

**DISTRIBUTION (Continued):**

US Geological Survey (2)  
Water Resources Division  
Attn: H. L. Case  
P. Davies  
Western Bank Bldg.  
505 Marquette NW, #720  
Albuquerque, NM 87102

State of New Mexico (3)  
Environmental Evaluation Group  
Attn: R. H. Neill, Director  
320 Marcy Street  
PO Box 968  
Santa Fe, NM 87503

NM Department of Energy & Minerals  
Attn: K. LaPlante, Librarian  
PO Box 2770  
Santa Fe, NM 87501

New Mexico Bureau of Mines and Mineral  
Resources (2)  
Attn: F. E. Kottolowski, Director  
J. Hawley  
Socorro, NM 87801

Battelle Pacific Northwest Laboratories  
Attn: D. J. Bradley  
Battelle Boulevard  
Richland, WA 99352

Battelle Memorial Institute (13)  
Project Management Division  
Attn: W. Carbiener, General Manager (3)  
J. Treadwell  
T. Naymik  
J. Kirchner  
V. Adams  
O. Swanson  
A. Razem  
S. Gupta  
W. Newcomb  
A. LaSala  
ONWI Library  
505 King Avenue  
Columbus, OH 43201

Bechtel Inc. (2)  
Attn: E. Weber  
M. Bethard  
PO Box 3965  
45-11-B34  
San Francisco, CA 94119

IT Corporation (2)  
Attn: W. E. Coons  
J. E. Zurkoff  
2340 Alamo, SE  
Suite 306  
Albuquerque, NM 87106

IT Corporation (5)  
Attn: W. Patrick  
R. McKinney  
D. Deal  
D. Winstanley  
D. W. Uhland  
PO Box 2078  
Carlsbad, NM 88221

INTERA Technologies, Inc. (24)  
Attn: G. E. Grisak  
J. F. Pickens (5)  
G. J. Saulnier  
V. A. Kelley (5)  
G. E. Freeze  
A. Haug (5)  
INTERA Library  
F. J. Pearson (5)  
6850 Austin Center Blvd., #300  
Austin, TX 78731

INTERA Technologies, Inc.  
Attn: W. Stensrud  
PO Box 2123  
Carlsbad, NM 88221

Martin Marietta Energy Systems, Inc.  
Oak Ridge National Laboratory  
Attn: J. A. Carter  
Box Y  
Oak Ridge, TN 37830

Martin Marietta Energy Systems, Inc.  
Oak Ridge National Laboratory  
Environmental Science  
Attn: E. Bondietti  
X10 Area, Bldg. 1505, Rm. 322  
Oak Ridge, TN 37831

RE/SPEC Inc.  
Attn: P. Gnirk  
PO 725  
Rapid City, SD 57701

RE/SPEC Inc.  
Attn: S. W. Key  
PO Box 14984  
Albuquerque, NM 87191

**DISTRIBUTION (Continued):**

Rockwell International  
Atomics International Division  
Rockwell Hanford Operations  
Attn: W. W. Schultz  
PO Box 800  
Richland, WA 99352

Serata Geomechanics  
Attn: S. Serata  
4124 Lakeside Drive  
Richmond, CA 94806-1941

G. O. Bachman  
Star Route Box 1028  
Corrales, NM 87048

Leonard Minerals Co.  
Attn: B. Donegan  
3202 Candelaria NE  
Albuquerque, NM 87107

Peters Technology Transfer  
Attn: L. Lantz  
PO Box 216  
Swarthmore, PA 19081

Stanford University  
Department of Geology  
Attn: K. B. Krauskopf  
Stanford, CA 94305

Vanderbilt University  
Department of Environmental and  
Water Resources Engineering  
Attn: F. L. Parker  
Nashville, TN 37235

Oak Ridge National Laboratory  
Attn: J. O. Blomeke  
PO Box X  
Oak Ridge, TN 37830

US Geological Survey  
Water Resources Division  
Attn: J. D. Bredehoeft  
Western Region Hydrologist  
345 Middlefield Road  
Menlo Park, CA 94025

K. P. Cohen  
928 N. California Avenue  
Palo Alto, CA 94303

F. M. Ernsberger  
1325 NW 10th Avenue  
Gainesville, FL 32601

Johns Hopkins University  
Department of Earth Sciences  
Attn: H. P. Eugster  
Baltimore, MD 21218

University of New Mexico  
Department of Geology  
Attn: R. C. Ewing  
Albuquerque, NM 87131

University of Minnesota  
Department of Geological Sciences  
Attn: C. Fairhurst  
Minneapolis, MN 55455

University of Texas at Austin  
Department of Geological Sciences  
Attn: W. R. Muehlberger  
Austin, TX 78712

D. A. Shock  
233 Virginia  
Ponca City, OK 74601

National Academy of Sciences  
Committee on Radioactive Waste Management  
Attn: P. Meyers  
2101 Constitution Avenue, NW  
Washington, DC 20418

New Mexico Junior College  
Pannell Library  
Attn: R. Hill  
Lovington Highway  
Hobbs, NM 88240

New Mexico Tech  
Martin Speere Memorial Library  
Campus Street  
Socorro, NM 87810

New Mexico Tech (3)  
Department of Geoscience  
Attn: J. Wilson  
D. Stephens  
C. S. Chen  
Socorro, NM 87801

DISTRIBUTION (Continued):

New Mexico State Library  
Attn: I. Vollenhofer  
PO Box 1629  
Santa Fe, NM 87503

US Geological Survey (2)  
Water Resources Division  
Attn: P. Hsieh  
A. F. Moench  
345 Middlefield Rd.  
Menlo Park, CA 94025

University of New Mexico  
Zimmerman Library  
Attn: Z. Vivian  
Albuquerque, NM 87131

Atomic Museum  
WIPP Public Reading Room  
Attn: G. Schreiner  
Kirtland East AFB  
Albuquerque, NM 87185

Carlsbad Municipal Library  
WIPP Public Reading Room  
Attn: L. Hubbard, Head Librarian  
101 S. Hallagueno St.  
Carlsbad, NM 88220

Thomas Brannigan Library  
Attn: D. Dresp, Head Librarian  
106 W. Hadley St.  
Las Cruces, NM, 88001

Roswell Public Library  
Attn: N. Langston  
301 N. Pennsylvania Avenue  
Roswell, NM 88201

University of Minnesota  
Dept. of Energy and Materials Science  
Attn: R. Oriani  
151 Amundson Hall  
421 Washington Ave SE  
Minneapolis, MN 55455

Texas A&M University  
Center of Tectonophysics  
Attn: J. Handin  
College Station, TX 77840

Texas A&M University  
Department of Geology  
Attn: P. A. Domenico  
College Station, TX 77843

University of British Columbia  
Department of Geological Sciences  
Attn: R. A. Freeze  
Vancouver, British Columbia V6T 1W5  
CANADA

University of Arizona (2)  
Department of Nuclear Engineering  
Attn: J. G. McCray  
J. J. K. Daemen  
Tucson, AZ 85721

University of Arizona  
Department of Hydrology  
Attn: S. P. Neuman  
Tucson, AZ 85721

University of New Mexico (2)  
Geology Department  
Attn: D. G. Brookins  
Library  
Albuquerque, NM 87131

University of Texas at El Paso  
Department of Geological Sciences  
Attn: D. W. Powers  
El Paso, TX 79968

Princeton University  
Department of Civil Engineering  
Attn: G. Pinder  
Princeton, NJ 08504

Scientific Software-Intercomp  
Attn: A. C. Gringarten  
1801 California, 3rd Floor  
Denver, CO 80202

University of California (2)  
Lawrence W. Berkeley Laboratory  
Attn: J. Long  
S. M. Benson  
Berkeley, CA 94720

DISTRIBUTION (Continued):

University of Wisconsin-Madison  
Department of Geology and Geophysics  
Attn: M. P. Anderson  
1215 W. Dayton St.  
Madison, WI 53706

Emcon Associates  
Attn: F. W. Fenzel  
1921 Ringwood Ave.  
San Jose, CA 95131

Gartner-Lee Associates  
Attn: K. G. Kennedy  
Toronto-Buttonville Airport  
Markham, Ontario L3P3J9  
CANADA

Netherlands Energy Research Foundation ECN (2)  
Attn: T. Deboer, Mgr.  
L. H. Vons  
3 Westerduinweg  
PO Box 1  
1755 ZG Petten  
THE NETHERLANDS

Nationale Genossenschaft für die  
Lagerung Radioaktiver Abfälle (3)  
Attn: P. Hufschmied  
C. McCombie  
M. Thury  
Parkstrasse 23  
CH5401 Baden  
SWITZERLAND

1540 W. C. Luth  
1543 W. H. Casey  
6000 D. L. Hartley  
6300 R. W. Lynch  
6310 T. O. Hunter  
6311 L. W. Scully  
6312 F. W. Bingham  
6314 J. R. Tillerson  
6330 W. D. Weart  
6330 Sandia WIPP Central Files (700H IND) (2)  
6331 A. R. Lappin  
6331 R. L. Beauheim (2)  
6331 D. J. Borns  
6331 M. M. Gonzales  
6331 A. L. Jensen  
6331 S. J. Lambert  
6331 K. L. Robinson  
6331 C. L. Stein  
6331 D. Tomasko  
6332 L. D. Tyler  
6332 F. G. Yost

6334 D. R. Anderson  
6334 L. H. Brush  
6416 P. A. Davis  
6416 K. Brinster  
6416 M. D. Siegel  
6431 C. D. Updegraff  
7100 C. D. Broyles  
7120 M. J. Navratil  
7125 R. L. Rutter  
7130 J. D. Kennedy  
7133 R. D. Statler  
7133 J. W. Mercer  
7135 P. D. Seward  
8024 P. W. Dean  
3141 S. A. Landenberger (5)  
3151 W. L. Garner (3)  
3154-1 C. H. Dalin (28)  
For DOE/OSTI (Unlimited Release)